High accurate 3-D photo-robotic nano-positioning for hybrid integrated optics

Houari Bettahar

▶ To cite this version:

Houari Bettahar. High accurate 3-D photo-robotic nano-positioning for hybrid integrated optics. Automatic Control Engineering. Université Bourgogne Franche-Comté, 2019. English. NNT : 2019UBFCD019 . tel-02363255

HAL Id: tel-02363255
https://theses.hal.science/tel-02363255v1

Submitted on 14 Nov 2019

HAL is a multi-disciplinary open access archive for the deposit and dissemination of scientific research documents, whether they are published or not. The documents may come from teaching and research institutions in France or abroad, or from public or private research centers.

L'archive ouverte pluridisciplinaire **HAL**, est destinée au dépôt et à la diffusion de documents scientifiques de niveau recherche, publiés ou non, émanant des établissements d'enseignement et de recherche français ou étrangers, des laboratoires publics ou privés.

THESE DE DOCTORAT DE L'ETABLISSEMENT UNIVERSITE BOURGOGNE FRANCHE-COMTE

PREPAREE A L'UNIVERSITÉ DE FRANCHE-COMTÉ

Ecole doctorale n°37

Science Pour l'Ingénieur et Microtechnique

Doctorat d'Automatique

Par

Houari BETTAHAR

High accurate 3-D photo-robotic nano-positioning for hybrid integrated optics.

Thèse présentée et soutenue à Besançon, le 18/07/2019

Composition du Jury :

Yassine HADDAB	Professeur des Universités, Université de Montpellier	Rapporteur
Frédéric LAMARQUE	Professeur des Universités, Université de Technologie de Compiègne	Rapporteur
Marcel TICHEM	Associate Professor, Delft University of Technology	Examinateur
Philippe ADAM	RDS, Direction Générale de l'Armement (DGA), Paris	Examinateur
Maria-Pilar BERNAL	Directrice de recherche CNRS, Institut FEMTO-ST, Besançon	Présidente
Olivier LEHMANN	FEMTO engineering, Institut FEMTO-ST, Besançon	Invité
Philippe LUTZ	Professeur des Universités, Université de Bourgogne Franche-Comté	Directeur de thèse
Cédric CLEVY	Maître de Conférences HDR, Université de Bourgogne Franche-Comté	Codirecteur de thèse
Nadège COURJAL	Maître de Conférences HDR, Université de Bourgogne Franche-Comté	Codirecteur de thèse

ACKNOWLEDGEMENTS

Firstly, I would like to express my sincere gratitude to my advisors, Dr. Philippe LUTZ, Dr. Cédric CLÈVY and Dr. Nadège COURJAL. Without their assistance and dedicated involvement in every step throughout the work, this PhD thesis would have never been accomplished. I would like to thank you very much for your support and understanding over these past four years.

My sincere thanks also goes to Olivier LEHMANN for his help during my thesis, especially for the robotic part of my thesis work. Without forgetting Alexis CASPAR and Florent BEHAGUE for their help for the optical part of my thesis.

I would not take the risk of then mentioning all those who helped me during this thesis within the department, for fear of forgetting some. I would like to think all those who have contributed to my work, those who made mechanical parts for me, those who allowed me to take a stepbacks, those who trained me on how research works, those with whom I simply had a good laugh. Thank you for everything the AS2M department, to all those who have been there since my arrival to those who will probably see my departure.

Many thanks to the members of my thesis jury, Yassine HADDAB, Frédéric LAMARQUE, Marcel TICHEM, Philippe ADAM and Maria-Pilar BERNAL for having agreed to evaluate my work and for the very interesting discussions that took place following my presentation.

Last but not the least, I would like to thank my family: my parents, my brothers and sisters for supporting me spiritually throughout writing this thesis and my life in general.

CONTENTS

List of abbreviations

DOF	Degree-Of-Freedom
SEM	Scanning Electron Microscope
CAD	Computer-aided design
FP	Fabry-Perot
MCS	Modular Control System
NC-AFM	Non-Contact Atomic Force Microscopy
3-D	3-Dimensions
MOB	Micro-Optical Bench
MEMS	Microelectromechanical systems
OCT	Optical coherence tomography
SMF	Single Mode Fiber
PCF	Photonic Crystal Fiber
PSA	Polarization State Analyzer
PSG	polarization state generator
MME	Mueller matrix ellipsometer
SiOB	Silicon Optical Bench
InP	indium phosphide
DGM	Direct Geometric Model
IGM	Inverse Geometric Model
DOP	Degree Of Polarization
FLP	Focusable Laser Point
PSD	Position Sensor Detector
CMM	Coordinate Measurement Machine
RCP	Right Circular Polarization
LCP	Left Circular Polarization
MgF_2	Magnesium fluoride
$LiNbO_3$	Lithium niobate

Main notations

E	Electric field
E_x	Electric field projection on the X-axis
E_y	Electric field projection on the y-axis
δ	Phase shift between E_x and E_y
λ	Wavelength of the electric field wave
T	Period of the electric field wave
ω	Angular frequency
k	Propagation constant
χ	Ellipticity angle
ψ	Orientation angle
S_0, S_1, S_2, S_3	Stokes parameters
L	Fabry-Perot cavity distance
R_w	Word reference frame
R_f	Fiber reference frame
R_t	Lamella reference frame
R_e	End-effector reference frame
T	Homogeneous transformation matrix
$Rot_X(\alpha)$	Rotation of α around the X-axis
$Trans_X(d)$	Translation of d along the X-axis
${}^{i-1}T_i$	Transformation matrix of the frame i with respect to frame $i-1$
q	Vector of joint coordinates
X	Vector of operational coordinates
P_r	Reflection point projection on the lamella plane
${}^{t}P_r$	Reflection point translational coordinates with respect to lamella reference frame
${}^{w}P_r$	Reflection point translational coordinates with respect to world reference frame
$\delta\lambda_{FSR}$	The free spectral range
ϵ	Intrinsic parameters error

GENERAL INTRODUCTION

Achieving fast, automated 3D complex tasks of micro-manipulation and micro-assembly with very high accuracy is strongly desired in many application fields, such as advanced integrated optics manufacturing (to achieve commercial success with reliable and cost-effective assembly, and packaging technologies). Many emerging industrial on-demand applications made the field of integrated optics particularly challenging, because of their increasing functions and complexity that require the integration of various building components fabricated from different technologies in order to achieve wide kinds microsystems. The possibility to achieve hybrid nano-photonic components by assembly feeds many original applications and it brings very relevant solutions to overcome the monolithical integration difficulties and to achieve 3D multi functions optical devices fabricated with different technologies [Agnus et al., 2013], [Zimmermann et al., 2011], [Benson, 2011]. Micro-assembly also enables to optimize the optical performances. Moreover, it permits the development of complex integrated optical devices, from different optical functionalities, which are assembled to form an integrated optical system.

Positioning and assembly for integrated optics industry is generally done manually based on passive and active positioning for many applications. In passive positioning, operator may use geometrical devices such as V-groove, or visual systems such as microscope or binocular to provide visual geometrical information which are used for positioning. However the optical performances are not guaranteed and the offered accuracy is not sufficient for many applications. For these reasons, the active approach is the mainly used for integrated optics industry and mostly in manual way. Micro and nano-positioning systems are used to adjust the position of the optical component in order to obtain the maximum optical irradiance. This requires dexterity and skills of the operator and a lot of precision and attention which is a tiring task for the operator. The repeatability and accuracy of the positioning may reach some μm but at a high cost due to the training of the human operator and the long time needed to achieve the task. Consequently, the performances and the quality of the assembled products are strongly operator-dependent. There are numerous very accurate machines like flip-chip that are used in integrated optics industry, but these technologies are limited to a specific type of products. In order to help human to get access to the usually inaccessible world, micro-robotic and micro-manipulation researches conducted in the last decade have led to the development of micro-robotic cells with sensing and control techniques.

Micro-robotic approaches enable to position a frame of a robot, typically an end-effector to the desired location through referenced robotic motions. To successfully perform micro-tasks, micro-systems or micro-robots with high positioning accuracy are required. However, this condition is difficult to obtain at the micro-scale, because of many extrinsic and intrinsic geometric parameters acting on micro-robots. The extrinsic geometric parameters are the parameters relating the robot end-effector to tool frame, world frame and measurement system frame. The intrinsic geometric parameters are the parameters due to assembly errors of different stages of the robot like perpendicularity, offset, length and parallelism errors. These extrinsic and intrinsic parameters affect the positioning accuracy. Robot calibration is a systematic way to identify and compensate these parameters and enhance positioning accuracy. However, at the micro-scale, there are lots of challenges to perform measurement meeting all requirements, i.e., resolution, accuracy, and range, etc. These challenges include sensing resolution, accuracy, range, bandwidth, sensor size, and multi-DOF (Degree-Of-Freedom). Moreover, there is a lack of knowledge at the micro-scale to succeed in reaching high positioning accuracy.

For this sake, an original photo-robotic approach has been proposed, relying on multi-DOF robot motion associated with the use of 1-D Fabry-Perot interferometry measure, to realize multi-DOF pose measure. This approach notably integrates the issue of 6-DOF robot calibration that has been studied through extrinsic and/or intrinsic geometric parameters calibration. In order to find the appropriate calibration strategy for high positioning accuracy and adapted to the context of micro-positioning of optical components, a quantification and durability analysis of optical and robotic performances has been investigated. Experimental investigations demonstrate that a rotational and translational positioning accuracy of 0.004 ° and 27.6 nm have respectively been obtained. This photo-robotic approach has especially been applied to achieve the 6-DOF positioning of an optical lamella relative to an optical fiber with high accuracy that also conduct to maximum optical performances. The approach has also been applied to control the optical polarization states at the output of an hybrid optical system through achieving high accurate rotations of a specific optical wave plate around the optical axis. The experimental results notably demonstrate that the high positioning accuracy enables to accurately control of the optical polarization state.

The document is organized in the following way:

In chapter 1, robotic positioning in micro and nano-scale is discussed by highlighting the existing challenges of applications in the state-of-art. To address these challenges, integrated optics field is chosen based on two reasons: the emerging on-demanding applications and high accuracy needs. These reasons justify the requirements and the thesis objectives to develop a robotic approach to realize a full automated and high accurate 6-DOF positioning of optical components for optimal optical performances.

In chapter 2, Fabry-Perot interferometry phenomenon happens during active alignment of optical components for integrated optics. Here, we are particularly interested in positioning an optical lamella with respect to an optical fiber. First, Fabry-Perot interferometry is presented. Then active alignment is discussed and analyzed by highlighting the geometric parameters that influence the Fabry-Perot interferometry figure. This analysis leads then to propose a new photo-robotic approach to achieve high accurate robotic positioning with high optical performances. This approach is based on the correlation between Fabry-Perot interference figure and a referenced robot multi-DOF motion, to achieve multi-DOF pose measure and to position then the optical lamella relative to the optical fiber, in order to reach maximum optical irradiance.

To go further, this chapter reviews the parameters that can affect the positioning accuracy. This leads to deal with geometric parameters calibration in order to improve the positioning accuracy. Afterward, the geometric parameters calibration steps: modeling, measurement, identification and correction are discussed. In this chapter, calibration for macro and micro-nano robotics is also reviewed, by discussing their calibration approaches. This enables to identify which calibration approaches that could be adapted for micro-nano robot calibration. In order to improve positioning accuracy, a robot extrinsic parameters calibration based on a photo-robotic approach is proposed. The photo-robotic approach relates a 1-D relative distance with a multi-DOF robot motion in order to identify extrinsic geometric parameters. The 1-D relative distance is realized based on high accurate Fabry-Perot interferometry principle. In order to validate our proposed approach, the experimental procedure for extrinsic robot calibration and the experimental set up dedicated for 6-DOF positioning of optical components are presented. Finally, the obtained results are discussed.

In chapter 4, A generalized photo-robotic approach for extrinsic and intrinsic parameters calibration of a 6-DOF robot is proposed. This approach relates a 1-D relative distance with a multi-DOF robot motion in order to identify extrinsic and intrinsic geometric parameters based on a generalized photo-robotic calibration model. A dedicated measurement strategy is proposed to cover the work space and to achieve a rich measurements with high accuracy. In order to validate the approach, the proposed experimental procedure is presented. The behavior study of the full calibrated robot is discussed based on the obtained experimental results. Finally, in order to find the appropriate calibration strategy for high positioning accuracy and adapted to the context of micro-positioning of optical components for high optical performances, a quantification knowledge is realized, by investigating and evaluating durability and performances of the fully calibrated robot.

In chapter 5, our objective is to integrate a thin wave plates (thickness $< 1\mu$m) inside a photonic waveguide, by taking advantage of the specific properties of wave plates hosted in a properly chosen material to modify the polarization state of light. The wave plate is attached to the calibrated robot presented in chapter 4. Rotating the phase wave plate provides different polarization states, which leads to control the polarization in order to reach the desired polarization state. After having controlled the polarization state, the wave plate is assembled to the optical system. For this sake, a dedicated experimental setup is implemented. In order to see the birefringence effect on polarization, a mirror is compared with a wave plate by rotating them around the optical axis and compare their results. Then polarization states repeatability is investigated. Finally polarization control is investigated based on non-calibrated robot, calibrated robot and calibrated robot with misalignment angle.

Finally, a general conclusion presents a summary of the results and contributions arising from this work. Some future works are outlined.

1

MICRO/NANO ROBOTIC POSITIONING FOR INTEGRATED OPTICS

1.1/ INTRODUCTION

Over the last two decades, many social, industrial or scientific issues associated to micro-objects and miniaturized systems have been significantly developed. They concern today very diverse fields such as space, instrumentation, telecommunications, surgery, biology, robotics, mechanics. One challenge is focused on mastering the micro-world by studying their behavior or characteristics. The second challenge is of more technological nature since it consists in proposing always smaller, smarter and more versatile functionalities.

For example, commercial systems presented in Figure 1.1 (a), (b), (d) represent three different integrated optical systems and Figure 1.1 (c) represents a miniaturized assembled sensor called KolibriSensor for ultimate non-contact atomic force microscopy. Theses systems result from the synergy between technologies of manufacturing of elementary components and means of micro-assembly of these elementary components to constitute a complex final system. For these systems, a small assembly error can result in functional problems in the assembled product. For the three different integrated optical systems, the assembly errors have to be less than half wavelength ($< 1\mu$m). The metallic tip of the KolibriSensor is about 7 μm. An error in it assembly can change considerably it oscillation frequency.

The realization of this type of complex products represents today one demanding purpose. The use of micro-robotic positioning and assembly is a particularly interesting and original approach, which can reach higher positioning accuracy with higher functional performances compared to the existing approaches.

Realizing 3-D complex tasks of micro-manipulation and micro-assembly involves positioning of one or more micro-objects with very high accuracy [Clévy et al., 2014] [Bettahar et al., 2016] [Gauthier et al., 2015]. Manual micro-positioning is one of the existing approaches used for micro-manipulation and micro-assembly. It consists of a human who uses some tools such as mechanical tweezers and/or micro and nano-positioners for handling and motion and uses microscope or binocular in order to see what's happening. It requires dexterity and skills of the operator and a lot of precision and attention which is a tired task for the operator. Furthermore, the accuracy of the positioning may reach some μm but at a high cost due to the training of the human operator and the long time needed to achieve the task. Consequently, the performances

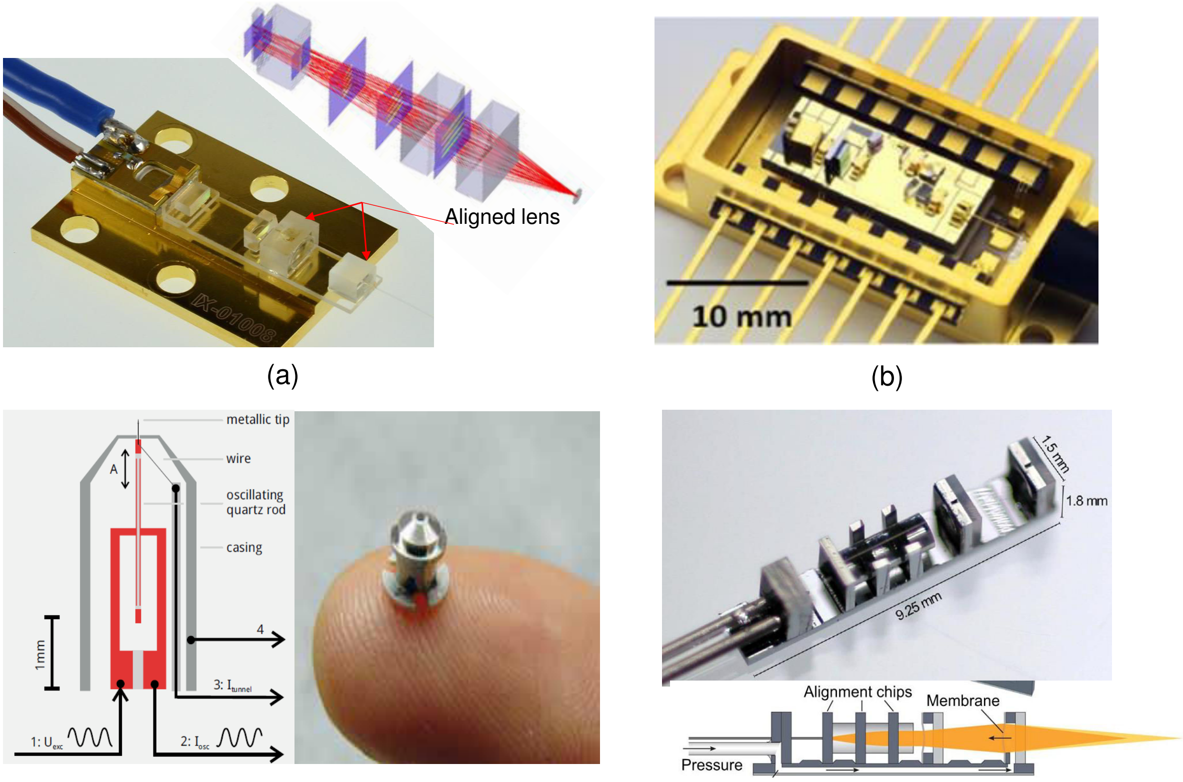

(a) (b)

(c) (d)

Figure 1.1: (a) Assembled multi-emitter/multilens/fiber[Böttger et al., 2016] (b) Assembled micro-optical bench (American company AXSUN) (c) KolibriSensor [Torbrügge et al., 2010] (German company SPECS) (d) Assembled optofluidic microsystem [Weber et al., 2012].

and the quality of the assembled products are variables. Furthermore, the commercial success of these products are limited and without reliable and cost-effective assembly and packaging technologies. There are numerous very accurate machines like flip-chip that are used in integrated optics industry, but this technology is limited to a specific type of products. For these reasons, researches conducted in the last decade have led to the definition of micro-manipulation and micro-assembly techniques, and the development of micro-positioning systems in order to assist the human operator for the handling and the positioning and then assembly of such micro-parts. Based required positioning accuracy, robotic micro-positioning can be categorized in terms of level of human intervention to teleoperated or automated as described below [Komati, 2014].

In teleoperated micro-positioning, a human operator controls a robotic station to perform the positioning task. The operator uses different types of sensors and visual systems in order to visualize the micro-part in order to grasp and then to position it in the desired position, i.e., the human is the loop. He makes the feedback. Once the micro-part is positioned at the final position, this position should be maintained by fixing the micro-part using several techniques.

Automated micro-positioning is used to achieve repeatable and fast micro-assembly process. The automation can be done using two principles:

- open loop control which consists of identifying and compensating the micro-positioning systems imperfections in order to improve the positioning accuracy, to perform successful micro-tasks. However, this condition is difficult to obtain at the micro-scale, because mainly, of many extrinsic and intrinsic geometric parameters and drift [Shiakolas et al., 2002] , [Veitschegger et al., 1986]. These parameters are acting on the micro-positioning systems. The extrinsic geometric parameters are the parameters relating the end-effector frame of the micro-positioning system to tool frame, world frame and measurement system frame. The intrinsic geometric parameters are the parameters due to assembly errors of different stages of the robot like perpendicularity, offset, length and parallelism errors. These extrinsic and intrinsic parameters combined affect the positioning accuracy. micro-positioning systems calibration is a systematic way to identify and compensate these parameters and enhance positioning accuracy.

- closed loop control using position and/or force feedback [Tamadazte et al., 2011] [Kratochvil et al., 2009] [Komati, 2014] [Komati et al., 2016]. Position sensors and/or vision feedback are used to measure the positions of the micro-part to be manipulated, the micro-gripper and the substrate. The force sensor may measure the interaction forces between the micro-part and the substrate as well as gripping forces. Hybrid force/position assembly uses the information of both the force and the position sensors [Guelpa et al., 2015].

In this chapter, issues and interests of micro-scale robotic nano-positioning for micro-manipulation applications are investigated. Then, the choice of integrated optics as a targeted application field is justified by analyzing the high 6-DOF positioning need for high optical performances based on the existing alignment approaches. Finally, theses analysis conduct to present the objective of the PhD thesis, which is the realization 6-DOF high accurate photo-robotic nano-positioning for integrated optics assembly. Robotic micro and nano-positioning for micro-manipulation in different application fields is investigated in the next section.

1.2/ ISSUES AND INTERESTS OF MICRO-SCALE ROBOTIC NANO-POSITIONING FOR MICRO-MANIPULATION

Robotic micro and nano-positioning appears as a powerful approach to develop systems at the micro-metric and nano-metric scales. In what follows, we propose an overview of the possibilities offered by robotic positioning, and we also show the current limitations to overcome:

- **Robotic manipulation based on visual control inside the SEM**

Many works in many application fields using robotic micro-positioning are present in the literature. The manipulation and assembly of colloidal particles offer a wide variety of micro- and nano-sized particle systems in terms of chemical and physical properties [Nie et al., 2010][Reiss et al., 2009]. If individual colloidal particle is arranged in specific spatial order, they can collectively interact electronically or with incident light waves, enabling novel applications for photonics, plasmonics or sensors. Automated robotic manipulation of Colloidal particles applying SEM supported vision-based control has been realized as shown in Figure 1.2 and in Figure 1.3 [Zimmermann et al., 2015]. Using scanning electron microscope (SEM) as visual feedback control information offers high accuracy, but it has very limited field of view and it is limited to the use of only conductive materials. Limited or non-conductive material samples require carbon and/or metal coating in order to avoid electrons discharge, which can change the physical properties of the materials.

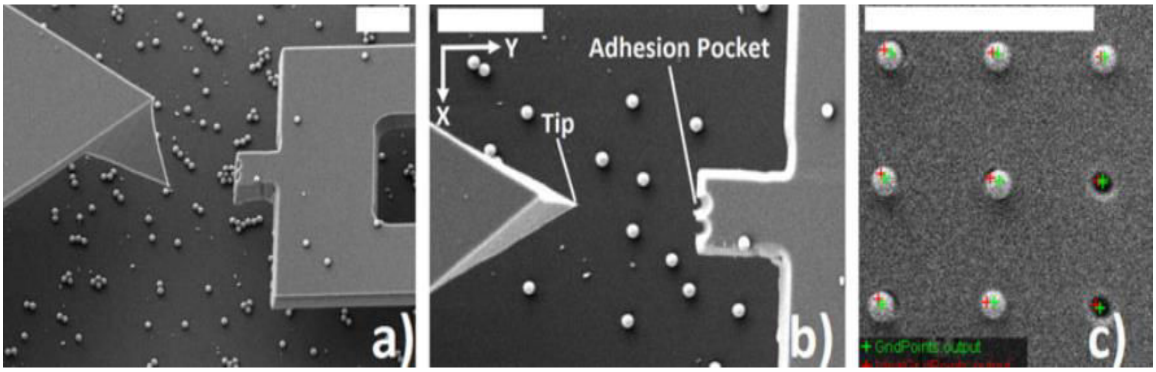

Figure 1.2: Scanning electron micrographs of: (a) two end effectors in side-view on top of the silica spheres, (b) two end effectors in top-view on top of the silica spheres, and (c) partially filled 2-D hole pattern on the target substrate as an excerpt from the automation sequence [Zimmermann et al., 2015]. Scale bar: 10 μm.

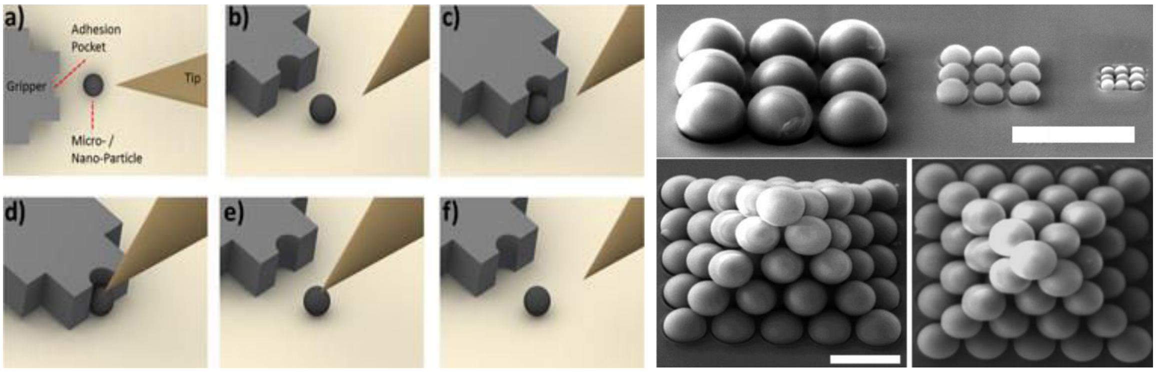

Figure 1.3: (left) Illustration of the robotic handling strategy. (a) Two end effectors are tailored to act as gripper or placer (tip). (b) and (c) Picking process and (d)–(f) placing and releasing process. (right) Scanning electron micrographs of silica particles with diameters of 1160, 519, and 237 nm inserted into a 2-D pattern (above) and scanning electron micrographs of 55 silica spheres with an average diameter of 1160 nm stacked to a 3-D pyramidal structure (below) [Zimmermann et al., 2015]. Scale bar: 2 μm.

- **Robotic positioning combined with self-alignment**

In some applications, robotic positioning is combined with self-alignment using capillary forces as presented in [Sariola et al., 2010]. A micro-gripper is used to position the micro-part near the desired position and the fine positioning (self-alignment) is performed by a water droplet. The positions of the water droplets are micro-fabricated which reduce the positioning error. Water droplets compensate the errors induced by a non precise robotic system. The micro-assembly steps and the handling techniques are shown in Figure 1.4. The dimensions of the tested micro-part go from 50 μm $\times$ 50 μm $\times$ 40 μm up to 300 μm $\times$ 300 μm $\times$ 70 μm. The yield of the assembly can reach more than 99% and the duration of self-alignment process was measured to range from 50 to 500 ms with a lateral accuracy of 0.8 μm. But still angular misalignment between the assembled micro-parts represents a problem for many photonic applications. And also, using water droplet can change the optical medium index between the two micro-parts which can reduce the optical performance of the assembled photonic system.

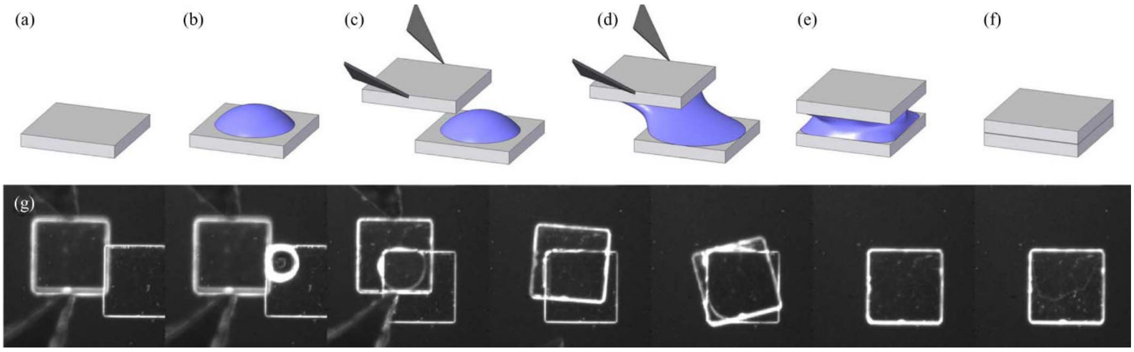

Figure 1.4: Hybrid handling technique [Sariola et al., 2010]. (a) Assembly site is on top of a micro-part. (b) Droplet of water is dispensed on the bottom part. (c) Micro-gripper approaches the release site with a part. (d) Droplet contacts with the top part and wets between the parts, which forms a meniscus. (e) Micro-gripper releases the part and the capillary force aligns the parts. (f) Water between the two parts evaporates, which leaves the two parts aligned. (g) Image sequence of the actual experiment, as viewed from the top side.

- **Robotic micro-assembly of photonic structures**

These is a new fabrication technology for a semiconductor 3-D photonic crystal which combines integrated circuit processing technology with micro-manipulation. This approach has been the subject of a particularly interesting proof of concept through the realization of a multi-layer [Aoki et al., 2003] as shown in Figure 1.5. In order to create air between the layers, four optical balls were put between each two layers. The manipulation principle here is dedicated to the same realized task using teleoperated approach, where human expertise is necessary to accomplish the task. This makes the approach not easily transposable to other tasks. Hence new versatile robotic solutions that can increase the positioning accuracy in multi-DOF way with reduced task time can be a promising solution for commercial success of these optical assembled products with reliable and cost-effective assembly.

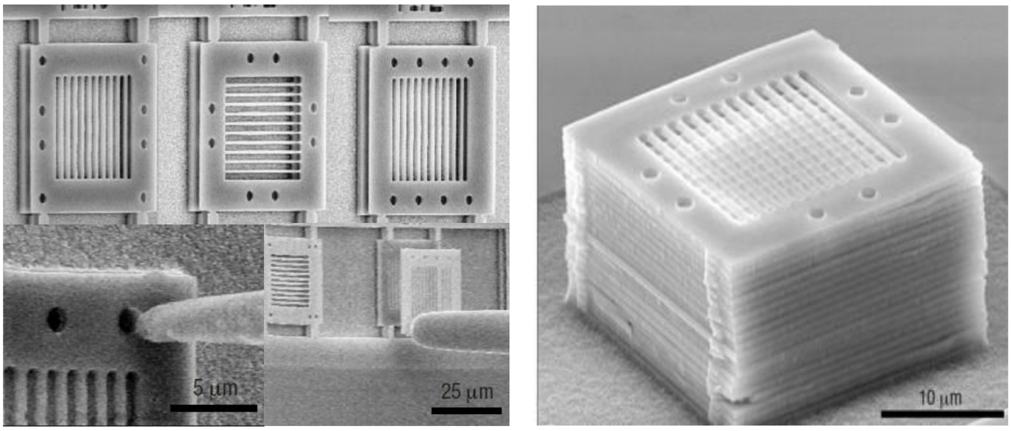

(a) (b)

Figure 1.5: (a) Teleoperated assembly of 2D crystal structures. (b) 3-D photonic component resulting from the assembly of 20 piled 2D crystal structures [Aoki et al., 2003]
.

- **Robotic micro-positioning to fabricate micro-optical benches (MOB)**

Some results published in [Clévy et al., 2014] show the measurement of positioning accuracies of micro-scale components assembled to fabricate micro-optical benches (MOB). The concept of MOB is presented in Figure 1.6. It clearly shows that micro-assembly is a possible way to fabricate complex, heterogeneous and 3-D optical MEMS with very good positioning accuracy up to 0.1°. The realized task in this work is teleoperated, based on CAD model and stereo vision to estimate the position in 3-D space. The work is realized for a specific complex task, based on human expertise for positioning. The further step is to propose a full automated robotic approach that can offer a very good solution, to realize repeatable tasks without human intervention with very high accuracy.

In summary, micro/nano-robotics have importantly impacted our life by offering new ways and opportunities for studying micro and nano-scale, to achieve commercial success with reliable and cost-effective assembly and packaging technologies, in many application fields, such as advanced manufacturing, high precision manipulation, material characterization, biological cell manipulation. For recent emerging on-demanding applications especially in integrated optics field, robotic micro/nano-positioning/assembly is an original approach, where the positioning accuracy is the main key for realizing successful micro-manipulation tasks. From the other side, the success of the realized micro-task relies on diverse and significant scientific and technical challenges, which will be discussed in the next section.

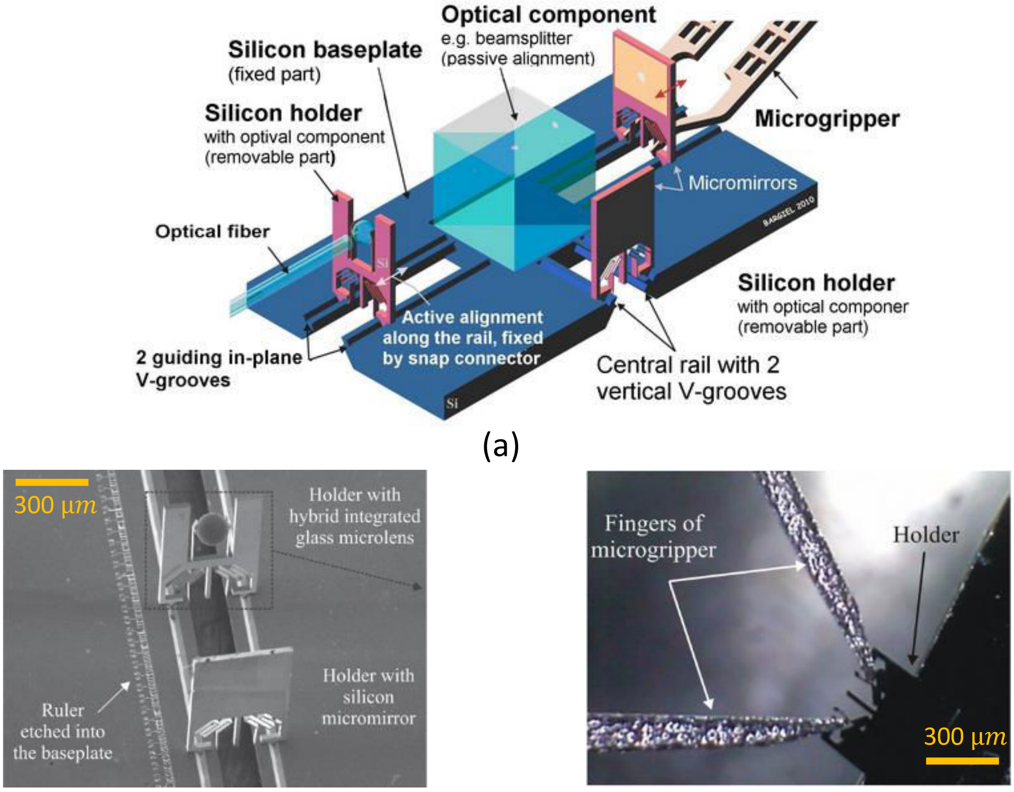

(a)

(b)

(c)

Figure 1.6: Example of assembled micro-optical bench [Clévy et al., 2014]. (a) Schematic diagram of an assembled optical bench. (b) SEM view of micro-assembly. (c) Micro-gripping

1.3/ CHALLENGES FOR ROBOTIC NANO-POSITIONING

The success of robotic micro/nano-positioning depends on many challenges, mainly high positioning accuracy requirements and micro and nano-scale specificities limits, to achieve high performances.

1.3.1/ POSITIONING ACCURACY

Positioning accuracy is one of the performance criteria of nano-positioning systems. This one characterizes the ability of the robot to position and orientate the end-effector to a desired pose. This assessment is based on the static measurement of deviations (position and orientation) between the desired pose and the pose reached by the end-effector [Ha, 2008]. The accuracy and repeatability of a position and an orientation are defined based on ISO 9283 standard. Figure 1.7 and Figure 1.8 show the geometric view of the two performances (accuracy and repeatability) for a position and an orientation respectively.

The position accuracy AP is defined as the difference between the position of a given

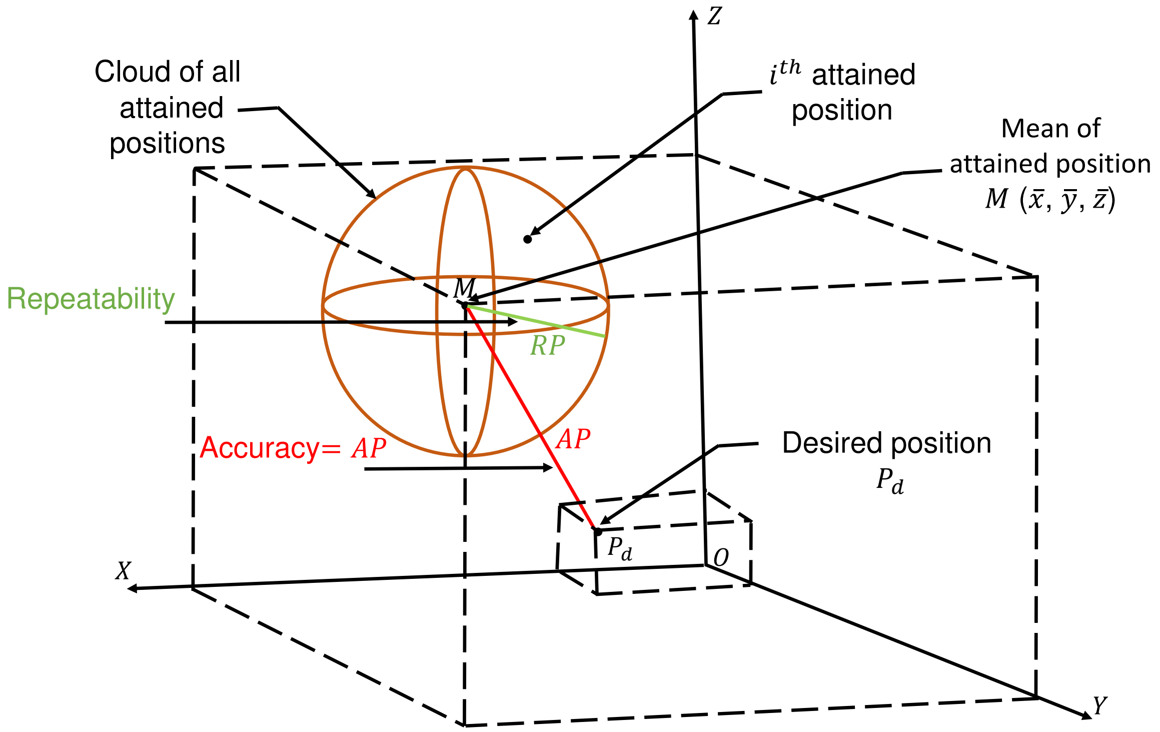

Figure 1.7: Accuracy vs repeatability.

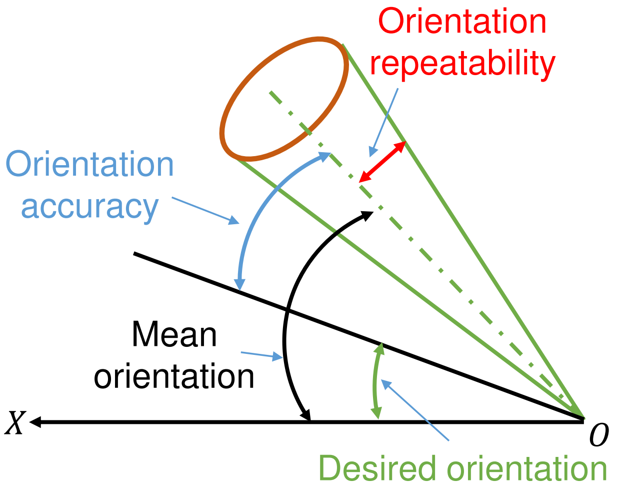

Figure 1.8: Orientation accuracy, orientation repeatability, mean orientation and command orientation[Khalil et al., 1999].

desired pose $P_d(x_d, y_d, z_d)$ and mean measured position center $M(\bar{x}, \bar{y}, \bar{z})$ of the attained measured positions $P_i\ (x_i, y_i, z_i)$:

$$AP = \sqrt{(x_d - \bar{x})^2 + (y_d - \bar{y})^2 + (z_d - \bar{z})^2}, \tag{1.1}$$

where $\bar{x} = \frac{1}{n}\sum_{i=1}^{n} x_i$, $\bar{y} = \frac{1}{n}\sum_{i=1}^{n} y_i$, $\bar{z} = \frac{1}{n}\sum_{i=1}^{n} z_i$.

Repeatability is another performance criterion related to the situation error of the end-effector. It corresponds to the ability of the robot to ”bring back” the effector on a situation already learned [Ha, 2008]. Based on ISO standard, to calculate the repeatability $n = 30$ cycles (control the same pose 30 times) need to be performed for every test. For a given position, the repeatability RP is expressed by the radius of the sphere whose center is the mean M.

$$RP = \bar{h} + 3\sigma, \tag{1.2}$$

with

$$\bar{h} = \frac{1}{n}\sum_{j=1}^{n} h_i, \tag{1.3}$$

where

$$h_i = \sqrt{(x_j - \bar{x})^2 + (y_j - \bar{y})^2 + (z_j - \bar{z})^2} \tag{1.4}$$

and the standard deviation σ is:

$$\sigma = \sqrt{\frac{\sum_{j=1}^{n}(h_i - \bar{h})^2}{n-1}} \tag{1.5}$$

Positioning accuracy is an headmost criterion evaluating task performance for any application field. Indeed, according to the objects to be carried out at the micro-scale, a small positioning error may lead to task failure. For example, nano-positioning in photonics assembly, requires to align transmitting and receiving components to minimize light loss in optical coupling. In fiber-to-fiber alignment, in order to maintain high communication quality, the optical alignment error is generally required to be smaller than 1.0 μm [Chiu et al., 2009]. For some small cells manipulation (e.g., biological cells) for tissue regeneration which have typical sizes ranging from 1 to 5 μm, the required accuracy of positioning should be in sub-micrometer range [Avci et al., 2015] [Miyazaki et al., 2000] to insure successful tissue regeneration.

In general, reaching high positioning accuracy for high success rates relies on the robotic platform, that generally consists of one or several micro-positioning systems. Since the accuracy of the robotic systems do not meet the requirements in many applications, and since the tasks at the micro-scale require more and more flexibility and accuracy, it is necessary to control positioning within a certain accuracy range to achieve any specific target position or/and orientation and not only taught positions [Tan et al., 2015b] [Agnus et al., 2008]. Realizing high positioning accuracy is always difficult to achieve. For example, if the perpendicularity error between X and Y axes is 0.1°, 1 mm motion along Y axis induces an error of 1.7 μm along X axis if this perpendicularity error is not taken into account in the robot control.

AFM scanners usually consist of XYZ nano-positioning stages whose motion behaviors affect the scanning performances. For some applications, the out-of-plane motion should be less than a few nano-meters over entire XY scan range when imaging a flat surface. In these cases, Z stages must be actively controlled, even though only XY planar motions are desired [Tan et al., 2015b]. The MEMS micromirror for OCT applications with a circular mirror plate was proposed and fabricated [Liu et al., 2012]. The measured lateral shift and tilt angle of the mirror plate are about 7 μm and 0.7° respectively, through the entire piston motion 227 μm and $\pm 11°$. Achieving smaller lateral shift and tilt angle would then require to identify the geometric errors of the nano-positioning stages inducing positioning errors.

Figure 1.9 gives a synthesis of the state-of-the-art, that illustrates the angular and the translational accuracy achieved together in each work. The objective now is to achieve a Translational accuracy under 1 μm and an angular accuracy under $0.005°$ to be able to manipulate and position micro and nano-objects in 6 DOF way with very high accuracy.

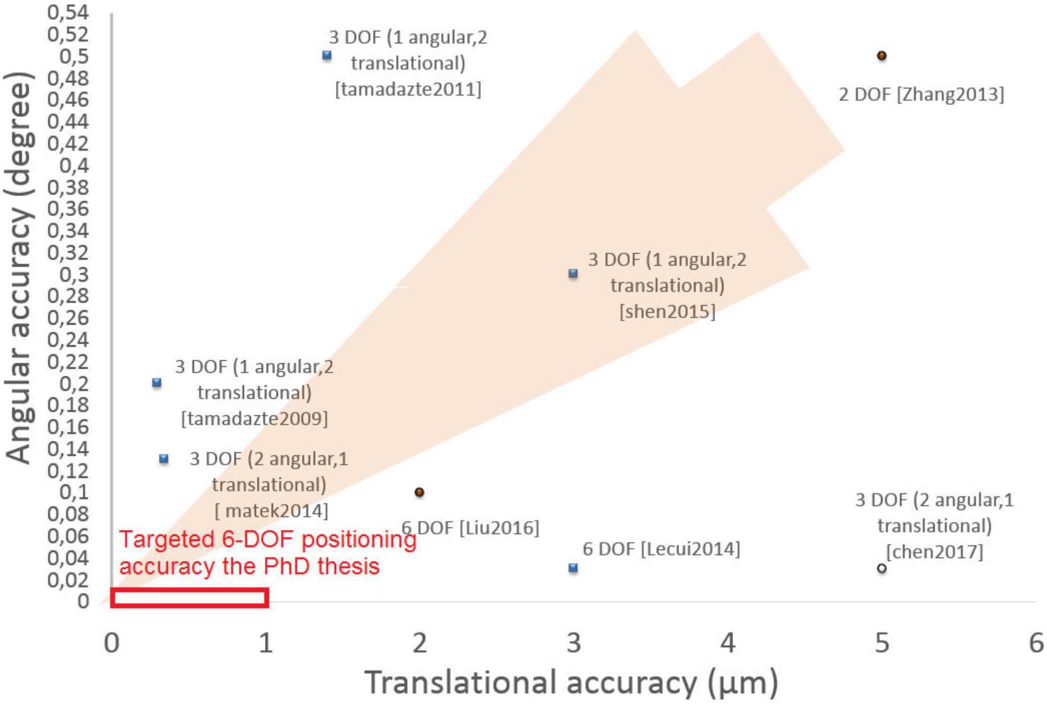

Figure 1.9: Some works illustration based on angular and translational accuracy.

1.3.2/ MICRO AND NANO-SCALE SPECIFICITIES

Robotic nano-positioning depends on many micro-scale specificities which can complicate the positioning task to be realized successfully. The main micro-scale specificities can be summarized by:

- Big ratio between the size of robots and the manipulated micro and nano-objects,
- Sensors and Sensing issues at micro-scale.

Big ratio between the size of robots and the manipulated micro and nano-objects

The works presented previously, as well as many others in the literature, show the extreme difficulty of performing accurate micro-manipulation or micro-positioning tasks. Beyond all the studies already done, either technological or methodological, this difficulty can be explained, in part, by the ratio between the relative dimensions of the robot and of the component it manipulates.

For example as shown in Figure 1.10, the error at the end-effector of a micro-positioning stage mounted with a 30 mm robotic arm could be around 6 μm at the end-point due to yaw deviation 200 μrad. This error is larger than most biological cells size like bacteria which have sizes of 1 to 2 microns and is very close to the optical fiber diameter (about 8 μm) for optical fiber manipulation. The size difference between the robotic micro-task platform and the micro-objects to be manipulated in general is huge ($\times$1000). This size difference can lead to high positioning error. Hence, the error on a micro-robot for manipulation must be identified and compensated. At the micro-scale, it is difficult to measure and even quantify the influence of these imperfections. Therefore, the accuracy or quality of position control of micro-robots can have a direct influence on task success and task quality.

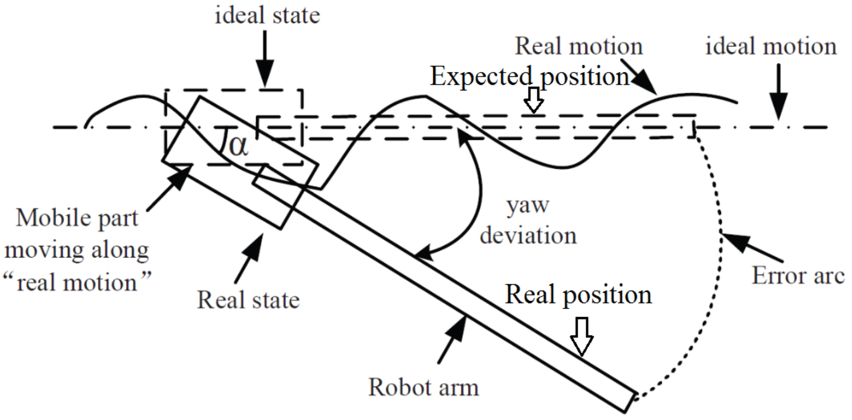

Figure 1.10: Example of error induced by yaw deviation [Tan et al., 2015b].

Sensors and Sensing issues at micro-scale

To achieve high positioning accuracy of a micro-object held on a nano-positioning system, the real position of this micro-object needs to be measured accurately. The measurement task can be realized by sensors. Nevertheless, sensing at the micro-scale is a very challenging issue. Micro-scale measurement requires sensors with high resolution (e.g., a few nanometers) and very small uncertainty (e.g., tens of nanometers) since motion and errors in this scale are very small. Only accurate enough sensors can detect such motion and errors otherwise they may immerse in measuring uncertainty of the sensors.

Sensors are influenced by medium variation, humidity and temperature. To minimize the environmental influence, sensors should be mounted as close as possible to the robot end-effector. The longer the measuring distance, the more the measurement will be affected by environmental changes. Capacitive sensors, vision systems and laser interferometer sensors are mostly used for micro-scale positioning sensing.

Measurement of the position of micro-objects usually uses visual systems. The vision system needs calibration to correlate real position and that in the image. The resolution of the vision system is often related to the measuring range. High resolution and wide measuring range are usually complex trade-off. To increase resolution, the measuring area must be reduced and vice versa [Guelpa et al., 2016]. High magnification microscope using usual algorithm is able to reach resolution of 1/10 pixel with pixel size 1 $\times$ 1 μm. We can achieve resolution of 1/1000 pixel but it requires specific patterns and algorithm which are not yet commercially available [Tan, 2013].

Capacitive sensors are the most commonly used sensors in short-range nano-positioning applications. They are relatively low cost and can provide excellent linearity, with a resolution of 2.4 nm and a bandwidth of 100 kHz [Fleming, 2013]. However, due to the electronics required for measuring the capacitance and deriving position, capacitive sensors are inherently more complex than sensors such as resistive strain gauges.

Laser interferometer sensors are the most attracting to use due to their high resolution of about 0.49 nm, accuracy, wide measuring range and bandwidth $>$ 100 kHz [Fleming, 2013]. They normally need reflecting objects (e.g. a mirror) to reflect the light beam they produce. The reflecting objects surfaces need to be very clean to avoid inaccuracies related to the reflection. It needs to find such reflecting objects and integrate them on the positioning systems, which is a tough task due to small free space availability.

Multi-DOF sensing is needed when the positioning system moves in multi-DOF. In market, there is a lack of sensing device satisfying multi-DOF measurement. The optical sensors usually can only offer 1-DOF measurement and the vision is able to give 2-DOF measurement. However, vision's performances on resolution, accuracy, and measuring range are less efficient than optical sensors. If realizing multi-DOF measurement, several sensors should be combined to build a measuring system. In this case, another problem may appear, that is, the workspace is too small to arrange all these sensors. Moreover, the relative position is difficult to be identified accurately. Optical sensors and vision systems usually have bulky sizes relative to the micro-robots, which make the workspace very crowded. How can we obtain a measurement based on a minimum number of sensors or with a small volume often appears as a key challenge.

The measuring range, resolution, repeatability, measuring DOF and volume for the mainly used commercially available external sensors are evaluated and summarized in Figure 1.11. interferometry sensors have the highest repeatability, resolution and measuring range compared to capacitive visual and piesoresistive sensors. Nevertheless, interferometry sensors measure only 1-DOF and occupy high volume. Sensors that satisfy all requirements are still under development in research laboratories and companies.

6-DOF nano-positioning accuracy is very challenging, it depends in part on some micro-scale specificities consideration. High positioning error yielded due to the big ratio between the robot size and the manipulated object. Some materials, such as piezoelectric materials or piezoresistive sensors, are widely influenced by temperature change, and the experiments can change from one day to other due to environment condition changes. So it is required to insure the most constant possible environmental conditions during the experiments by integrating temperature sensor in the experimental set up for monitoring. For measurement, the following requirements are needed:

- high resolution and accuracy
- suitable sensing range and bandwidth

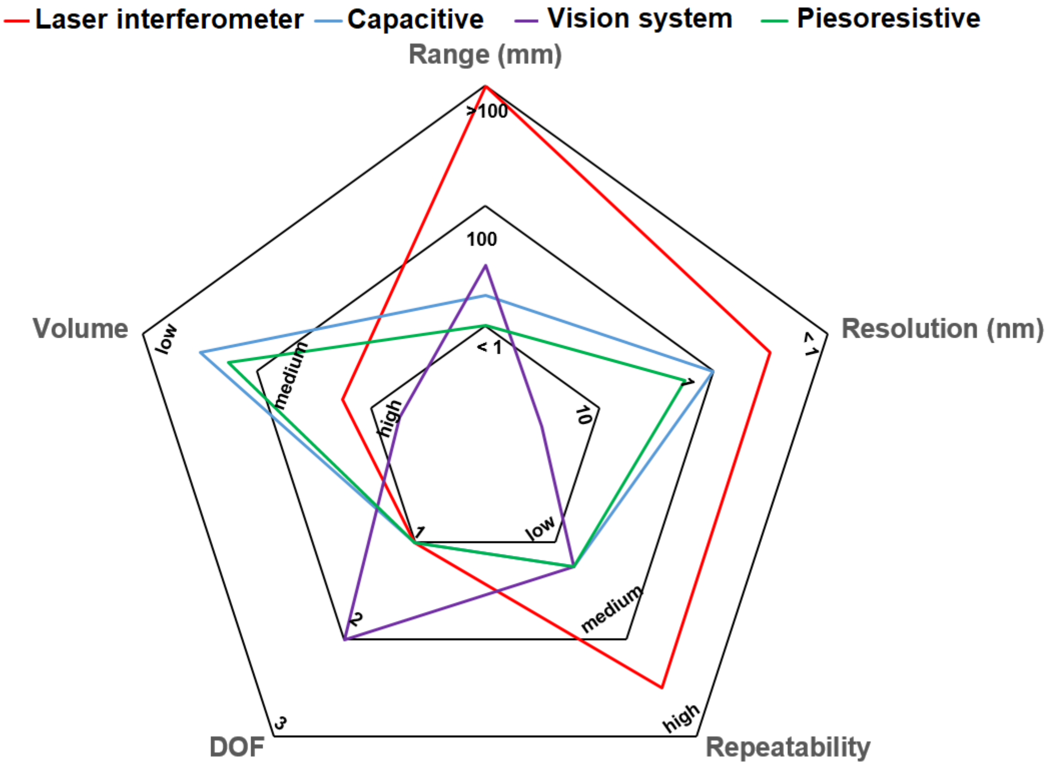

Figure 1.11: External sensors for position measurement at the micro-scale comparison.

- small volume
- noises reduction
- low sensitivity to environmental influence
- multi-DOF sensing depending on the application requirements.

In the presented thesis, we use interferometry measurements with fibers,and we will show how it can be used for multi-DOF applications.

1.4/ INTEGRATED OPTICS AS TARGETED APPLICATION FIELD

1.4.1/ THE CHOICE OF INTEGRATED OPTICS

The fabrication of hybrid integrated optical micro and nano-circuits usually passes through micro-fabrication technologies in clean room. As a result, their optical characteristics are tested only at the end of the process flow. This can lead to high yield losses. As an example, it can be seen in Figure 1.12 that a short Bragg mirror inscribed in an optical waveguide ineluctably shows angles due to the fabrication process, inducing losses and low reflectivity. A promising alternative is to manufacture each of the optical building components separately and optimize their optical performances through robotic micro-assembly. This approach appears as promising because it may provide high performances, propose new optical functionalities and products and exploit new modes of propagation of light beams in air or vacuum. This approach relies on the ability of accurate multi-DOF positioning of optical components. Such competitive micro-scale challenge is attained using robotic multi-DOF micro-positioning platform, where high positioning and alignment accuracy allows to perform more complex tasks. As an example, an alternative to integrated Bragg mirrors is the post-integration of optical multilayer within the waveguides as depicted in Figure 1.13. A highly reflective multilayer inserted inside the waveguide can advantageously replace the inscribed Bragg mirror and consequently enhance the reflectivity. Such an approach requires an accurate active photonic positioning to reduce the optical losses due to parasitic angles.

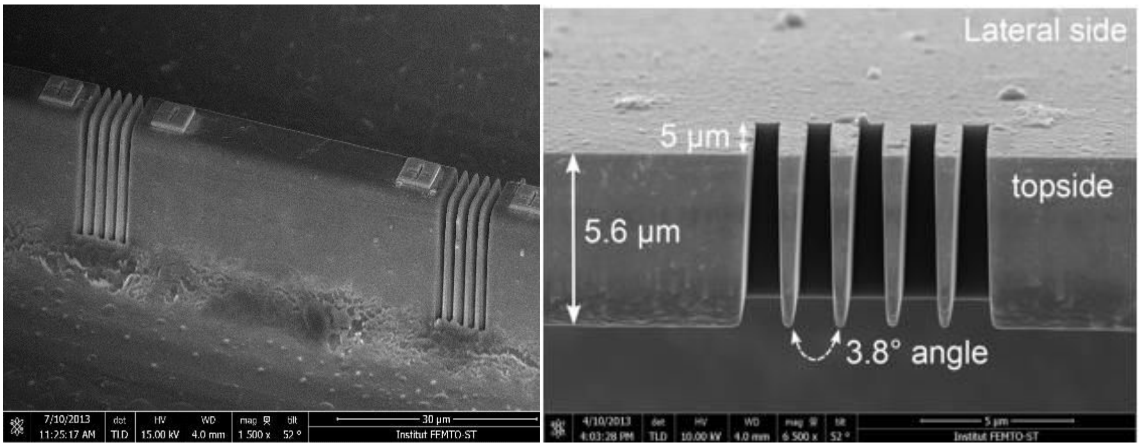

Figure 1.12: Left: a SEM view of a Bragg mirrors integrated in a LiNbO3 waveguides. Right: the angles between the walls of the Bragg mirror cause a significant reduction of reflectivity[Guyot et al., 2014].

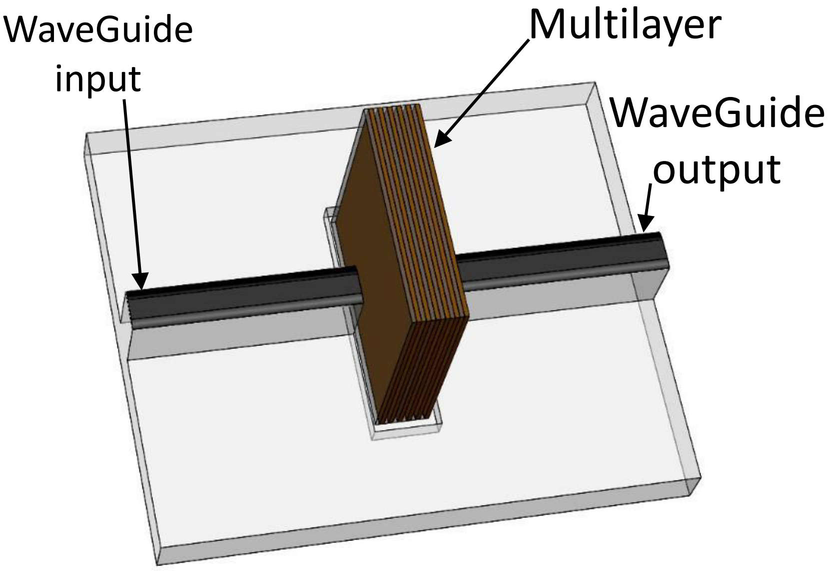

Figure 1.13: Post-integration of a multilayer in an optical waveguide.

Controlling and analyzing the polarization state of a light beam is crucial in applications ranging from optical sensing to optical communications, both in the classical and quantum regime. The current existing systems rely on remote bulky wave plates which are made of birefringent materials. However, the size and collimation of these configurations prevent optical systems miniaturization and generate parasitical noise. The signal-to-noise ratio is expected to be greatly improved by using integrated wave plates. But controlling and manipulating the polarization state of light propagating in an optical waveguide is, in general, not trivial. This crucial need has been addressed notably by laser femto-second writing [Corrielli et al., 2014] or by using specific photonic integrated circuits [Dai et al., 2012]. However, even shorter devices would be preferable, especially for the production of minimally invasive sensors. On the other hand, metamaterial architectures have shown the ability to control polarization states of light beams with ultra-thin (< 1 μm) plates [Li et al., 2015][Dahdah et al., 2012][Mousavi et al., 2015]. This is achieved by using periodic sets of asymmetrical elementary patterns that induce strong artificial anisotropy. Such a purpose requires performing tools for testing and positioning the photonic elements with nanometric accuracy, which orients attention toward robotic approaches.

For example, the biplate that consists of two single wave plates made from birefringent materials with their fast axes oriented perpendicular to each other is one of the most commonly used retarders in many integrated optics systems. The internal alignment of the optical axes of the two single wave plates is a key procedure in the fabrication of a biplate to reduce the spurious artifacts of oscillations in polarization properties due to the misalignment error and to improve the accuracy and precision of the systems using such biplates. In [Gu et al., 2016] a method is proposed to accurately align the axes of an arbitrary biplate by minimizing the oscillations in the characteristic parameter spectra of the biplate detected by a spectroscopic Mueller matrix ellipsometer (MME). An analytical relation between the characteristic parameters and the misalignment error in the biplate were derived, which helps to analyze the sensitivity of the characteristic parameters to the misalignment error and to evaluate the alignment accuracy quantitatively. Experimental results performed on a house-developed MME demonstrate that the alignment accuracy of the proposed method is better than 0.01° in aligning the optical axes of a quartz biplate. But in this approach, the non parallelism between the two surfaces are not taken into account, while an angle between two wave plates could introduce large changes in polarization states.

In summary, the choice of integrated optics as targeted field is done based on two main aspects. First, many emerging industrial applications demands made the field of integrated optics particularly challenging scientifically and technologically. The possibility to achieve hybrid original nanophotonic components and outstanding performances by assembly feeds many particularly original applications. With many outlooks related to the attractive physical properties. It makes possible the integration of thin metamaterial-based layers controlling the polarization. It also gives the opportunity to make the best choice of material and technology for each of the photonic building blocks. By dynamically optimizing the positioning and the assembling of the photonic building blocks, this approach allows optimized photonic circuits with minimal waste. Secondly, integrated optics is a very good case of study for robotics (very high 6-DOF positioning accuracy requirements). The existing possible accuracy based on manual active positioning does not satisfy the high positioning accuracy required for these emerging photonic applications. These two aspects lead to the definitive and well-argued choice of the integrated optics as the targeted application field for my PhD thesis, to realize high accurate positioning of optical components in multi-DOF way through robotics for integrated optics.

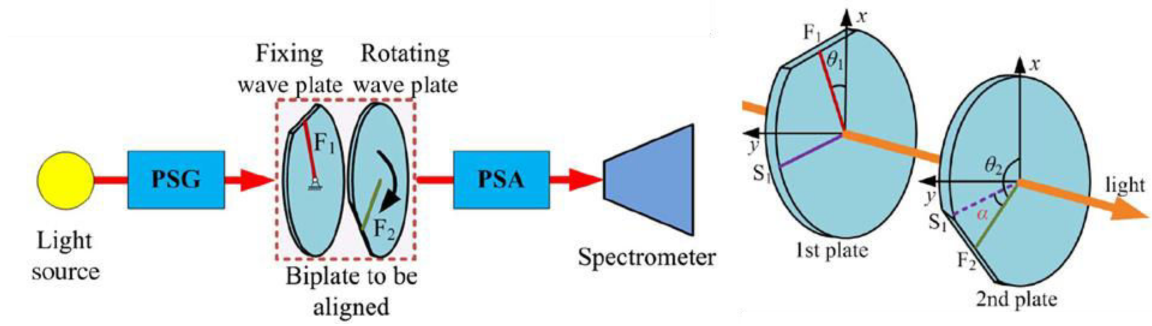

Figure 1.14: (left) Scheme of the experimental setup for alignment of the biplate based on the MME. PSG, polarization state generator; PSA, polarization state analyzer; F1, fast axis of first single wave plate; F2, fast axis of second single wave plate, (right) Scheme of a general biplate. S1 is the slow axis of the first wave plate, and $(F_i\ ,\ \theta_i)$ $(i = 1, 2)$ denote the fast axis of the i-th wave plate and its azimuth with respect to the x axis; α denotes the angular misalignment error between the fast axis of the first wave plate and the slow axis of the second wave plate [Gu et al., 2016].

1.4.2/ Nano-ROBOPTIC, COLAMIR and CEPAGE projects

The original inspiration of integrated optics came from the technology of electronic integrated circuits, which has shown rapid development over several decades and has led to key achievements, such as complex and powerful microprocessors containing many millions of transistors, specialized signal processors and computer memory chips with huge data storage capacity.

Integrated optics aims at constructing so-called integrated optical devices or photonic integrated circuits or planar light-wave circuits, containing several or many optical components such as optical filters, modulators, amplifiers, lasers and photo-detectors .... They can, e.g., be fabricated on the surface of various crystalline material (such as silicon, silica, or $LiNbO_3$) and connected with waveguides.

Integrated optics is emerging as an attractive alternative to electronics in high bit rate telecommunication systems, sensors or signal processing devices. In this context, there is a need of specific 3D integrated optics architectures that cannot be easily engineered by clean-room processes. As an example, detection applications would benefit from thin-plate-based polarization controllers. But the production and integration of these building blocks is far from being trivial. The Nano-ROBOPTIC (Robotic nano-assembly of photonic structures), COLAMIR (Collaborative Agile Miniaturized Robotics for ultra-precise assembly) and CEPAGE (Circuits Electro-Photoniques hybrides par usinAge, manipulation et assemblaGe dynamiquEs) are ANR projects that address this issue by proposing innovative approaches. One of these approaches, in which we are participating relies on the dynamic high accurate positioning and assembling of photonic building blocks (waveguides, resonators, thin plates) for the development of new 3D hybrid electro-photonic circuits with very high performances. The projects open up an interdisciplinary field at the boundary between micro-optics and robotics for positioning and assembly of photonic elements through the collaboration between the two departments of Optics and AS2M (Control and Micro-Mechatronic Systems) of FEMTO-ST institute.

In this thesis, an optical lamella and an optical fiber are chosen for research . The robotic nano-positioning of an optical lamella with respect to the optical fiber in 6-DOF way is studied and the corresponding optical performances are investigated. The optical polarization control based on specific optical wave plate angular positioning is also studied. For this sake, the existing alignment approaches for integrated optics are discussed in the next section.

1.5/ ALIGNMENT APPROACHES FOR INTEGRATED OPTICS

Alignment of optical components for integrated optics is realized based on passive, active and hybrid approaches [Takigawa et al., 2011] [Zheng et al., 2012] [Landry et al., 2013] [Karioja et al., 2000] [Sassen et al., 2008].

1.5.1/ PASSIVE APPROACH

Passive alignment approach is based on geometric information of the components to be assembled. Optical elements may, for instance be aligned manually by using passive alignment structures such as V-grooves [Takigawa et al., 2011] as shown in Figure 1.15 or patterned alignment marks [van Gurp et al., 2013] as shown in Figure 1.16 . This kind of approaches enable to reach a positioning accuracy of about 1 μm [Li et al., 2005], it is enough accurate for many dedicated specific applications as demonstrated for passive alignment of two photonic chips on a silicon optical bench [van Gurp et al., 2013].

Passive alignment of single mode fibers in V-grooves has been a research focus for decades. A depth analysis of V-groove alignment is given in [Li et al., 2005], proving alignment accuracies down to 1 μm. In case of alignment of a single mode fiber with respect to a tapered waveguide, this is usually sufficient compared with the approximate 8 μm mode field diameter of a single mode fiber. Well known error sources in this particular case are the eccentricity of the core with respect to the cladding and the variation in cladding diameter [Cohen et al., 1992].

For chip-to-chip alignment, the required alignment accuracy can be as good as 0.1 μm [Guo et al., 2004]. However, with current passive alignment methods, 1 μm accurate waveguide to waveguide alignment is more or less the best that can be reached. For example, Friedrich [Friedrich et al., 1992] overcomes the classical problem of inaccuracies between the waveguides and the edge of the chip by using features defined in the waveguiding layer to initiate a precision cleave. An accuracy of 2 μm is reached between a laser chip and a silicon optical bench (SiOB). A similar technique was applied in [Kaufmann et al., 1986] to define the edge of an GaAs chip yielding comparable results. In [Krishnamoorthy et al., 2009], two silicon photonic chips are aligned on top of each other with an alignment accuracy less then 1 μm by means of ball-pit alignment features and facet mirrors. Also with solder self-alignment accuracies of $\sim 1\mu$m can be achieved [Hayashi, 1992].

There are other robotic passive approaches using visual geometrical feedback information to control the optical component poses [Kudryavtsev et al., 2015] as shown in Figure 1.17. These approaches are more generic, it can also reach a positioning accuracy of

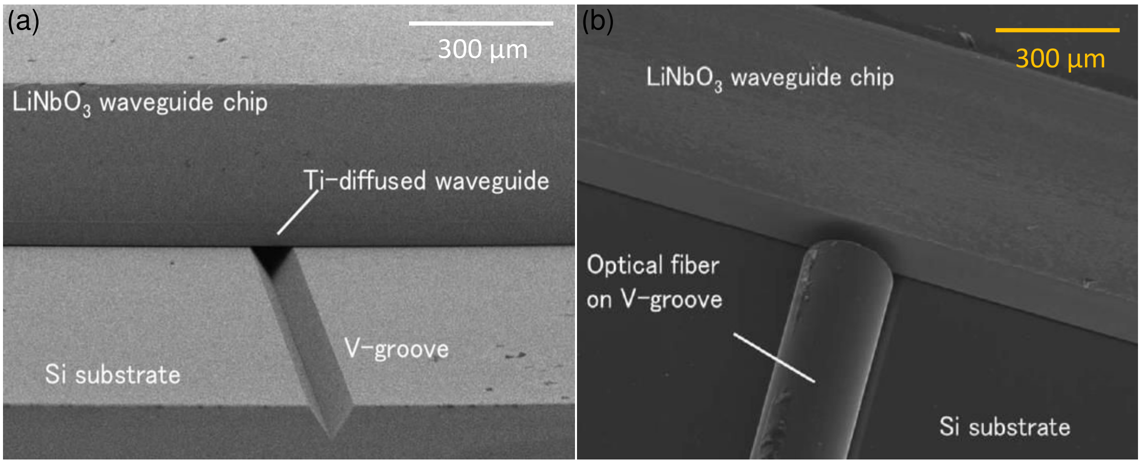

Figure 1.15: LiNbO3 waveguide chip on a Si substrate (a) without an optical fiber in the Si V-groove and (b) with an optical fiber in the Si V-groove [Takigawa et al., 2011].

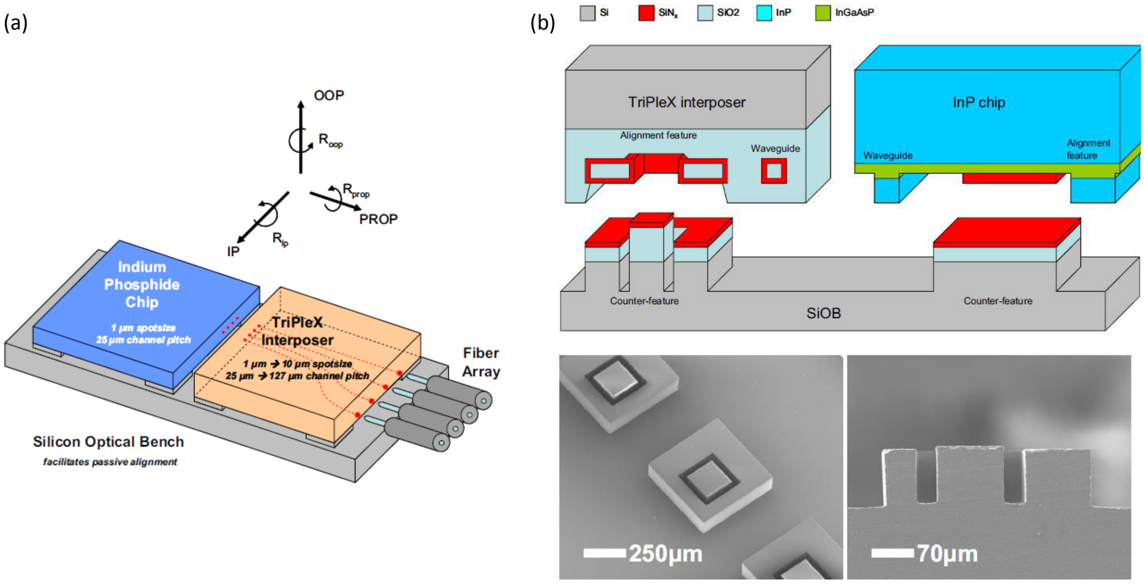

Figure 1.16: a) Schematic overview of the case study. An indium phosphide (InP) chip to a fiber array via an interposer chip called TriPleX. Both photonic chips are passively aligned upside-down (flip-chipped) on a SiOB, b) Alignment counter-features on the SiOB: schematic (top), SEM overview (bottom left), and SEM detailed cross section (bottom right). The detailed cross section shows the sidewalls of the 80-μ m deep DRIE etch. In addition, the deposited layers on top of the pedestal are visible, creating a 4-μ m height difference between the inner and outer tower. The photonic chips align against the sidewalls of these thin layers [van Gurp et al., 2013].

about 10 μm for complex 3D tasks [Clévy et al., 2014].

However, geometric positioning for either manual or robotic way does not provide the optimal optical performances, which is the main reason for which active positioning is the mostly used in integrated optics industry.

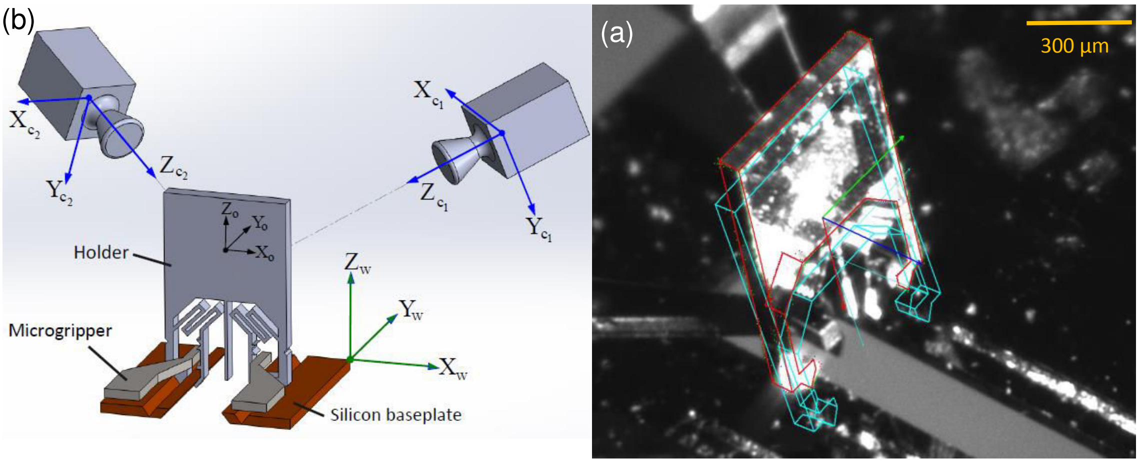

Figure 1.17: Example of assembled micro-optical bench (a) and its CAD-model (b)[Kudryavtsev et al., 2015].

1.5.2/ ACTIVE APPROACH

In active alignment approaches (conventional active alignment approach), the optical system properties are used as a feedback information for the operator. The feedback signal is usually the transmission power measured by an optical power meter [Zheng et al., 2012] as shown in Figure 1.18. micro-positioning systems are employed in general manually to adjust the position of the optical component in order to obtain maximum optical power [Tseng et al., 2005]. Some others use automated adjustment of the motion stages for alignment by using some optimization algorithms to reach the maximum optical power like hill-climbing algorithm [Zheng et al., 2009][Tang et al., 2001], Hamiltonian algorithm [Zhang et al., 2003], genetic algorithm [Zhang, 2004], and particle swarm algorithm [Landry et al., 2013]. As a result, the reached translational alignment accuracy is much more satisfactory compared to the passive approaches, and it can typically reach about 100 nm positioning accuracy. This approach is mostly used to fiber-to-fiber alignment [Tseng et al., 2005], fiber-to-waveguide or fiber-to-chip alignment [Carminati et al., 2015] as shown in figure. 1.19 (a) shows the conventional approach for the alignment to photonic chips, that requires an input fiber from the laser to the chip, and an output fiber that feeds an external photo-detector, the idea is to align the in out fiber in order to maximize the transmitted power. Figure 1.19 (b) represents the proposed approach in [Carminati et al., 2015] , based on an integrated transparent light monitor (CLIPP), that requires only one fiber. The square boxes labeled with “IN” and “OUT” represent the positioning stages of the fibers.

Active alignment approach requires dexterity and skills of the operator and a lot of accuracy and attention which is a tired task for the operator. The repeatability and accuracy of the positioning may reach hundreds nm but at a high cost due to the training of the human operator and the long time needed to achieve the task. Consequently, the performances and the quality of the assembled products are variables. Furthermore, the commercial success of these products are limited and without reliable and cost-effective assembly and packaging technologies.

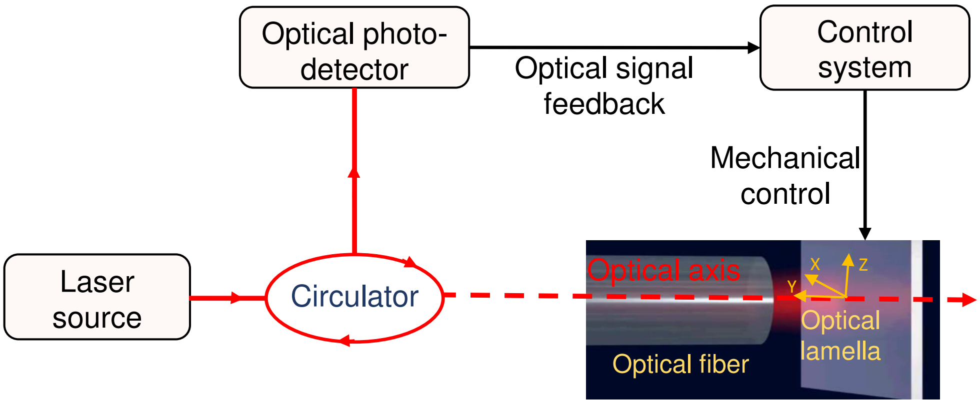

Figure 1.18: Active alignment technique.

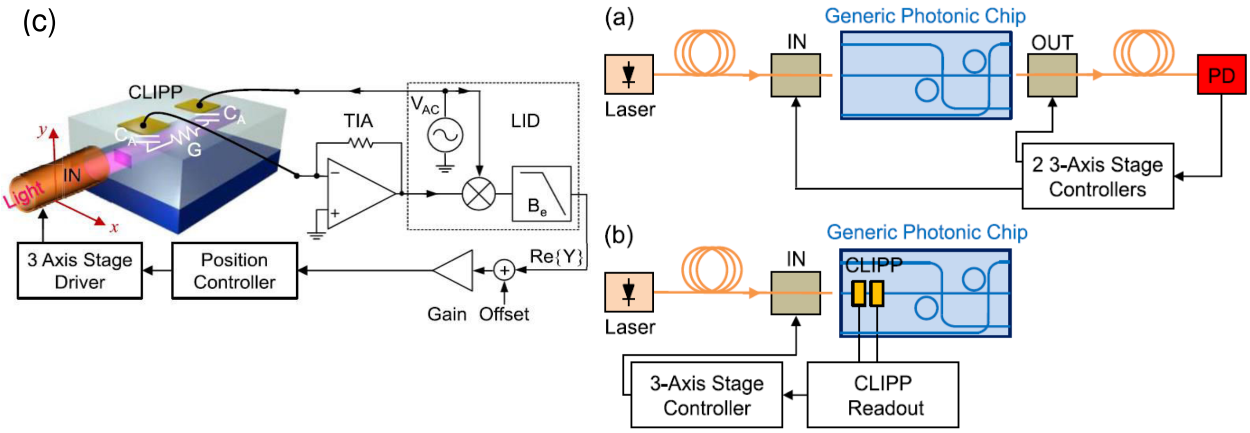

Figure 1.19: Architecture of the system that performs the CLIPP readout operations, and uses the CLIPP feedback signal to drive the fiber-to-waveguide alignment position [Carminati et al., 2015].

1.5.3/ HYBRID PASSIVE-ACTIVE- APPROACH

Optic system alignment consists of the so-called coarse and fine alignment steps. The coarse alignment is for detection of the 'first light beam' and is a passive approach. In practice, the spiral or square scanning and machine vision are the most widely used methods. After finding the first light, an active alignment process must be carried out to search the position with maximum optical coupling efficiency. This step is regarded as the fine alignment step [Datta et al., 2003], as shown in Figure 1.20. The hybrid form can be used as well in only fine alignment, where passive alignment is performed in some DOF and active alignment in the other(s) [Kapulainen et al., 2008].

In summary, alignment and assembly for integrated optics industry is realized mainly manually based on active positioning for many applications. Manual and robotic passive positioning is utilized also for some specific applications. However since passive approach is based on geometrical information for positioning, optical performances are not insured

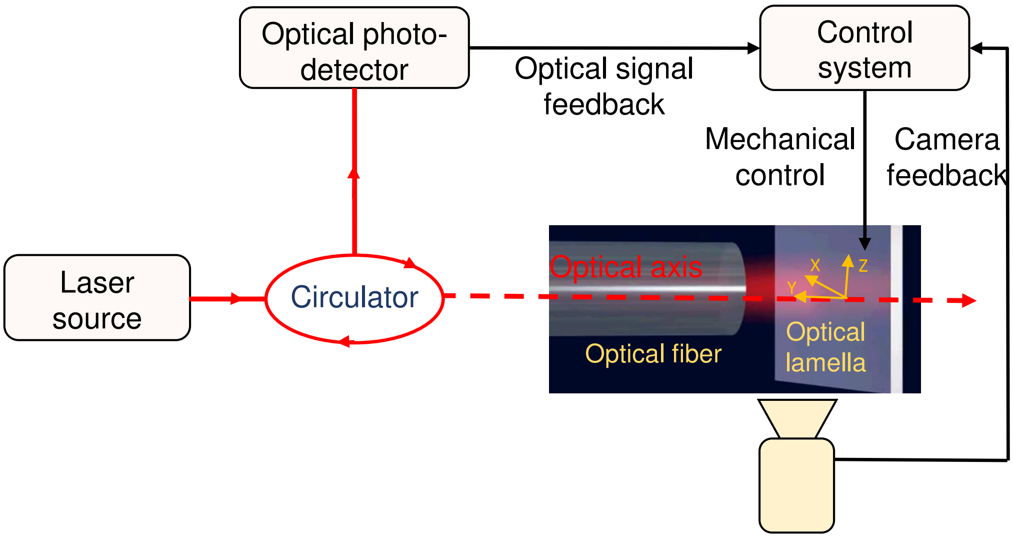

Figure 1.20: Hybrid passive-active alignment technique.

and the offered accuracy is not sufficient for many applications. For these reasons the active approach is mainly used for integrated optics industry and mostly in manual way, where human expertise represents the main factor for the task success. Moreover, it is time consuming especially for multi-DOF alignment process to reach maximum optical power. In the next section, the proposed contribution in this thesis, based on robotic and active positioning of optical building elements for integrated optics, will be discussed.

1.6/ 6-DOF HIGH ACCURATE PHOTO-ROBOTIC NANO-POSITIONING FOR INTEGRATED OPTICS ASSEMBLY

As summarized in Figure 1.21, manual and robotic passive positioning use geometrical information for positioning. Therefore, optical performances are not insured and the offered accuracy is not sufficient for many emerging on-demand applications, even it is used for some dedicated applications. For these reason, positioning for integrated optics industry is realized mainly manually and in teleoperated way. But from the other hand, it suffers from time consumption especially for multi-DOF alignment, where human expertise represents the main factor for the task success. Our objective is to overcome the active positioning approach disadvantages, by proposing a photo-robotic approach for positioning and assembly of photonic elements for integrated optics, through combining robotics and active positioning in order to realize:

- Very high accuracy,
- 6 DOF positioning,
- Full automated positioning,
- High optical performances,
- Fast time positioning

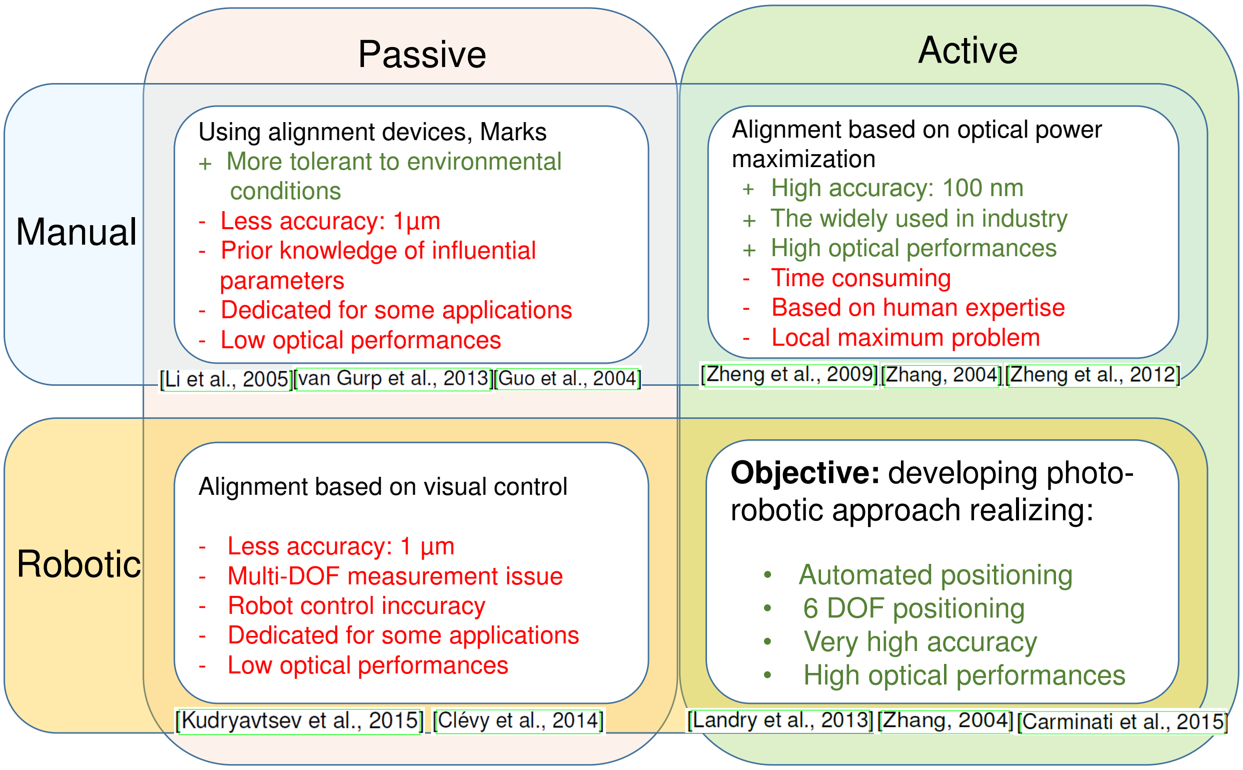

Figure 1.21: The targeted objective based on the existing positioning approaches for Integrated optics assembly.

The originality of the approach relies on using robotics associated with active positioning through the use of interfered reflected light irradiance as feedback signal rather than transmitted power. The Fabry-Perot interference principle for the conventional active alignment approach is especially used to provide a fast and high accurate measurement in our approach, in order to achieve a high multi-DOF positioning accuracy.

1.7/ CONCLUSION

Achieving fast, automated 3D complex tasks of micro-manipulation and micro-assembly with very high accuracy is an ultimate goal in many application fields. such as advanced integrated optics manufacturing, to achieve commercial success with reliable and cost-effective assembly, and packaging technologies.

Many emerging industrial on-demand applications made the field of integrated optics particularly challenging. The possibility to achieve hybrid nano-photonic components by assembly feeds many particularly original applications. The high positioning accuracy required for these emerging photonic applications is also quite challenging for robotics. This leads to the definitive and well-argued choice of the integrated optics as the targeted application field for my PhD thesis, to realize high accurate positioning of optical components in multi-DOF way through robotics.

Positioning and assembly for integrated optics industry is realized mainly manually based on active positioning for many applications. Manual and robotic passive positioning is used also for some specific applications. However since passive approach is based on geometrical information for positioning, optical performances are not insured and the offered accuracy is not sufficient for many applications. For these reason the active approach is the mainly used for integrated optics industry and mostly in manual way, even it is based on human expertise, where human expertise represents the main factor for the task success. Moreover, it is a time consuming especially for multi-DOF alignment process to reach maximum optical power. Our objective is to develop an approach for positioning and assembly of photonic elements for integrated optics, through robotics and active positioning combination in order to realize: very high accuracy, full automated 6 DOF positioning, high optical performances and in fast time.

2

PHOTO-ROBOTIC POSITIONING BASED ON FABRY-PEROT INTERFEROMETRY PRINCIPLE

Contents

2.1/ INTRODUCTION

Our objective is to achieve high accurate multi-DOF positioning for integrated optics. An optical fiber and an optical lamella are chosen for the case study. As mentioned in chapter 1, integrating thin lamellas into a photonic systems are indeed of great interest. As an example, thin mirrors can be integrated to create optical cavities, a thin birefringent lamellas can be used to control some polarization effects. Here, we are particularly interested in integrating thin birefringent lamellas with optical fibers. Such a system, dedicated in Figure 2.1 allows to prepare whatever desired polarization for a further pigtailing with an optical component. This is of particular interest for fibered sensors relying on the evaluation of the polarization changes. However, such an approach requires to position accurately the lamella with respect to the fiber. To do so, the optical lamella is held on a nano-positioner to be positioned actively relative to the optical fiber. This leads to use the Fabry-Perot phenomenon to realize very accurate 1-D displacement measure. Then, a photo-robotic approach is proposed, which combines the high accurate 1-D Fabry-Perot interferometry displacement measure information results during active positioning with a multi-DOF nano-positioner motion to realize multi-DOF pose measure. The photo robotic approach is then used to maximize the optical irradiance. However, in order to maximize the optical irradiance, the contact detection is required, which is discussed at the end.

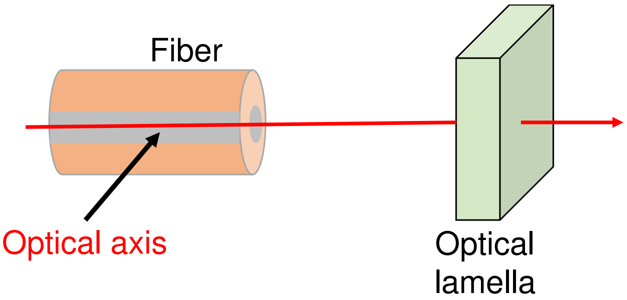

Figure 2.1: Schematic diagram of the case study system (fiber, optical lamella).

2.2/ FABRY-PEROT INTERFEROMETRY

Interferometer sensors are very attracting to use due to their high resolution, accuracy, wide measuring range and bandwidth. These interferometer sensors can be operating based on different interferometry principles such as Michelson and Fabry-Perot interferometry. Active alignment of the optical lamella with respect to the optical fiber produces the Fabry-Perot interferometry phenomenon. The Fabry-Perot interferometry results from the phenomenon of multiple beam interferences that arises when light shines through a cavity bounded by two reflective surfaces as shown in Figure 2.2. In our case, the involved surfaces are the fiber extremity (R_1) in one hand and the lamella surface (R_2) in the other hand. Each time the light encounters one of the surfaces, a portion of it is transmitted out, and the remaining part is reflected back. The net effect is to split a single beam into multiple beams which interfere with each other. The system behaves like the Fabry-Perot interferometer, where interferences result from the recombination of multiple reflections between the reflective surfaces R_1 and R_2 respectively.

Based on Fabry-Perot interferometry principle, when the reflective surface (R_2) moves along the optical axis (X-axis), the Fabry-Perot cavity length (L) changes and modifies the reflected light signal accordingly. Therefore, there is a correlation between the FP cavity length L and the interference figure. A slight variation of the FP cavity length can be identified on the interference figure.

The periodicity of the irradiance signal directly depends on the wavelength of the laser signal ($\lambda = 1560$ nm). If p is a natural number, the distance between two resonances can be written as in equation 2.1 (see Figure 2.3), i.e. the distance variation between two peaks (δL) is a multiple of half wavelength λ of the laser irradiance, such as :

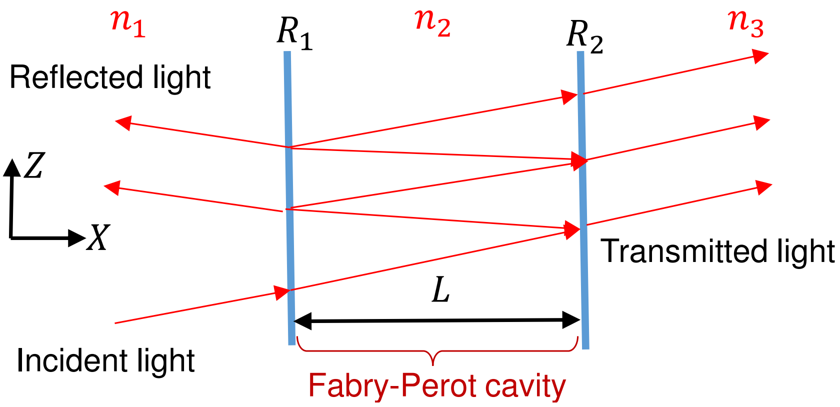

Figure 2.2: Schematic diagram representing the interferences in a Fabry-Perot optical cavity. n_1, n_2 and n_3 are different refractive index of different mediums (materials), yielding different diopters.

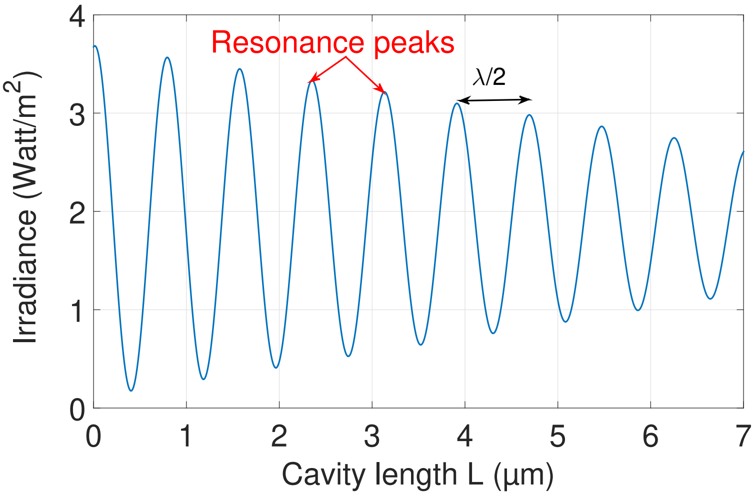

Figure 2.3: Reflected irradiance versus Fabry-Perot (FP) cavity length L, at wavelength $\lambda = 1560$ nm .

$$\delta L = \frac{\lambda}{2} \cdot p \qquad with \quad p \in \mathbb{N} \tag{2.1}$$

Active positioning and assembly of optical components gives the opportunity to measure a high accurate 1-D relative position along the optical axis with very high resolution. This 1-D Fabry-Perot measure is chosen to be used as a feedback information for the control loop. The main geometric parameters influencing the Fabry-Perot interferometry figure during active positioning need to be analyzed, which is the objective of the next section.

2.3/ ACTIVE POSITIONING APPROACH FOR HIGH ACCURATE NANO-POSITIONING

Our objective is to reach multi-DOF measurement from 1-D Fabry-Perot measurement. For this sake, active positioning setup of an optical lamella with respect to a fiber is proposed, it is based on reflected light response. A positioning system is used to hold the optical lamella to align it to a fixed fiber as shown in Figure 2.4. The positioning system is controlled via the computer using Matlab/Simulink platform. The incident light beam coming from the laser source passes through the fiber to strike the optical lamella, creating a Fabry-Perot cavity. Then, the interfered reflected light is measured using the photo-detector, where the fibered circulator is used to separate the reflected interfered light from the incident light. The measured reflected light by the photo-detector is acquired using an acquisition card interfaced with Matlab/Simulink platform.

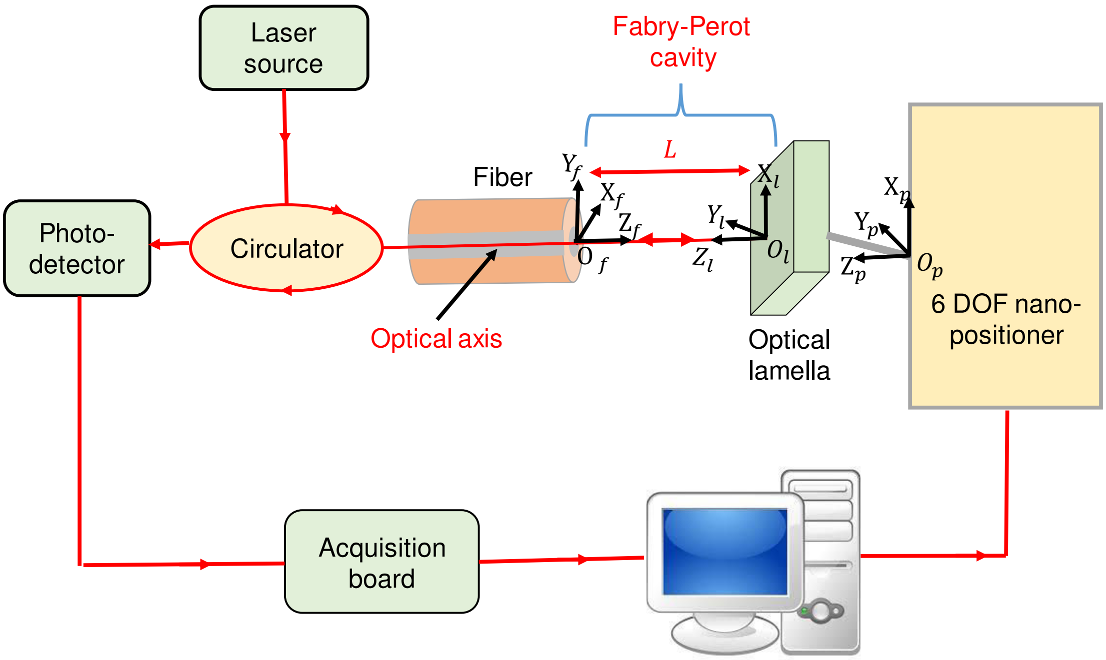

Figure 2.4: The experimental set up scheme: a 6-DOF nano-positiner holds and moves the optical lamella relative to the optical fiber through active alignment.

In active positioning, optical lamella is adjusted using positioning system in order to search the maximum optical irradiance. As a result, different coupled geometric parameters are modified. This leads to modify the interferometry figure. Therefore, the main parameters influencing the Fabry-Perot interferometry figure during active positioning need to be analyzed.

For this reason, three reference frames are defined, one is assigned to the positioning system, the second is assigned to the optical lamella and the last is assigned to the fiber as shown in Figure 2.4. The frame $(O_p\ X_p\ Y_p\ Z_p)$ is assigned to the positioning system, the origin O_p is assigned to its real rotational center of the positioning system, the $\overrightarrow{O_pX_p}$, $\overrightarrow{O_pY_p}$ and $\overrightarrow{O_pZ_p}$ are the expected motion directions of the positioning system. The reference frame ($O_l\ X_l\ Y_l\ Z_l$) is assigned to the optical lamella, its origin is assigned to the intersection point between the optical axis and the lamella plane. The axis $\overrightarrow{O_lZ_l}$ is perpendicular to the optical lamella plane and it is directed toward the fiber. The axes $\overrightarrow{O_lY_l}$ and $\overrightarrow{O_lX_l}$ are perpendicular to each other and they are on the lamella plane. The frame ($O_f\ X_f\ Y_f\ Z_f$) is assigned to the fiber, its origin O_f is assigned to the intersection point between the optical axis and the fiber plane. The axis $\overrightarrow{O_fZ_f}$ is perpendicular to the optical lamella plane and it is carried by the optical axis and it is directed toward the optical lamella. The axes $\overrightarrow{O_fY_f}$ and $\overrightarrow{O_fX_f}$ are perpendicular to each other and they are on the fiber plane.

First, a rotation of the optical lamella is done using the nano-positioner. Then we apply a rotation around O_pX_p or O_pY_p axis, a translation δL is ineluctably induced simultaneously. This is illustrated in Figure 2.5 (a), where it can be seen that the nano-positioner induces a translation of the optical lamella along the optical axis. By doing so, the distance between the fiber and the lamella changes, which induces oscillation in the reflected response (irradiance), as seen in Figure 2.5 (b). Now, if the rotation is done around the Z_p axis, the same effect (variation of the cavity length leading to oscillations) is observed.

Secondly, if the optical lamella is aligned with the optical fiber (see Figure 2.6 (a)), then a vertical displacement of the optical lamella using the nano-positioner along the X_p axis is expected to induce no cavity distance variation. Consequently, it should generate constant reflected light irradiance at the same time. But, if the optical lamella has initially a β_i misalignment angle between the fiber and the lamella (see Figure 2.6 (b)), then a vertical displacement of the optical lamella along the X_p axis is expected to induce a continuous cavity distance variation δL. Consequently, it generates an oscillating reflected light irradiance at the same time as shown in Figure 2.7.

In general, in conventional active alignment, the real applied motion from the nano-positioner is not referenced with respect to the fiber reference frame. For example, the real orientation displacement axis X_p is not parallel to the fiber surface as in ideal and desired case. This produces a new parameter β_l called frames referencing angle as shown in Figure 2.8, where β_i is the angle between the surface of the optical lamella and the Y_f-axis in the ($Z_fO_fY_f$) plan and β_l is the angle between Y_f-axis and the X_p-axis in the ($Z_fO_fY_f$) plan. As a result, it is difficult to analyze and to identify the source of the optical irradiance oscillations (due to Fabry-Perot cavity variation) in the interferometry figure.

In summary, in conventional active alignment, optical lamella is moved using a nano-positioner in order to search the maximum optical irradiance, where the nano-positioner motion is not referenced with respect to the fiber reference frame. As result, different parameters are modified. This different coupled parameters modifications at the same time during active positioning induces fringes (peaks) in the optical irradiance signal due to the existence of Fabry-Perot interferometry cavity variation. Hence, it is difficult to analyze the source of this Fabry-Perot cavity variation. As a results, conventional active alignment leads to:

- Time consumption especially for multi-DOF alignment process to reach maximum irradiance;
- Local maximum problem;

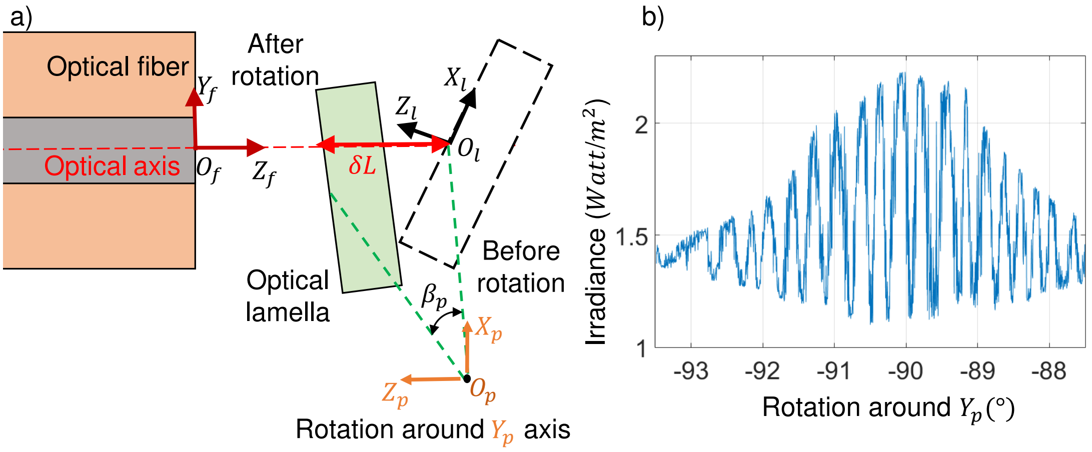

Figure 2.5: (a) A Rotation of the optical lamella around Y_p axis, induces a displacement δL along the optical axis. (b) The same rotation of the optical lamella around Y_p axis induces oscillations of the optical irradiance due to the variation of Fabry-Perot cavity length.

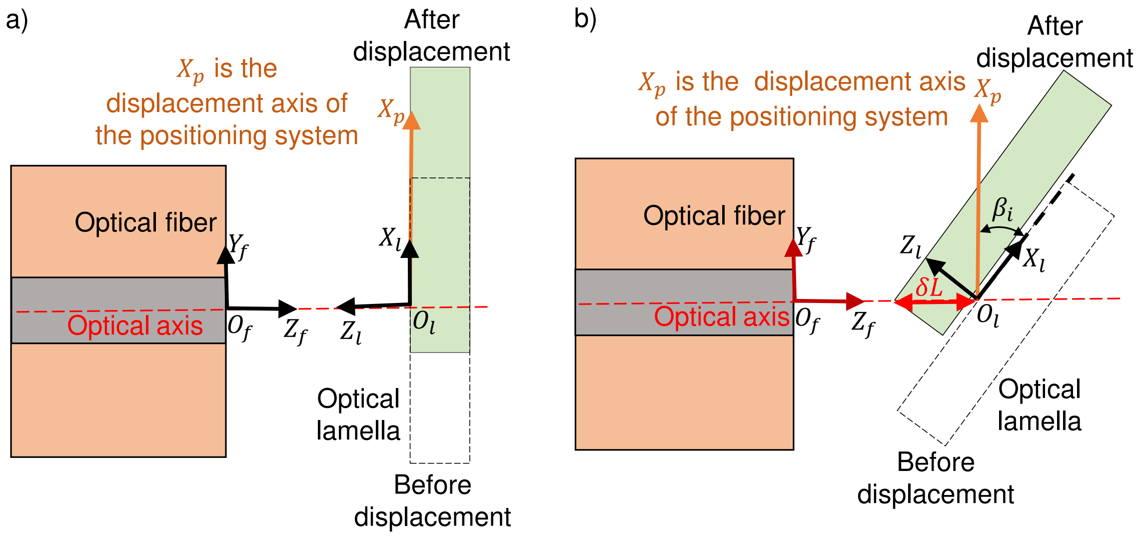

Figure 2.6: (a) Optical lamella displacement along X_p axis without misalignment angles. (b) Optical lamella displacement along X_p axis with misalignment angle β_i. β_i is the angle between the laemlla surface and the X_p axis in the $(Z_f O_f Y_f)$ plan.

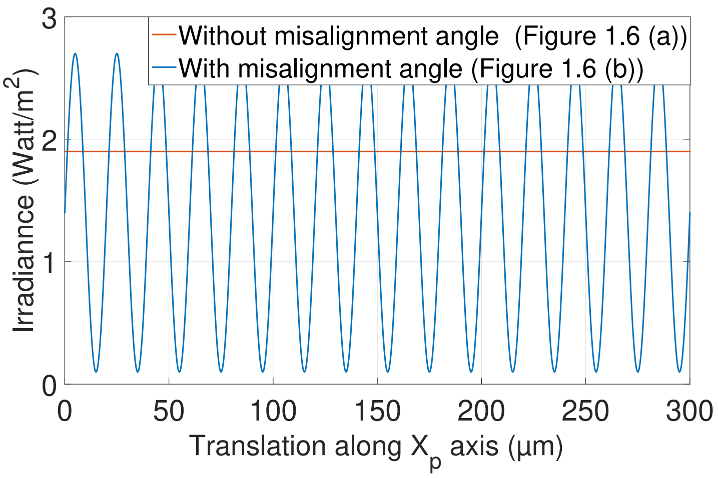

Figure 2.7: The optical irradiance with and without misalignment angle for translation along X_p-axis.

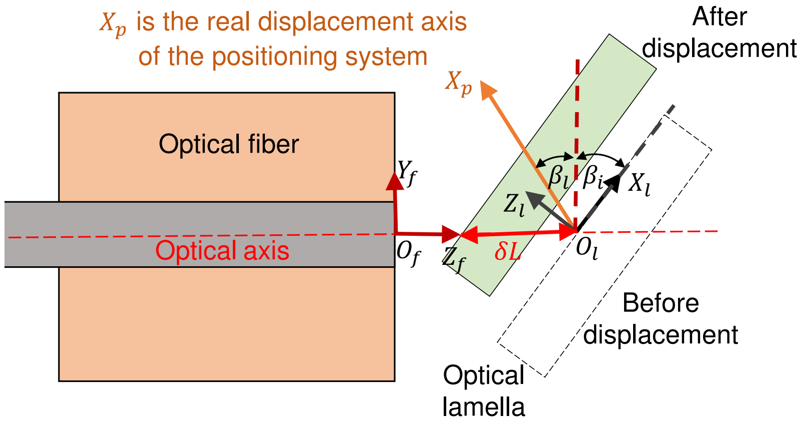

Figure 2.8: Real displacement is along X_p axis, it is coupled with misalignment angle β_i, frames referencing angle β_l and δL displacement along the optical axis. β_i is the angle between the plan of the optical lamella and the axis parallel to Y_f axis passing by the origin O_l, in the $(Y_f O_f Z_f)$ plan. β_l is the angle between the real axis X'_p and the axis parallel to Y_f axis passing by the origin O_l in the $(Y_f O_f Z_f)$ plan.

- The alignment task success relies on human expertise.

2.4/ PHOTO-ROBOTIC APPROACH FOR MULTI-DOF NANO-POSITIONING

As shown in Figure 2.9, in conventional active alignment, the operator adjust the optical lamella by using trial and error approach to maximize the interfered optical irradiance. In order to overcome the previously mentioned disadvantages of the conventional active alignment, a photo-robotic approach is proposed. The approach combines the high accurate 1-D Fabry-Perot interferometry measure information results during active positioning of optical components with a multi-DOF robot motion to realize multi-DOF pose measure. The photo-robotic approach is used to identify the parameters inducing the FP cavity variation.

For example, the photo-robotic approach can be used to accurately identify the relative misalignment and frames referencing angles β_i and β_l respectively. When the optical lamella has initially a β_i and β_l the orientation angles (see Figure 2.10), then a translation along the X_p axis with a known displacement δX_p is expected to induce a continuous cavity distance variation δL. Consequently, it generates an oscillating reflected light irradiance at the same time. From the number of maxima of this oscillating signal, the propagated distance δL can be evaluated using equation 2.1. From the twice assessment of the distance δL, and for a given scan distance δX_p, the angle β_i and β_l can be calculated using the following equation:.

$$\beta_i = \arctan\left(\frac{\delta L - \delta X_p \sin(\beta_l)}{\delta X_p \cos(\beta_l)}\right) \tag{2.2}$$

The relative misalignment and frames referencing angles β_i and β_l respectively can be identified by applying two different translations for two different corresponding optical lamella poses.

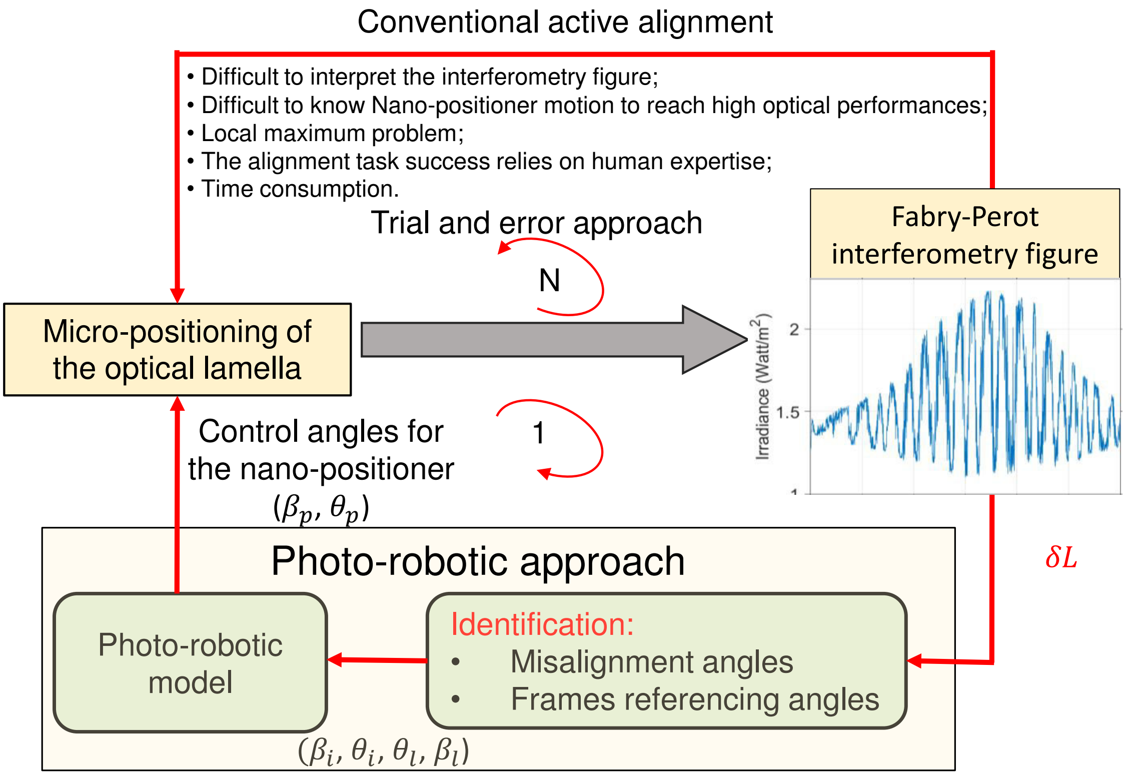

Figure 2.9: Photo-robotic approach.

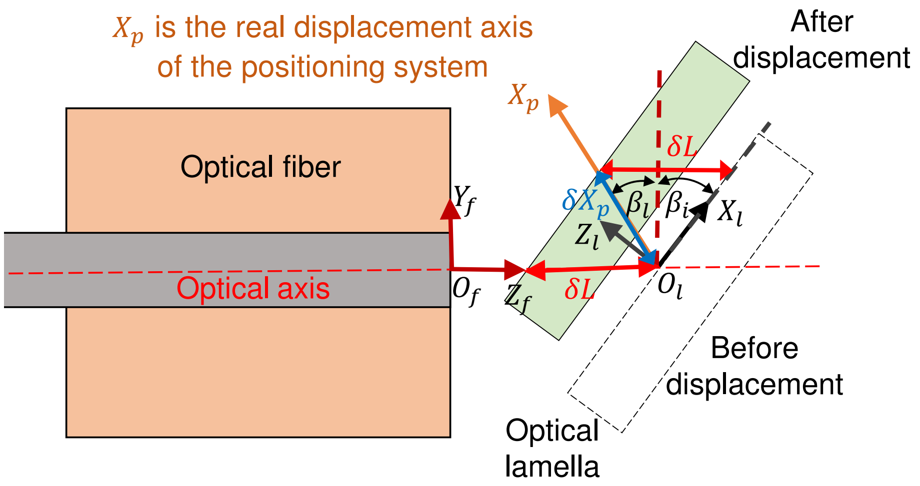

Figure 2.10: Real displacement is along X_p and it is coupled with misalignment angle β_i, frames referencing angle β_l and δL displacement along the optical axis. β_i is the angle between the plan of the optical lamella and the axis parallel to Y_f axis passing by the origin O_l, in the $(Y_f O_f Z_f)$ plan. β_l is the angle between the real axis X_p and the axis parallel to Y_f axis passing by the origin O_l in the $(Y_f O_f Z_f)$ plan.

The same steps are followed as previously mentioned for the relative misalignment and the frames referencing angles θ_i and θ_l respectively, where θ_i is the angle between the surface of the optical lamella and the axis parallel to X_f axis passing by the origin O_l, in the $(X_f O_f Z_f)$ plan. θ_l is the angle between the Y_p-axis (real displacement axis) and the axis parallel to X_f axis passing through the origin O_l, in the $(X_f O_f Z_f)$ plan.

The photo-robotic approach is implemented based on the experimental setup shown in Figure 2.4. The experiments are realized within a constant environmental conditions $(T = 20°)$.

Before investigating the identified angles repeatability, the optical signal (irradiance) repeatability is investigated. By applying 30 displacements along X_p axis for the same lamella pose, the corresponding irradiance signal is shown in Figure 2.11. Table 2.1 shows the obtained mean, maximum, minimum and the standard deviation after identification of the displacement along the optical axis for 30 times. The estimated standard deviation of the identified displacement on the optical axis is of 27.6 nm.

Table 2.1: The estimated displacement δL along the optical axis for a given lamella pose.

Displacement	Mean value	maximum value	minimum value	standard deviation
δL (μm)	9.4898	9.5485	9.4218	0.0276

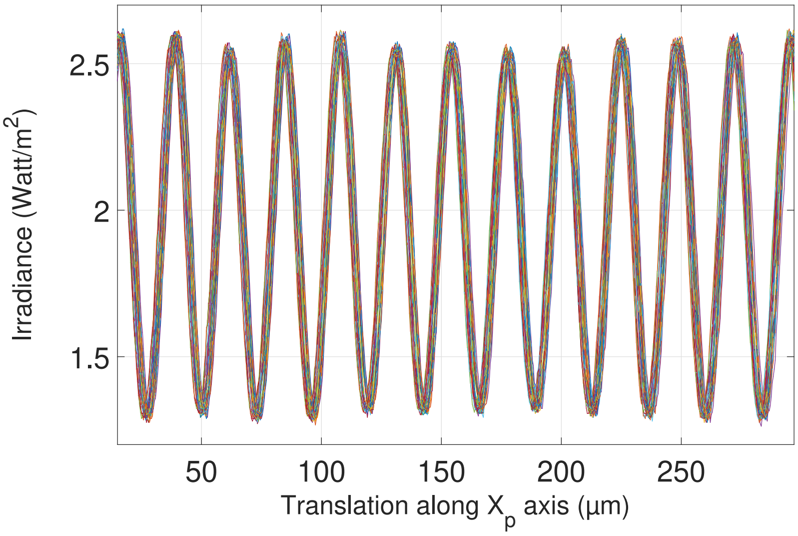

Figure 2.11: Repeatability of the reflected light irradiance during experimentation for 30 translations.

In order to investigate the identified angles repeatability, 20 different angular pose were given from the nano-positioner to the optical lamella with a constant $(\delta\beta_p = 0.25°)$ steps between each angular pose. β_p is the given nano-positioner rotation around Y_p-axis. For each angular pose, a translation of 300 μm is realized along X_p-axis. Therefore, from each two angular poses two equations can be extracted. Different sets of 2 equations can be composed from equation 2.2. each combination of two equations system can identify the optical misalignment angle β_i and the frames referencing angles β_l. 30 different combinations were taken. The obtained results presented in Table 2.2 show the obtained results for average values, minimum values, maximum values and standard deviations.

Table 2.2: The identified frames referencing and relative misalignment angles

Angles	Mean value	maximum value	minimum value	standard deviation
$\beta_l(^\circ)$	0.7453	0.7517	0.7436	0.0021
$\theta_l(^\circ)$	0.8415	0.8512	0.8387	0.0032
$\beta_i(^\circ)$	1.7538	1.7602	1.7507	0.0021
$\theta_i(^\circ)$	1.8523	1.8612	1.8481	0.0032

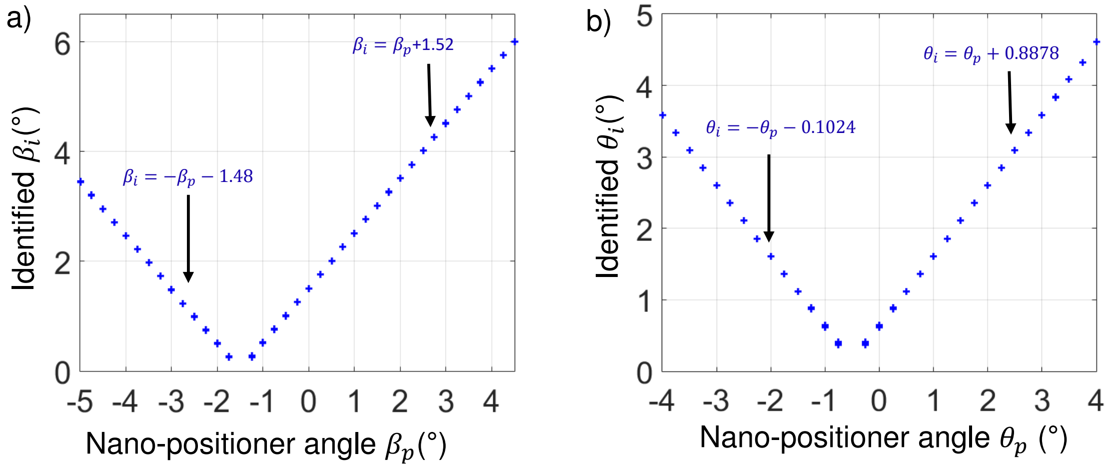

Figure 2.12: (a) The identified angle β_i (output) and nano-positioner angle β_p (input) linear relationship. (b) The identified angle θ_i (output) and the robot angle θ_p (input) linear relationship.

After having identified the relative misalignment angles, a photo-robotic model needs to be identified, by making the relationship between the nano-positioner angles (β_p, θ_p) and the corresponding identified angles (β_i and θ_i). Different angular poses were given to the optical lamella around Y_p and then around X_p with a constant steps ($\delta\beta_p = 0.25°$,$\delta\theta_p = 0.25°$) respectively between each configuration. A 30 times identification process is performed for each angular pose.

Figure 2.12 (a) and (b) shows the linear relationship between the identified and the nano-positioner angles. This relationship represents a first order linear regression equations, where all slopes equal 1.

The intersection point between the two lines equations in each figure gives the nano-positioner control angles, that correspond to $\beta_i = 0$ for Figure 2.12 (a) and to $\theta_i = 0$ for Figure 2.12 (b). Applying the obtained control angles to the nano-positioner allows to reach alignment between the optical lamella and the fiber.

Figure 2.13 shows the uncertainty distribution of the identified relative misalignment angles β_i for each given nano-positioner angle. Based on the obtained results, the uncertainty increases when the identified peaks number is less than 7 (peaks number $\leq$ 7).
Thanks to this uncertainty analysis which allows to identify angles with very small uncertainty. By taking relative misalignment angles having the corresponding peaks number greater than 7 ((peaks number $\geq$ 7)) permits to avoid the large uncertainty zone for identification.

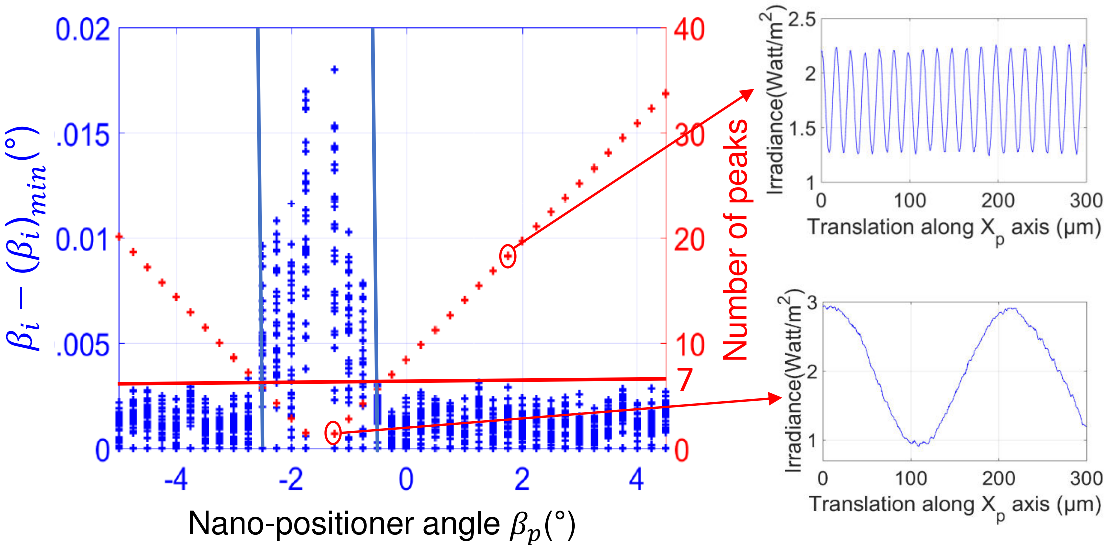

Figure 2.13: The β_i angle uncertainty illustration for each given nano-positioner angle.

Figure 2.14 shows the whole schematic diagram of the photo-robotic approach. Realizing a multi-DOF nano-positioner motion permits to position the optical lamella. A 1-D relative distance measure is realized using the interferometry figure for each nano-positioner motion. Using the 1-D relative distance measure and the multi-DOF nano-positioner motion, different optical lamella geometric parameters ($\beta_i, \theta_i, \beta_l, \theta_l$) can be identified. Finally, a photo-robotic model is used to calculate the control angles for the nano-positioner (β_p, θ_p) to be applied.

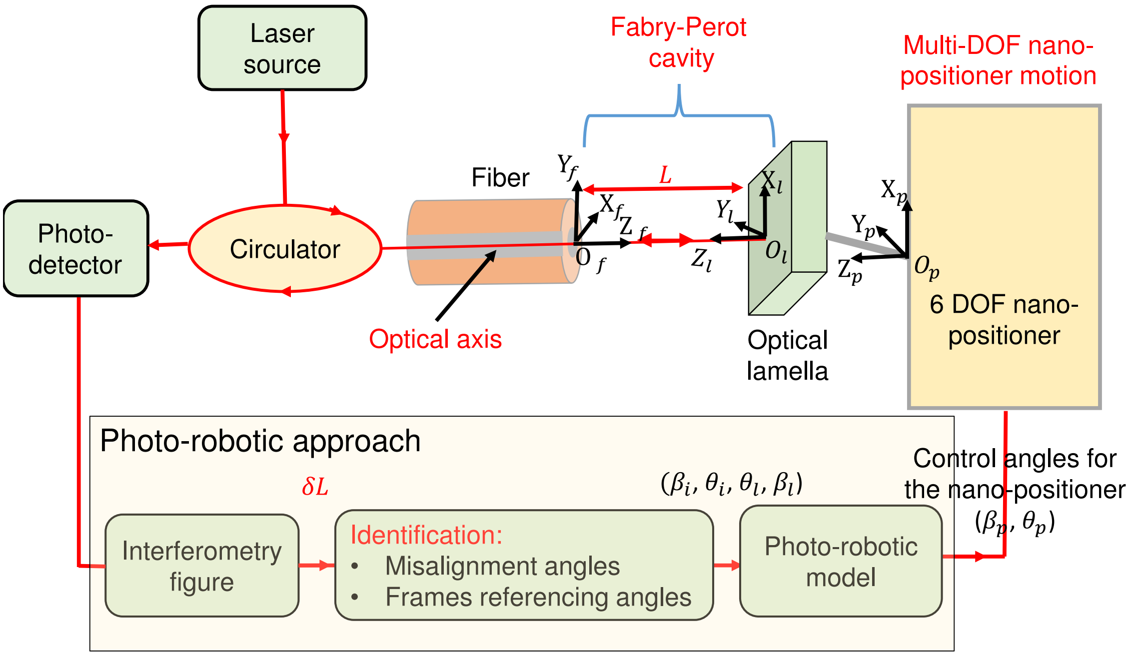

Figure 2.14: The photo-robotic approach experimental implementation.

2.5/ MAXIMIZATION OF OPTICAL IRRADIANCE

Now, we suppose that, a robotic referenced displacement without relative misalignment angles is applied along Y_f or X_f axis. The obtained optical irradiance is expected to be constant, but the maximum optical irradiance is not guaranteed. When the optical lamella is translated along the optical axis, toward the fiber without misalignment angles as shown in Figure 2.15, the corresponding optical irradiance varies increasingly as shown in Figure 2.16, where the closest the optical lamella to the fiber is, the highest oscillation amplitudes (peaks) of the optical irradiance are. If the optical lamella is placed on different FP cavity length, from the farthest to the closest (L_1, L_2, L_3) respectively as shown in Figure 2.15, the corresponding optical irradiance to the closest FP cavity length L_3 is the lowest compared to those correspond to cavity length L_1, L_2 even if it is the closest to the optical fiber. The optical irradiance which corresponds to the FP cavity length L_2 is higher than the optical irradiance which corresponds to the FP cavity length L_3 even it is farther to the optical fiber than FP cavity length L_3 (see Figure 2.17). Therefore, the optical irradiance depends on if the induced cavity length corresponds to a maximum peak or not. The correlation between FP cavity length and the interference figure is indispensable to guarantee the maximum optical irradiance. But, in order to achieve the optimal maximum irradiance, the first closest peak before contact has to be attained. Contact detection is discussed in the next section.

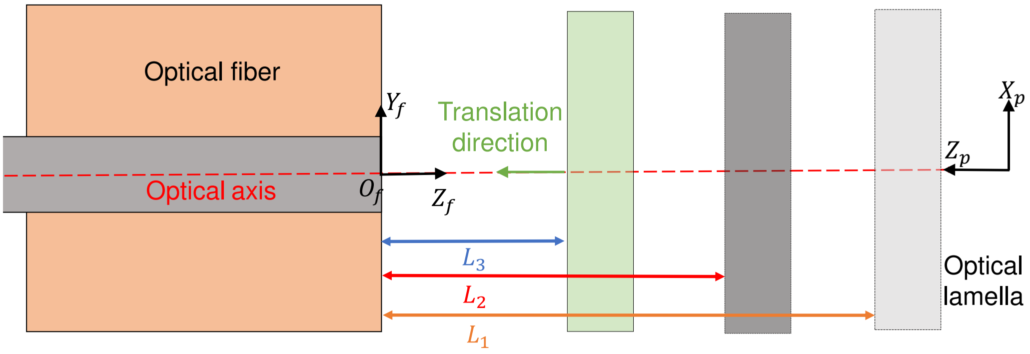

Figure 2.15: Translation along the optical axis (Z_f-axis) toward the fiber.

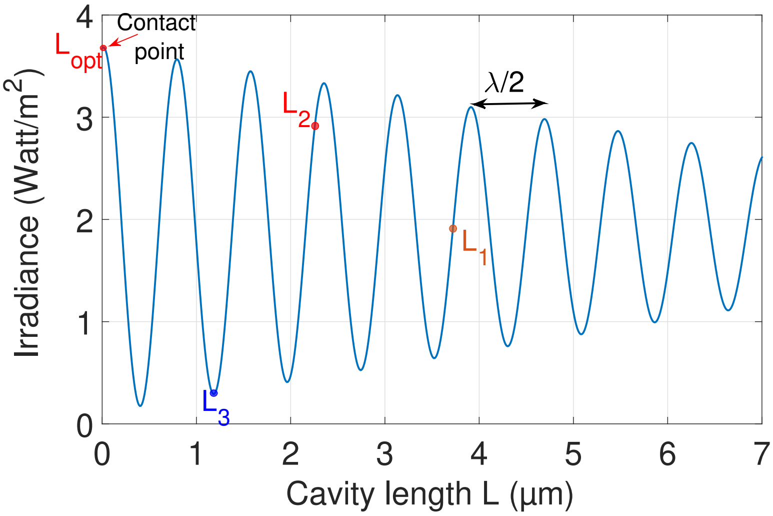

Figure 2.16: Correlation between the FP cavity length L and FP interference for translation along the optical axis toward the fiber.

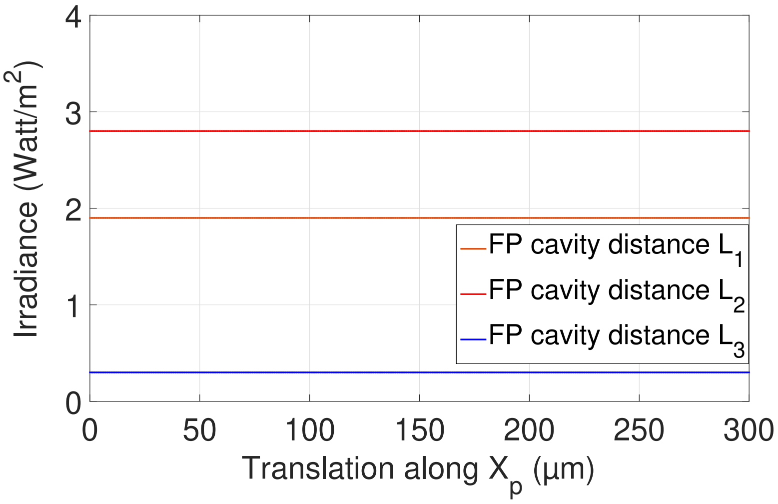

Figure 2.17: The optical irradiance corresponding to different Fabry-Perot (FP) cavity length when translating along X_p-axis.

2.6/ CONTACT DETECTION BASED ON FABRY-PEROT INTERFEROMETRY

The alignment of the optical lamella with respect to the optical fiber does not imply maximum reflected optical irradiance. The correlation between FP cavity length and the interference figure is indispensable to guarantee the maximum optical irradiance. As it is explained previously, in order to achieve the maximum optical irradiance, the first closest peak before contact has to be attained. Therefore, in order to reach maximum optical irradiance, contact detection between the optical lamella and the fiber is indispensable, Once the contact is identified, the first maximum peak before contact can be reached.

The contact detection can be realized by integrating a force sensor to detect contact. In this work we propose to realize contact detection and force estimation based on Fabry-Perot interferometry measure. In order to validate the proposed approach a force sensor is integrated to the experimental set-up. In this way, the results obtained from force estimation based on Fabry-Perot interferometry measure are compared to those obtained from the force sensor.

To study the proposed principle, an experimental set-up has been developed as schematically shown in Figure 2.18 and the real experimental set up can be seen on Figure 2.19. It is composed of a fiber, and a optical lamella placed on compliant structure, itself being the tool of a 6 Degrees-of-Freedom nano-positioning robot. A reference force sensor (compliant) is also placed at the tool tip of the 6-DOF nano-positioner and will be used to validate the experimental estimation of force based on optical Fabry-Perot signal.

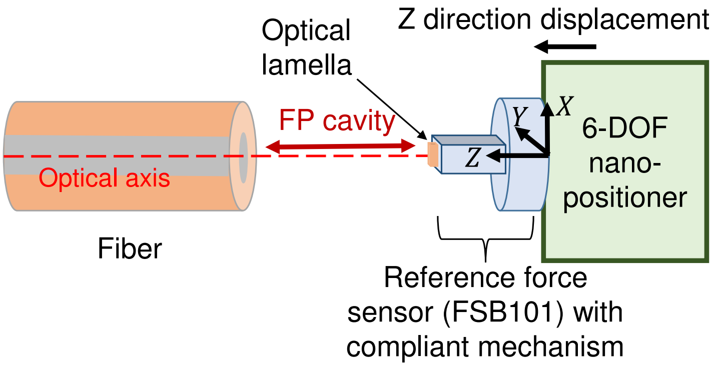

Figure 2.18: Experimental set-up scheme for force estimation and contact detection .

The first step in the validation process is to investigate the repeatability of the force sensor placed at the end-effector of the 6-DOF nano-positioner. For this sake, a forward-backward motion on the Z-axis is realized as shown in Figure 2.20, where the contact of the optical lamella with the fiber is reached for each forward motion and the displacement continues to estimate the force. The pull-off effect appears for each backward motion at the moment when the optical lamella get separated from the fiber. Forward-backward motion on the Z-axis will allow repeatability investigation of the detected force. The corresponding force sensor response for the forward-backward motion is shown in Figure 2.21, where the effect of the pull-off can be clearly seen on the force signal. The pull-off force is the force required to separate two surfaces.

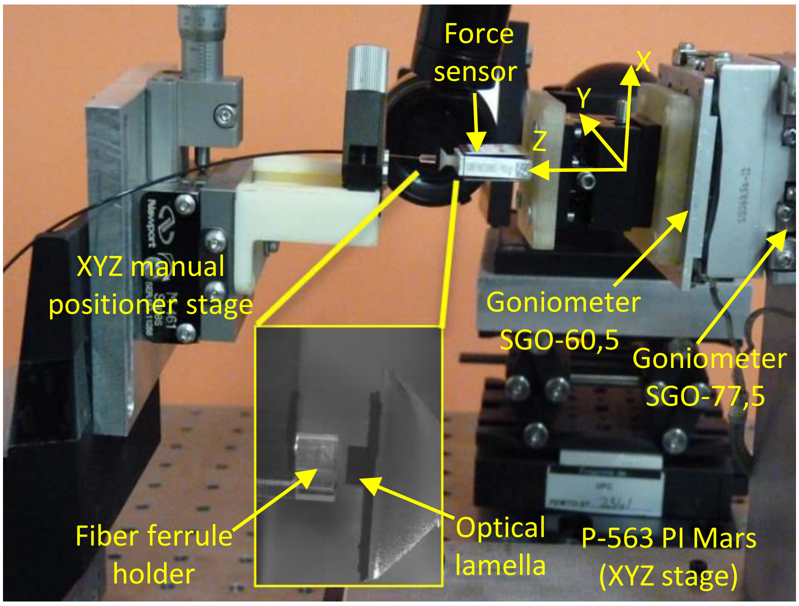

Figure 2.19: Experimental set-up: a 6 Degrees-of-Freedom nano-positioner enables to move a photonic component in front of a fiber, a Fabry-Perot cavity happens providing interferences used for position and force estimation.

Since we are interested in the contact detection, the repeatability of the detected force signal for forward displacement is visualized as shown in Figure 2.22.

Figure 2.23 displays a typical curve that can be obtained through the optical detector. The signal consists in an irradiance having a sine shape but whose frequency varies. First 6.16 μm (sensed by the internal Nano-positioning system) motion does not induce contact between the optical lamella and the fiber. Indeed, the period of the signal is 780 nm corresponding to half of the 1560 nm laser wavelength used. After 6.16 μm motion, a contact happens conducting to a reduction of the frequency of the measured signal. The difference between this measured signal and the one when no contact happens (red curve named expected irradiance without contact) enables to estimate the compression of the compliant structure. Knowing the stiffness of the compliant structure ($k = 1.15$ mN/μm), it could also be possible to estimate the applied force. The estimated force can be calculated using equation 2.3.

$$F_e = k(X_e - X_r), \tag{2.3}$$

where X_e is the expected displacement without contact. X_r is the real displacement after contact, it is calculated using Fabry-Perot principle like previously explained.

In order to validate the force estimation after contact based on Fabry-Perot interferometry, it is compared with the force measured by the reference sensor as shown in Figure 2.24. Results highlight a very good correspondence between both curves. They also show that it is possible to estimate the location of the contact with high precision. These results validate the proposed approach and clearly state the interest for force measurement based on optical Fabry-Perot principle.

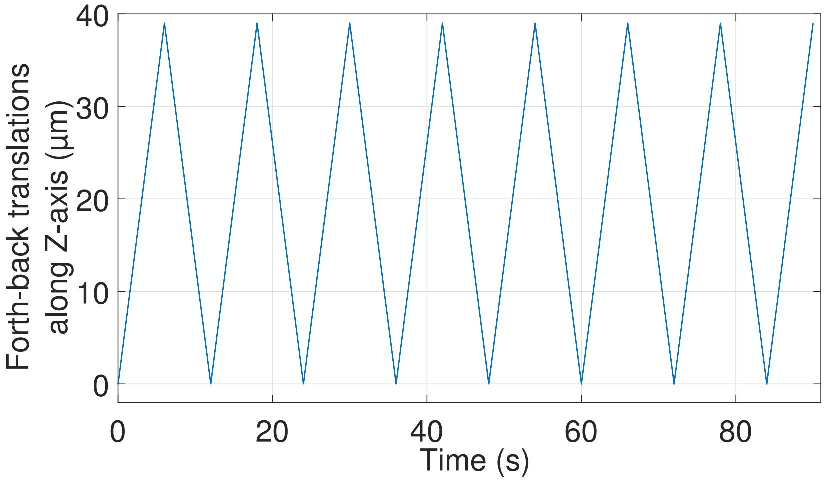

Figure 2.20: Forth-back motion along the Z-axis.

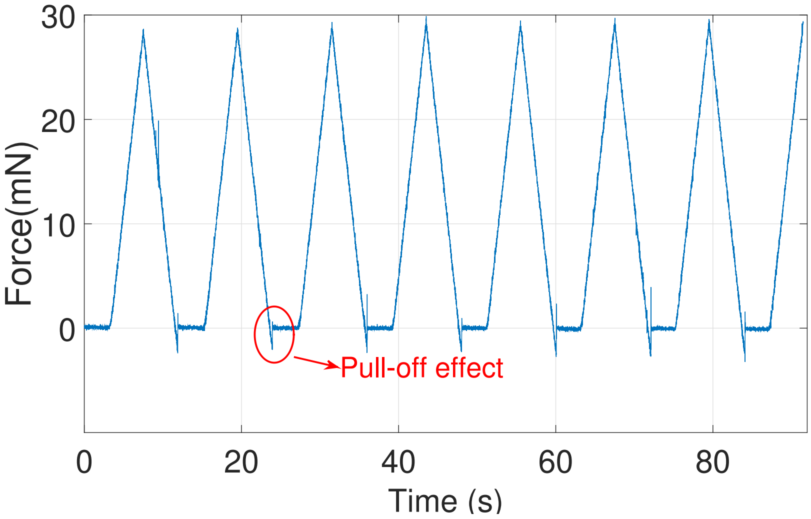

Figure 2.21: The corresponding sensed force for forth-back motion along the Z-axis.

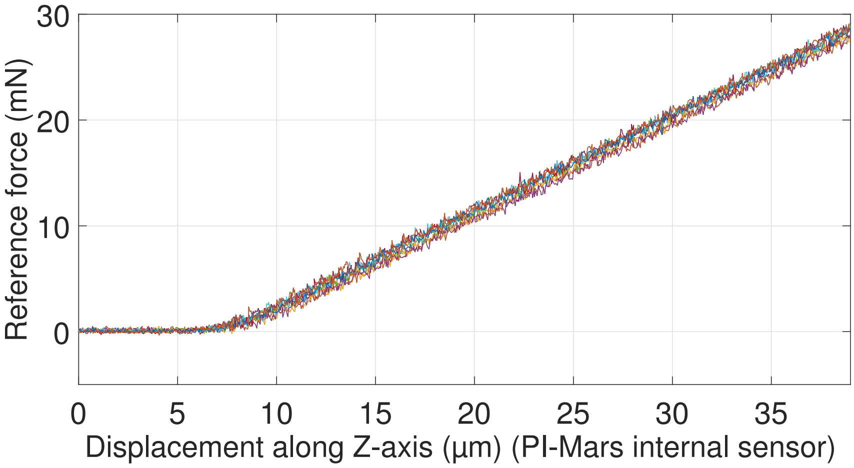

Figure 2.22: The corresponding sensed force for 7 forth motion along the Z-axis.

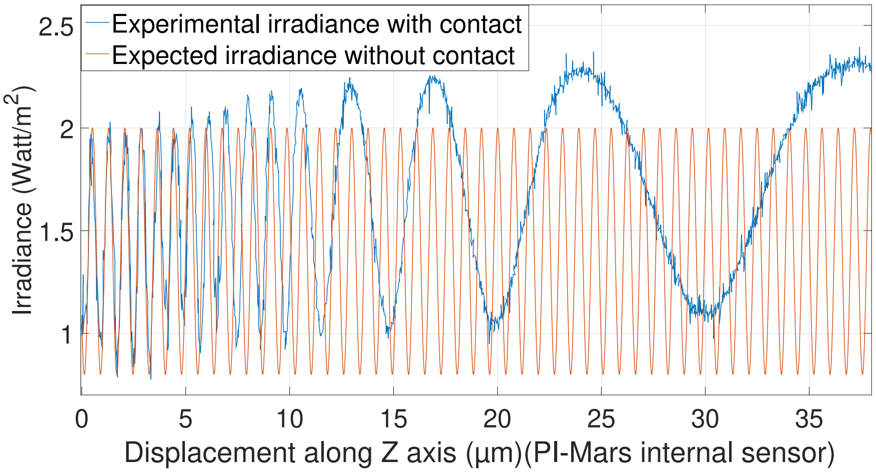

Figure 2.23: Experimental Fabry-Perot interferences evolution when the photonic component is translated along the optical axis, a contact happens at t = 0.3s.

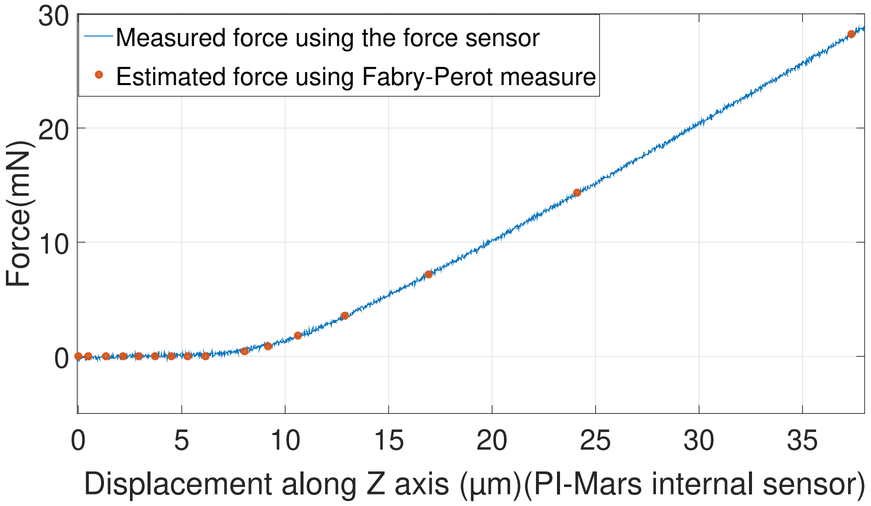

Figure 2.24: Reconstruction of the contact force estimation based on Fabry-Perot interferences.

When the contact happens, the frequency of the measured irradiance reduce. The difference between this measured irradiance and the one when no contact happens (red curve named expected irradiance without contact) enables contact detection as shown in Figure 2.25. The corresponding flowchart for contact detection using Fabry-perot interferometry irradiance measure is shown in Figure 2.26. By taking the case when there is no contact, the experimental optical irradiance uncertainty of Figure 2.11 corresponds to a 27.6 nm measurement uncertainty of displacement. When there is a contact the frequency of oscillation of the optical irradiance gets slower. By fixing a periodicity threshold more than the measurement uncertainty, hence, if the optical irradiance periodicity is more than periodicity threshold, then there is a contact detection. This threshold is fixed to 80 nm.

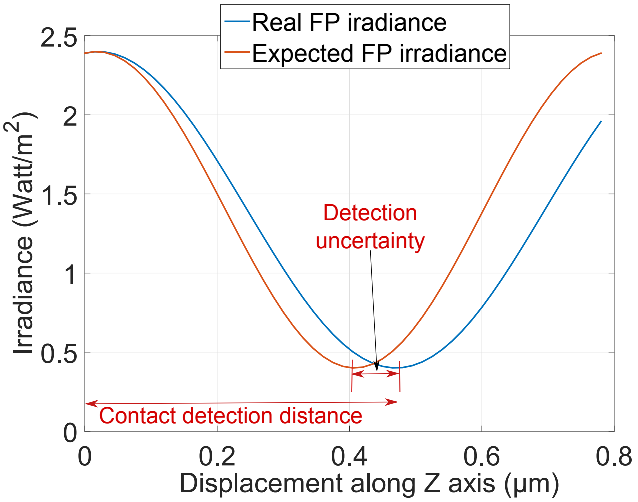

Figure 2.25: Contact detection from expected and real FP irradiance periodicity difference.

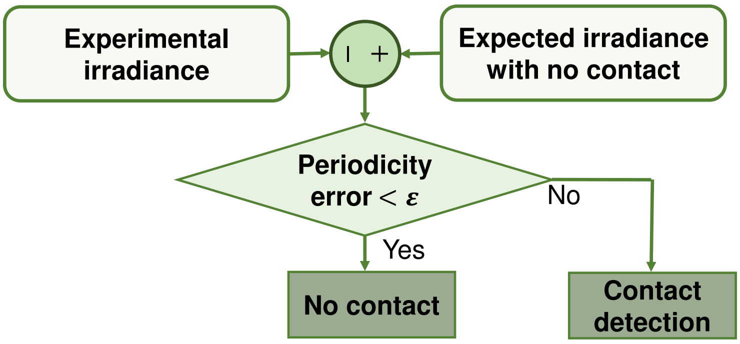

Figure 2.26: Flowchart for contact detection based on Fabry-Perot interferometry measure.

2.7/ CONCLUSION

In conventional active alignment, the non-referenced motion of the nano-positioner holding the optical component in order to search the maximum irradiance induces Fabry-Perot cavity variation, due to different coupled parameters modifications at the same time. As a result, it is difficult to analyze the source of this Fabry-Perot cavity variation, which leads to three main drawbacks: time consumption especially for multi-DOF alignment process to reach maximum irradiance, local maximum problem and the alignment task success relies on human expertise.

The photo-robotic approach is to use Fabry-Perot interferometry figure to identify the parameters yielding the FP cavity variation, by applying robotic referenced rotations and translations (motion). This overcomes the active alignment drawbacks and proposes a robotic, automated and accurate 6 DOF positioning for integrated optics. Fabry-Perot interferometry allows to measure 1-D relative distance along the optical axis. By combining Fabry-Perot interferometry and 6 DOF referenced nano-positioner motion, a multi-DOF measurements are realized. Rotational measurements are realized with an uncertainty based on standard deviation of 2.1 m°, and translational measurements with an uncertainty based on standard deviation of 27.6 nm.

Photo-robotic approach makes the correlation between FP cavity length and the interference figure in order to guarantee the maximum optical irradiance, where the first optical irradiance peak before contact has to be attained. Therefore, the contact detection is required in order to reach the optimal maximum optical irradiance. A new approach for contact detection based on Fabry-Perot interferometry is proposed. Contact detection realizes a high accurate contact detection with an error of 80 nm. The obtained off-line contact detection is very promising to realize on-line high accurate contact detection, by replacing the force sensor by a compliant structure with reflective surface.

The next objective is to generalize the photo-robotic approach to realize robot parameters calibration to attain a very high 6-DOF positioning accuracy for complex tasks. This represents a very challenging objective in many application fields especially integrated optics field for optical polarization control. The measurement system for calibration is based on 1-D Fabry-Perot interferometry relative distance measure. This challenging calibration purpose is treated in detail in the next chapter.

3

EXTRINSIC GEOMETRIC ROBOTIC CALIBRATION BASED ON FABRY-PEROT INTERFEROMETRY RELATIVE DISTANCE MEASURE

Contents

3.1/ INTRODUCTION

Nano-positioning stages are used for a wide range of applications that are constantly expanding at the micro-scale. Most of these applications need to control very accurately the relative position and/or trajectories between a sample (for example, component to handle, tissue or living cell) and a tool used for manipulation or characterization purposes. In most cases, this ability influences directly and strongly the results such as the success rate, performances of the assembled micro-system and resolution of the characterization or analysis [Chaillet et al., 2013].

Nano-positioning stages are usually used to build the micro-nano-positioning robots, because of their capability to provide high-resolution motions. Based on the compliant or stick-slip principle, such stages are designed with active-material-based actuators that are able to produce translations. The compliant structure can also amplify the actuators movement. The compliant mechanisms generally provide a small range of motion (smaller than 500 μm) but very high resolution (in the nanometer range), straightness, and flatness [Wang et al., 2014] [Devasia et al., 2007] [Li et al., 2012] [Lin et al., 2013], which make nano-positioning stages a key technology for applications requiring a high positioning accuracy. However, despite the widespread use, high potential, and strong efforts done to design and fabricate new nano-positioning stages, several negative specificities still have to be overcome to reach the desired performances:

- Micro-nano-positioning robots suffer usually from different intrinsic geometric defaults due to assembly from nano-positioning stages. These geometric defaults parameters affect the positioning accuracy.

- Sensors integrated (if any) in the stage suffer from extremely complex trade-off because many conditions must be reunited at the same time, such as small volumes, nanometer resolutions, motion ranges of several hundred micrometers, and high bandwidths. Moreover, integrated sensors usually measure the local motion generated by the actuator in front of the compliant structure or at a location of the compliant structure with a maximum mechanical strain (i.e., in the compliant joints). This indirect measurement technique (meaning that the output motion of the stage is not measured directly) requires a model to estimate the motion of the stage. In spite of using the efficient closed-loop control, the problem of locating accurately the mobile-part output of the stage remains.

- Actuators have nonlinear and sometimes time-varying behaviors, e.g., hysteresis and creep [Rakotondrabe et al., 2010].

- The mechanical structure is influenced by environmental conditions. Very small change in temperature may influence the positioning accuracy.

In addition to these difficulties, achieving the micro-nano tasks usually requires control of the nano-positioning stage and position the end-effector with respect to a fixed reference frame, for instance, to position an optical component with respect to the measurement system frame, where the extrinsic geometric parameters between the optical component frame and the measurement system frame are required to be identified and integrated, to achieve high relative positioning accuracy. On one hand, additional sensors may be used to provide an outer-loop control (the often used inner-loop feedback one is based on internal sensors of the stages) [Clark et al., 2015]. However, a key limitation is the complexity of integrating sensors able to measure a relative position with required range, resolution, bandwidth and number of DOF (Degree-Of-Freedom) [Clévy et al., 2011]. For example, dedicated machines used for microsystems fabrication enable to position a component relative to the others in the plane with an accuracy of a few tens of nanometers. Nevertheless, they are usually designed for single purposes and extremely costly (in the millions of euros range). On the other hand, it is possible to control nano-positioning stages in open loop at the task level while keeping the inner loop based on internal nano-positioning stage sensors [Maroufi et al., 2015]. The open loop method can be realized with the calibration approach where a good and reliable model is required to depict the whole system including all the influential parameters.

To go further, this chapter reviews the parameters that can affect the positioning accuracy. This leads to deal with geometric parameters calibration in order to improve the positioning accuracy. Afterward, the geometric parameters calibration steps: modeling, measurement, identification and correction are discussed. In this chapter, calibration for macro and micro-nano robotics is also reviewed, by discussing their calibration approaches. This enables to identify which calibration approaches that could be adapted for micro-nano robot calibration. In order to improve positioning accuracy, a robot extrinsic parameters calibration based on a photo-robotic approach is proposed. The photo-robotic approach relates a 1-D relative distance with a multi-DOF robot motion in order to identify extrinsic geometric parameters. The 1-D relative distance is realized based on high accurate Fabry-Perot interferometry principle. In order to validate our proposed approach, the experimental procedure for extrinsic robot calibration and the experimental set up dedicated for 6-DOF positioning of optical components are presented. Finally, the obtained results are discussed. In the next section, Parameters affecting positioning accuracy are discussed.

3.2/ PARAMETERS AFFECTING POSITIONING ACCURACY

The positioning accuracy is affected by different parameters acting on micro-robotic systems, that can be geometric or non-geometric.

The non-geometric parameters are induced by environments, such as temperature [Zhou et al., 2002], humidity [Jääskeläinen et al., 2009], and noise [Boudaoud et al., 2012]. Acoustic influence could also become an issue of positioning accuracy when the micro-robotic systems are working in a noisy environment. Vibration can be minimized by placing the micro-robotic systems on the anti-vibration tables and isolation bases [Shiakolas et al., 2002].

The geometrical parameters themselves can be divided into two sets: intrinsic and extrinsic.

1. Intrinsic geometric parameters

Micro-nano-positioning robots suffer usually from different intrinsic geometric defaults due to their assembly from nano-positioning stages. In applications using micro-nano-positioning robots, several micro-positioning stages often have to be assembled to accomplish some functionalities. In such applications, errors about parallelism and perpendicularity (twist) may be induced during the manual assembly process. In Figure 3.1 (a) the angle δ between two axes $\overrightarrow{z}$ and $\overrightarrow{y}$ is usually desired to be right angle, however, it is difficult to get an exact right angle by manual assembly.

Some errors come from fabrication process or wear and tear during the normal use of robots. For example, the structure and dimension of the robot varies more or less after they left the factory (depending to the environmental conditions). ΔH and ΔL are height and length errors of the base and the arm. The values of nominal geometric parameters (L, H in Figure 3.1 (b)) are not consistent with real parameters. So the control models based on the nominal geometric values may generate a deviation between the real position and the desired position of the end-effector.

Another kind of imperfection is due to the inherent characteristics (flatness and straitness) along axes or actuators. Machine tool industry pays more attention to these imperfections than robot manufactures. However, these imperfections become significant at the micro-scale where high positioning accuracy is desired. For positioning, linear motion is required, but at the micro-scale we cannot consider it as perfectly linear. Figure 3.1 (c) shows position errors such as flatness and straightness errors as well as roll, pitch, and yaw angles. The absolute values of these parameters are usually small but induce errors to be considered or influential at the micro or nano-scale. The example of Figure 1.10 shows that the position error induced by the small yaw angle 150 μrad is amplified by the 20 mm length robot arm to 3 μm.

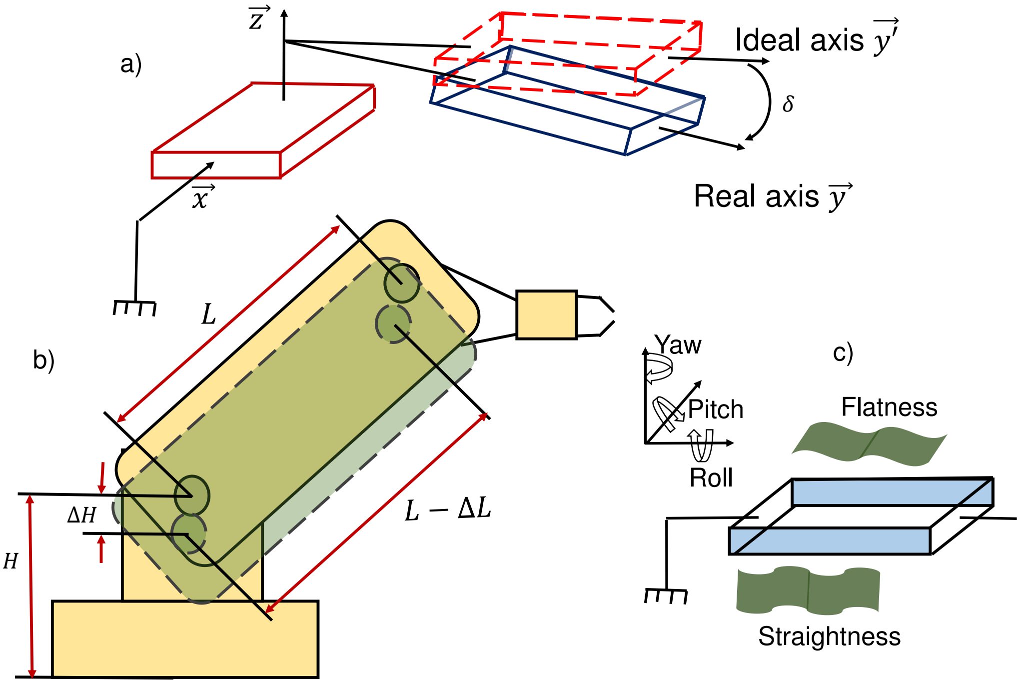

Figure 3.1: Intrinsic geometric imperfections: a) Assembly errors between two axes. b) Structure and dimension errors of the robotic manipulator where ΔH and ΔL are height and length errors of the base and the arm. c) Position-dependent errors along single axis.

2. Extrinsic geometric parameters

Extrinsic parameters also have to be considered to achieve high positioning accuracy, notably to position the base frame with respect to the cell frame (world frame), and tool frame with respect to the end-effector (see Figure 3.2). These kinds of parameters can come from the tool object dimensions, object prehension errors, and world frame to base frame estimation.

The main parameters are summarized in the flowchart of Figure 3.3. The parameters presented previously do not all have the same influence on the positioning accuracy of the robot. The classification of the parameters according to their influence has given rise to many discussions [Shiakolas et al., 2002] , [Veitschegger et al., 1986]. However, the study of publications made since the first work on calibration leads to the following conclusion: the influence of geometric errors are often predominant than the non-geometric ones. But, in micro-scale calibration, more precautions need to be taken experimentally like to ensure constant environmental conditions to avoid non-geometric parameters influence. In the next section, geometric robotic calibration is discussed.

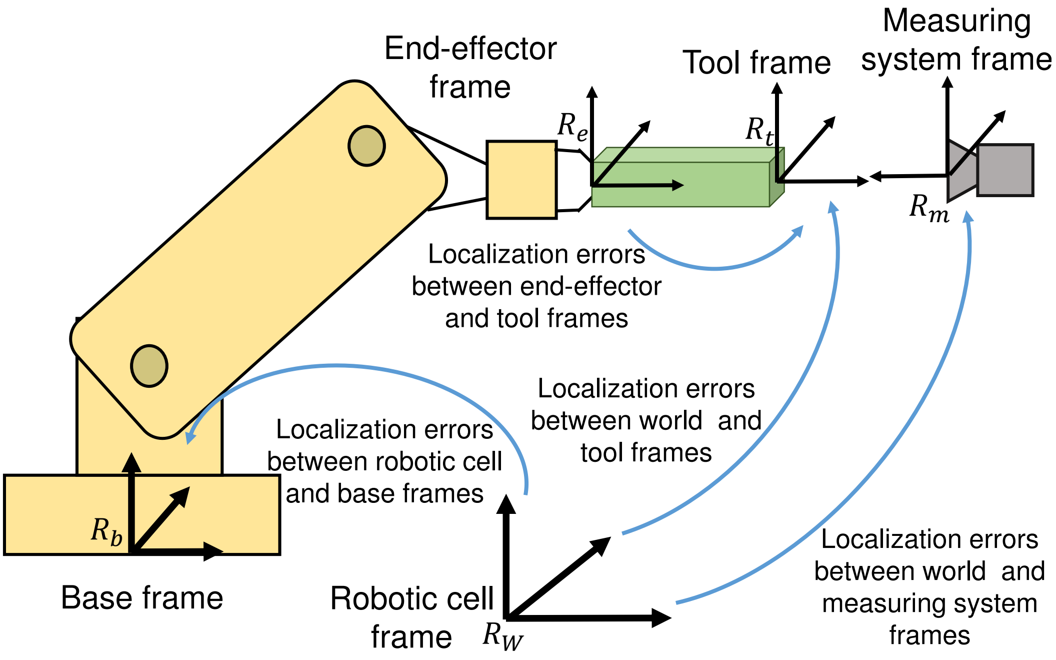

Figure 3.2: Extrinsic geometric parameters.

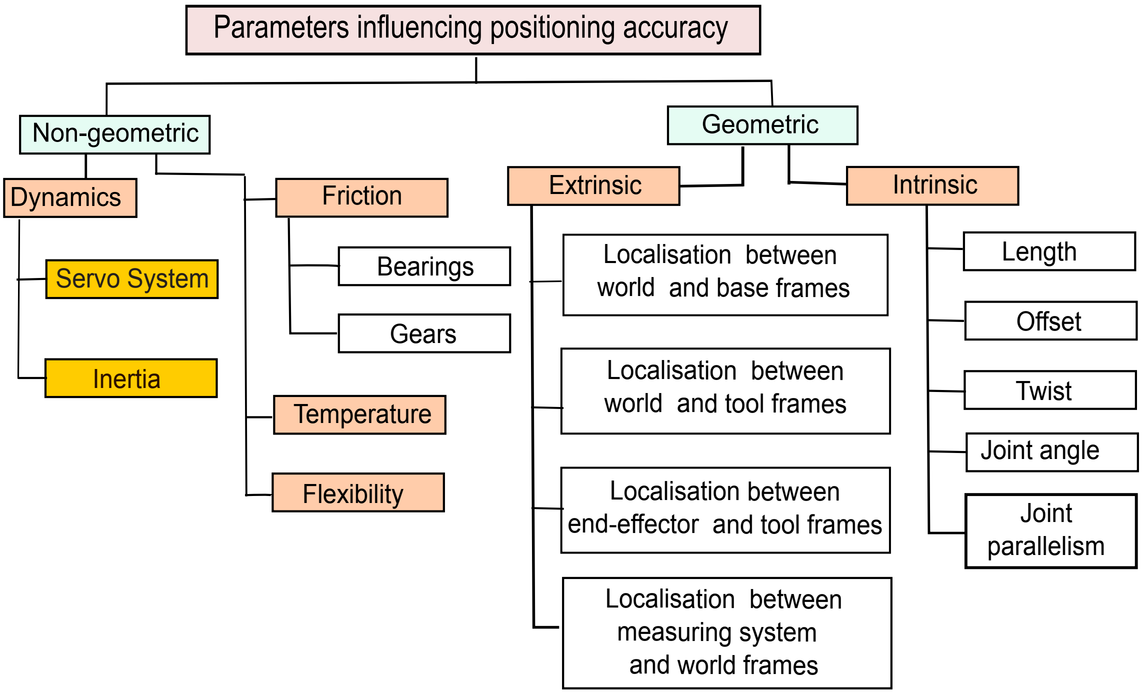

Figure 3.3: Parameters influencing robots positioning accuracy.

3.3/ GEOMETRIC-BASED ROBOT CALIBRATION

Generally, geometric-based robot calibration is considered as a global calibration method that improve robots positioning accuracy in the entire volume of the robots workspace.

Geometric- based calibration is a procedure that includes four distinct steps [Zhuang et al., 1996]:

- Step 1: geometric modeling;
- Step 2: pose measurement;
- Step 3: identification;
- Step 4: compensation or correction.

The steps are described below:

Step 1: Geometric Modeling

Geometric model regard the relationship between the joint and operational coordinates (coordinates with respect to the world reference frame), by modeling the robot geometric parameters. Geometric model involves establishment of the robot DGM (Direct Geometric Model) and IGM (Inverse Geometric Model), which are successively used to control the robot. This task usually consists in determining mathematical description that describes the required coordinate transformations based on different approaches for the geometric representation.

A number of different approaches exist for developing the geometric model of a robot manipulator. One of the most known method has been accomplished by Denavit and Hartenberg [Denavit, 1955]. The method based on homogeneous transformation matrices. The procedure consists of establishing coordinate systems on each joint axis. Each coordinate system is then related to the next through a specific set of parameters in the homogeneous transformation matrices. Afterwards, many researchers mentioned the model singularity problem raised in D-H representation. Ibara and Perreira [Ibarra et al., 1986] used the D-H procedure and changed each transformation matrix with a differential screw matrix for small misalignment. A new notation is derived from the popular D-H method by Khalil and Kleinfinger [Khalil et al., 1986] which can be used to describe the open-loop robots and the closed-loop robots with a minimum of parameters and without ambiguities or difficulties. Khalil and Kleinfinger representation is one of the mostly used conventions for the geometric models used in most existing robot control systems. However, Khalil and Kleinfinger representation faces a problem when two joint axes are parallel. When two consecutive joint axes $i-1$ and i are parallel, the x_{i-1} axis is chosen arbitrarily along one of the common normals between them. If z_i or z_{i-1} gets slightly misaligned, the common normal becomes uniquely defined and a big variation in the parameter d_i might occur. To overcome this problem, Hayati introduced a new parameter β_i representing a rotation around the Y_{i-1} axis [Hayati et al., 1985]. β_i is the angle around the axis Y_{i-1} between the axes Z_{i-1} and Z'_{i-1}.

Khalil and Kleinfinger modeling that includes additional Hayati parameter was established based on two main assumptions: the links are perfectly rigid and the joints are ideal in a sense that there is neither backlash nor elasticity. A serial robot is composed of a sequence of $n-1$ links and n joints where link 0 is the base of the robot and link n is the terminal link. Joint i connects the link i to the link $i-1$ and its variable is denoted by θ_i. A frame R_i is attached to each link i with [Khalil et al., 2004] :

- The Z_i axis is located along the axis of joint i;
- The X_i axis is located along the common normal between the Z_i and Z_{i+1} axes. If Z_i and Z_{i+1} axes are parallel or collinear, the choice of X_i is not unique: considerations of symmetry or simplicity then allow a rational choice;
- The Y_i axis is located using the right-hand rule to form (X_i, Y_i, Z_i) coordinate system.

The transformation matrix from frame R_{i-1} to frame R_i is expressed using the following four geometric parameters (Figure 3.4):

- Joint parallelism: β_i is the angle around the axis Y_{i-1} between the axes Z_{i-1} and Z'_{i-1};
- Link twist: α_i is the angle around the axis X'_{i-1} and between the axes Z'_{i-1} and Z_i;
- Link length: d_i is the distance along the axis X'_{i-1} between the axes Z'_{i-1} and Z_i;
- Joint angle:θ_i is the angle around the axis Z_i between the axes X'_{i-1} and X_i;
- Link offset: r_i is the distance along the axis Z_i between the axes X'_{i-1} and X_i.

The variable of the joint i denoted by q_i is θ_i if i is rotational and r_i if i is prismatic. Hence

$$q_i = \theta_i(1-\rho_i) + r_i\rho_i, \tag{3.1}$$

where

$$\rho_i = \begin{cases} 0, & \text{for rotational joint} \\ 1, & \text{for prismatic joint} \end{cases}. \tag{3.2}$$

The transformation matrix defining the frame R_i in the frame R_{i-1} is given by

$$^{i-1}T_i = Rot_{Y_{i-1}}(\beta_i) * Rot_{X'_{i-1}}(\alpha_i) * Trans_{X'_{i-1}}(d_i) * Rot_{Z_i}(\theta_i) * Trans_{Z_i}(r_i). \tag{3.3}$$

The matrices associated with these operations are:

$$Rot_{X'_{i-1}}(\alpha_i) = \begin{bmatrix} 1 & 0 & 0 & 0 \\ 0 & \cos\alpha_i & -\sin\alpha_i & 0 \\ 0 & \sin\alpha_i & \cos\alpha_i & 0 \\ 0 & 0 & 0 & 1 \end{bmatrix}; \tag{3.4}$$

$$Rot_{Z_i}(\theta_i) = \begin{bmatrix} \cos\theta_i & -\sin\theta_i & 0 & 0 \\ \sin\theta_i & \cos\theta_i & 0 & 0 \\ 0 & 0 & 1 & 0 \\ 0 & 0 & 0 & 1 \end{bmatrix}; \tag{3.5}$$

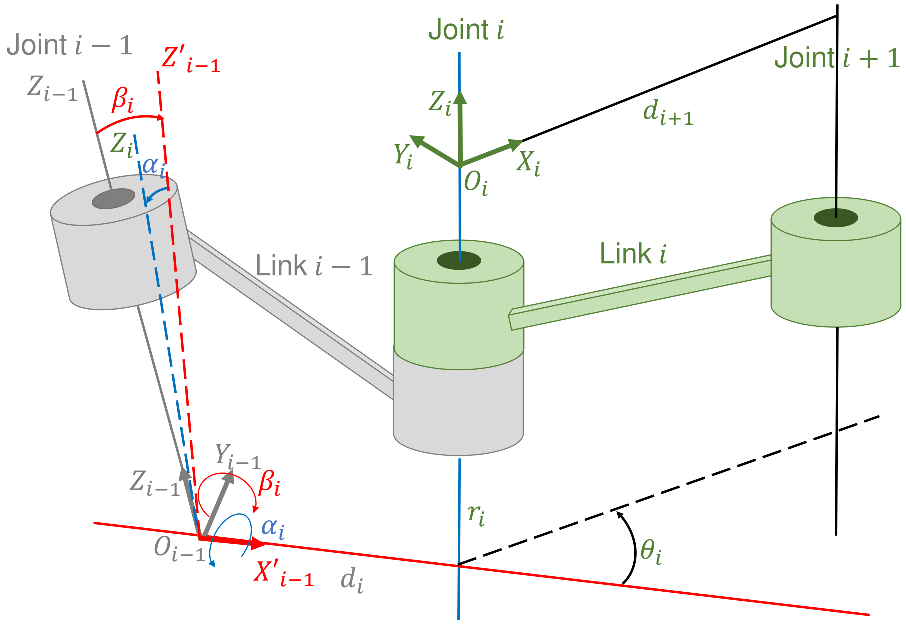

Figure 3.4: The additional Hayati parameter β_i about Y_{i-1} is employed for nearly parallel axes.

$$Trans_{X'_{i-1}}(d_i) = \begin{bmatrix} 1 & 0 & 0 & d_i \\ 0 & 1 & 0 & 0 \\ 0 & 0 & 1 & 0 \\ 0 & 0 & 0 & 1 \end{bmatrix}; \tag{3.6}$$

$$Trans_{Z_i}(r_i) = \begin{bmatrix} 1 & 0 & 0 & 0 \\ 0 & 1 & 0 & 0 \\ 0 & 0 & 1 & r_i \\ 0 & 0 & 0 & 1 \end{bmatrix}; \tag{3.7}$$

$$Rot_{Y_{i-1}}(\beta_i) = \begin{bmatrix} \cos\beta_i & 0 & \sin\beta_i & 0 \\ 0 & 1 & 0 & 0 \\ -\sin\beta_i & 0 & \cos\beta_i & 0 \\ 0 & 0 & 0 & 1 \end{bmatrix}. \tag{3.8}$$

Thus, the general transformation matrix between two frames with consecutive parallel joints becomes [Khalil et al., 2004]:

$$^{i-1}T_i = \begin{bmatrix} C\beta_i C\theta_i + S\alpha_i S\beta_i S\theta_i & S\alpha_i S\beta_i C\theta_i - C\beta_i S\theta_i & C\alpha_i S\beta_i & d_i C\beta_i + r_i C\alpha_i S\beta_i \\ C\alpha_i S\theta_i & C\alpha_i C\theta_i & -S\alpha_i & -r_i S\alpha_i \\ S\alpha_i C\beta_i S\theta_i - S\beta_i C\theta_i & S\beta_i C\theta_i + S\alpha_i C\beta_i S\theta_i & C\alpha_i C\beta_i & r_i C\alpha_i C\beta_i - d_i S\beta_i \\ 0 & 0 & 0 & 1 \end{bmatrix}, \tag{3.9}$$

where $C\gamma$ stands for $\cos\gamma$ and $S\gamma$ stands for $\sin\gamma$.

The modified version by Khalil and Kleinfinger with additional Hayati parameter β_i is used to establish the direct geometric model of our robot throughout this thesis.

The direct geometric model for a serial-chain manipulator is defined as finding the pose (position and orientation) of the end-effector relative to the base given the values of the joint variables and the geometric link parameters. It can be solved by calculating the transformation between the frames fixed in the end-effector and in the base. This transformation can be obtained by simply concatenating the transformations between the fixed frames of the adjacent links [Khalil et al., 2004]:

$$^{0}T_n(q) = ^{0}T_1(q_1) *^{1} T_2(q_2) \ldots ^{n-2}T_{n-1}(q_{n-1}) *^{n-1} T_n(q_n), \tag{3.10}$$

where R_0 is the base frame and R_n is the end-effector frame.

The direct geometric model can also be represented by:

$$X = f(q), \tag{3.11}$$

where q is the vector of joint coordinates as defined by:

$$q = [q_1 \;\; q_2 ... q_n]^T. \tag{3.12}$$

And X is the vector of operational coordinates as defined by:

$$X = [x, y, z, \theta_x, \theta_y, \theta_z]^T. \tag{3.13}$$

The direct geometric model of a robot enables to calculate the operational coordinates of the end-effector giving the joint coordinates. The inverse problem is to calculate the joint coordinates corresponding to a given operational coordinates of the end-effector as shown in Figure 3.5. When exists, the form that gives all the possible solutions (there is rarely a single solution) is The Inverse Geometric Model (IGM).

The IGM can be calculated explicitly, using Paul method [Paul, 1981], Pieper's method [Peiper, 1968] or Raghavan and Roth [Raghavan et al., 1993].

Another choice is to calculate the inverse geometric model numerically. By using optimization algorithms [Escande et al., 2010][Sugihara, 2011][Hasan et al., 2010], which is the choice we used to calculate IGM of our 6 DOF robot, by using MATLAB optimization toolbox.

Step 2: Pose measurement

The measurement step regards the sensing of the operational coordinates of the robot end-effector or tool pose. The measured poses of the robot end-effector are then compared with the poses predicted by the theoretical model to get the workspace error data.

Measurement systems and measurement procedures used for robot calibration are very important in terms of identifying the model parameters and estimating the robot performance. There are different measurement systems employed in robot calibration studies such as laser trackers [Zhao et al., 2018], optical sensors [Nubiola et al., 2014], photogrammetric [Filion et al., 2018], coordinate measuring machines [Santolaria et al., 2008] [Santolaria et al., 2009], stereo vision [Švaco et al., 2014] and theodolites [Zhuang et al., 1995].

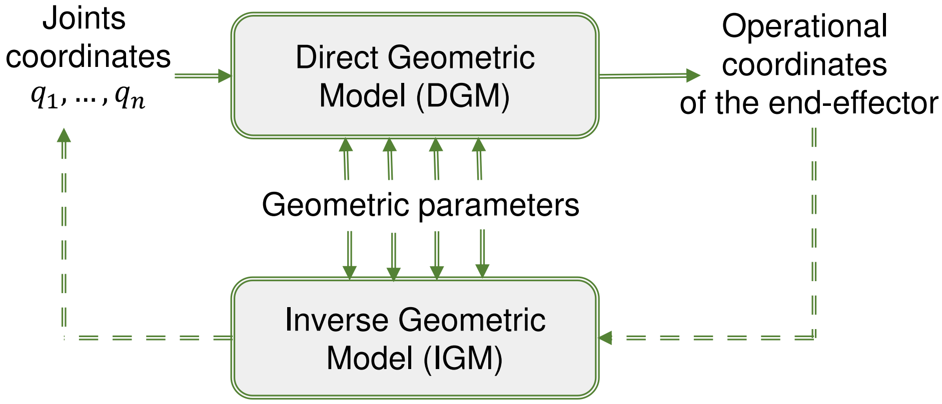

Figure 3.5: Inverse and Direct Geometric Model relationship.

These measurement systems should agree with calibration process requirements in terms of accuracy and effectiveness. The choice of measurement system depends on the realized task, the approach used for calibration and finally the required accuracy. High accurate measurement system is expected to achieve high identified parameters accuracy.

Step 3: Identification

Parameters identification regards numerical methods. The methods must be reliable and effective to reach a solution in adequate level of accuracy in the resulting identified parameter values. The identification of the parameters in a robot kinematic model is a difficulty that has been conducted by several studies [Zhao et al., 2015][Wu et al., 2010][Bingül et al., 2011] using different models and identification methods.

In this step, geometric parameter errors are identified, by minimizing the collected workspace errors. The geometric identification can be done based on a standard non-linear or linear least square optimization method. When linear least square algorithms are applied, they require less computation time to converge, but suffer from numerical problems of ill-conditioning of the Jacobian identification. To solve this difficulty, Levenberg-Marquardt algorithm [Guelpa et al., 2018][Blöchliger et al., 2017][Messay et al., 2016] is used for geometric parameters identification throughout the thesis.

Step 4: Correction

The last step of robot calibration is to correct the identified errors of the robot. The simplest way is to update the identified parameter values directly inside the robot control system. However, most robot control systems use only the nominal geometric parameters on their model. Furthermore, not all robot control systems allow to change the nominal model parameters. Another method is to modify the robot program by correcting the robot joint coordinates.

Joint corrections are made to the joint encoders readings of the robot obtained by solving the inverse geometric model of the calibrated robot. Since the inverse geometric model of the calibrated robot generally are not solvable analytically, numerical algorithms approaches are usually used to solve the model to obtain the joint corrections needed to compensate for Cartesian errors. With numerical algorithms, on-line compensation is a problem due to the computation time and the algorithms usually breaks down in the vicinity of robot singular configurations, because the approach is based on the iterative inversion of the compensation Jacobian [Elatta et al., 2004]. In order to avoid the mentioned on-line correction problems, off-line correction is the mostly used in robot calibration. The next section discusses the existing approaches in macro robot calibration.

3.4/ GEOMETRIC ROBOT CALIBRATION AT THE MACRO-SCALE

Robot calibration has been extensively studied over the last three decades. Most of these studies can be categorized into two types based on measurement. One type requires external sensor to measure full or partial robot end-effector pose. Using full parameters measurements, as it is very convenient to identify all geometric parameters, as it leads to many drawbacks. Data collection is tiring and time-consuming, the set-up and measurement procedures require a lot of human intervention, which make them unsuitable for robot on-site calibration in an industrial environment. Also trained staff are required to operate the measuring devices properly. Theses drawbacks gave raise to other robot calibration methods based on constrained and partial measurements methods.

The second type of methods imposes some constraints on the end-effector. There are two approaches based on constrained calibration: point-point position constraint and Point-surface position constraint. The constraints in the two approaches can be realized either with contact or virtually.

[Khalil et al., 1995] used point-point position constraints with contact based on visual check of point-point constraint contact. A point of the end-effector is taken by learning on a point known to the environment under various directions. Using the joint coordinates recorded for each configuration verifying the constraint, an error model is developed considering the difference between the relative Jacobians in two consecutive configurations. Subsequently, the singular value decomposition techniques of the differential model are used to determine the identifiable parameters.

[Hage et al., 2011] used point-surface position constraints with contact, where a probe was used to constrain the end-effector of the robot to move parallel to several reference planes placed in the robot's workspace. The advantage of using such a sensor lies in the fact that the measurements are automatic. The elaborated model also consider the errors of orientation of the plan, since the orientation of the plan is also identified.

Virtual constraints methodology [Du et al., 2012] is used to constrain the robot end-effector to follow rectilinear trajectories. For this purpose, Position Sensitive Detector (PSD) device and a Focusable Laser Point (FLP) were used. The portable dual PSD device comprises two fixed PSDs tilted in an angle to reflect the laser line from one PSD to another. The FLP, attached to the robot end-effector, aims at both centers of the two PSDs at the same time, effectively creating a virtual line constraint for the robot end-effector.

The main advantages of these constrained methods are related to their ease of implementation and their low cost. But, only a small volume of the robot's workspace can be explored what can lead to non observability or poor estimation of some parameters. Moreover, at the micro-scale, using constrained approaches with contact is not convenient, in the case where the connection is mechanical, significant efforts can be generated at the end-effector which may damage the robot on one hand, and on the other hand the constrained mechanism. In addition, these deformations introduce potential large inaccuracies in the measurements.

Instead, several partial specified pose measurements were raised, leading to other robot calibration methods such as relative position and distance measure [Zhang et al., 2018]. The relative distance measure method uses the minimum distance between two points to calibrate kinematic parameters of a robot. Many recent researches have been conducted on this method. [REN et al., 2008] used relative distance measure between two points in space to measure the absolute positioning accuracy of robots. Therefore, the distance error model for robot was established to avoid the error caused by the coordinate transformation. [Zhenhua et al., 2014] conducted a geometric parameter calibration model of industrial robots based on distance accuracy. The experimental results proved that the calibration model could improve the robot's distance and absolute positioning accuracy for higher performances.

From the existing geometric calibration approaches in literature, relative distance measure calibration method is chosen to calibrate our robot, which also appears fully relevant for optical components manipulation and assembly. The first argument of our choice is that positioning optical components for optical polarization control and integrated optics assembly can measure high accurate relative distance using Fabry-Perot interferometry principle on the optical axis, which can be used as a measurement system for calibration. The second argument is that relative distance measure calibration method demonstrated its efficiency to reach high positioning accuracy for higher performances. In the next section, we will see the existing approaches for geometric calibration for micro-scale applications.

3.5/ GEOMETRIC ROBOT CALIBRATION AT THE MICRO-SCALE

Comparing with macro-robotics, calibration of micro-robotics is rarely studied. With the fast development of micro-robotics during the last decades, research about calibration of micro-robots is getting more and more attention, in order to fulfill high accurate micro-manipulation tasks. However, measurement at the micro-scale is a very challenging issue. Micro-scale measurement requires sensing devices with high resolution (e.g., a few nanometers) and accuracy (e.g., tens of nanometers) because motion and errors at this scale are very small. Only accurate enough sensors can detect such motion and errors. Multi-DOF sensing is required when the micro-robot realize motions in multi-DOF. In current market, there is a lack of sensing device satisfying multi-DOF measurement. The optical sensors usually can only offer 1-DOF measurement and the vision is able to provide 2-DOF measurement. However, vision's performances on resolution, accuracy, and measuring range are less efficient than optical sensors. If performing multi-DOF measurement, several sensors should be combined to build a measuring system. In this case, another problem may appear, that is, the workspace is too small to arrange all these sensors. Optical sensors and vision systems usually have bulky sizes relative to the micro-robots. Beside the measurement problem in micro-scale robot calibration, there are others micro-scale specificities issues like drift and noise influence.

In order to overcome the micro-scale specificities and measurement issues, some researchers investigated robot calibration for micro-scale applications based on different measurement strategies and calibration approaches. There is a work realized in [Popa et al., 2009]. They illustrated the calibration method through extrinsic geometric parameters identification and compensation of micro-manipulation station, by a vision system for measurement as shown in Figure 3.6 (a). First the tilt angle was manually adjusted in order to guarantee that end-effectors were vertical enough to pick up all parts. Then, finding the transformation from world frame into R1 frame, and then into the gripper tool manipulator R2 frame. The schematic diagram of the relative position of several local/global frames is shown as shown in Figure 3.6 (b). The obtained positioning accuracy result is based on only extrinsic geometric parameters compensation, which led positioning error of 35 μm of the aligned MEMS die to the carrier.

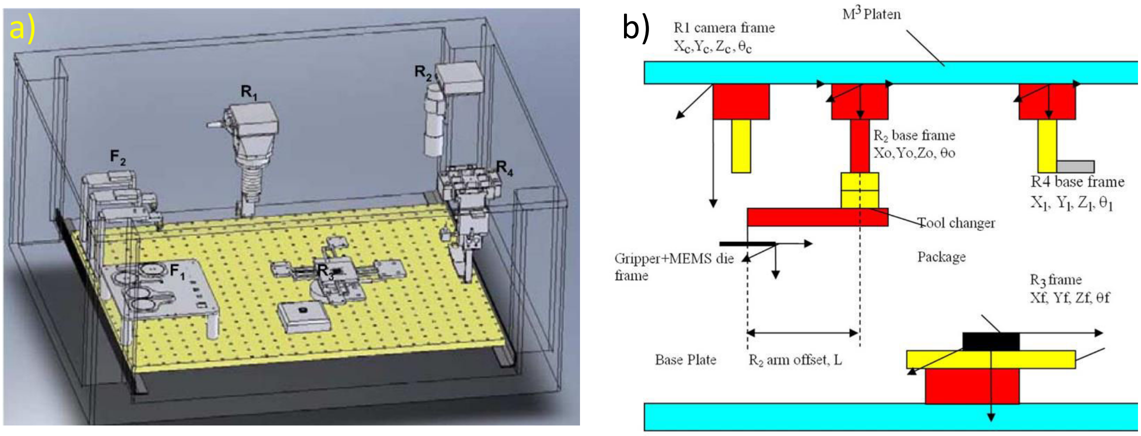

Figure 3.6: a) Three manipulators hardware diagram, b) Coordinate frame assignment for four robots manipulators in the shared workspace [Popa et al., 2009] .

A hybrid scheme [Mattos et al., 2009] was proposed combining open loop calibration and closed loop visual servoing, in order to avoid drift typically at the micro-scale. The approach was applied on a 2 DOF robot. The robot calibration based on camera measurement was realized first, and then the tool positioning drift were calibrated using continuous recalibration. Fine positioning was achieved through visual control. Here, calibration and recalibration were used for coarse positioning which brought a micro-pipette inside the field-of-view of the camera. For the task of reaching over 300 targets in a workspace 400$\times$300 μm, the average positioning error was achieved 5.65 μm using calibration and 1.75 μm using recalibration.

The work realized in [Tan et al., 2015c] as shown in Figure 3.7 targeted to quantify the positioning accuracy of a XYθ serial micro-positioning robot and to identify the main influential parameters. For this sake, a measuring system that combines vision and pseudoperiodic patterns with an extremely large range-to-resolution ratio is used to quantify the positioning accuracy of the robot for in-plane motions. Then, an open-loop control approach based on robot calibration is used. Experiments show that positioning accuracy can be improved by more than 35 times from 96 μm to 2.5 μm by compensating geometric influencing parameters. The same researchers conducted works about calibration of 2 DOF nanopositioning stage [Tan et al., 2015a], by modeling the thermal drift and the geometric errors. A calibration procedure was proposed based on measurements of interferometer and thermocouples. Validation experiments were conducted over a long period (several days) and demonstrated that the performance of the calibration procedure largely depended on the consistency of conditions before and after training (measurement step). If the drift behavior and temperature range after training were close to those during training, the calibration model can guarantee efficient compensation based on training knowledge. Results showed that accuracy was better then 400 nm in this case.

But, for other complex applications using 6 DOF micro-robots, the positioning accuracy still represents the main challenge. From the most recent work realized on 6 DOF robot geometric calibration dedicated for micro-scale applications, we selected the work realized in [Guelpa et al., 2018]. They realized geometric calibration of 6-DOF robot, using virtual constraint method in a SEM environment (see Figure 3.8). The idea in their approach is to place the robot in many different configurations and ensure that for every configuration the position of the tool is the same (with an arbitrary orientation), a visual servoing control was used to maintain the object in the center of the image as shown in Figure 3.9, this implies the need to measure the relevant displacement and to compensate it by moving the robot accordingly. This work represents a very good advance in 6 DOF calibration for micro-scale, but 10 μm reached positioning accuracy is still not satisfying for many on-demanding positioning requirement in integrated optical. Moreover, the angular positioning accuracy was not quantified.

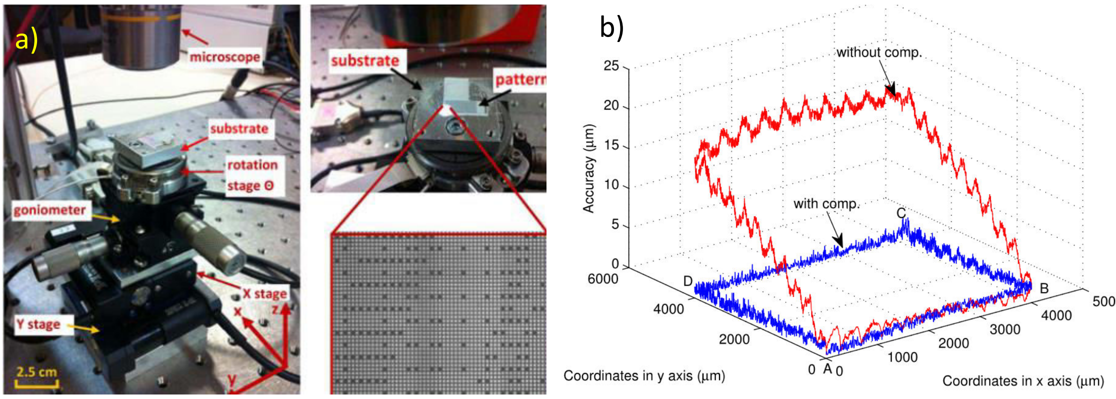

Figure 3.7: a) Large and close view of the XYθ serial micro-positioning robot used as experimental case study. The microscope provides a top view of the pattern that is attached on the substrate, b) Accuracy of tracking square with and without compensation [Tan et al., 2015c] .

The above cited works concerning geometric calibration of micro robotic systems are summarized based on the number of DOF dealt with, the measurement system used and the achieved positioning in Table 3.1. From Table 3.1 and the detail of the realized work above, it can be noticed that the highest positioning accuracy was achieved with less number of DOF and simple realized tasks. The number of DOF increases, the positioning accuracy decreases.

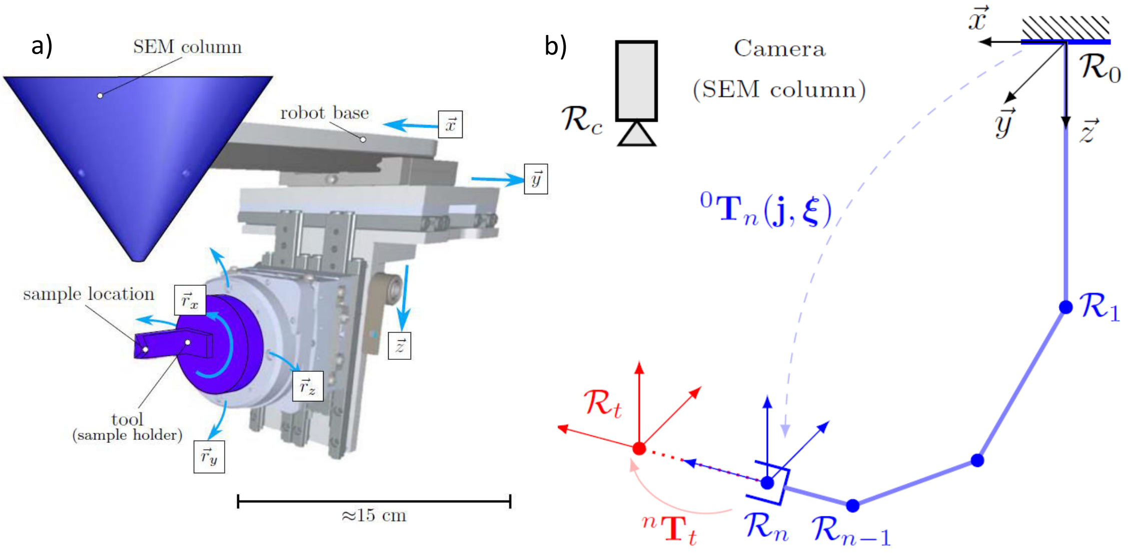

Figure 3.8: a)View of the CAD models of the 3P3R robot and the SEM column, inside the μrobotex SEM vacuum chamber, b) Kinematic model of the robot installed inside SEM chamber [Guelpa et al., 2018] .

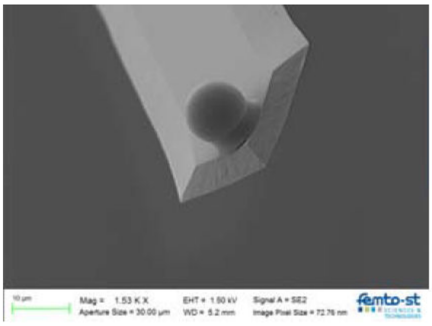

Figure 3.9: 10 μm sphere putted on a micro-beam, maintained in position during the displacements of the robot [Guelpa et al., 2018].

Table 3.1: Calibration of micro robotic systems.

Work	DOF	Measurement system	Positioning accuracy after calibration
[Popa et al., 2009]	3	Vision	35 μm
[Mattos et al., 2009]	2	Vision	5.65 μm
[Tan et al., 2015c]	3	Vision	2.5 μm
[Guelpa et al., 2018]	6	Vision	10 μm

3.6/ ROBOT EXTRINSIC PARAMETERS CALIBRATION BASED ON 1-D FABRY-PEROT RELATIVE DISTANCE MEASURE

The tool (optical component) and the measuring system (fiber) are usually removable, which means that the extrinsic robot parameters are more influenced (changeable) in time then intrinsic robot parameters when the robot is not disturbed or disassembled, moreover for each new experiment the tool (optical component) and the measuring system (fiber) may be replaced. Therefore, our aim is to find the quickest method (to avoid the drift effect), which is appropriate for good level of calibration, well adapted to the context of micro-positioning of optical components in order to reach high optical performances. For this reason, an extrinsic parameters calibration approach is proposed. But, first, our 6-DOF robot geometric modeling is presented in the next subsection.

3.6.1/ 6-DOF ROBOT GEOMETRIC MODELING

For simplification, we choose the same origin for all the frames, which corresponds to the real rotational center of the robot (intersection of joint 4 and 5) when $q_1 = q_2 = q_3 = q_4 = q_5 = q_6 = 0$. The world (base) frame R_w is assigned to be aligned with the first frame when $q_1 = 0$. The nominal geometric parameters of the robot are then determined. The assignment of frames is shown in Figure 3.10, which represents the robot geometric model and the geometrical parameters are given in Table 3.2 .

Table 3.2: Nominal parameters of robot Direct Geometric Model (DGM) following the Hayati modified convention of Khalil and Kleinfinger.

Link	ρ_i	β_i	α_i	d_i	θ_i	r_i
1	1	0	0	0	0	q_1
2	1	0	-90	0	-90	q_2
3	1	0	-90	0	-90	q_3
4	0	0	0	0	q_4	0
5	0	0	-90	0	$q_5 - 90$	0
6	0	0	-90	0	q_6	0

By replacing variables from equation (3.9) using Table 3.2, The transformation matrix defining the frame R_i in the frame R_{i-1} is given as follow:

$$^{W}T_1 = \begin{bmatrix} 1 & 0 & 0 & 0 \\ 0 & 1 & 0 & 0 \\ 0 & 0 & 1 & q_1 \\ 0 & 0 & 0 & 1 \end{bmatrix}, \quad ^{1}T_2 = \begin{bmatrix} 0 & 1 & 0 & 0 \\ 0 & 0 & 1 & q_2 \\ 1 & 0 & 0 & 0 \\ 0 & 0 & 0 & 1 \end{bmatrix}, \quad ^{2}T_3 = \begin{bmatrix} 0 & 1 & 0 & 0 \\ 0 & 0 & 1 & q_3 \\ 1 & 0 & 0 & 0 \\ 0 & 0 & 0 & 1 \end{bmatrix}$$

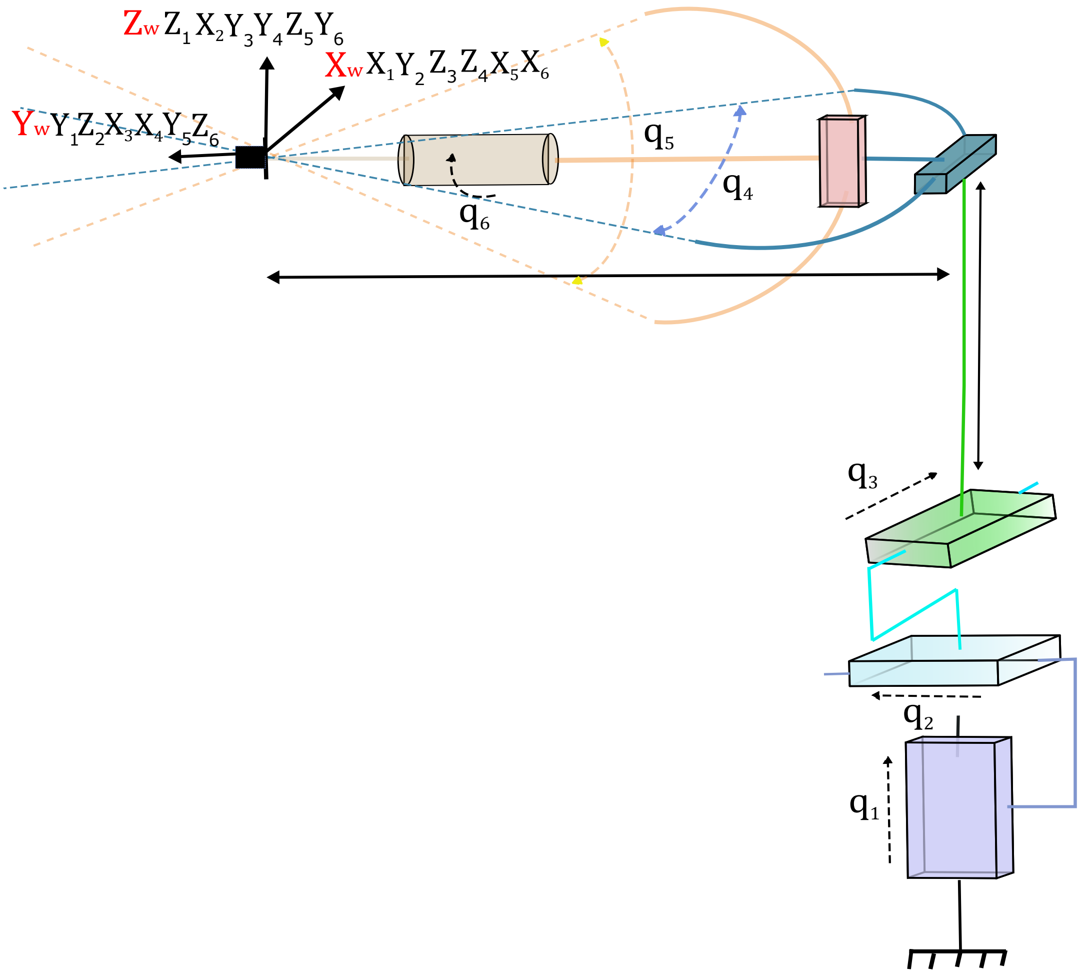

Figure 3.10: Robot kinematic model.

$$
{}^{3}T_4 = \begin{bmatrix} \cos q_4 & -\sin q_4 & 0 & 0 \\ \sin q_4 & \cos q_4 & 0 & 0 \\ 0 & 0 & 1 & 0 \\ 0 & 0 & 0 & 1 \end{bmatrix}, \; {}^{4}T_5 = \begin{bmatrix} \sin q_5 & \cos q_5 & 0 & 0 \\ 0 & 0 & 1 & 0 \\ \cos q_5 & -\sin q_5 & 0 & 0 \\ 0 & 0 & 0 & 1 \end{bmatrix}
$$

$$
{}^{5}T_6 = \begin{bmatrix} \cos q_6 & -\sin q_6 & 0 & 0 \\ 0 & 0 & 1 & 0 \\ -\sin q_6 & -\cos q_6 & 0 & 0 \\ 0 & 0 & 0 & 1 \end{bmatrix}.
$$

3.6.2/ EXTRINSIC GEOMETRIC PARAMETERS CALIBRATION

The objective of this section is to achieve the robot extrinsic geometric calibration based on relative distance measure. The distance measure is realized based on very high accurate Fabry-Perot interferometry principle measurement as presented in chapter 2. In order to go through the calibration process, the main reference frames are defined as schematically in Figure 3.11. R_f is assigned to the fiber frame, its origin is defined as the intersection point between the optical axis and the outer surface of the fiber. R_e

corresponds to the robot end-effector frame, its origin corresponds to the real rotational center of the robot (intersection of joint 4 and 5). The $\overrightarrow{O_eX_e}$, $\overrightarrow{O_eY_e}$ and $\overrightarrow{O_eZ_e}$ are the expected motion directions of the robot. R_t corresponds to the tool frame, its origin O_t is defined as the intersection between the $\overrightarrow{O_eZ_e}$ and the optical lamella plane ($Y_tO_tX_t$). R_w is assigned to the world frame, its origin corresponds to the real rotational center of the robot (intersection of joint 4 and 5) when all axes are at zero (initial configuration), with the same directions as the first stage axes R_1.

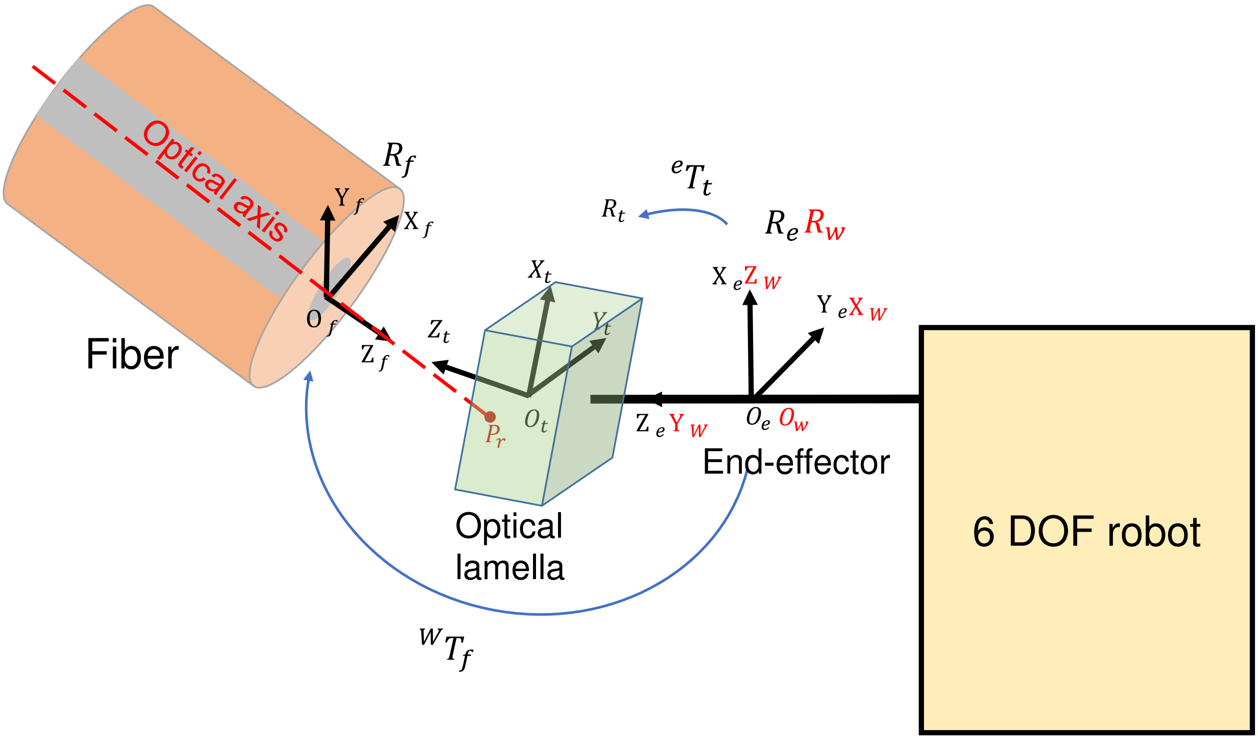

Figure 3.11: The photo-robotic positioning scheme with frames assignment.

For simplification, the rotation of the fiber around Y_w is supposed to be zero, the rotation of the lamella around Z_e axis and the translations of the lamella along X_e and Y_e axis all are supposed to be zero. The vector $\overrightarrow{O_eZ_e}$ is supposed to be collinear with the vector $\overrightarrow{O_wY_w}$. Thus, the homogeneous transformation matrix from the world frame to the fiber frame is given in equation (3.14), and the transformation matrix from the end-effector frame to the tool frame is given in equation (3.15).

$$
\begin{aligned}
{}^wT_f &= Trans_{X_w}(x_{wf}) * Trans_{Y_w}(y_{wf}) * Trans_{Z_w}(z_{wf}) * Rot_{X_w}(\beta_{wf}) * Rot_{Z_w}(\theta_{wf}) = \\
&\begin{bmatrix} \cos(\theta_{wf}) & -\sin(\theta_{wf}) & 0 & x_{wf} \\ \cos(\beta_{wf})\sin(\theta_{wf}) & \cos(\theta_{wf})\cos(\beta_{wf}) & -\sin(\beta_{wf}) & y_{wf} \\ \sin(\beta_{wf})\sin(\theta_{wf}) & \cos(\theta_{wf})\sin(\beta_{wf}) & \cos(\beta_{wf}) & z_{wf} \\ 0 & 0 & 0 & 1 \end{bmatrix},
\end{aligned} \tag{3.14}
$$

where x_{wf}, y_{wf} and z_{wf} are the translational coordinates of the origin of the fiber frame O_f with respect to the world frame, along X_w, Y_w and Z_w axis respectively. β_{wf} is the angle between Y_f and Z_w around X_w axis and θ_{wf} is the angle between X_f and X_w around Z_w axis.

$$
{}^eT_t = Trans_{Z_e}(Z_{et}) * Rot_{X_e}(\beta_{et}) * Rot_{Y_e}(\theta_{et}) = \begin{bmatrix} cos(\theta_{et}) & 0 & \sin(\theta_{et}) & 0 \\ \sin(\theta_{et})\sin(\beta_{et}) & \cos(\beta_{et}) & -\cos(\theta_{et})\sin(\beta_{et}) & 0 \\ -\cos(\beta_{et})\sin(\theta_{et}) & \sin(\beta_{et}) & \cos(\theta_{et})\cos(\beta_{et}) & Z_{et} \\ 0 & 0 & 0 & 1 \end{bmatrix}, \tag{3.15}
$$

where Z_{et} is the translational coordinate of the origin of the optical lamella O_t with respect to the end-effector frame, along Z_e axis. β_{et} and θ_{et} are the rotational coordinates of X_t and Y_t axes of the optical lamella with respect to the end-effector frame, around the X_e and Y_e respectively.

P_r is the reflection point projection of the laser spot on the optical lamella plane $(Y_t O_t X_t)$. ${}^wP_r({}^wP_{rx}, {}^wP_{ry}, {}^wP_{rz})$ is the reflection point projection in the world frame R_w. ${}^tP_r({}^tP_{rx}, {}^tP_{ry}, 0)$ is the reflection point in the tool frame R_t.

All the required transformations are defined, and they are used for the proposed extrinsic parameters calibration. The identification step of the proposed extrinsic geometric parameters calibration consists of three steps:

- identification of the optical lamella plane orientation and the optical axis orientation with respect to the world frame $(\beta_{et}, \theta_{et}, \beta_{wf}, \theta_{wf})$;
- identification of the Cartesian coordinates of the two origins O_t et O_f of the optical lamella and the fiber respectively with respect to the world frame $(Z_{et}, x_{wf}, y_{wf}, z_{wf})$;
- calculation of the reflection point projection P_r on the plane $(Y_t O_t X_t)$ with respect to the tool frame and the world frame $({}^tP_{rx}, {}^tP_{ry}, {}^wP_{rx}, {}^wP_{ry}, {}^wP_{rz})$.

1- identification of the optical lamella plane orientation and the optical axis orientation with respect to the world frame $(\beta_{et}, \theta_{et}, \beta_{wf}, \theta_{wf})$

The parametric form of the equation of optical axis line is defined by a point on the optical axis line O_f and its direction vector $\overrightarrow{Z_f}$. The point O_f (x_{wf}, y_{wf}, z_{wf}) is a point with respect to the world frame R_w through which the optical axis line passes. The unit vector $\overrightarrow{Z_f}$ (a_{wf}, b_{wf}, c_{wf}) is the direction vector of the optical axis line with respect to the world frame R_w.
The 3-dimensional parametric equations of the line carrying the vector $\overrightarrow{O_f Z_f}$ (optical axis) can be written as in equation. (3.16):

$$
\begin{cases} x = a_{wf}t + x_{wf} \\ y = b_{wf}t + y_{wf} \\ z = c_{wf}t + z_{wf} \end{cases}, \tag{3.16}
$$

where $\sqrt{a_{wf}^2 + b_{wf}^2 + c_{wf}^2} = 1$.

The intersection point between the lamella plane $(Y_t O_t X_t)$ and the line carries the vector $\overrightarrow{O_e Z_e}$ is O_t (x_{wt}, y_{wt}, z_{wt}). The optical lamella plane is defined by the point O_t (x_{wt}, y_{wt}, z_{wt}) in the plane with respect to the world frame and the normal unit vector to the plane $\overrightarrow{Z_t}$ (a_{wt}, b_{wt}, c_{wt}). If $M(x, y, z)$ is any other point which belongs to the lamella plane, then the equation of the lamella plane can be written as follows:

$$\overrightarrow{O_t M} \cdot \overrightarrow{O_t Z_t} = 0. \tag{3.17}$$

This yields:

$$a_{wt}(x - x_{wt}) + b_{wt}(y - y_{wt}) + c_{wt}(z - z_{wt}) = 0. \tag{3.18}$$

By considering $d_{wt} = -a_{wt}x_{wt} - b_{wt}y_{wt} - c_{wt}z_{wt}$, then:

$$a_{wt}x + b_{wt}y + c_{wt}z + d_{wt} = 0, \tag{3.19}$$

where: $\sqrt{a_{wt}^2 + b_{wt}^2 + c_{wt}^2} = 1.$

Differentiating the 3 dimensional optical axis line equation (3.16) and the optical lamella plane equation (3.19) at the intersection point between the optical axis line and the lamella plane respectively gives :

$$\begin{cases} dx = a_{wf}dt \\ dy = b_{wf}dt \\ dz = c_{wf}dt \end{cases}, \tag{3.20}$$

$$a_{wt}dx + b_{wt}dy + c_{wt}dz + dd_{wt} = 0. \tag{3.21}$$

Then by replacing the differentiated optical axis line equation (3.20) in the differentiated optical lamella plane equation (3.21) and by replacing dd_{wt}, the equation is yielded:

$$a_{wt}a_{wf}dt + b_{wt}b_{wf}dt + c_{wt}c_{wf}dt = a_{wt}dx + b_{wt}dy + c_{wt}dz. \tag{3.22}$$

Equation (3.22) is a non-linear equation relating the relative distance along the optical axis with the 3 relative robot translations. The dx, dy and dz are calculated from the Direct Geometric Model (DGM), dt is calculated using Fabry-Perot measure.

The dedicated measurement strategy for identification of the coordinates of the unit vector $\vec{Z}_f(a_{wf}, b_{wf}, c_{wf})$ and the coordinates of the unit vector $\vec{Z}_t(a_{wt}, b_{wt}, c_{wt})$ is discussed in the next section.

β_{wf}, θ_{wf} calculation from the coordinates of the unit vector $\vec{Z}_f(a_{wf}, b_{wf}, c_{wf})$ and β_{et}, θ_{et} calculation from the coordinates of the unit vector $\vec{Z}_t(a_{wt}, b_{wt}, c_{wt})$:

In order to calculate the $(\beta_{et}, \theta_{et}, \beta_{wf}, \theta_{wf})$ angles, the mathematical relationship between the identified $(a_{wt},\ b_{wt},\ c_{wt},\ a_{wf},\ b_{wf},\ c_{wf})$ and the $(\beta_{et}, \theta_{et}, \beta_{wf}, \theta_{wf})$ angles need to be established.

The transformation matrix ${}^{w}T_t$ of the tool frame in the world frame can be written as follows:

$$ {}^{w}T_t = {}^{w}T_e *^{e} T_t = \begin{bmatrix} x & x & a_{wt} & x \\ x & x & b_{wt} & x \\ x & x & c_{wt} & x \\ 0 & 0 & 0 & 1 \end{bmatrix}, \tag{3.23} $$

where at the same time the ${}^{e}T_t$ transformation can be written as follows:

$$ {}^{e}T_t = \begin{bmatrix} x & x & a_{et} & 0 \\ x & x & b_{et} & 0 \\ x & x & c_{et} & Z_{et} \\ 0 & 0 & 0 & 1 \end{bmatrix}. \tag{3.24} $$

The transformation matrix ${}^{w}T_e$ which represents the Direct Geometric Model of the robot (DGM) is supposed nominal. Thus, when $q_1 = q_2 = q_3 = q_3 = q_4 = q_5 = q_6 = 0$, the yielded ${}^{w}T_e$ is given:

$$ {}^{w}T_e = \begin{bmatrix} 1 & 0 & 0 & 0 \\ 0 & 0 & 1 & 0 \\ 0 & -1 & 0 & 0 \\ 0 & 0 & 0 & 1 \end{bmatrix}. \tag{3.25} $$

By substituting equation (3.15) and equation (3.25) in equation (3.23), this yields:

$$ {}^{w}T_t = ^{w} T_e *^{e} T_t = \begin{bmatrix} cos(\theta_{et}) & 0 & \sin(\theta_{et}) & 0 \\ -\cos(\beta_{et})\sin(\theta_{et}) & \sin(\beta_{et}) & \cos(\theta_{et})\cos(\beta_{et}) & Z_{et} \\ -\sin(\beta_{et})\sin(\theta_{et}) & -\cos(\beta_{et}) & \cos(\theta_{et})\sin(\beta_{et}) & 0 \\ 0 & 0 & 0 & 1 \end{bmatrix} = \begin{bmatrix} x & x & a_{wt} & x \\ x & x & b_{wt} & x \\ x & x & c_{wt} & x \\ 0 & 0 & 0 & 1 \end{bmatrix}. \tag{3.26} $$

By substituting equation (3.24) and equation (3.25) in equation (3.23). This yields:

$$ {}^{w}T_t = \begin{bmatrix} x & x & a_{et} & x \\ x & x & c_{et} & Z_{et} \\ x & x & -b_{et} & x \\ 0 & 0 & 0 & 1 \end{bmatrix} = \begin{bmatrix} x & x & a_{wt} & x \\ x & x & b_{wt} & x \\ x & x & c_{wt} & x \\ 0 & 0 & 0 & 1 \end{bmatrix}. \tag{3.27} $$

By matching, we deduce:

$a_{et} = a_{wt}$; $b_{et} = -c_{wt}$; $c_{et} = b_{wt}$ (will be used for the 2nd step).

And by matching, we deduce:

$a_{wt} = \sin\theta_{et}$; $b_{wt} = \cos\theta_{et}\cos\beta_{et}$; $c_{wt} = \cos\theta_{et}\sin\beta_{et}$.

Then, the optical lamella plane orientation angles with respect to the robot end-effector frame can be easily calculated as follow:

$$\beta_{et} = atan2(c_{wt}, b_{wt});$$

$$\theta_{et} = atan2(a_{wt}\cos\beta_{et}, b_{wt}).$$

With the same way, using equation (3.28), β_{wf}, θ_{wf} can be deduced by matching.

$$^{w}T_f = \begin{bmatrix} \cos(\theta_{wf}) & -\sin(\theta_{wf}) & 0 & X_{wf} \\ \cos(\beta_{wf})\sin(\theta_{wf}) & \cos(\theta_{wf})\cos(\beta_{wf}) & -\sin(\beta_{wf}) & Y_{wf} \\ \sin(\beta_{wf})\sin(\theta_{wf}) & \cos(\theta_{wf})\sin(\beta_{wf}) & \cos(\beta_{wf}) & Z_{wf} \\ 0 & 0 & 0 & 1 \end{bmatrix} = \begin{bmatrix} x & a_{wf} & x & x \\ x & b_{wf} & x & x \\ x & c_{wf} & x & x \\ 0 & 0 & 0 & 1 \end{bmatrix}, \tag{3.28}$$

which gives:

$$a_{wf} = -\sin\theta_{wf}; \qquad b_{wf} = \cos\theta_{wf}\cos\beta_{wf}; \qquad c_{wf} = \cos\theta_{wf}\sin\beta_{wf}.$$

Then the optical axis orientation angles with respect to the world frame can be calculated as follow:

$$\beta_{wf} = atan2((c_{wf}, b_{wf}),$$

$$\theta_{wf} = atan2(-a_{wf}\cos\beta_{wf}, b_{wf}).$$

2- Identification of the Cartesian coordinates of the two origins $O_t(0,0,Z_{et})$ et $O_f(x_{wf}, y_{wf}, z_{wf})$ of the optical lamella and the fiber respectively with respect to the world frame:

When $q_1 = q_2 = q_3 = q_3 = q_6 = 0$, and by applying two axis-by-axis rotations q_4 and q_5, equation (3.23) can be written as follows:

$$^{w}T_t = \begin{bmatrix} cos(q_5) & 0 & -\sin(q_5) & 0 \\ \sin(q_5)\cos(q_4) & \sin(q_4) & \cos(q_5)\cos(q_4) & 0 \\ \sin(q_5)\sin(q_4) & -\cos(q_4) & \cos(q_5)\sin(q_4) & 0 \\ 0 & 0 & 0 & 1 \end{bmatrix} * \begin{bmatrix} x & x & a_{et} & 0 \\ x & x & b_{et} & 0 \\ x & x & c_{et} & Z_{et} \\ 0 & 0 & 0 & 1 \end{bmatrix}. \tag{3.29}$$

This yields:

$$^{w}T_t = \begin{bmatrix} x & x & \cos(q_5)a_{et} - \sin(q_5)c_{et} & -Z_{et}\sin(q_5) \\ x & x & \cos(q_4)\sin(q_5)a_{et} + \sin(q_4)b_{et} - \cos(q_4)\cos(q_5)c_{et} & Z_{et}\cos(q_4)\cos(q_5) \\ x & x & \sin(q_4)\sin(q_5)a_{et} - \cos(q_4)b_{et} + \cos(q_5)\sin(q_4)c_{et} & Z_{et}\cos(q_5)\sin(q_4) \\ 0 & 0 & 0 & 1 \end{bmatrix}. \tag{3.30}$$

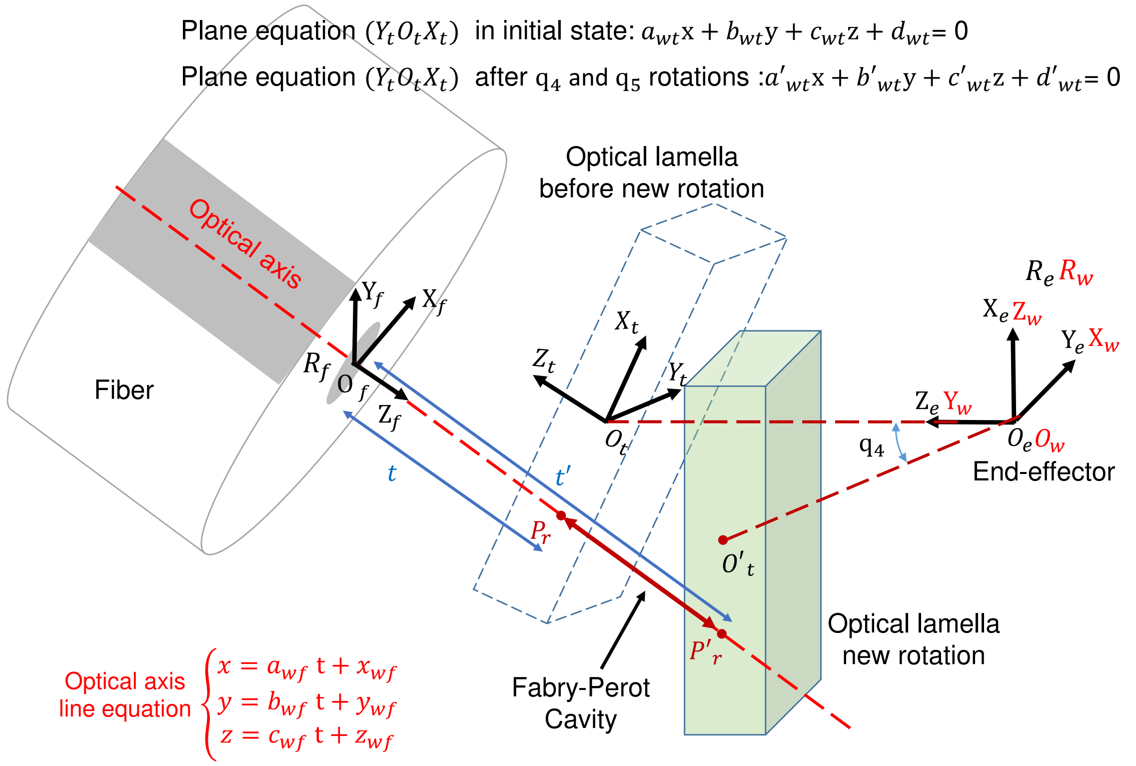

Figure 3.12: Optical lamella before the new rotation and after the new rotation (around q_5) .

The new optical lamella plane equation after rotation with respect to the world frame and as shown in Figure 3.12 is given:

$$a'_{wt}x + b'_{wt}y + c'_{wt}z + d'_{wt} = 0, \tag{3.31}$$

$$\begin{cases} a'_{wt} = \cos(q_5)a_{et} - \sin(q_5)c_{et} \\ b'_{wt} = \cos(q_4)\sin(q_5)a_{et} + \sin(q_4)b_{et} - \cos(q_4)\cos(q_5)c_{et} \\ c'_{wt} = \sin(q_4)\sin(q_5)a_{et} - \cos(q_4)b_{et} + \cos(q_5)\sin(q_4)c_{et} \\ d'_{wt} = a'_{wt}Z_{et}\sin(q_5) - b'_{wt}Z_{et}\cos(q_4)\cos(q_5) - c'_{wt}Z_{et}\cos(q_5)\sin(q_4) \end{cases}. \tag{3.32}$$

By taking the two optical lamella plane equations in the initial pose and after rotation with respect to the world frame as shown in Figure 3.12 and the optical axis line equation in the world frame as given in equation (3.16), the following equation can be obtained.

$$\begin{cases} a_{wt}x + b_{wt}y + c_{wt}z + d_{wt} = 0 \\ \\ a'_{wt}x + b'_{wt}y + c'_{wt}z + d'_{wt} = 0 \end{cases}. \tag{3.33}$$

The intersection of the optical axis line with the first optical lamella plane (before rotation) gives:

$$a_{wt}(a_{wf}t + x_{wf}) + b_{wt}(b_{wf}t + y_{wf}) + c_{wt}(c_{wf}t + z_{wf}) + d_{wt} = 0. \tag{3.34}$$

The intersection of the optical axis line with the first optical lamella plane (after rotation) gives:

$$a'_{wt}(a_{wf}t' + x_{wf}) + b'_{wt}(b_{wf}t' + y_{wf}) + c'_{wt}(c_{wf}t' + z_{wf}) + d'_{wt} = 0. \tag{3.35}$$

Then, t and t' can be calculated as follow:

$$t = \frac{-(a_{wt}x_{wf} + b_{wt}y_{wf} + c_{wt}z_{wf} + d_{wt})}{a_{wt}a_{wf} + b_{wt}b_{wf} + c_{wt}c_{wf}}, \tag{3.36}$$

$$t' = \frac{-(a'_{wt}x_{wf} + b'_{wt}y_{wf} + c'_{wt}z_{wf} + d'_{wt})}{a'_{wt}a_{wf} + b'_{wt}b_{wf} + c'_{wt}c_{wf}}. \tag{3.37}$$

The optical lamella distance change dt along the optical axis after rotation can be deduced as shown follows:

$$dt = t' - t = \frac{(a_{wt}x_{wf} + b_{wt}y_{wf} + c_{wt}z_{wf} + d_{wt})}{a_{wt}a_{wf} + b_{wt}b_{wf} + c_{wt}c_{wf}} - \frac{(a'_{wt}x_{wf} + b'_{wt}y_{wf} + c'_{wt}z_{wf} + d'_{wt})}{a'_{wt}a_{wf} + b'_{wt}b_{wf} + c'_{wt}c_{wf}}. \tag{3.38}$$

At the same time this optical lamella distance change on the optical axis after rotation can be measured from the Fabry-Perot interferometry measure.

The parameters (a_{wt}, b_{wt}, c_{wt}, a_{wf}, b_{wf}, c_{wf}) have already been identified. By applying different rotations q_4 and q_5, we build a system of linear equations, which will permit to calculate the four parameters $(Z_{et}, x_{wf}, y_{wf}, z_{wf})$, the dedicated measurement strategy for identification of $O_t(0, 0, Z_{et})$ et $O_f(x_{wf}, y_{wf}, z_{wf})$ is discussed in the next section.

3- calculation of the reflection point projection P_r on the plane $(Y_tO_tX_t)$ with respect to the tool frame and the world frame $({}^tP_{rx}, {}^tP_{ry}, {}^wP_{rx}, {}^wP_{ry}, {}^wP_{rz})$:

The Cartesian coordinates of O_t and O_f in the world frame have been identified, the orientations of the optical lamella plane and the optical axis line with respect to the world frame have also been identified. Hence, the point of intersection between the optical axis and the plane of the optical lamella in the world frame can be calculated by calculating the distance t between the optical lamella and the fiber using equation (3.36), and then calculating the Cartesian coordinates of the reflection point ${}^wP_r({}^wP_{rx}, {}^wP_{ry}, {}^wP_{rz})$ in the world frame using:

$$\begin{cases} {}^wP_{rx} = a_{wf}t + x_{wf} \\ {}^wP_{ry} = b_{wf}t + y_{wf} \\ {}^wP_{rz} = c_{wf}t + z_{wf} \end{cases}. \tag{3.39}$$

The Direct Geometric Model (DGM) of the robot ${}^{w}T_e$ is supposed nominal, therefore when $q_1 = q_2 = q_3 = q_3 = q_4 = q_5 = q_6 = 0$, the Direct Geometric Model (DGM) transformation matrix can be deduced as shown in the following equation:

$$ {}^{w}T_e = \begin{bmatrix} 1 & 0 & 0 & 0 \\ 0 & 0 & 1 & 0 \\ 0 & -1 & 0 & 0 \\ 0 & 0 & 0 & 1 \end{bmatrix}. \tag{3.40} $$

By replacing the already deduced vector ${}^{w}P_r$ and the transformation matrices ${}^{e}T_t$ and ${}^{w}T_e$, the vector ${}^{t}P_r$ can be deduced as follows:

$$ {}^{t}P_r =^{e} T_t^{-1} * {}^{w}T_e^{-1} * {}^{w}P_r. \tag{3.41} $$

In this section, the proposed methodology for extrinsic parameters identification is presented. The next section presents the experimental procedure for robot extrinsic parameters calibration.

3.7/ EXPERIMENTAL PROCEDURE OF ROBOT EXTRINSIC PARAMETERS CALIBRATION

The whole experimental procedure of extrinsic parameters calibration includes measurement and identification, parameters integration and validation phases. Each phase is presented in detail.

1-Measurement and identification

There are two adopted measurement strategies:

a- Measurement strategy for the identification of the coordinates of the unit vector $\vec{Z}_f(a_{wf}, b_{wf}, c_{wf})$ and the coordinates of the unit vector $\vec{Z}_t(a_{wt}, b_{wt}, c_{wt})$;

b- Measurement strategy for the identification of the Cartesian coordinates of the two origins $O_t(0, 0, Z_{et})$ et $O_f(x_{wf}, y_{wf}, z_{wf})$ of the optical lamella and the fiber respectively with respect to the world frame.

Each measurement strategy is detailed below.

a- Measurement strategy for the identification of the coordinates of the unit vector $\vec{Z}_f(a_{wf}, b_{wf}, c_{wf})$ and the coordinates of the unit vector $\vec{Z}_t(a_{wt}, b_{wt}, c_{wt})$:

Equation (3.22) is a non-linear equation relating the relative displacement on the optical axis with the 3 relative robot translations. dx, dy and dz are calculated from the Direct

Geometric Model (DGM), dt is calculated using Fabry-Perot measure. Based on Fabry-Perot interferometry principle, when the lamella moves along the optical axis, it produces systematically Fabry-Perot interferometry phenomenon and a change of the Fabry-Perot cavity length (L) happens. Therefore, there is a correlation between the FP cavity length L and the interference figure. A slight variation of the FP cavity length can be identified on the interference figure.

Notice: in this case, the orientation of the optical lamella and the fiber has to stay constant, which means only translations are allowed.

The adopted measurement strategy uses different lamella position combinations and translations. For each lamella position along the axis Z_1 of $q_1 = (-150, 0, 150)$ μm, a continuous translation of 300 μm is applied along X_w and a translation of 20 μm along Y_w axis, this gives 6 equations. For each lamella position along the axis Z_2 of $q_2 = (-150, 0, 150)$ μm, a continuous translation of 300 μm is applied along X_w and Z_w, this gives other 6 equations. For each lamella position along the axis Z_3 of $q_3 = (-150, 0, 150)$ μm, a continuous translation of 300 μm is applied along Z_w and a translation of 20 μm along Y_w axis, this gives again other 6 equations. The overall number of non-linear equations is 18 by applying the 3 translations.

For the translation along X_w and Z_w axes, the sign of dt is required. For this sake, a wavelength scan is used to calculate the distance L between the fiber and the optical lamella before and after each translation along X_w and Z_w axes. The difference between the measured distance before and after each translation gives the sign of Fabry-Perot measure of the applied translation.

The free spectral range in wavelength ($\delta\lambda_{FSR}$) of the Fabry-Perot cavity in general is given by:

$$\delta\lambda_{FSR} = \frac{\lambda^2}{2nL}, \tag{3.42}$$

where λ is the vacuum wavelength of light. For a linear cavity, such as the Fabry-Perot, L is the length of the cavity, n is the medium index within the cavity.

And at the same time, the free spectral range in wavelength ($\delta\lambda_{FSR}$) can be calculated as follows:

$$\delta\lambda_{FSR} = \delta T \frac{\lambda_{step}}{t_{step}}, \tag{3.43}$$

where λ_{step} and t_{step} are the wavelength and time steps respectively. δT can be identified from the reflected irradiance as shown in Figure 3.13 After calculating the free spectral range in wavelength from equation (3.43), the cavity distance L can be deduced from equation (3.42).

The resolution of these non-linear equations using non-linear least-squares solver permits to identify the parameters (a_{wt}, b_{wt}, c_{wt}, a_{wf}, b_{wf}, c_{wf}), which are the orientations of the optical axis line and the optical lamella plane.

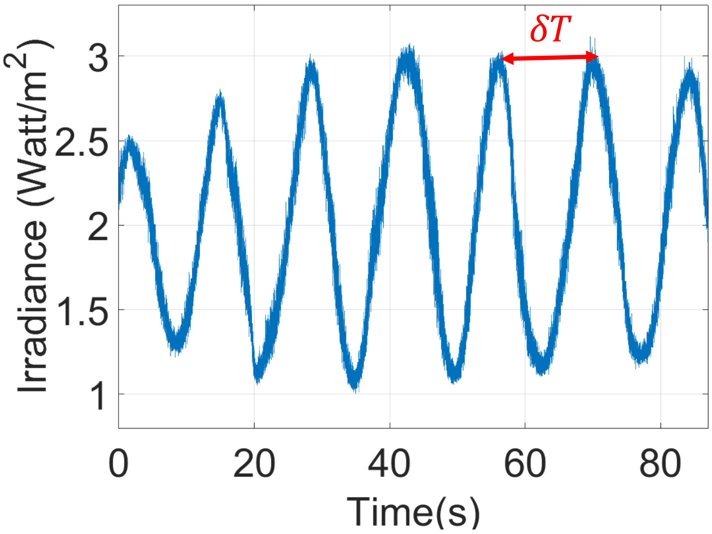

Figure 3.13: Wavelength scan where $\lambda_{step} = 0.01\mu$m and $t_{step} = 0.01$s.

b- Measurement strategy for identification of the Cartesian coordinates of the two origins $O_t(0, 0, Z_{et})$ et $O_f(x_{wf}, y_{wf}, z_{wf})$ of the optical lamella and the fiber respectively with respect to the world frame:

The adopted measurement strategy uses different combinations of poses. A continuous axis-by-axis rotation is applied around the axis Z_4 of $q_4 = -4°$ to $4°$ for different angles of $q_5 = -4°, -2°, 0°, 2°, 4°$. Then, a continuous axis-by-axis rotation is applied around the axis Z_5 of $q_5 = -4°$ to $4°$ for different angles of $q_4 = -4°, -2°, 0°, 2°, 4°$. The rotations are applied based on velocity control. For each continuous rotation, the lamella distance change along the optical axis is measured, each rotation gives 1 equation. Therefore, the final number of equations is 10.

A system of 10 equations with 4 unknowns is built. The system is overdetermined, since there are more equations than unknowns. The method of ordinary least squares can be used to find an approximate solution to overdetermined systems. For the system $AX = b$, the least squares formula is obtained from the problem $\underset{X}{min}||AX - b||$, the solution of which can be written as follows: $X = (A^TA)^{-1}A^Tb$ [Wold et al., 1984], where T indicates a matrix transpose.

2-Extrinsic parameters integration

The identification of the previously presented parameters leads to build the transformations ${}^tT_{P_r}$, ${}^wT_{P_r}$ and ${}^eT_t$. The integration scheme of the identified extrinsic parameters is shown in Figure 3.14. The inverse kinematic model of the robot is supposed nominal.

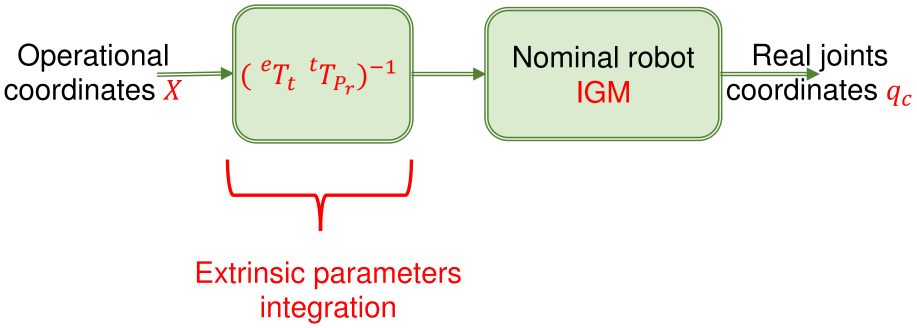

Figure 3.14: Extrinsic parameters integration.

3-Validation

Our objective is to rotate the optical lamella around X_f, Y_f and Z_f axes with a fixed reflection point P_r, and to translate the optical lamella perpendicular to the optical axis Z_f. For this sake, in the validation step, a 100 μm square translation of the lamella along X_f and Y_f is applied and for each vertex of the square (reflection point of laser spot P_r), 3 rotations are applied around X_f, Y_f and Z_f axes (see Figure 3.11 for frames assignment). The vertex that corresponds to the reflection point P_{r1} is the starting reflection point. A rotation from $-3°$ to $+3°$ around X_f and Y_f a rotation from $0\circ$ to $90°$ for rotation around Z_f (see Figure 3.15).

Choosing different reflection points of the laser spot P_r (new tool points) and rotating around is realized using the Inverse Geometric Model (IGM).

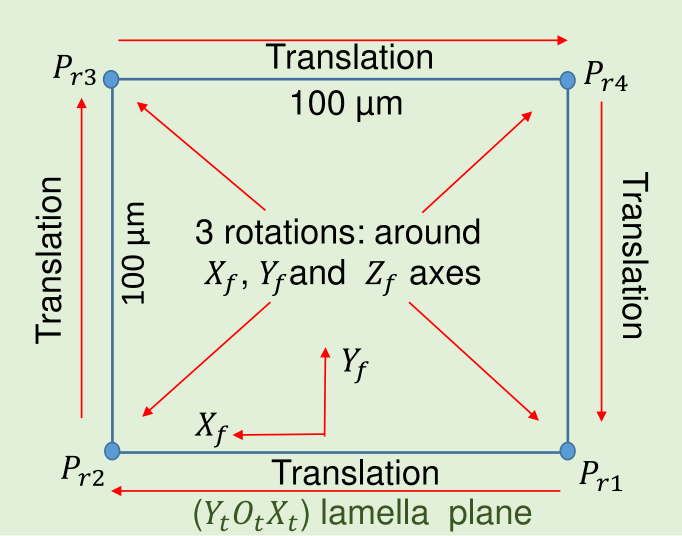

Figure 3.15: Robot trajectory for validation procedure.

The next section presents the experimental setup dedicated to study and investigate the extrinsic parameters calibration approach.

3.8/ EXPERIMENTAL SETUP

The experimental set up proposed for 6-DOF automated positioning of optical components is schematically depicted in Figure 3.16. A 6 DOF serial micro-positioning robot, is proposed to position the optical lamella and control its poses. Further is referred as a robot. An other XYZ manual positioner is fixed in front of the 6 DOF robot, it is used to hold the fiber ferrule and pre-position it. The whole system is referred as photo-robotic system.

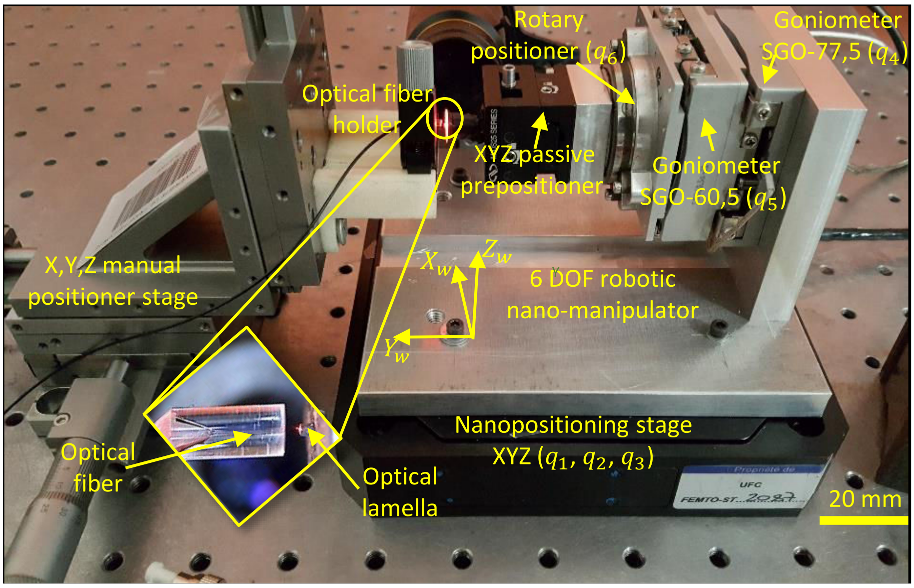

Figure 3.16: Photo-robotic experimental platform.

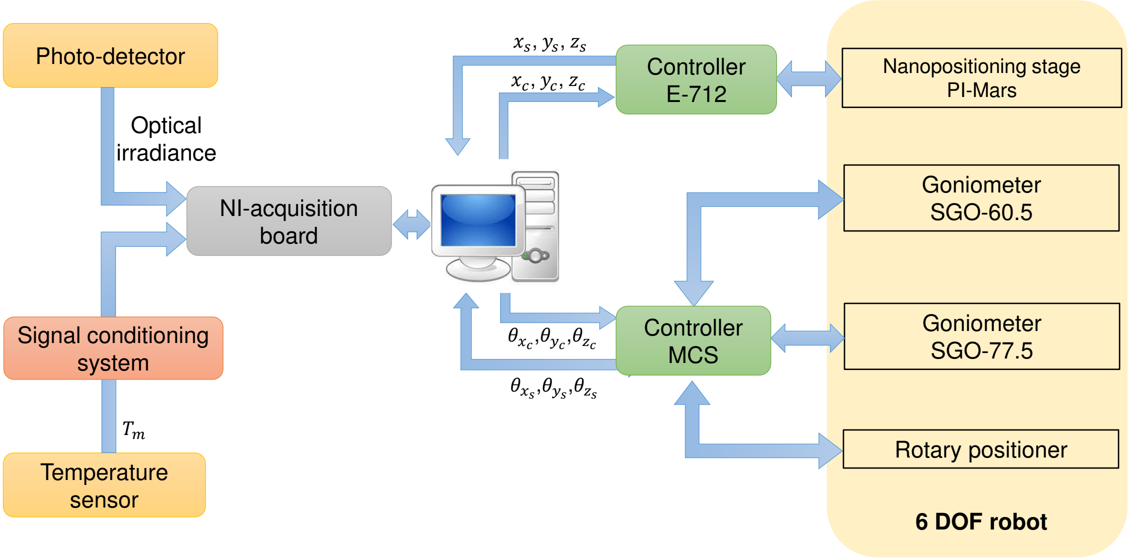

Figure 3.17: Schematic diagram of the hardware interfacing with the computer.

The photo-robotic system is mounted on an anti-vibration table. The 6-DOF robot is assembled with minimum geometric errors based on one (XYZ) translation stage followed by a bracket, which is made specifically to join the (XYZ) translation stage (q_1, q_2, q_3) to a set of two gomiometers (q_4, q_5) and a rotary positioner (q_6) (see Figure 3.16). The two gomiometers are used for rotation about X-axis and Z-axis and the rotary positioner for rotation around Y-axis. A passive XYZ pre-positioner is mounted after the rotary positioner for coarse adjustment of the rotation center of the whole assembled robot.

The (XYZ) translation stage is a PIMars P-563.3CD equipped with a E-712 controller. The two goniometers are SGO-60.5 and SGO-77.5, which use the stick-slip principle and is controlled by MCS-3D unit. The SGO-60.5 goniometer's center of rotation is 60.5 mm. The SGO-77.5 goniometer's center of rotation is extended to 77.5 mm. Rotary positioner is SmarAct SR-3610-S which uses the piezo principle and is controlled by MCS-3D unit. All the micro-positioning stages are equipped with internal sensors and are closed-loop controlled in joint layers already. The specifications of the two goniometers, rotary positioner and translation stage XYZ from the datasheets are given in Table 3.4 and 3.3 respectively.

Figure 3.17 shows the hardware interfacing with the computer. The E-712 controller sends the control inputs (x_c, y_c, z_c) to PI-Mars nano-positioning stage and receives measurements (x_s, y_s, z_s) from internal sensors for closed loop control in joint layer. The Modular Control System (MCS) gives $(\theta_{x_c}, \theta_{y_c}, \theta_{z_c})$ to the two goniometers and the rotary positioner and receives measurements $(\theta_{x_s}, \theta_{y_s}, \theta_{z_s})$ from internal sensors for closed loop control in actuator layer. The NI-acquisition card is connected to the computer. The reflected irradiance detected by the photo-detector is acquired using the NI-acquisition card. The measured temperature T_m is also acquired using the NI-acquisition card.

The optical set up consists in a laser light source (wavelength $\lambda = 1560\ n$m) connected to a circulator and then to the fiber ferrule. This configuration permits to align and assemble the optical lamella to the fiber. The reflected irradiance from optical lamella through the fiber ferrule is the closed loop information for the robotic micro-manipulator poses control. This set up permits the acquisition of irradiance signal from the reflected light from the optical lamella surface, returning back through the fiber ferrule and then through the beam circulator. Fabry-Perot measurement is used to control the relative position between fiber ferrule/optical lamella actively.

Table 3.3: Specifications of the SGO-60.5, SGO-77.5 goniometers and the rotary positioner in datasheet.

Stage	Gomiometer	SmarAct SR-3610-S
Travel range	$10°$	$360°$
Resolution	$0.01\ \mu$rad	$< 1.1\ \mu°$
Step width	$0.7\ \mu$rad to $7\ \mu$rad	$0.3\ m°$ to $3\ m°$
Scan range	$10.5\ \mu rad$	$\simeq 4.3\ m°$

The next section studies and investigates the optical performances after having applied robot extrinsic parameters calibration approach.

Table 3.4: Specifications of PIMars nano-positioning stage (P-563.3CD) in datasheet.

Stage	PIMars nanopositioning stage
reference	P-563.3CD
Traval range	$300 \times 300 \times 300$ μm
Resolution	0.5 nm
Unidirectional repeatability in X/Y/Z	$2/2/4$ nm
Pitch angle deviation	$\pm 2\ \mu rad$
Yaw angle deviation	$\pm 10\ \mu rad$
Flatness in X, Y	± 25 nm

3.9/ BEHAVIOR STUDY OF THE CALIBRATED ROBOT EXTRINSIC PARAMETERS

Figure 3.18 represents axis-by-axis rotations q_4, q_5 and q_6 around Z_4, Z_5 and Z_6 axes respectively before calibration, and square translation on the optical lamella plane before calibration. The fringes (peaks) on the optical irradiance are due to Fabry-Perot cavity variation along the optical axis. This proves the existence of some geometric errors, that can be extrinsic and/or intrinsic. The type of optical irradiance in Figure 3.18 appears in active positioning of optical components, which leads to local maximum problem. As a result, it is a time consuming especially for multi-DOF alignment process to reach maximum optical power.

The objective of robot geometric parameters calibration is to realize 6-DOF positioning without Fabry-Perot cavity variation on the optical axis i.e, realizing rotations around X_f, Y_f and Z_f axes and translation along the optical lamella plane without translating along the optical axis (The reflection point on the lamella plane is kept fixed). For this sake, first extrinsic parameters calibration of the 6-DOF robot is realized. The duration of the measurement and identification phase is about 30 minutes. After achieving measurement and identification phases, the identified extrinsic parameters are obtained and shown in Table 3.5. Then, integration of the obtained extrinsic parameters is performed as shown in Figure 3.14, where the inverse kinematic model of the robot is supposed nominal. A validation test is then realized which aims at quantifying the performances of the robot after calibration of the extrinsic parameters. The validation trajectory is shown in Figure 3.15. The validation test is realized in about 30 minutes.

Figure 3.19, 3.20, 3.21 and 3.22 represents the obtained results after having integrated extrinsic parameters for, 3 rotations around X_f, Y_f and Z_f, for different reflection point projection on the lamella P_{r1}, P_{r2}, P_{r3} and P_{r4} respectively (see Figure 3.15). For rotations around X_f, Y_f, the corresponding optical irradance and the 3 translational joints are plot-

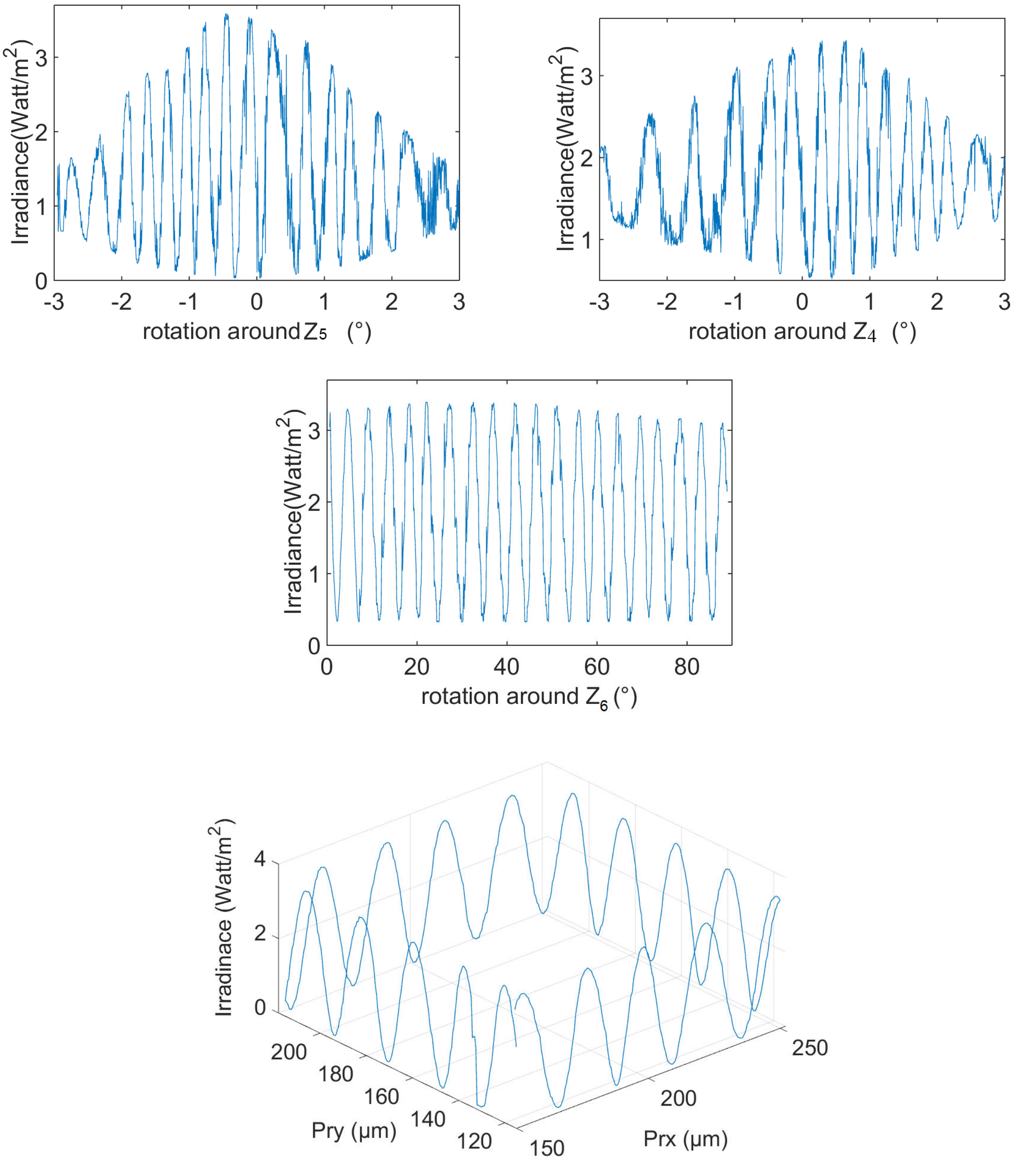

Figure 3.18: Rotations around Z_4, Z_5 and Z_6 axes and square translation on the optical lamella plane before calibration.

ted (since they are the only joints which intervene for these two rotations). For rotations around Z_f, the corresponding optical irradiance and the 3 translational joints and the 2 rotational joints (joint 4 and 5) are plotted.

We can notice that after having calibrated robot extrinsic parameters, for each reflection point projection on the lamella (P_{r1}, P_{r2}, P_{r3} and P_{r4}), the joints intervene in order to move the rotation center of robot to the reflection point of the laser spot P_r and maintain rotation

Table 3.5: Identified extrinsic parameters.

Parameters	β_{et}	θ_{et}	β_{wf}	θ_{wf}	Z_{et}	x_{wf}
Values	0.744°	-0.595°	0.732°	-0.520°	1.52 μm	112.40 μm
y_{wf}	z_{wf}	$^wP_{rx}$	$^wP_{ry}$	$^wP_{rz}$		
900.0 μm	113.3 μm	155.2 μm	-2.7 μm	-111.34 μm		

at that point (reflection point P_r).

For rotations around X_f and Y_f, there exist some fringes on the optical irradiance, which are interpreted by the existence of small Fabry-Perot cavity variation during the two rotations. The estimated Fabry-Perot cavity variation for the two rotations around X_f and Y_f of rotation range of 6 °, for the four reflection points projection (P_{r1}, P_{r2}, P_{r3} and P_{r4}) is shown in Table 3.6.

For a rotation around Z_f, the translational and rotational joints intervene in order to maintain the rotation at the reflection point P_r. There exist some fringes on the optical irradiance, which are interpreted by the existence of small Fabry-Perot cavity variation during the rotation. When at least one translational joint is saturated, the frequency of the fringes increase, which represent an increase in Fabry-Perot cavity variation during the rotation. The estimated Fabry-Perot cavity variation for the rotation around Z_f for the four reflection points projection (P_{r1}, P_{r2}, P_{r3} and P_{r4}) is shown in Table 3.7.

In order to investigate the the optical irradiance repeatability, 3 rotations around X_f, Y_f and Z_f axes for forth and back to the reflection point P_{r1} are applied. The corresponding optical irradiance for forth rotations and back rotations are shown in Figure 3.23. We can notice that the number of fringes is almost the same for forth rotations and back rotations.

Figure 3.24 and 3.25 show the optical irradiance corresponding to square and circular translations respectively along the optical lamella plane before and after extrinsic parameters calibration. We can notice that the number of fringes decrease considerably after robot extrinsic parameters calibration, but there still exist about half of fringe, which corresponds to about 0.39 μm Fabry-Perot cavity variation.

In summary, robot extrinsic parameters calibration based on the photo-robotic approach reduced considerably Fabry-Perot cavity variation during rotations around X_f, Y_f and Z_f for each different chosen reflection point of the laser spot. Applying square and circular translation on the optical lamella plane after extrinsic parameters calibration for the robot reduced considerably Fabry-Perot cavity variation. We have achieved a Fabry-Perot cavity variation of about 0.39 μm during a square translations of (100 ×100) μm. And we have also achieved a Fabry-Perot cavity variation of about 1.56 μm for a rotation range of 6° around X_f and Y_f and a Fabry-Perot cavity variation of about 0.858 μm for a rotation range of 45.5° around Z_f. But, the existing Fabry-Perot cavity variation during positioning is supposed to be because of the non calibration of intrinsic parameters of the robot.

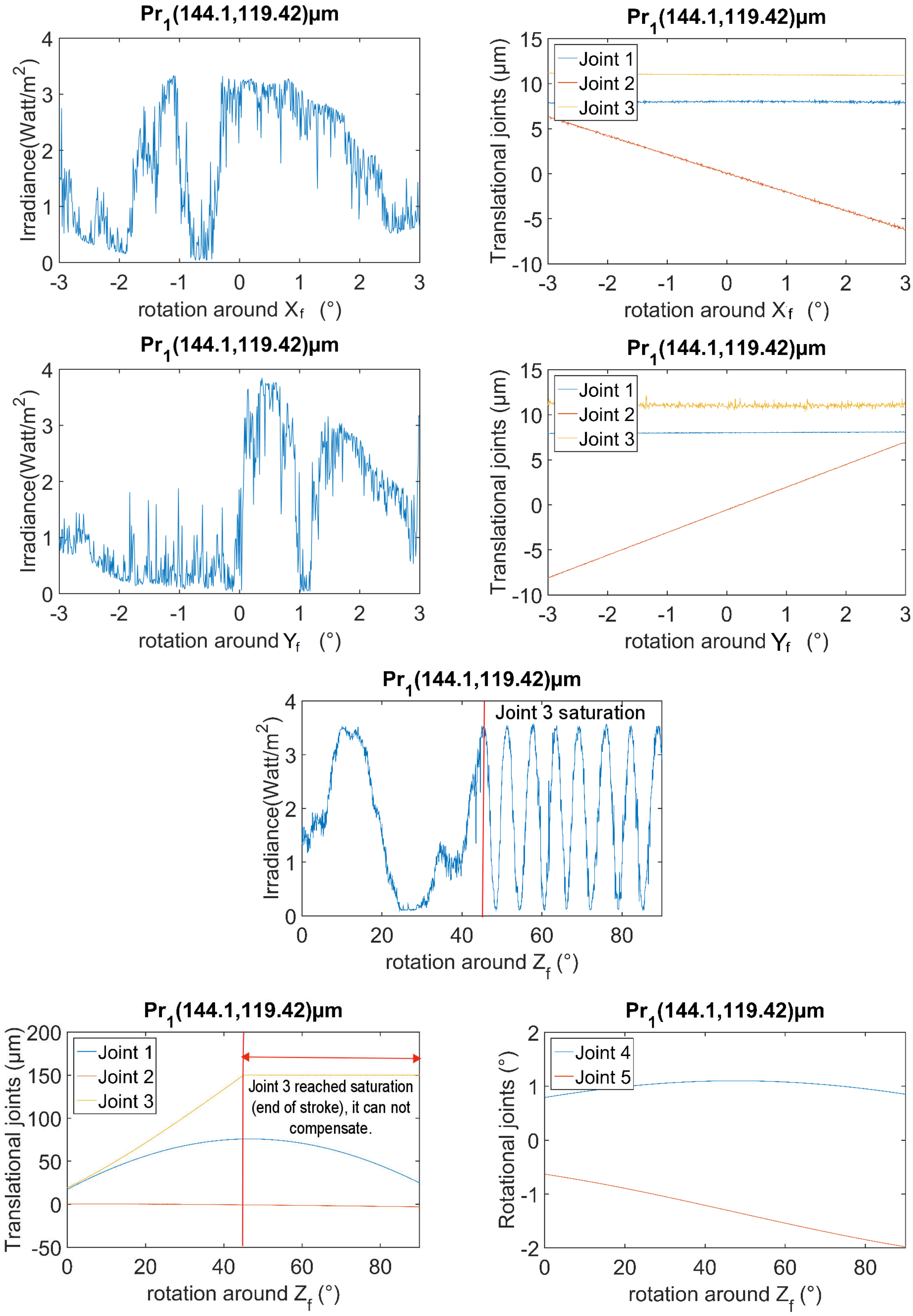

Figure 3.19: 3 rotations around X_f, Y_f and Z_f axes when the reflection point projection is in the reflection point P_{r1}, after robot extrinsic parameters calibration (see Figure 3.15).

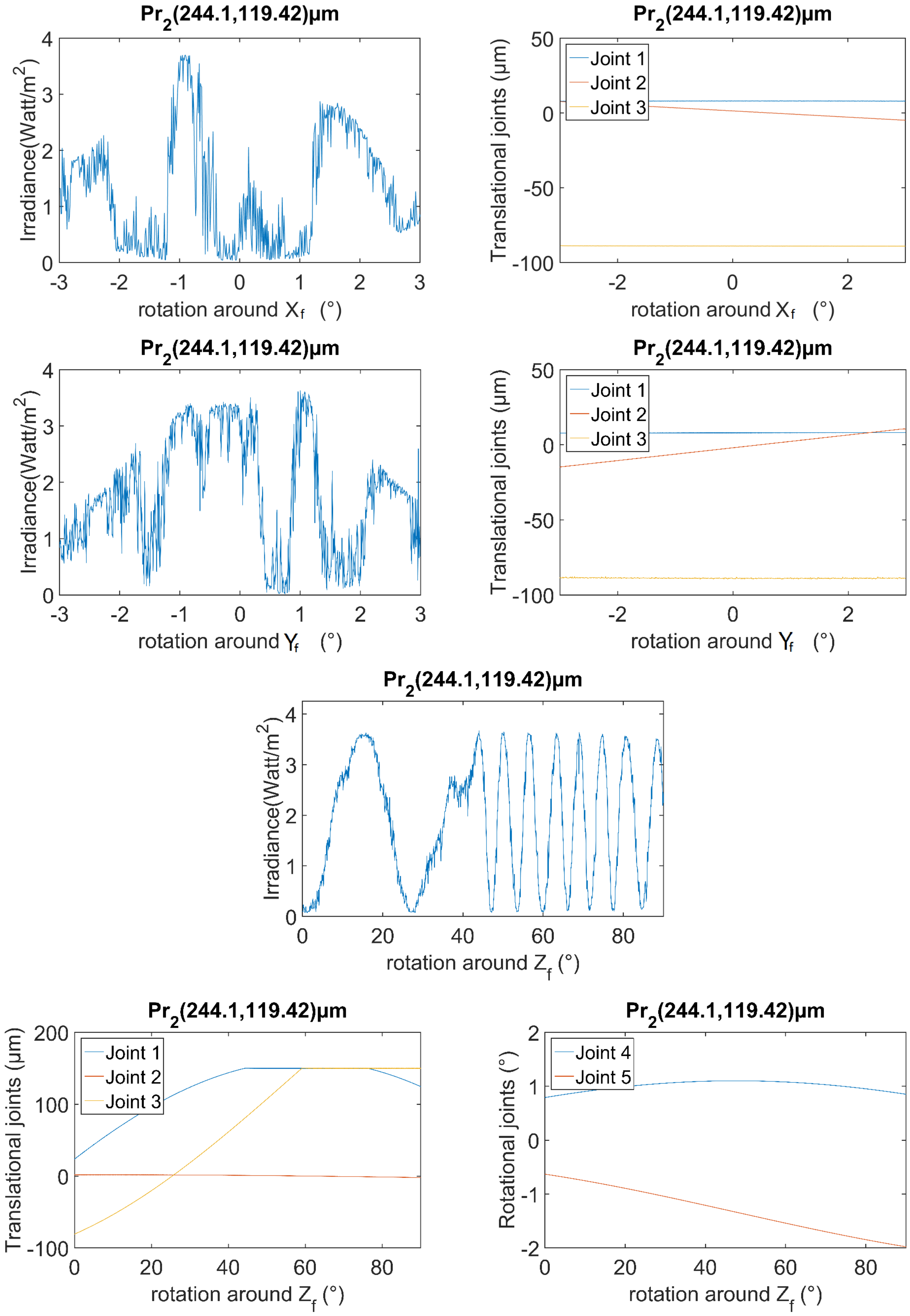

Figure 3.20: 3 rotations around X_f, Y_f and Z_f axes when the reflection point projection is P_{r2}, after robot extrinsic parameters calibration.

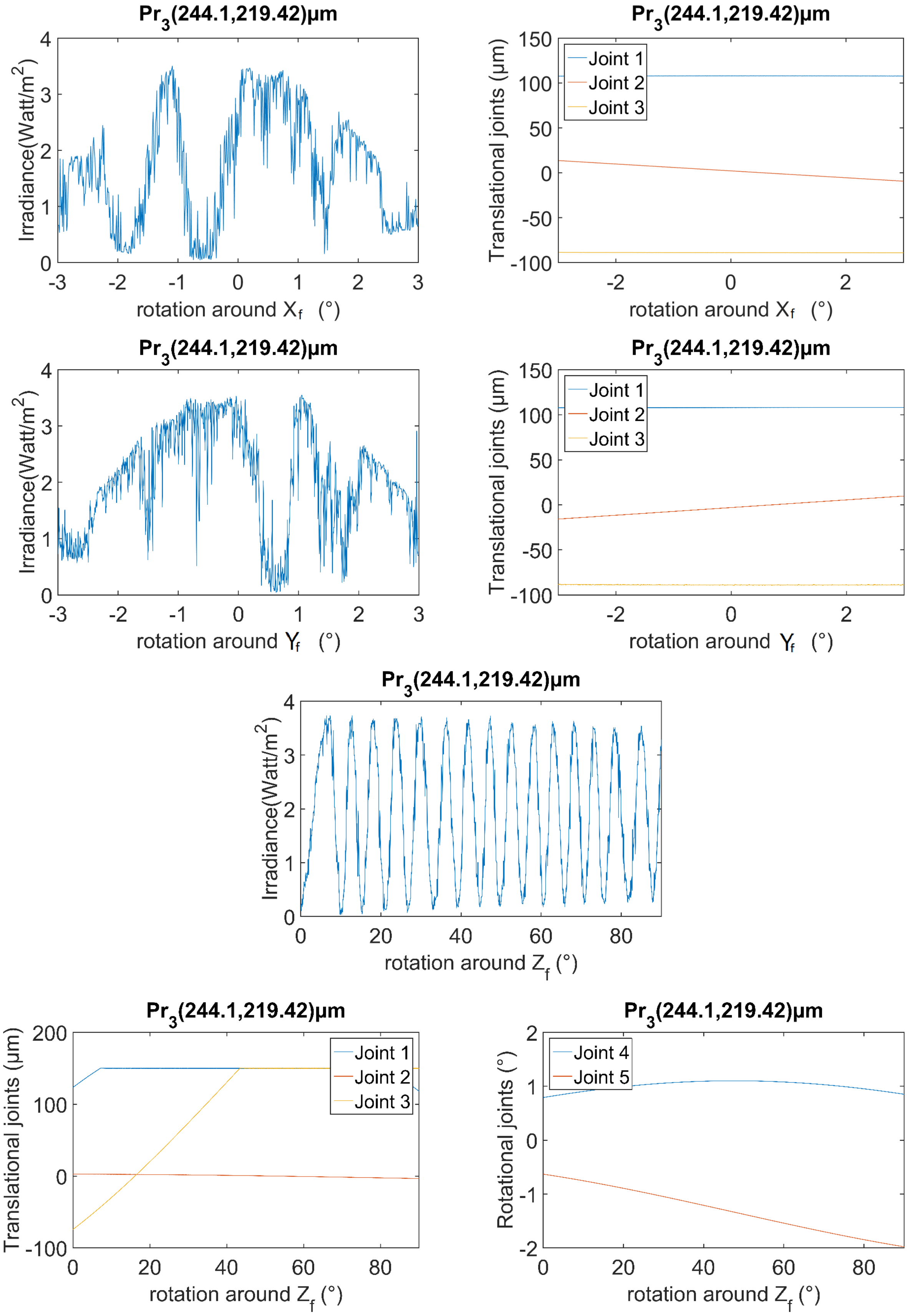

Figure 3.21: 3 rotations around X_f, Y_f and Z_f axes when the reflection point projection is P_{r3}, after robot extrinsic parameters calibration.

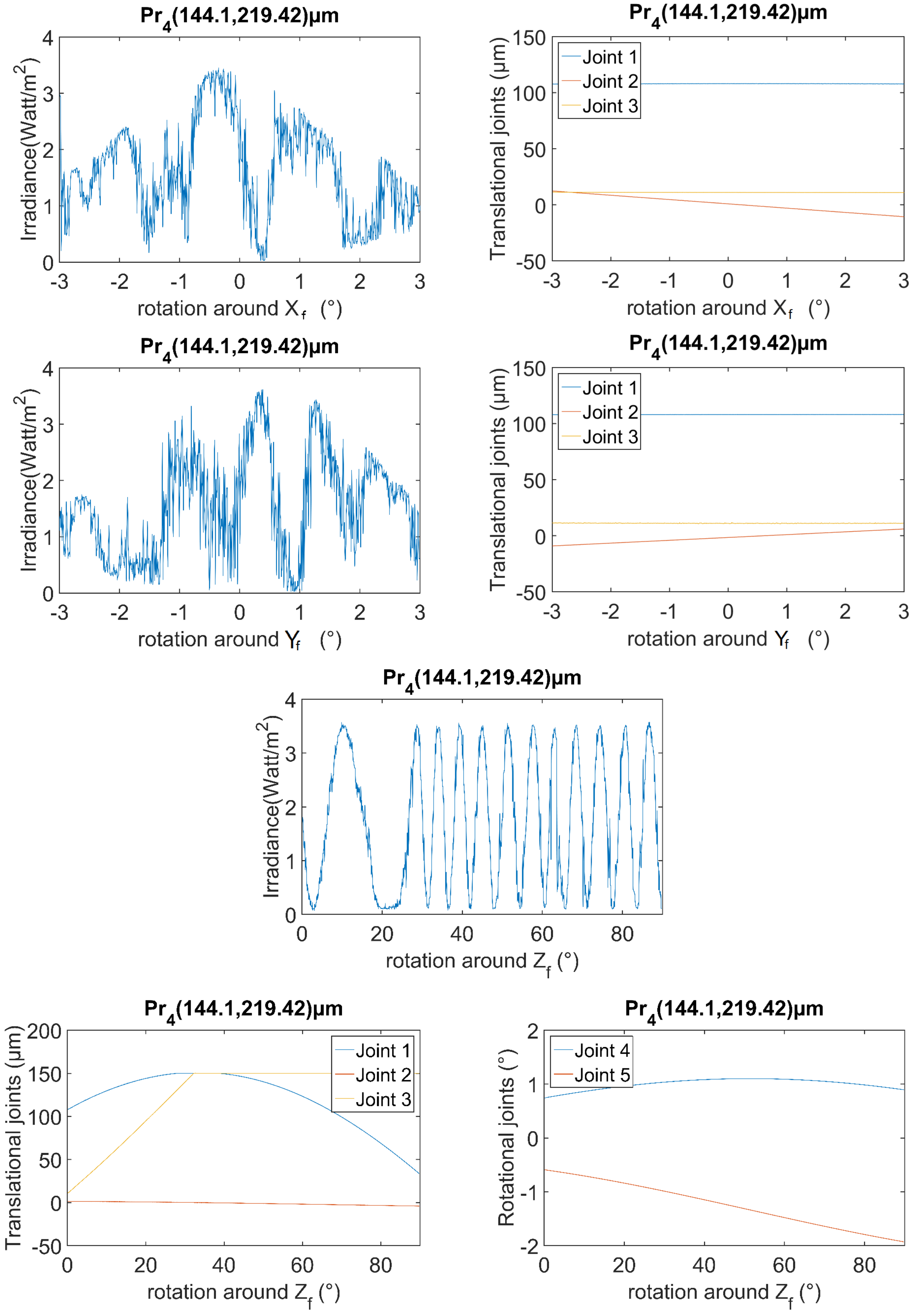

Figure 3.22: 3 rotations around X_f, Y_f and Z_f axes when the reflection point projection is P_{r4}, after robot extrinsic parameters calibration.

Table 3.6: The estimated Fabry-Perot cavity variation for rotations around X_f and Y_f axes, for a rotation range of 6 °, for the four reflection points projection (P_{r1}, P_{r2}, P_{r3} and P_{r4}).

Reflection point projection	Rotation around X_f axis	Rotation around Y_f axis
P_{r1}	1.56 μm	1.56 μm
P_{r2}	2.34 μm	3.12 μm
P_{r3}	2.73 μm	2,34 μm
P_{r4}	3.12 μm	3,9 μm

Table 3.7: The estimated Fabry-Perot cavity variation for the rotation around Z_f axis, for the four reflection points projection (P_{r1}, P_{r2}, P_{r3} and P_{r4}).

Reflection point projection	Rotation around Z_f axis	Rotation range
P_{r1}	0.858 μm	45.5 °
P_{r2}	1.17 μm	44.3 °
P_{r3}	0.31 μm	7.3 °
P_{r4}	1.09 μm	27.7 °

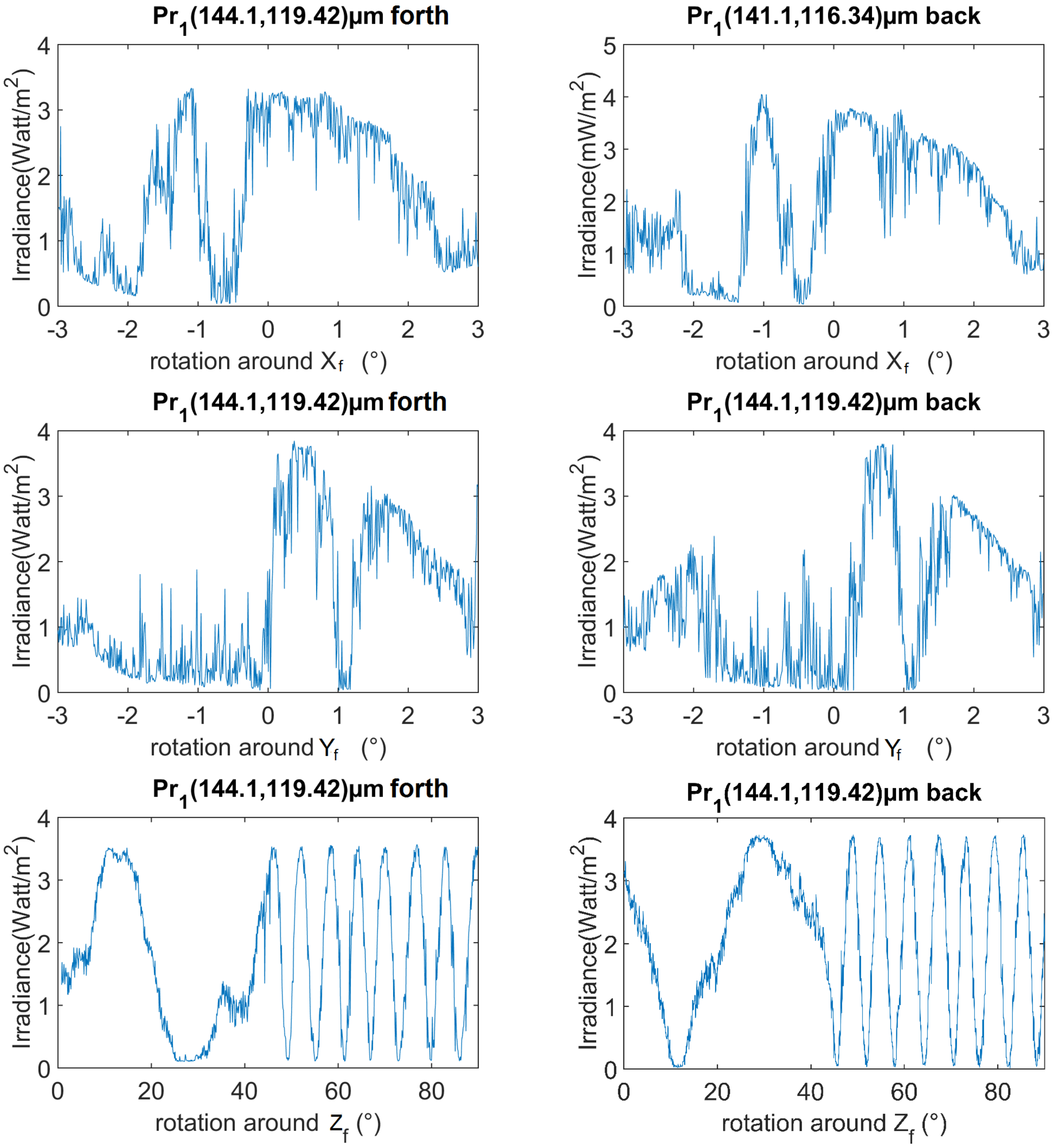

Figure 3.23: Comparison between the optical irradiance (forth and back to the reflection point P_{r1}), for 3 rotations around X_f, Y_f and Z_f axes, after robot extrinsic parameters calibration.

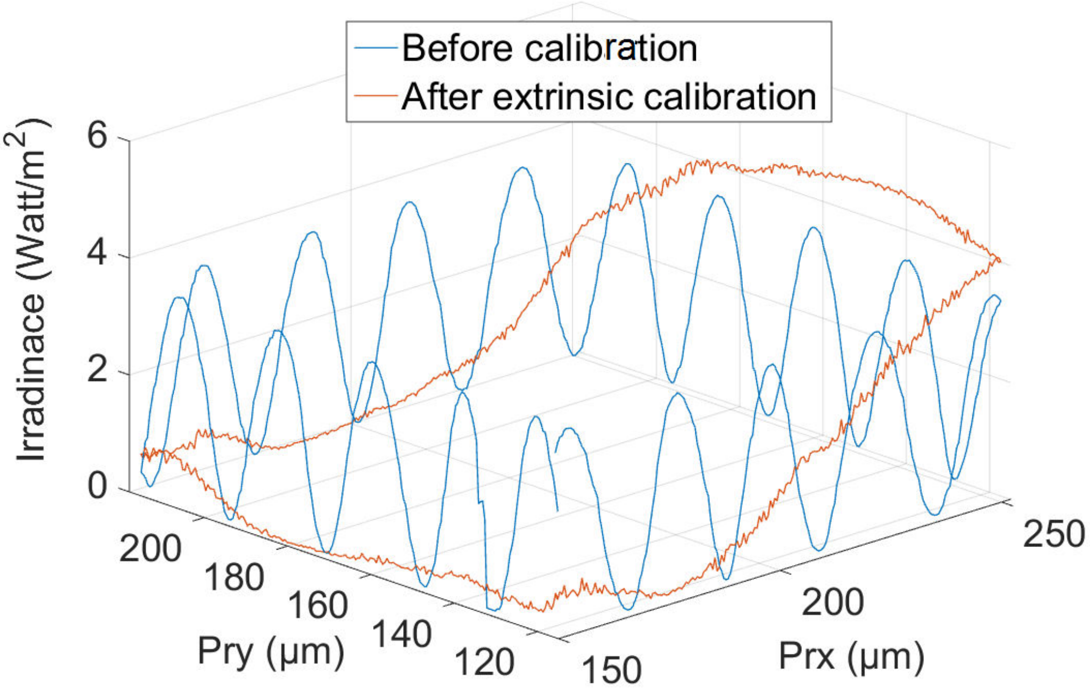

Figure 3.24: The optical irradiance corresponding to square translation on the optical lamella plane before and after extrinsic parameters calibration.

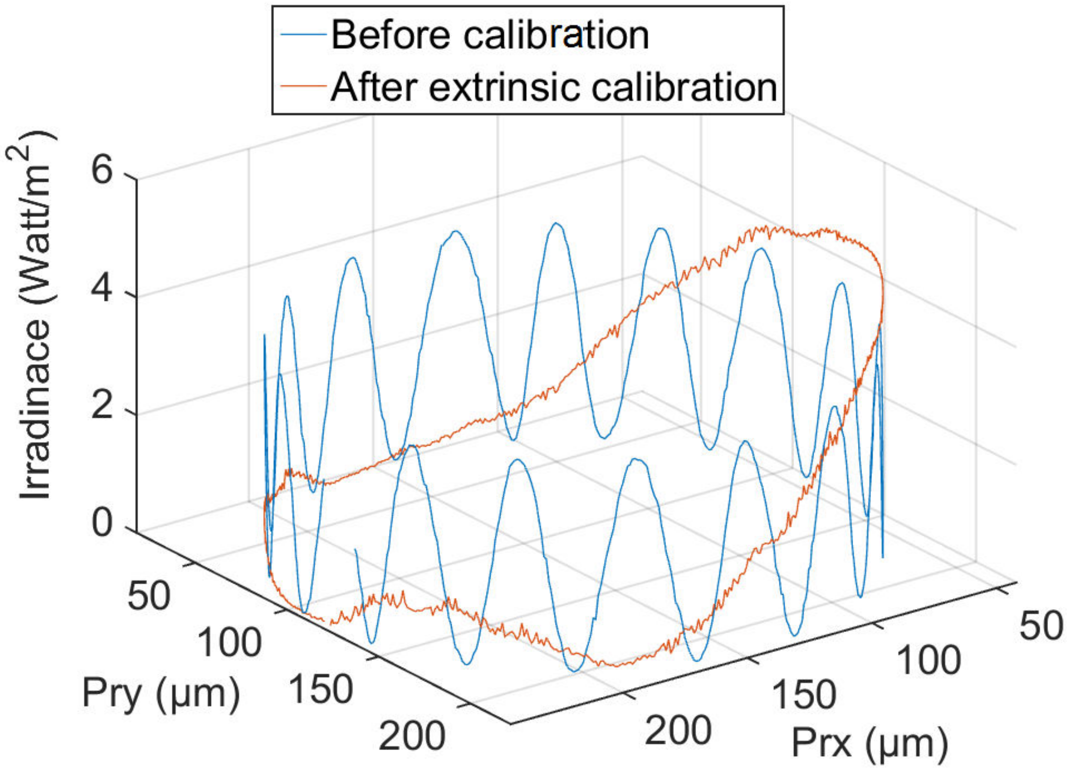

Figure 3.25: The optical irradiance corresponding to circular translation on the optical lamella plane before and after extrinsic parameters calibration.

3.10/ CONCLUSION

Geometric parameters are generally predominant. In order to achieve high positioning accuracy, these geometric parameters need to be identified and compensated through robotic calibration process. Robot calibration process involves four main steps: modeling, measurement, identification, and compensation. The parameter identification process uses a mathematical calibration model and end-effector data measurement to identify parameter errors as accurately as possible. Afterwards, correction of this identified parameters improves the end-effector pose positioning accuracy.

The discussed literature review about geometric calibration at macro-scale proved the effectiveness of relative distance calibration method to improve the robot end-effector positioning accuracy.

However, measurement at the micro-scale is a very challenging issue in robot calibration. Micro-scale measurement requires sensing devices with high resolution (e.g., a few nanometers) and accuracy (e.g., tens of nanometers), because motion and errors in this scale are very small. In order to overcome the micro-scale measurement issue, some researchers investigated robot calibration for micro-scale applications based on different measurement strategies and calibration approaches. Based on the discussed literature review about geometric calibration at the micro-scale, the highest positioning accuracy was achieved with less number of DOF and simple realized tasks. When the number of DOF or the task complexity increases the positioning accuracy decreases.

A photo-robotic approach was proposed for robot extrinsic parameters calibration. This approach relates a 1-D relative distance with a multi-DOF robot motion in order to identify extrinsic geometric parameters based on a photo-robotic calibration model. A dedicated measurement strategy was proposed for high measurement accuracy, where the 1-D relative distance measure is achieved based on the high accurate 1-D Fabry-Perot interferometry measure.

A photo-robotic platform dedicated for optical components 6-DOF nano-positioning and assembly was proposed. A 6-DOF serial robot is proposed, which is built based on high accurate nano-positioning stages commonly used for micro-manipulation.

Applying the proposed photo-robotic extrinsic parameters calibration reduced considerably Fabry-Perot cavity variation during rotations around X_f, Y_f and Z_f for each different chosen reflection point of the laser spot. Applying square and circular translation on the optical lamella plane after robot extrinsic parameters calibration reduced also considerably Fabry-Perot cavity variation. We have achieved a Fabry-Perot cavity variation of about 0.39 μm during a square translations of (100 $\times$100) μm. And we have also achieved a Fabry-Perot cavity variation of about 1.56 μm for a rotation range of 6° around X_f and Y_f and a Fabry-Perot cavity variation of about 0.858 μm for a rotation range of 45.5° around Z_f. But, the existing Fabry-Perot cavity variation during positioning is supposed to be because of the non calibration of intrinsic parameters of the robot. For this reason, a second photo-robotic approach is proposed for 6-DOF robot extrinsic and intrinsic calibration in the next chapter.

4

EXTRINSIC AND INTRINSIC GEOMETRIC PARAMETERS CALIBRATION OF A 6-DOF ROBOT BASED ON FABRY-PEROT INTERFEROMETRY RELATIVE DISTANCE MEASURE

Contents

4.1/ INTRODUCTION

This chapter deals with the calibration of micro-robotic systems in order to achieve high positioning accuracy. Micro-robotic systems comprising several micro-positioning stages are commonly used in micro-manipulation systems. Many factors influence the accuracy of micro-robotic systems, such as the quality of fabrication, linearity, backlashes, weight of the axes. Since the tasks at the micro-scale require high flexibility, micro-robotic systems consisting of several micro-positioning stages have to be constructed according to specific tasks [Das et al., 2012]. Each of these stages usually has limited Degrees-of-Freedom. Then, several of them have to be assembled together to meet multi-DOF requirements. Tools such as gripper, probe, and sensors are fixed onto the stages as end-effector. The assemblies of micro-positioning stages and end-effectors are usually performed by hands and not in an accurate way at this scale. Therefore, to achieve a high positioning accuracy, some intrinsic geometric parameters (e.g., perpendicularity of two stages and position of end-effector with respect to the stages) must be identified and corrected. This leads to propose a generalized photo-robotic approach for extrinsic and intrinsic parameters calibration of a 6-DOF robot. This approach relates a 1-D relative distance with a multi-DOF robot motion in order to identify extrinsic and intrinsic geometric parameters based on a generalized photo-robotic calibration model. A dedicated measurement strategy is proposed to cover the work space and to achieve a rich measurements with high accuracy. In order to validate the approach, the proposed experimental procedure is presented. The behavior study of the full calibrated robot is discussed based on the obtained experimental results. Finally, in order to find the appropriate calibration strategy for high positioning accuracy and adapted to the context of micro-positioning of optical components for high optical performances, a quantification knowledge is realized, by investigating and evaluating durability and performances of the fully calibrated robot. This generalized photo-robotic 6-DOF robot extrinsic and intrinsic calibration approach is presented in the next section.

4.2/ 6-DOF ROBOT EXTRINSIC AND INTRINSIC GEOMETRIC PARAMETERS CALIBRATION

The objective of this section is to achieve robot extrinsic and intrinsic geometric calibration based on relative distance measure. The distance measure is realized based on very high accurate Fabry-Perot interferometry principle measurement as presented in chapter 2. For this sake, the transformation matrix from the world frame to the tool (optical lamella) frame including the robot extrinsic and intrinsic parameters is given as follows:

$$ {}^{w}T_t(q,\epsilon,\beta_{et},\theta_{et},Z_{et}) = {}^{w}T_e(q,\epsilon) *^{e} T_t(\beta_{et},\theta_{et},Z_{et}) = \begin{bmatrix} x & x & a_{wt} & x_{wt} \\ x & x & b_{wt} & y_{wt} \\ x & x & c_{wt} & z_{wt} \\ 0 & 0 & 0 & 1 \end{bmatrix}. \tag{4.1} $$

${}^{w}T_e$ is Direct Geometric Model (DGM), ϵ is the vector of the real (unknown intrinsic) parameters of the geometric errors, and q is the joint coordinates vector.

From the other side, the optical lamella plane equation given in chapter 3, in equation (3.19), can be deduced from the transformation matrix between the world frame and the tool (lamella) frame given in equation. 4.1, where:

$a_{wt} = {}^{w}T_t(1,3)$, $b_{wt} = {}^{w}T_t(2,3)$, $c_{wt} = {}^{w}T_t(3,3)$, $x_{wt} = {}^{w}T_t(1,4)$, $y_{wt} = {}^{w}T_t(2,4)$, $z_{wt} = {}^{w}T_t(3,4)$.

The direction vector $\overrightarrow{Z_t}$ (a_{wt},b_{wt}, c_{wt}) is orthogonal to the lamela plane and passes through the origin O_t (x_{wt},y_{wt}, z_{wt}) of the tool frame (optical lamella frame).

The 3-dimensional parametric equation of the line carrying the vector $\overrightarrow{O_f Z_f}$ (optical axis) is given in equation (3.16).

As shown in Figure 4.1, the fiber is fixed, which means that the optical axis equation stays unchanged. From the other side, displacing the optical lamella from one pose to another yields two plane equations (before and after the new pose).

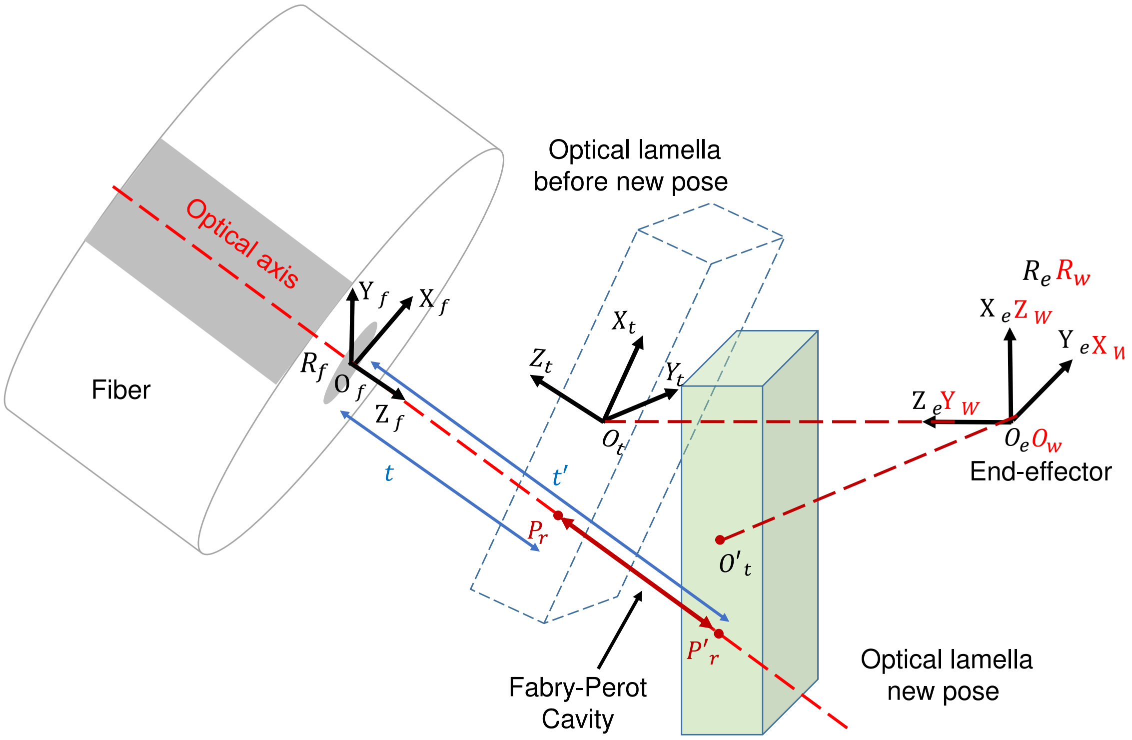

Figure 4.1: Optical lamella before the new pose and after the new pose.

The optical lamella plane equation before and after the new pose is given as follows:

$$\begin{cases} a_{wt}x + b_{wt}y + c_{wt}z + d_{wt} = 0 \\ a'_{wt}x + b'_{wt}y + c'_{wt}z + d'_{wt} = 0 \end{cases} . \tag{4.2}$$

Using the optical axis line equation given in equation (3.16). The intersection of the optical axis line with the optical lamella plane before the new pose gives:

$$a_{wt}(a_{wf}t + x_{wf}) + b_{wt}(b_{wf}t + y_{wf}) + c_{wt}(c_{wf}t + z_{wf}) + d_{wt} = 0. \tag{4.3}$$

The intersection of the optical axis line with the optical lamella plane after the new pose gives:

$$a'_{wt}(a_{wf}t' + x_{wf}) + b'_{wt}(b_{wf}t' + y_{wf}) + c'_{wt}(c_{wf}t' + z_{wf}) + d'_{wt} = 0. \tag{4.4}$$

Then, t and t' can be calculated respectively as follow:

$$t = \frac{-(a_{wt}x_{wf} + b_{wt}y_{wf} + c_{wt}z_{wf} + d_{wt})}{a_{wt}a_{wf} + b_{wt}b_{wf} + c_{wt}c_{wf}}, \tag{4.5}$$

$$t' = \frac{-(a'_{wt}x_{wf} + b'_{wt}y_{wf} + c'_{wt}z_{wf} + d'_{wt})}{a'_{wt}a_{wf} + b'_{wt}b_{wf} + c'_{wt}c_{wf}}. \tag{4.6}$$

The optical lamella displacement along the optical axis after the new pose can be deduced as follows:

$$dt = t' - t = \frac{(a_{wt}x_{wf} + b_{wt}y_{wf} + c_{wt}z_{wf} + d_{wt})}{a_{wt}a_{wf} + b_{wt}b_{wf} + c_{wt}c_{wf}} - \frac{(a'_{wt}x_{wf} + b'_{wt}y_{wf} + c'_{wt}z_{wf} + d'_{wt})}{a'_{wt}a_{wf} + b'_{wt}b_{wf} + c'_{wt}c_{wf}}, \tag{4.7}$$

where:

$$a_{wt} = {}^{w}T_t(1,3), \qquad b_{wt} = {}^{w}T_t(2,3), \qquad c_{wt} =^{w} T_t(3,3),$$

$$a'_{wt} = {}^{w}T'_t(1,3), \qquad b'_{wt} = {}^{w}T'_t(2,3), \qquad c'_{wt} = {}^{w}T'_t(3,3),$$

$$d_{wt} = -a_{wt} * {}^{w}T_t(1,4) - b_{wt} * {}^{w}T_t(2,4) - c_{wt} * {}^{w}T_t(3,4),$$

$$d'_{wt} = -a'_{wt} * {}^{w}T'_t(1,4) - b'_{wt} * {}^{w}T'_t(2,4) - c'_{wt} * {}^{w}T'_t(3,4).$$

And at the same time, this optical lamella displacement along the optical axis after the new pose is measured from the Fabry-Perot interferometry measure, presented in chapter 2 .

Finally, this displacement measure using Fabry-Perot interferometry can be written as a function of robot intrinsic and extrinsic geometric parameters as follows:

$$dt = f(q, \epsilon, \theta_{et}, \beta_{et}, a_{wf}, b_{wf}, c_{wf}, x_{wf}, y_{wf}, z_{wf}, Z_{et}). \tag{4.8}$$

Equation 4.8 represents the photo-robotic model for extrinsic and intrinsic parameters calibration. Displacing the optical lamella in different poses using the 6 DOF robot, will lead to form a system of non-linear equations, where the unknowns are the intrinsic and the extrinsic geometric parameters. The system of equations can be solved using different optimization algorithms (it is detailed in the next section).

When the intrinsic and the extrinsic parameters of the robot are identified, the point of intersection between the optical axis and the plane of the optical lamella with respect to the world frame can be deduced by calculating the distance t between the optical lamella and the fiber using equation (4.5) and then calculating the Cartesian coordinates of the reflection point ${}^{w}P_r({}^{w}P_{rx},\ {}^{w}P_{ry},\ {}^{w}P_{rz})$ in the world frame using equation (3.39).

At the initial lamella pose ($q_1 = q_2 = q_3 = q_3 = q_4 = q_5 = q_6 = 0$), the Direct Geometric Model (DGM) transformation matrix is written as a function of intrinsic parameters errors ${}^{w}T_e(q = 0, \epsilon)$.

By replacing the already deduced vector ${}^{w}P_r$ and the transformation matrices ${}^{e}T_t$ and ${}^{w}T_e$, the vector ${}^{t}P_r$ can be deduced as follows:

$$ {}^{t}P_r ={}^{e} T_t^{-1} * {}^{w}T_e^{-1} * {}^{w}P_r. \tag{4.9} $$

After having developed the photo-robotic model for extrinsic and intrinsic parameters calibration, this model combines 6-DOF robot motion with a high accurate 1-D Fabry-Perot measure in order to identify the extrinsic and the intrinsic parameters of the robot. In order to detail the photo-robotic calibration approach, the next section presents the experimental procedure for robot extrinsic and intrinsic parameters calibration.

4.3/ EXPERIMENTAL PROCEDURE OF ROBOT EXTRINSIC AND INTRINSIC PARAMETERS CALIBRATION

The whole procedure of robot extrinsic and intrinsic parameters calibration is shown in Figure 4.2 which includes measurement, identification, parameters integration and validation step.

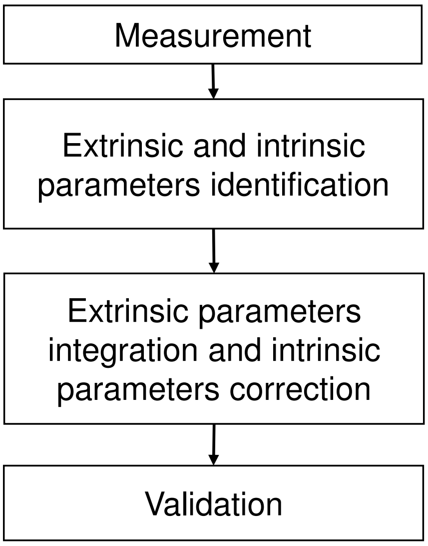

Figure 4.2: Flowchart for extrinsic and intrinsic parameters calibration.

1- Measurement

In order to cover all the workspace and to achieve a rich measurement with high accuracy, a measurement strategy is proposed. The proposed measurement strategy consists of 2 steps:

- A cubical workspace with 15 nodes is chosen as shown in Figure 4.3. For each node, three continuous rotations are applied, around X_w, Y_w, Z_w. Rotation of $[-3^\circ \;\; 3^\circ]$ is applied around X_w and Y_w, and $[0^\circ \;\; 90^\circ]$ around Z_w with angular velocity control. Each rotation around an axis represents one equation, so for each node there are 3 equations, which means for 15 nodes 45 equations can be obtained;

- Different lamella orientation are given. By choosing two angular values for each rotation, $Rot_{X_w}(q_4 = (0°, 3°))$, $Rot_{Z_w}(q_5 = (0°, 3°))$ and $Rot_{Y_w}(q_6 = (0°, 90°))$, 2^3 angular combinations are obtained. For each angular combination (each orientation), three translations are applied along X_w, Y_w and Z_w (3 equations), thus yields 24 equations. Translation of $[-150 \quad +150]\ \mu m$ is applied along X_w and Z_w and $[-20 \quad +20]\ \mu m$ along Y_w with translational velocity control. Wavelength scan distance measure is done based on Fabry-Perot interferometry before and after each translations along X_w and Z_w axes.

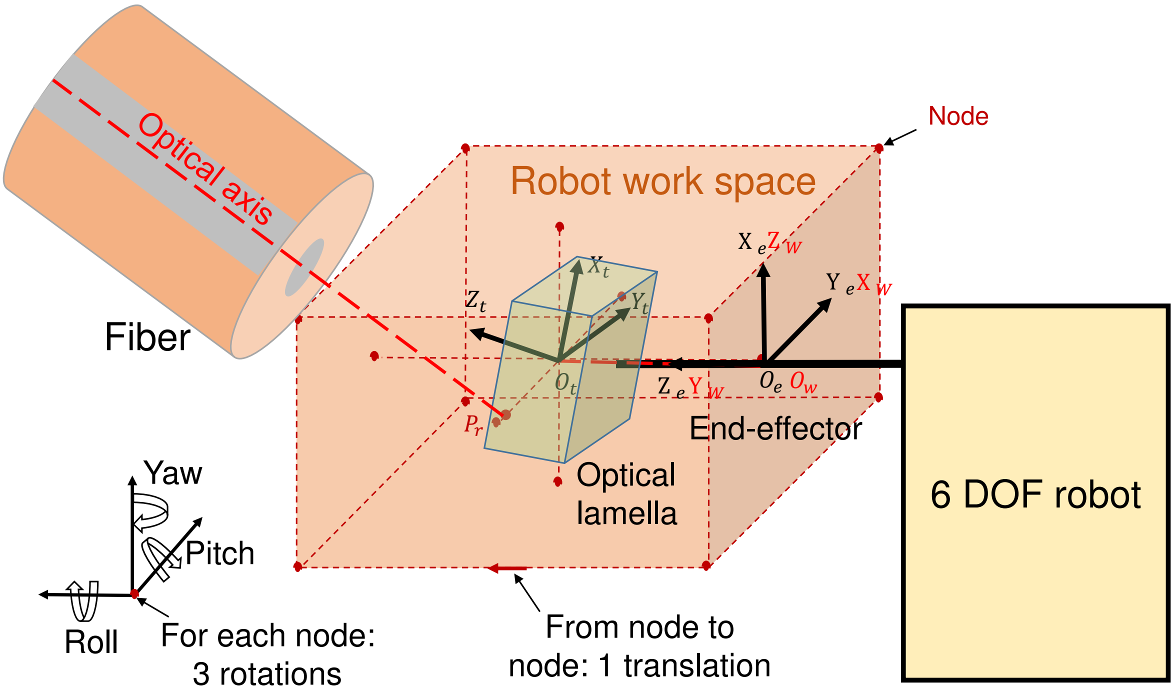

Figure 4.3: Measurement strategy for robot calibration.

2- Extrinsic and intrinsic parameters identification

The two previous measurement steps can give 69 equations.

This non-linear minimization problem can be solved using various algorithms.

The algorithms conventionally used to solve such problems are relative to the four following estimation methods:

- Newton's method;
- Gradient method;
- Method of conjugate directions;

- Levenberg-Marquardt method.

The Levenberg-Marquardt method is most often cited and used in the literature. Such a method makes a compromise between the gradient method (launch of the algorithm far from the minimum) and Newton's method (neighborhood of the solution, acceleration of convergence). In addition, such method frees itself from the problems of singularities of the Hessian matrix.

3- Extrinsic parameters integration and Intrinsic parameters correction

Once the extrinsic and the intrinsic parameters of the robot are identified. The integration of the identified extrinsic parameters and the correction of the intrinsic identified parameters are shown the scheme in Figure 4.4, where the inverse kinematic model of the robot is calculated using the real identified intrinsic parameters of the robot.

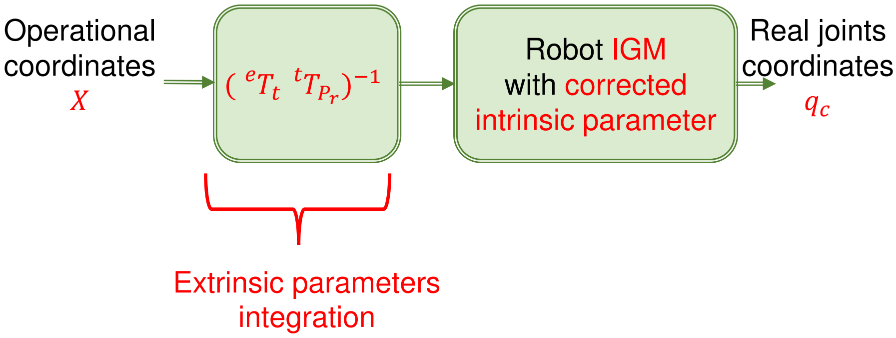

Figure 4.4: Extrinsic parameters integration and intrinsic parameters errors correction.

4-Validation

Our objective is to rotate the optical lamella around X_f, Y_f and Z_f axes with a fixed reflection point P_r, and to translate the optical lamella perpendicular to the optical axis Z_f. For this sake, in the validation step, a 100 μm square translation of the lamella along X_f and Y_f is applied and for each vertex of the square (reflection point of laser spot P_r), 3 rotations are applied around X_f, Y_f and Z_f axes (see Figure 3.11 for frames assignment). The vertex that corresponds to the reflection point P_{r1} is the starting reflection point. A rotation from $-3°$ to $+3°$ around X_f and Y_f a rotation from $0\circ$ to $90°$ for rotation around Z_f (see Figure 4.5).

Choosing different reflection points of the laser spot P_r (new tool points) and rotating around is realized using the Inverse Geometric Model (IGM).

The proposed experimental procedure for robot extrinsic and intrinsic parameters calibration was presented. The proposed approach is applied on the same experimental setup

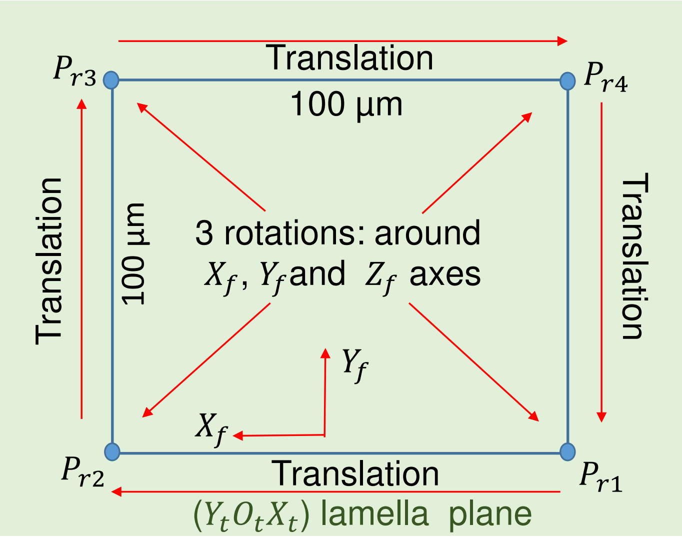

Figure 4.5: Robot trajectory for validation procedure.

presented in the previous chapter. The next section studies and investigates the optical performances after having applied robot extrinsic and intrinsic parameters calibration approach.

4.4/ BEHAVIOR STUDY OF THE CALIBRATED ROBOT EXTRINSIC AND INTRINSIC PARAMETERS

After robot extrinsic parameters calibration, there were still some fringes because of Fabry-Perot cavity variation along the optical axis. For this sake, a full (extrinsic and intrinsic) robot geometric parameters calibration is done. Robot extrinsic and intrinsic parameters calibration procedure follows the flowchart shown in Figure 4.2. The duration of the measurement step is about 2 hours. The duration of identification step is about 2 hours. The identified extrinsic and intrinsic parameters are obtained and shown in Table 4.1 and 4.2. Then, the integration of the obtained extrinsic parameters and the correction of robot intrinsic parameters are done as shown in Figure 4.4, where the inverse kinematic model of the robot is corrected. The validation test is then performed which aim at quantifying performances of the fully calibrated robot. The validation test is done in about 30 minutes.

Figure 4.6, 4.7, 4.8 and 4.9 represent the obtained results after having integrated extrinsic parameters and having corrected the intrinsic parameters of the 6-DOF robot for 3 rotations around X_f, Y_f and Z_f, for different reflection point projection on the lamella P_{r1}, P_{r2}, P_{r3} and P_{r4} respectively (see Figure 4.5). For rotations around X_f and Y_f, the corresponding optical irradiance and the 3 translational joints are plotted (since they are the only joints which intervene for these two rotations). For rotations around Z_f, the corresponding optical irradiance, the 3 translational joints and the 2 rotational joints (joint 4 and 5) are plotted.

We can notice after robot extrinsic and intrinsic parameters calibration that for each reflection point projection on the lamella (P_{r1}, P_{r2}, P_{r3} and P_{r4}), the joints intervene in

Table 4.1: Identified extrinsic parameters.

Parameters	β_{et}	θ_{et}	β_{wf}	θ_{wf}	$\mathbb{Z}_{et}$	x_{wf}
Values	$0.768°$	$-0.613°$	$0.721°$	$-0.533°$	1.61 μm	113.40 μm
y_{wf}	z_{wf}	${}^{w}P_{rx}$	${}^{w}P_{ry}$	${}^{w}P_{rz}$		
916.1 μm	115.3 μm	155.5 μm	-3.82 μm	-109.78 μm		

Table 4.2: Identified robot intrinsic parameters.

Link	ρ_i	$\beta_i(°)$	$\alpha_i(°)$	d_i (μm)	$\theta_i(°)$	r_i (μm)
1	1	0	0	0	0	q_1
2	1	0	-90.13	0	-89.22	q_2
3	1	0	-90.29	0	-89.47	q_3
4	0	-0.26	0.25	-4.20	$q_4 - 0.07$	0
5	0	0	-89.45	-2.21	$q_5 - 90.49$	0
6	0	0	-90.57	0	$q_6 + 0.14$	0

order to move the rotation center of the robot to the reflection point of the laser spot P_r and maintain the rotation center at that point (reflection point P_r). For rotations around X_f and Y_f, there is only the envelope of the optical irradiance during rotations without any fringes, which means that there is no Fabry-Perot cavity variation during the two rotations.

For rotation around Z_f, the translational and rotational joints intervene in order to maintain the rotation at the reflection point P_r, where the optical irradiance is constant until the saturation of at least one translational joint, the frequency of the fringes (peaks) increase, which represents an increase in Fabry-Perot cavity variation during the rotation.

In order to investigate the optical irradiance repeatability, 3 rotations around X_f, Y_f and Z_f axes for forth and back to the reflection point P_{r1} are applied. The corresponding optical irradiance for forth rotations and back rotations are shown in Figure 4.10. We can notice that the envelope of the optical irradiances are almost the same for forth and back rotations around X_f, Y_f and Z_f axes at P_{r1}.

Figure 4.11 and 4.12 show the optical irradiance corresponding to a square and circular translation respectively along the optical lamella plane before, after extrinsic parameters calibration, and after extrinsic and intrinsic parameters calibration. We can notice that the number of fringes decrease considerably after robot extrinsic parameters calibration, but there still exist about half of fringe. After extrinsic and intrinsic parameters calibration, the irradiance is constant and maximum. This demonstrates that the Fabry-Perot cavity variation after extrinsic parameters calibration was because of the intrinsic parameters errors.

Figure 4.13 represents translational joints comparison between robot extrinsic parameters calibration (p) and robot extrinsic and intrinsic calibration(g), for rotations around X_f and Y_f axes, for the four reflection points (P_{r1}, P_{r2}, P_{r3} and P_{r4}). We can notice a slight difference in translational joints values between robot extrinsic parameters calibration (p) and robot extrinsic and intrinsic calibration (g). Figure 4.14 represents translational and rotational joints comparison between robot extrinsic parameters calibration (p) and robot extrinsic and intrinsic calibration (g), for rotation around Z_f axis, for the four reflection points (P_{r1}, P_{r2}, P_{r3} and P_{r4}). We can notice also a slight difference in translational and rotational joints values between robot extrinsic parameters calibration (p) and robot extrinsic and intrinsic calibration (g), these slight differences are yielded because of the intrinsic parameters correction.

In order to estimate positioning accuracy, after integration of extrinsic parameters and correction of intrinsic parameters, a translation along Y_f axis (parallel to the plane of the fiber) is applied after having modified the identified parameter β_{et} by adding each time $0.002°$ (misaligning the optical lamella from the fiber plane). The obtained optical irradiance for each translation is shown in Figure 4.15. We can notice that the optical irradiance starts to derive after having modified β_{et} by $0.004°$.

In summary, after having done robot extrinsic and intrinsic parameters calibration, no Fabry-Perot fringes appears on the optical irradiance for rotations around X_f, Y_f and Z_f axes for each different reflection points P_r in validation step, neither for square translations along the optical lamella plane. The estimated positioning accuracy is estimated experimentally by $0.004°$. The next section deals with the durability and performances of the calibrated robot parameters.

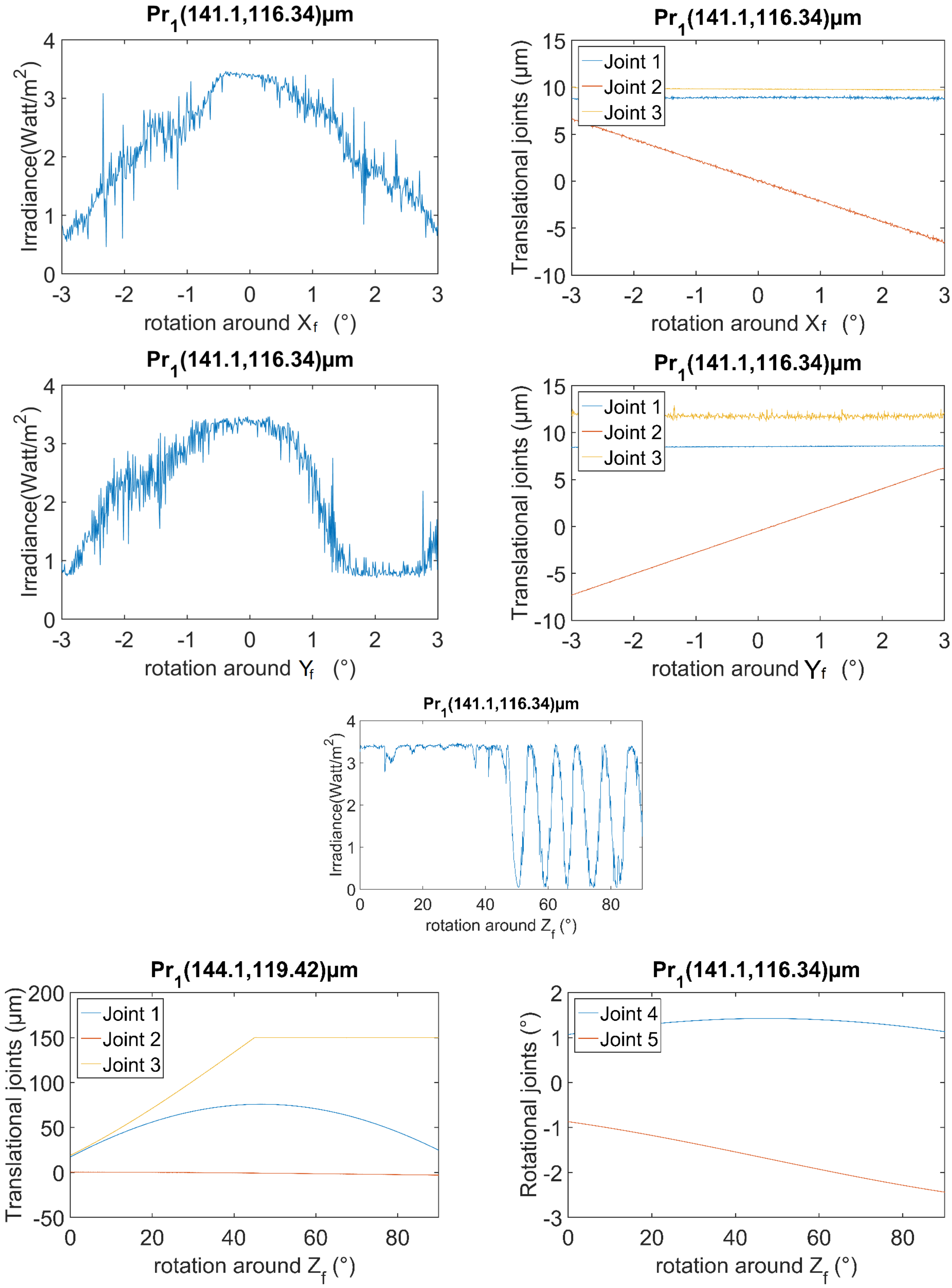

.

Figure 4.6: 3 rotations around X_f, Y_f and Z_f axes when the reflection point projection is in P_{r1}, after robot extrinsic and intrinsic parameters calibration.

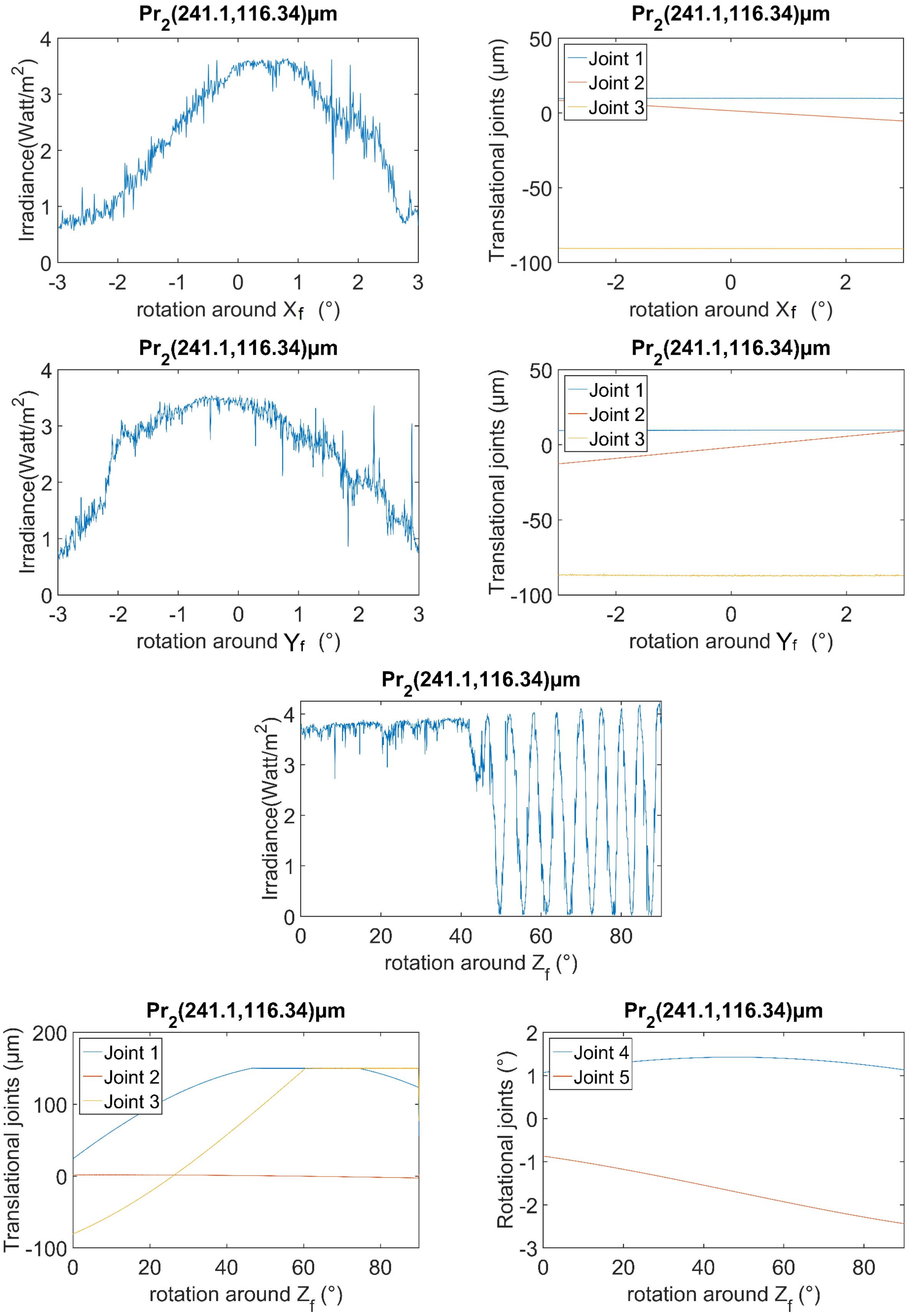

Figure 4.7: 3 rotations around X_f, Y_f and Z_f axes when the reflection point projection is in P_{r2}, after robot extrinsic and intrinsic parameters calibration.

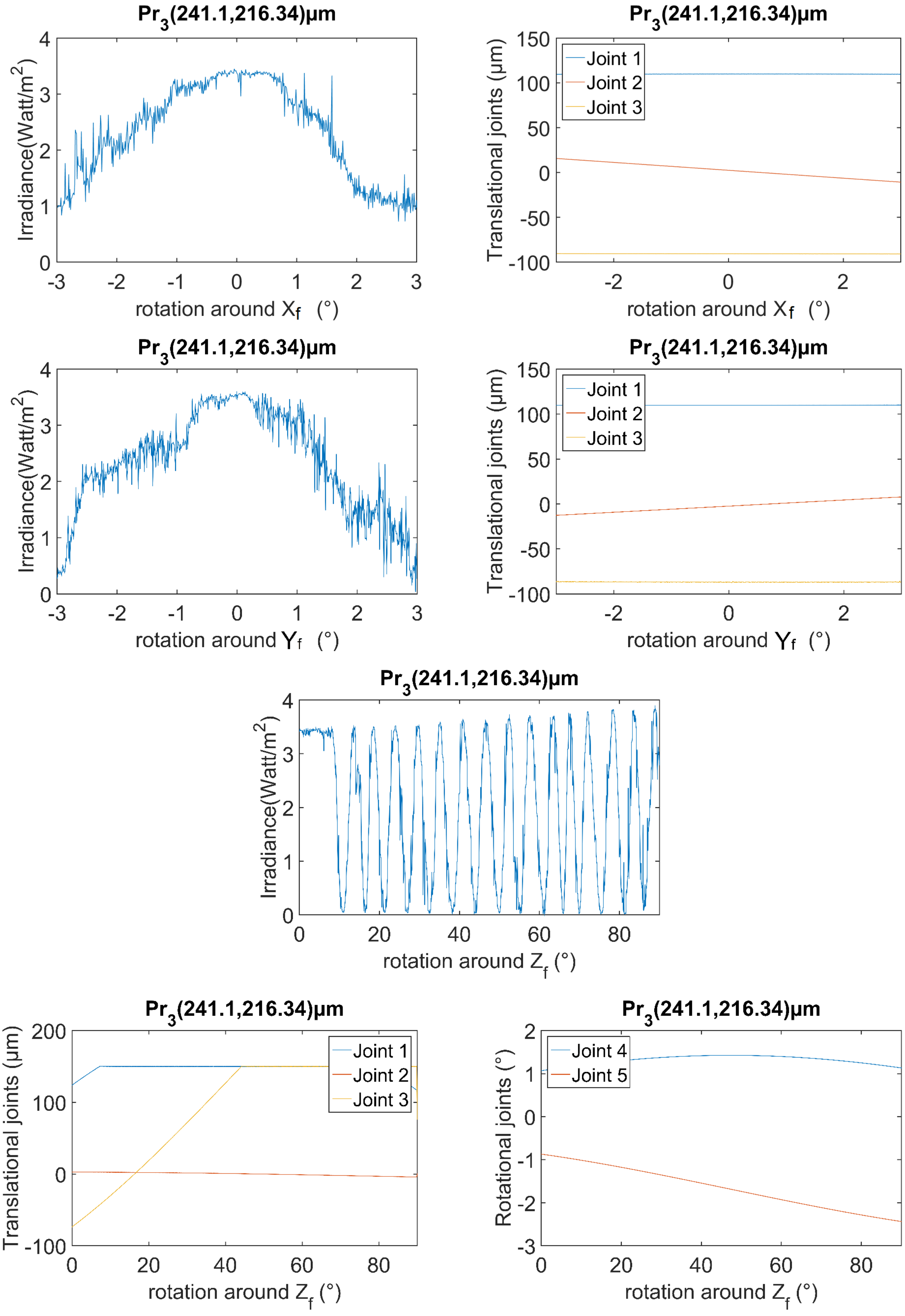

Figure 4.8: 3 rotations around X_f, Y_f and Z_f axes when the reflection point projection is in P_{r3}, after robot extrinsic and intrinsic parameters calibration.

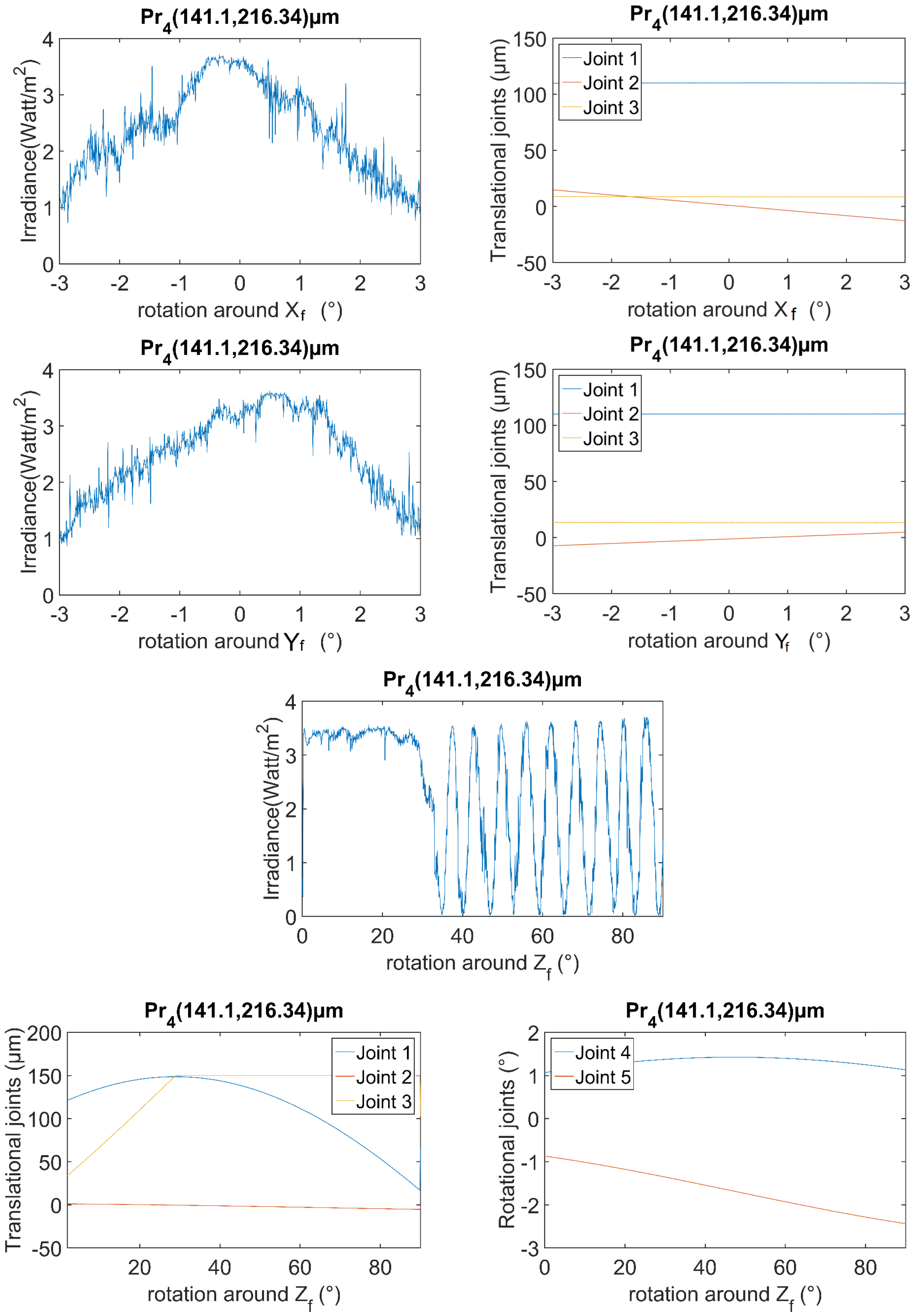

Figure 4.9: 3 rotations around X_f, Y_f and Z_f axes when the reflection point projection is in P_{r4}, after robot extrinsic and intrinsic parameters calibration.

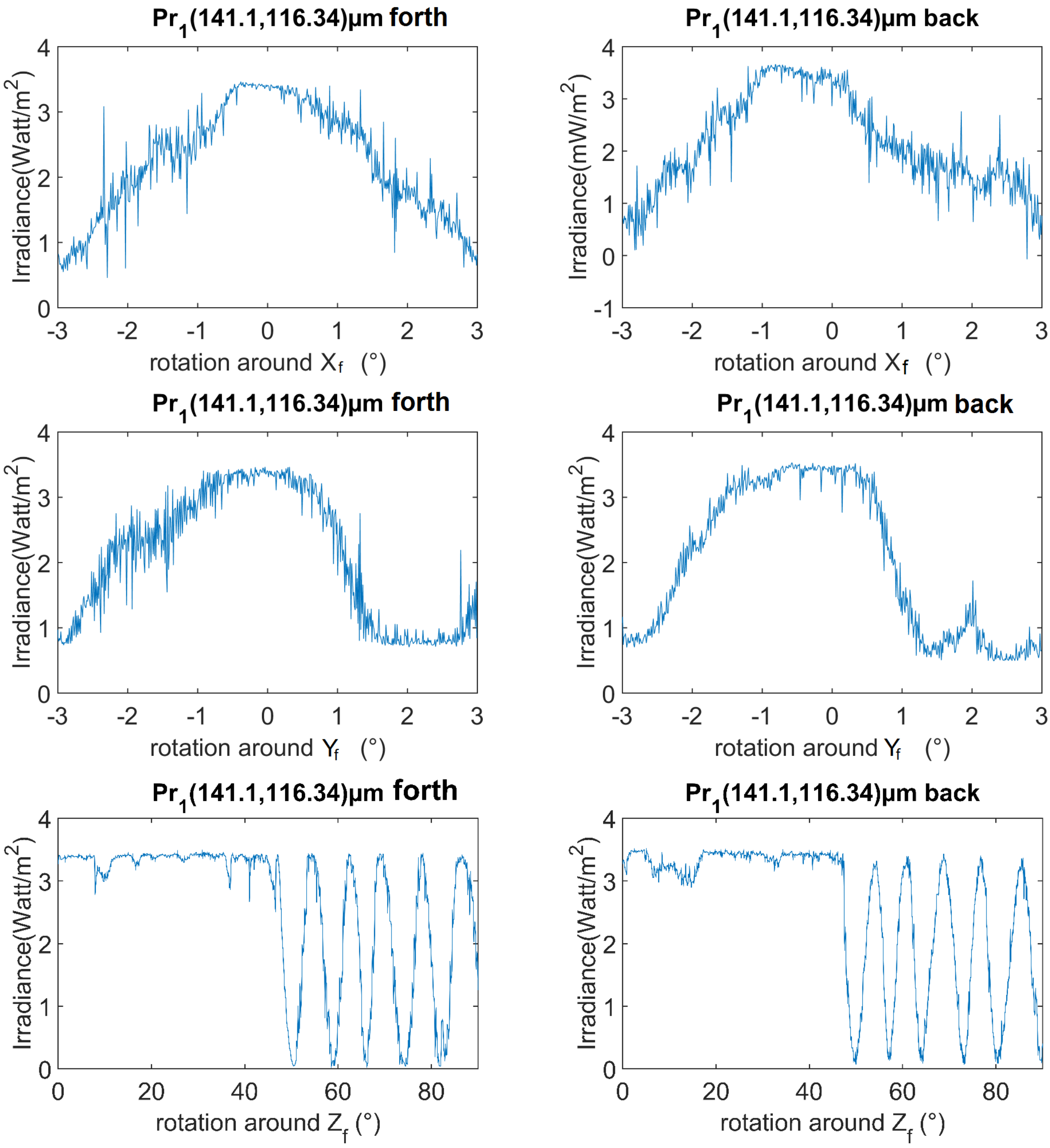

Figure 4.10: Comparison between the optical irradiance for 3 rotations around X_f, Y_f and Z_f axes for forth and back to the reflection point projection P_{r1}, after robot extrinsic and intrinsic parameters calibration.

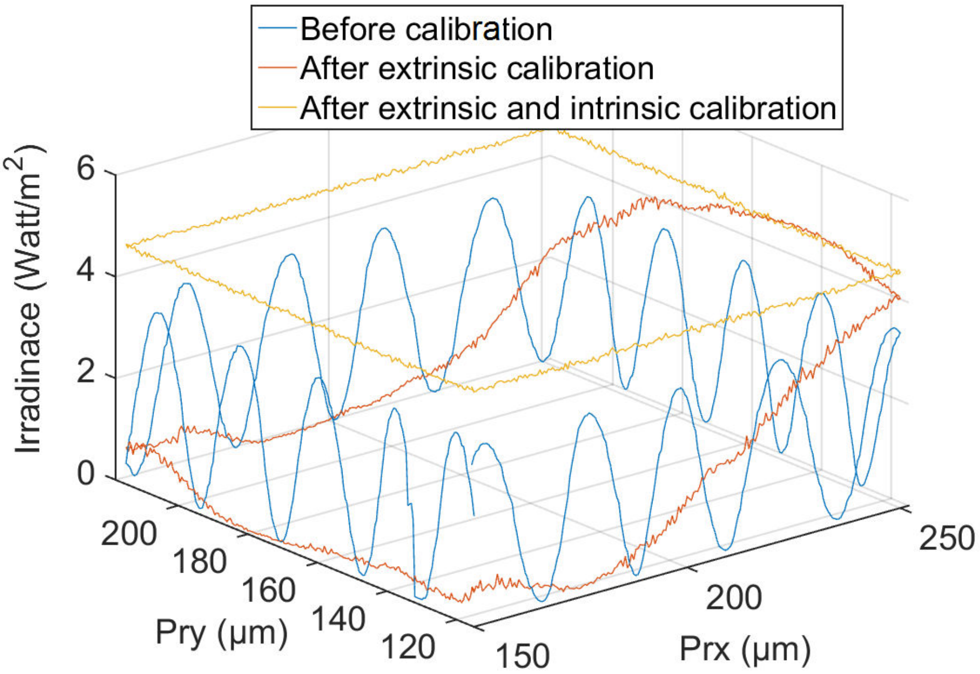

Figure 4.11: The optical irradiance corresponding to a square translation on the optical lamella plane before calibration, after robot extrinsic parameters calibration and after robot extrinsic and intrinsic parameters calibration.

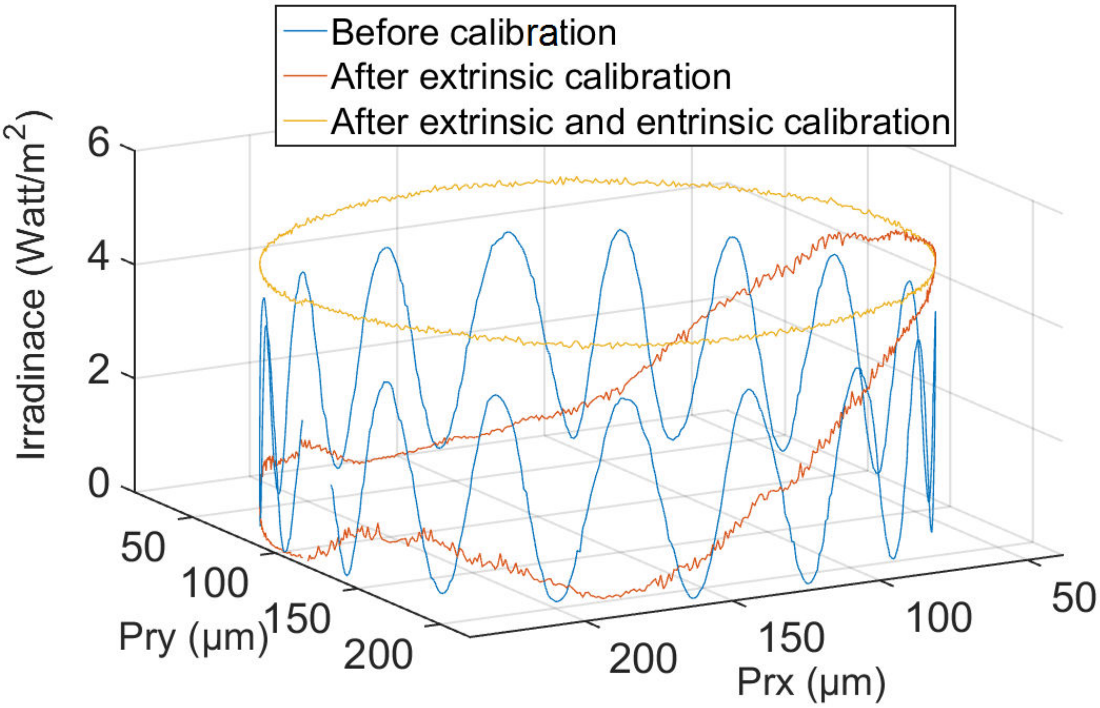

Figure 4.12: The optical irradiance corresponding to a circular translation on the optical lamella plane before robot calibration, after robot extrinsic parameters calibration and after robot extrinsic and intrinsic parameters calibration.

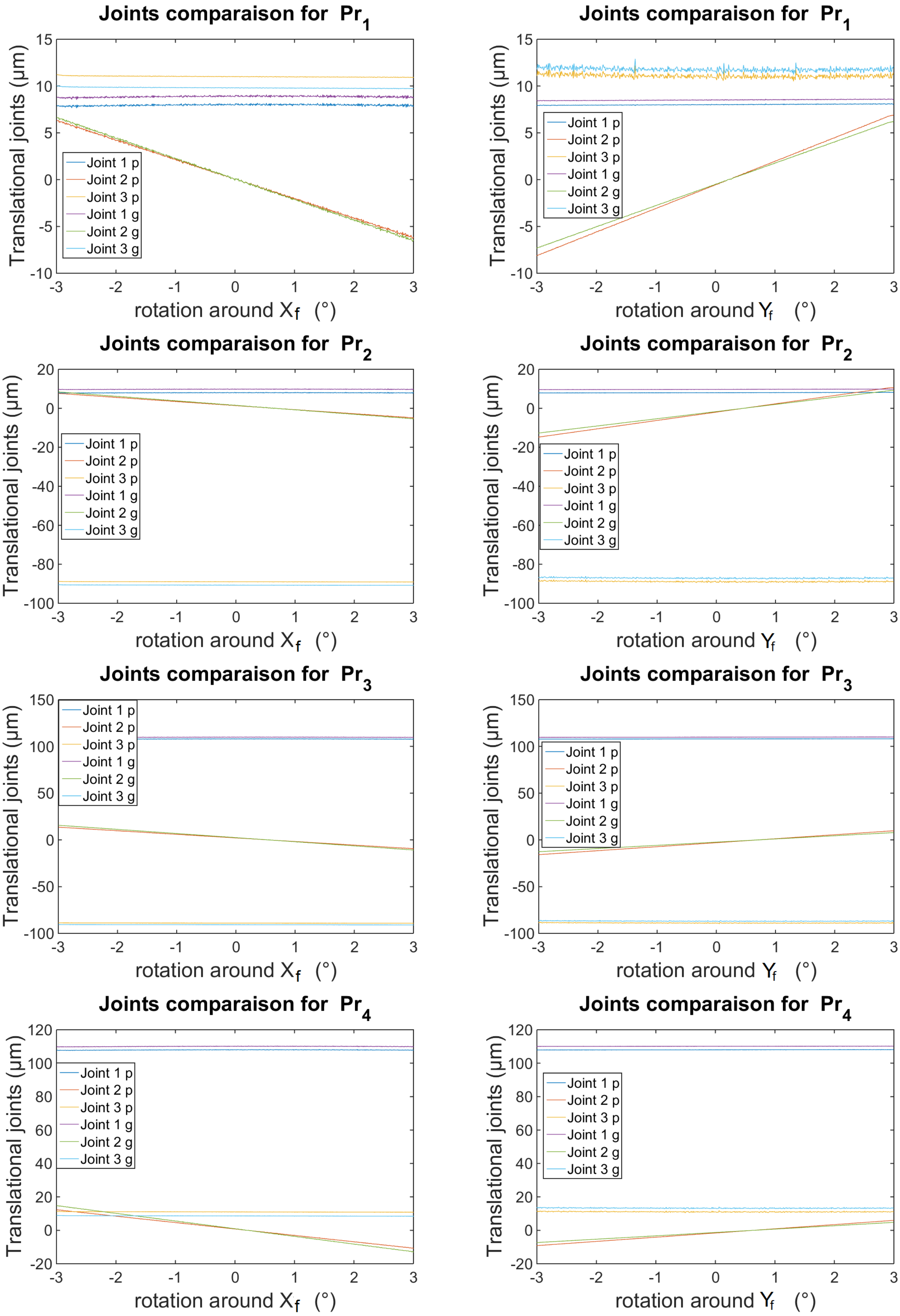

Figure 4.13: Translational joints comparison between robot extrinsic parameters calibration (p) and robot extrinsic and intrinsic calibration (g), for rotations around X_f and Y_f axes, for the four reflection points projection (P_{r1}, P_{r2}, P_{r3} and P_{r4}).

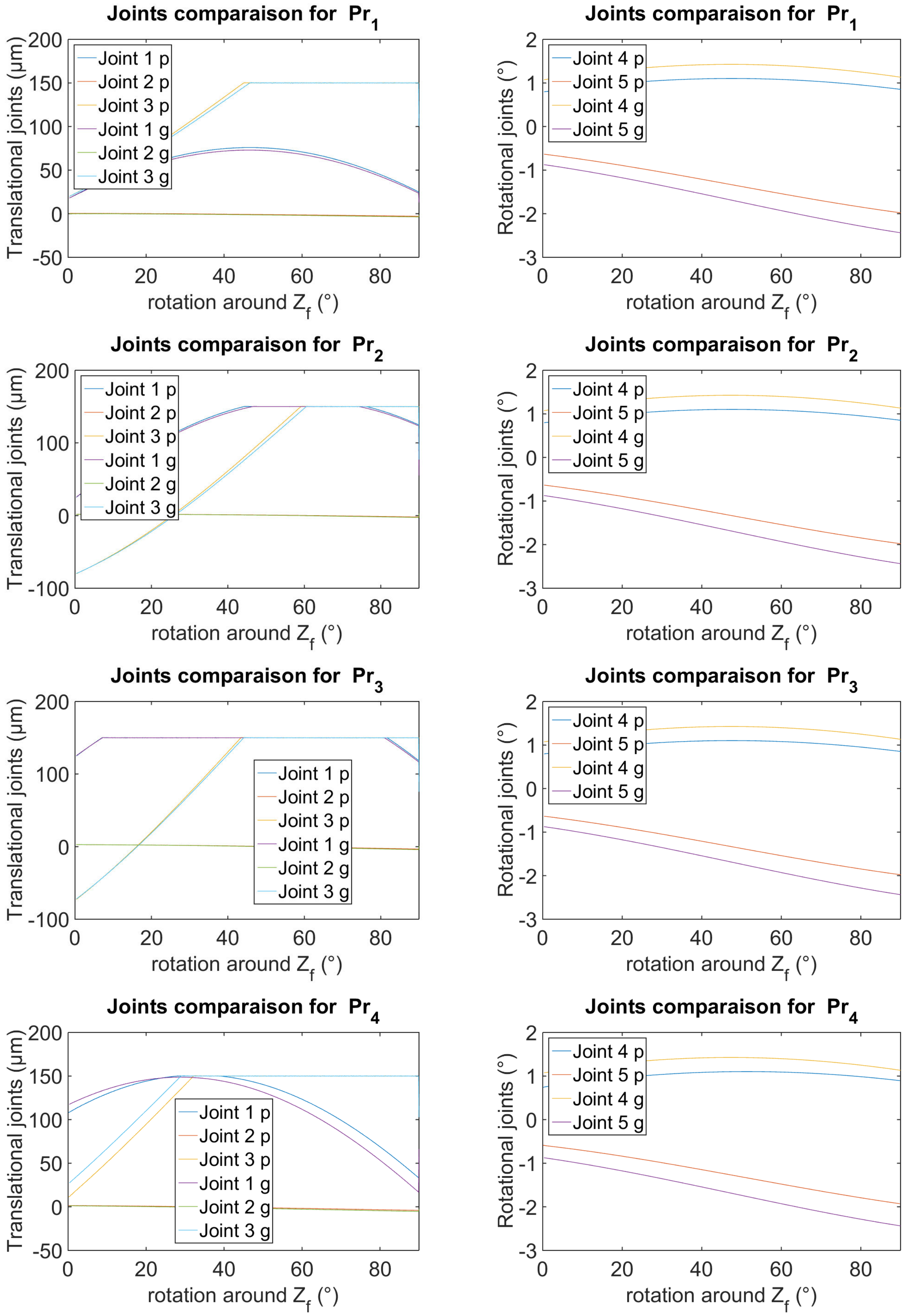

Figure 4.14: Translational and rotational joints comparison between robot extrinsic parameters calibration (p) and robot extrinsic and intrinsic calibration (g), for rotation around Z_f axis, for the four reflection points projection (P_{r1}, P_{r2}, P_{r3} and P_{r4}).

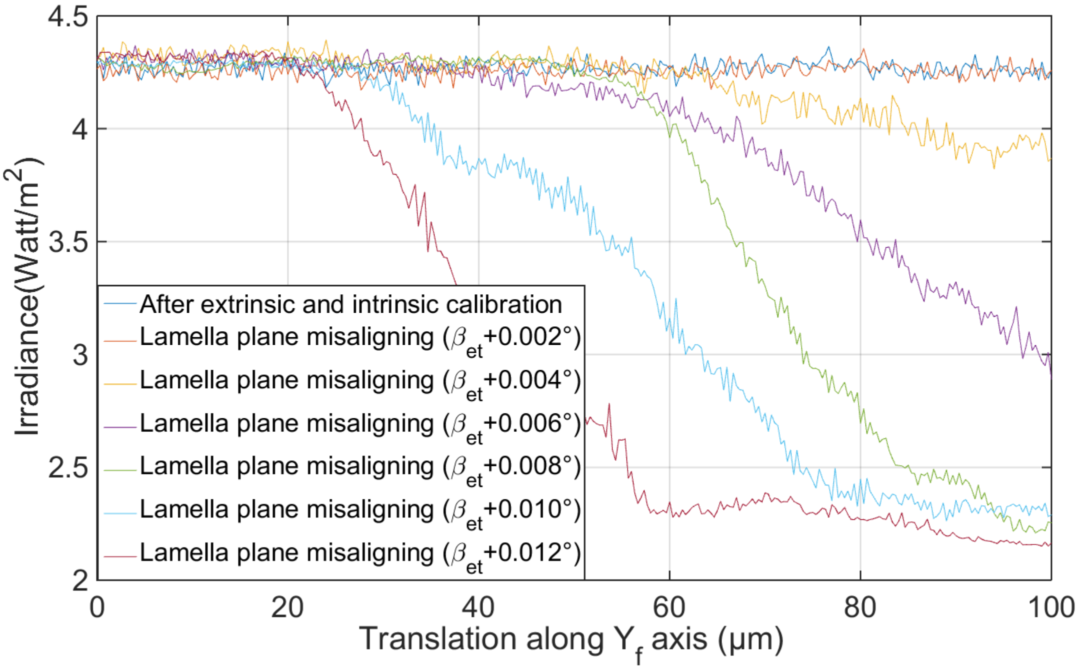

Figure 4.15: Experimental estimation of angular accuracy when a small compensation error of β_{et} parameter is created.

4.5/ DURABILITY AND PERFORMANCES OF THE CALIBRATED 6-DOF ROBOT

Our aim is to find the appropriate calibration strategy for high positioning accuracy and adapted to the context of micro-positioning of optical components for high optical performances. For this sake, the whole experimental procedure is defined in flowchart shown in Figure 4.16, where robot performances are tested before calibration, after robot extrinsic parameters calibration and after robot extrinsic and intrinsic parameters calibration. Then, the durability and the parameters behavior of the calibrated extrinsic and intrinsic parameters of the robot are investigated. Finally, only robot extrinsic parameters calibration is realized after having already realized full (extrinsic and intrinsic) robot calibration, where the performances are tested.

In order to evaluate the durability of the calibrated extrinsic and intrinsic parameters of the 6-DOF robot, a circular translation along the optical lamella plane is chosen for the evaluation. A circular translation along the optical lamella plane is applied every 2 hours for 14 hours.

Figure 4.17 shows the obtained optical irradiance for each circular translation along the optical lamella plane and the one yielded from only robot extrinsic parameters calibration. we can notice that the optical irradiance starts to derive after 10 hours and then it derives increasingly after 12 and 14 hours, but it is still better than after robot extrinsic parameters calibration. Figure 4.18 shows the temperature evaluation during the durability test. The temperature is almost constant, it is about 21°. This demonstrates that the optical irradiance derivation is not because of environmental conditions.

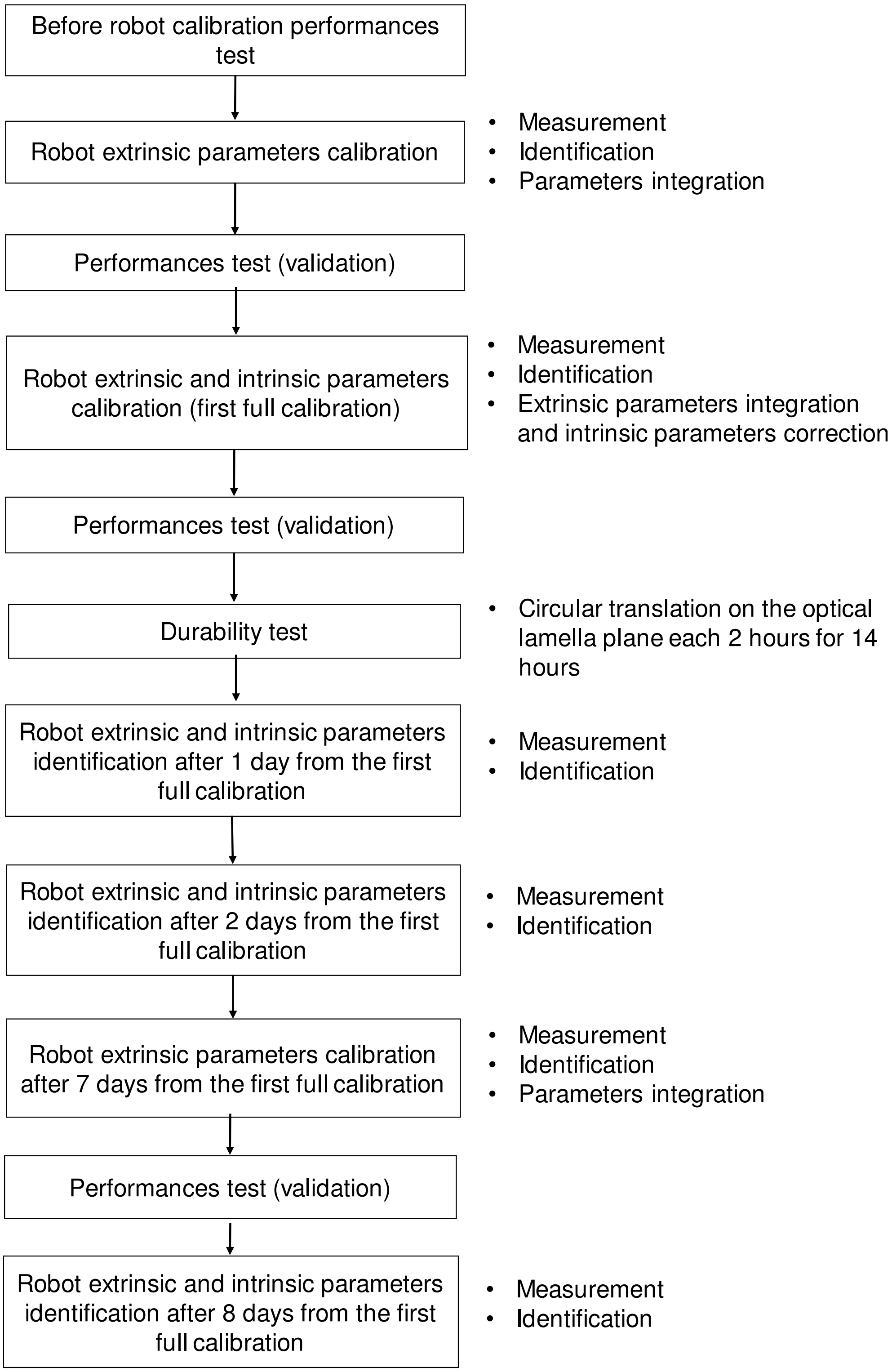

Figure 4.16: The whole experimental procedure.

In order to investigate the source of the derivation, two robot extrinsic and intrinsic parameters identifications are realized. One is realized one day after the first full robot calibration, and the obtained identified extrinsic and intrinsic parameters are shown in

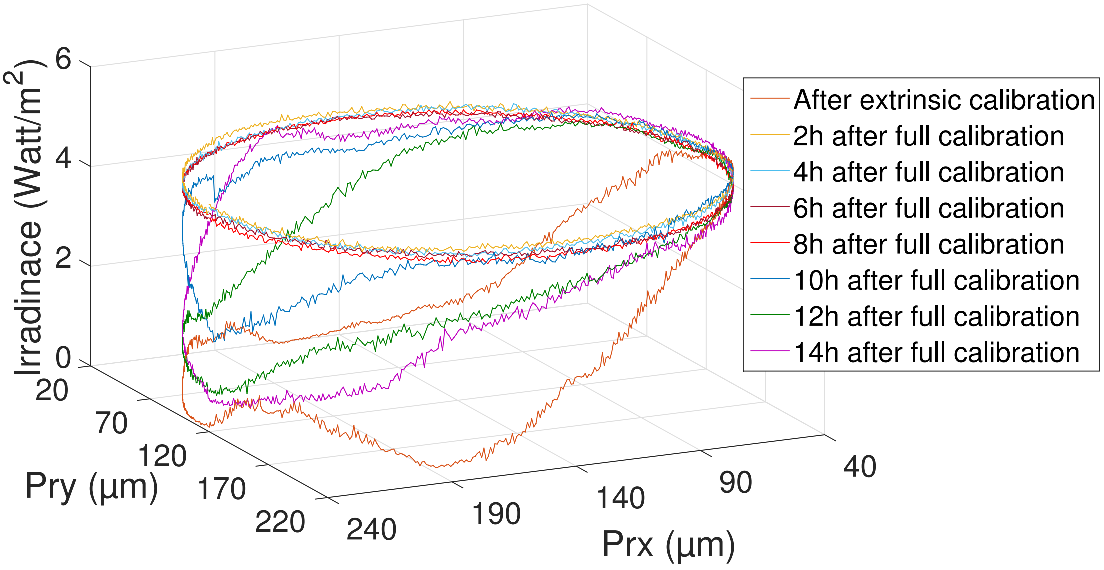

Figure 4.17: Durability evaluation of the calibrated robot extrinsic and intrinsic parameters by applying circular translation on the optical lamella plane every 2 hours for 14 hours.

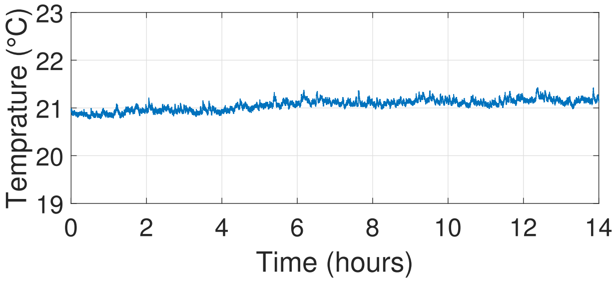

Figure 4.18: Temperature measure for the durability test.

column one of Table 4.3 and Table 4.4 respectively. The second one is realized two days after the full calibration and the obtained identified extrinsic and intrinsic parameters are shown in column two of Table 4.3 and Table 4.5 respectively. From the obtained identified parameters, we can notice that all robot extrinsic parameters change from one day to another and only one intrinsic parameter that changes, which is β_4. θ_6 is dependent to θ_{et}, therefore it can be fixed.

After 7 days from the first full robot calibration, only robot extrinsic parameters calibration is realized, the obtained identified extrinsic parameters are shown in column three of Table 4.3. The obtained optical irradiance which corresponds to the circular translation along the optical lamella plane is highlighted in red color in Figure 4.19. The obtained optical irradiance is not maximum and is not constant, which means that there is small Fabry-Perot cavity variation. Hence, we can conclude that during the 7 days some intrinsic parameters were slightly changing. In order to verify that some intrinsic parameters are changing, a full extrinsic and intrinsic robot parameters is identified one day after (8 days from the first full robot calibration). The obtained identified extrinsic and intrinsic parameters are shown in column four of Table 4.3 and Table 4.6 respectively. The obtained identified parameters prove that some intrinsic parameters are changing slowly with time.

Table 4.3: Identified extrinsic parameters after, 1, 2, 7 and 8 days from the first full robot calibration.

Parameters	After 1 day	After 2 day	After 7 day	After 8 day
β_{et}	$0.781°$	$0.785°$	$0.802°$	$0.811°$
θ_{et}	$-0.615°$	$-0.619°$	$-0.710°$	$-0.702°$
β_{wf}	$0.729°$	$0.725°$	$0.784°$	$0.763°$
θ_{wf}	$-0.561°$	$-0.565°$	$-0.591°$	$-0.561°$
$\mathbb{Z}_{et}$	$1.42\ \mu$m	$1.52\ \mu$m	$2.1\ \mu$m	$2.3\ \mu$m
x_{wf}	$112.9\ \mu$m	$112.3\ \mu$m	$112.4\ \mu$m	$113.1.3\ \mu$m
y_{wf}	$917.2\ \mu$m	$917.8\ \mu$m	$920\ \mu$m	$918.8\ \mu$m
z_{wf}	$115.7\ \mu$m	$116.4\ \mu$m	$113.1\ \mu$m	$112.2\ \mu$m
$^{w}P_{rx}$	$154.8\ \mu$m	$154.4\ \mu$m	$149.2\ \mu$m	$148.7\ \mu$m
$^{w}P_{ry}$	$-3.75\ \mu$m	$-3.61\ \mu$m	$-3.4\ \mu$m	$-3.54\ \mu$m
$^{w}P_{rz}$	$-109.08\ \mu$m	$-109.87\ \mu$m	$-106.54\ \mu$m	$-107.53\ \mu$m

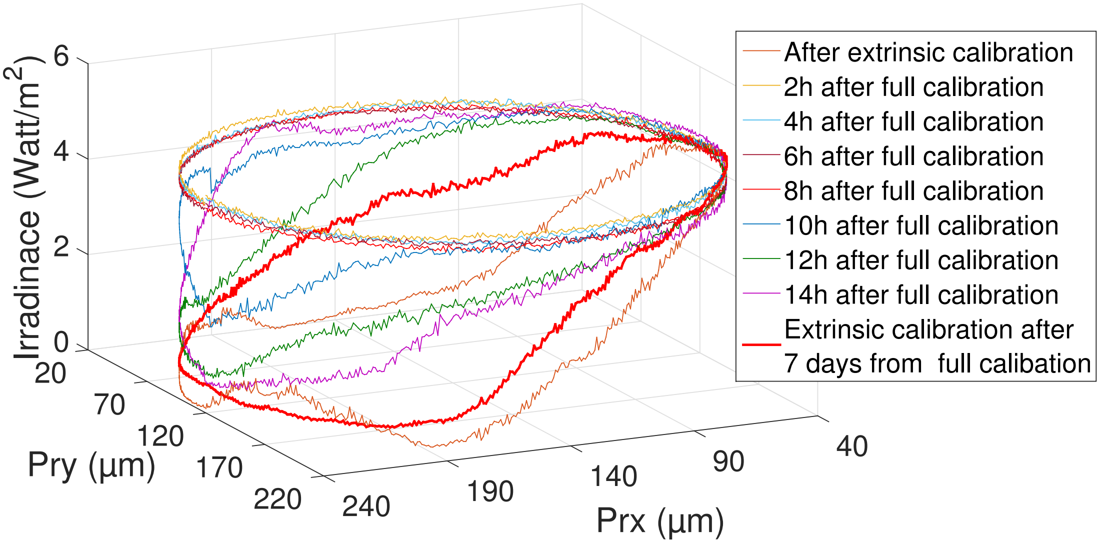

Figure 4.19: The obtained optical irradiance (highlighted in red color) for circular translation on the optical lamella plane for only robot extrinsic parameters calibration, after 7 days from the first full calibration.

Table 4.4: Identified robot intrinsic parameters, one day after the first full robot calibration.

Link	ρ_i	$\beta_i(^\circ)$	$\alpha_i(^\circ)$	d_i (μm)	$\theta_i(^\circ)$	r_i (μm)
1	1	0	0	0	0	q_1
2	1	0	-90.13	0	-89.22	q_2
3	1	0	-90.29	0	-89.47	q_3
4	0	-0.29	0.25	-4.2	$q_4 - 0.07$	0
5	0	0	-89.45	-2.21	$q_5 - 90.49$	0
6	0	0	-90.57	0	$q_6 + 0.16$	0

Table 4.5: Identified robot intrinsic parameters, two days after the first full robot calibration.

Link	ρ_i	$\beta_i(^\circ)$	$\alpha_i(^\circ)$	d_i (μm)	$\theta_i(^\circ)$	r_i (μm)
1	1	0	0	0	0	q_1
2	1	0	-90.13	0	-89.22	q_2
3	1	0	-90.29	0	-89.47	q_3
4	0	-0.30	0.25	-4.2	$q_4 - 0.07$	0
5	0	0	-89.45	-2.21	$q_5 - 90.49$	0
6	0	0	-90.57	0	$q_6 + 0.17$	0

Table 4.6: Identified intrinsic parameters after 8 days from the first full robot calibration.

Link	ρ_i	$\beta_i(^\circ)$	$\alpha_i(^\circ)$	d_i (μm)	$\theta_i(^\circ)$	r_i (μm)
1	1	0	0	0	0	q_1
2	1	0	-90.13	0	-89.22	q_2
3	1	0	-90.29	0	-89.47	q_3
4	0	-0.42	0.29	-4.2	$q_4 - 0.07$	0
5	0	0	-89.38	-2.21	$q_5 - 90.49$	0
6	0	0	-90.57	0	$q_6 + 0.19$	0

In summary, extrinsic and intrinsic calibration can be maintained for about 8 hours, without parameters change. Optical irradiance derivation starts after 10 hours. The optical irradiance derivation is not because of environmental conditions. All robot extrinsic parameters change from one day to another and only one intrinsic parameter that changes, which is β_4. θ_6 is dependent to θ_{et}, so it can be fixed. Therefore, the optical irradiance derivation is because of extrinsic geometric parameters change. Realizing extrinsic parameters calibration after 7 days from full parameters calibration and based on the obtained results, it demonstrates that some intrinsic parameters were changing slowly with time.

4.6/ CONCLUSION

A photo-robotic approach for extrinsic and intrinsic parameters calibration was proposed. A photo-robotic model is proposed that relates a 1-D relative distance with a multi-DOF robot motion in order to identify extrinsic and intrinsic geometric parameters. A dedicated measurement strategy was proposed in order to cover the whole workspace of the robot and to achieve a rich measurement with high accuracy, where the 1-D relative distance measure is achieved based on the high accurate 1-D Fabry-Perot interferometry measure. The approach was validated experimentally and discussed. The durability and the behavior of the calibrated parameters were studied.

After having realized the full robot extrinsic and intrinsic parameters calibration, no Fabry-Perot fringes appears on the optical irradiance for rotations around X_f, Y_f and Z_f axes for different reflection points P_r in the validation phase, neither for square translation along the optical lamella plane. The experimental estimated positioning accuracy is $0.004°$.

Extrinsic and intrinsic calibration can be maintained for about 8 hours, without parameters change. Optical irradiance derivation starts after 10 hours. The optical irradiance derivation is not because of environmental conditions. All robot extrinsic parameters change from one day to another and only one intrinsic parameter that changes, which is β_4. θ_6 is dependent to θ_{et}, so it can be fixed. Therefore optical irradiance derivation is because of a slight extrinsic geometric parameters change. Realizing extrinsic parameters calibration after 7 days from full parameters calibration and based on the obtained results, it demonstrates that some intrinsic parameters were changing slowly with time.

Based on the obtained results, for very high positioning accuracy demand, full robot extrinsic and intrinsic parameters calibration can be realized, with optimal optical performances. For some dedicated applications, calibrating extrinsic parameters appears far enough (0.39 μm).

5

ACTIVE AUTOMATED POLARIZATION CONTROL FOR INTEGRATED OPTICS

Contents

5.1/ INTRODUCTION

In this chapter, we are going to use the photo-robotic system for positioning a birefringent waveplate as compared with a fiber. A birefringent waveplate is a lamella that can change the polarization state of light by inducing a differential delay between the two components of an electric field propagating through it. When the lamella is made of an electro-optic material, the birefringence can be changed through an applied voltage: it becomes a Pockells cell. In other cases, the birefringent plate can just be used to change a linear polarization into another state, that will be further injected in a component: for example it can be a quaterwaveplate at the input of an electro-optical electric field sensor. Hence, producing fibers with birefringent waveplates at their extremities, or at a certain distance of their extremities, is of great interest in many applications, but the positioning of the plate as compared with the fiber is critical for producing the desired polarization. In this chapter, we first remind the reader of several basic features about polarization. We then show how our device can successfully be used to control the polarization states. In order to verify the effect of the lamella position on polarization, a mirror is first used as a reference. Then the polarization states are repeatability investigated. Finally polarization control is investigated based on non-calibrated robot, calibrated robot and calibrated robot with misalignment angle.

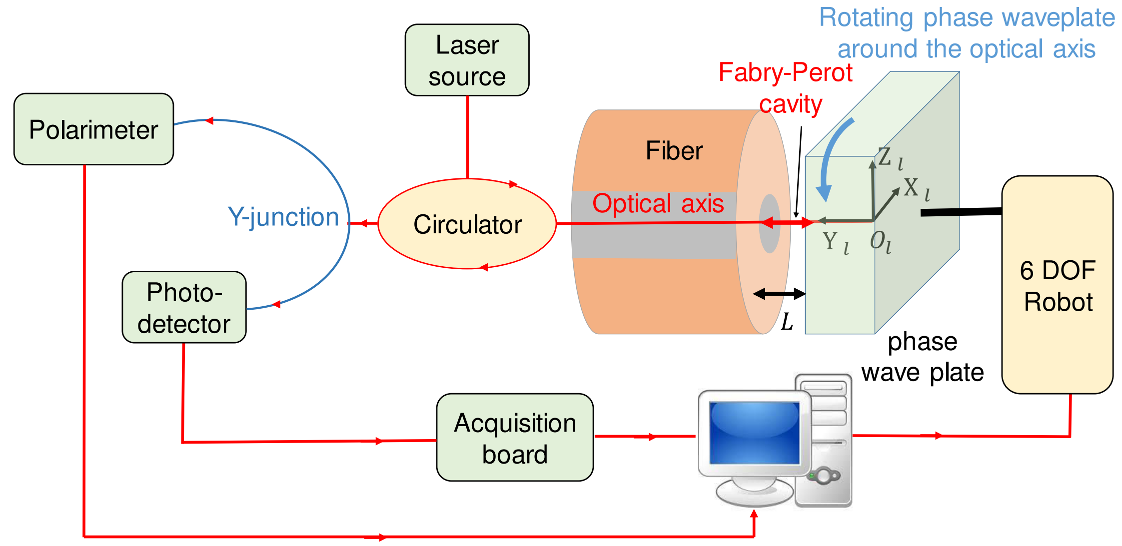

Figure 5.1: Experimental setup for robotic automated polarization control.

5.2/ PROBLEM STATEMENT OF POLARIZATION CONTROL FOR INTEGRATED OPTICS

Various thin birefringent waveplates are being commercialized, dedicated to macro or micro-optic systems (see for example eksmaoptics products). As mentioned above, integrating them with a fiber would open the way to many attractive applications. But to do so, an accurate technique is needed to control their positioning and orientation as compared with the fibers.

To show how our technique can be used for polarization control, we have produced a 5.83 μm-thick $LiNbO_3$ birefringent wave plate which has been attached to our calibrated robot is presented in chapter 4. Rotating the wave plate can produce a polarization change. The challenge is to rotate the wave plate around its optical axis accurately by maintaining the plane of the lamella perpendicular to the optical axis.

For this sake, the experimental setup shown in Figure 5.1 is implemented. The 6 DOF robot presented in chapter four holds the wave plate and control its poses. A laser light source (wavelength λ = 1560 nm) is connected to a circulator and then to a fixed fiber. The circulator is used to separate the emitted light from the reflected light in the fiber. The reflected light irradiance goes to the photo-detector and the polarimeter using optical Y-junction. The polarimeter is used to measure the polarization states, where it is synchronized with Matlab/Simulink platform. The photo-detector is used to measure the optical irradiance, where it acquired with Matlab/Simulink platform.

5.3/ OPTICAL POLARIZATION

To understand the influence of rotation on the optical response, let us first take a look at the possible polarization states.

5.3.1/ THE POLARIZATION ELLIPSE

A plane wave propagating in a given direction in an isotropic medium is polarized only in the transverse plane. Therefore, the electric field E of a monochromatic plane wave of wavelength λ is propagating along the Oz axis as shown in Figure 5.2 is [Born et al., 1999]:

$$\mathbf{E}(z,t) = E_x(z,t) + E_y(z,t) = E_{0x}\cos(wt - kz + \delta_x)\,\mathbf{e}_x + E_{0y}\cos(wt - kz + \delta_y)\,\mathbf{e}_y, \quad (5.1)$$

where E_{0x} and E_{0y} the amplitudes of the two components of the electric field, ω is the angular frequency, k is propagation constant, and δ_x and δ_y are the phases of the components. The phase shift δ $(0 < \delta < 2\pi)$ between the two components E_x and E_y defined as:

$$\delta = \delta_x - \delta_y \quad (5.2)$$

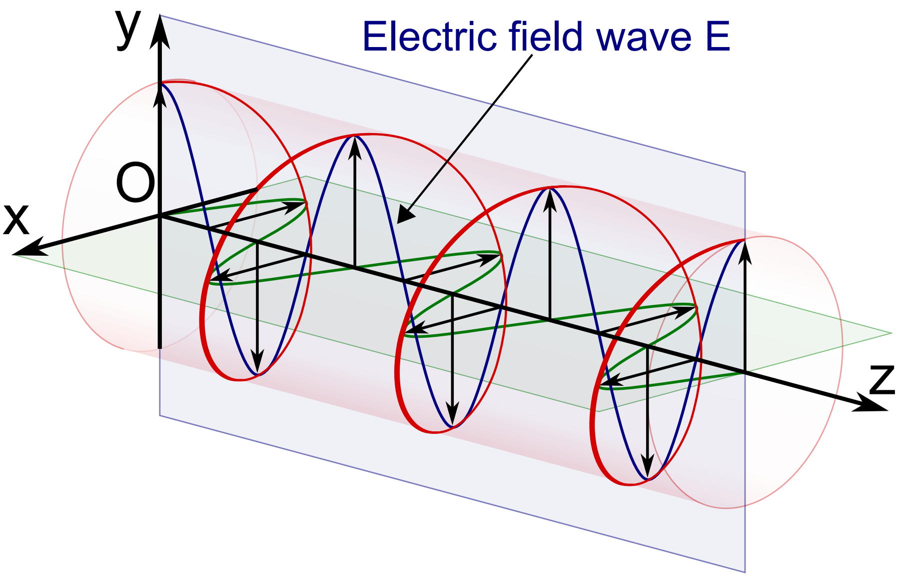

Figure 5.2: The electric field propagation along the Oz axis. [1]

The polarization state of a wave is defined by the curve described by the end of the electrical field vector as a function of time, projected in the plane orthogonal to the direction of propagation. If we eliminate the time dependence ωt between the E_x and E_y components and if we place ourselves for example in the plane $z = 0$, the end of the electric field vector follows a corresponding trajectory to the following equation:

$$\left(\frac{E_x}{E_{0x}}\right)^2 + \left(\frac{E_y}{E_{0y}}\right)^2 - 2\frac{E_x}{E_{0x}}\frac{E_y}{E_{0y}}\cos\delta = \sin^2\delta. \quad (5.3)$$

The wave is depolarized when δ is not determined over time. In the case where δ is constant over time, equation 5.3 corresponds to an ellipse, described in a rectangle of sides parallel to the Ox and Oy and $2E_{0x}$ and $2E_{0y}$ lengths (see Figure 5.3). The wave

---

[1] online image at https://commons.wikimedia.org/w/index.php?curid=9861663

is then elliptically polarized. The direction of path of the end of the electric field vector on the ellipse is related to the parameter δ which is determined by an observer looking in the direction of the source. When the latter looks into the direction of the source, he sees the end of the electric field vector describing an ellipse in the clockwise direction (i.e. $\sin\delta > 0$), the polarization of the wave is called right. On the other hand, when the end of the electric field vector describes an ellipse in a counter-clockwise direction (i. e. $\sin\delta < 0$), the polarization is called left.

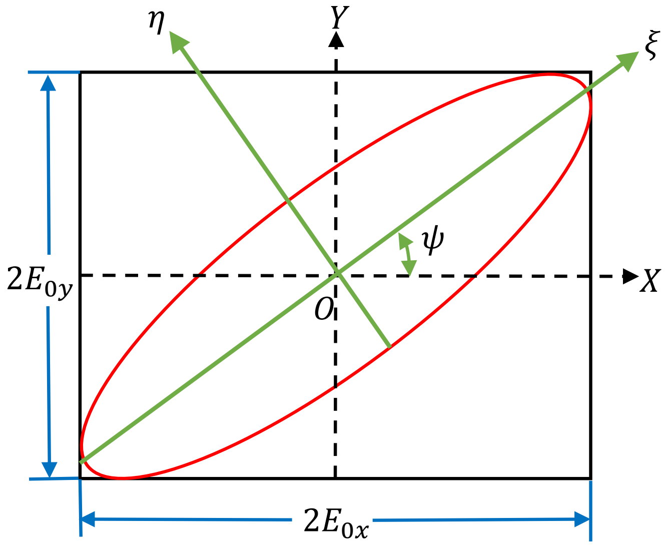

Figure 5.3: Polarization ellipse. Inspired from [Collett, 2003].

The polarization ellipse can be characterized by two other angular parameters: χ and ψ which respectively represent the ellipticity angle ($-pi/4 \leq \chi \leq pi/4$) and the orientation angle ($0 \leq \psi \leq pi$) [Collett, 2003]. These angles can be defined according to the parameters of the polarization ellipse:

$$\begin{cases} \sin 2\chi = 2\frac{E_{0x}E_{0y}}{E_{0x}^2+E_{0y}^2}\cos\delta \\ \\ \tan 2\psi = 2\frac{E_{0x}E_{0y}}{E_{0x}^2-E_{0y}^2}\sin\delta \end{cases}. \tag{5.4}$$

The right-hand side of both of these equations consists of algebraic and trigonometric terms. The two equations can be rewritten completely in trigonometric terms by introducing an angle known as the auxiliary angle α (0$\leq$ α $\leq$ pi/2) defined by the following relationship [Collett, 2003]:

$$\tan\alpha = \frac{E_{0y}}{E_{0x}}. \tag{5.5}$$

This leads to purely trigonometric equations:

$$\begin{cases} \tan 2\psi = (tan2\alpha)cos\delta \\ \sin 2\chi = (sin2\alpha)sin\delta \end{cases} . \tag{5.6}$$

As a conclusion, polarization states depend on the phase shift δ and the ratio $\frac{E_{0y}}{E_{0x}}$.

5.3.2/ MAIN POLARIZATION STATES

According to the values of E_{0x}, E_{0y} and δ, The polarization ellipse can be reduced to a line segment or a circle.

5.3.2.1/ LINEAR POLARIZATION

The polarization state of the wave is linear when $\delta = m\pi$ with ($m = 0, \pm 1, \pm 2, \ldots$). The equation 5.3 can then be written by:

$$\frac{E_y}{E_x} = (-1)^m \frac{E_{0y}}{E_{0x}}. \tag{5.7}$$

The ellipse is reduced to a line segment and the electric field **E** oscillates along an inclined line of the angle α with respect to the reference frame (**e**$_x$, **e**$_y$).

When $E_{0y} = 0$ ($\alpha = 0$), the electric field **E** oscillates only along the Ox axis. The light is called linearly polarized along the Ox axis and called horizontally polarized light (LHP, linearly horizontal polarized light). On the other hand, when $E_{0x} = 0$ ($\alpha = \pi/2$), it is called vertically polarized light (LVP, linearly vertical polarized light).

When $\delta = 0$ or π, The equation 5.3 can be reduced to:

$$E_y = \pm \frac{E_{0y}}{E_{0x}} E_x, \tag{5.8}$$

which corresponds to line equation of a slope of $\pm\frac{E_{0y}}{E_{0x}}$. When $E_{0y} = E_{0x}$ ($\delta = 0$ and $\alpha = \pi/4$), the slope is positive and the light is said linearly polarized at $45°$(L+45P, linear $45°$ polarized light). Similarly, if $E_{0y} = -E_{0x}$ ($\delta = \pi$ and $\alpha = -\pi/4$),the slope is negative and the light is said linearly polarized at $-45°$(L-45P, linear $-45°$ polarized light).

5.3.2.2/ CIRCULAR POLARIZATION

The polarization ellipse is reduced to a circle if $E_{0y} = E_{0x} = E_0$ and $\delta = m\pi/2$ ($m = \pm 1, \pm 3, \pm 5, \ldots$). The equation 5.3 can then be written by:

$$\left(\frac{E_x}{E_{0x}}\right)^2 + \left(\frac{E_y}{E_{0y}}\right)^2 = 1, \tag{5.9}$$

which corresponds to the equation of a circle. Under these conditions, the light is said to be polarized circularly. When $\sin\delta > 0$ is positive, the polarization of the wave is called right circular (RCP, right circularly polarized light). On the other hand, when $\sin\delta < 0$, the polarization is said to be circular left (LCP, left circularly polarized light).

These six polarization states are called degenerate states of polarization.

So far, we have seen that three independent parameters (amplitudes E_{0x} and E_{0y} and the phase difference δ) were required to characterize the polarization ellipse. However, only the intensities are directly measurable in the optical domain. During his work on partially polarized light, Sir G. G. Stokes introduced four dimensionless real quantities in 1852, to represent the polarization states of light [Stokes, 1851].

5.4/ OPTICAL POLARIZATION REPRESENTATION

5.4.1/ STOKES PARAMETERS

By multiplying the equation 5.3 by $4E_{0x}^2 E_{0y}^2$ and by taking the average value, we obtain the following equation:

$$4E_{0y}^2 \left\langle E_x^2(z,t) \right\rangle + 4E_{0x}^2 \left\langle E_y^2(z,t) \right\rangle - 8E_{0x}E_{0y} \left\langle E_x^2(z,t)E_y^2(z,t) \right\rangle \cos\delta = (2E_{0x}E_{0y}\sin\delta)^2, \tag{5.10}$$

where the average values of the different terms in equation 5.10 are:

$$\left\langle E_x^2(z,t) \right\rangle = \frac{1}{2}E_{0x}^2 \tag{5.11}$$

$$\left\langle E_y^2(z,t) \right\rangle = \frac{1}{2}E_{0y}^2 \tag{5.12}$$

$$\left\langle E_x^2(z,t)E_y^2(z,t) \right\rangle = \frac{1}{2}E_{0x}, E_{0y}\cos\delta \tag{5.13}$$

this gives:

$$2E_{0x}^2E_{0y}^2 + 2E_{0x}^2E_{0y}^2 - (2E_{0x}E_{0y}\cos\delta)^2 = (2E_{0x}E_{0y}\sin\delta)^2. \tag{5.14}$$

By adding and subtracting the term $E_{0x}^4 + E_{0y}^4$ in the left side, we can rewrite equation 5.3 as follows:

$$(E_{0x}^2 + E_{0y}^2) - (E_{0x}^2 - E_{0y}^2) - (2E_{0x}E_{0y}\cos\delta)^2 = (2E_{0x}E_{0y}\sin\delta)^2. \tag{5.15}$$

From this equation, it is possible to write the Stokes parameters in the following form:

$$\begin{cases} S_0 = E_{0x}^2 + E_{0y}^2 \\ S_1 = E_{0x}^2 - E_{0y}^2 \\ S_2 = 2E_{0x}E_{0y}\cos\delta \\ S_3 = 2E_{0x}E_{0y}\sin\delta \end{cases} . \tag{5.16}$$

The parameter S_0 represents the total intensity of the light beam, parameter S_1 describes the quantity of light of horizontal or vertical linear polarization, parameter S_2 describes the amount of linear polarization light at $45°$ or $-45°$, parameter S_3 describes the amount of light from right or left circular polarization contained in the light beam. The four parameters of Stokes written in the form of a column matrix build up the Stokes vector [Huard, 1993]:

$$\begin{bmatrix} S_0 \\ S_1 \\ S_2 \\ S_3 \end{bmatrix} = \begin{bmatrix} E_{0x}^2 + E_{0y}^2 \\ E_{0x}^2 - E_{0y}^2 \\ 2E_{0x}E_{0y}\cos\delta \\ 2E_{0x}E_{0y}\sin\delta \end{bmatrix} = \begin{bmatrix} I_0 + I_{90} \\ I_0 - I_{90} \\ I_{45} + I_{-45} \\ I_R + I_L \end{bmatrix}, \tag{5.17}$$

where $I_0, I_{90}, I_{45}, I_{-45}$ correspond to intensities measured using a power meter placed behind a linear polarizer oriented at 0°, 90°; 45°, -45° and behind a right and left circular polarizer. The Stokes vector is often normalized to the S_0 component. Stokes vectors of six degenerate polarization states mentioned above can thus be expressed as follows:

$$\{S_0, S_{90}, S_{45}, S_{-45}, S_R, S_L\} = \left\{ \begin{pmatrix} 1 \\ 1 \\ 0 \\ 0 \end{pmatrix}, \begin{pmatrix} 1 \\ -1 \\ 0 \\ 0 \end{pmatrix}, \begin{pmatrix} 1 \\ 0 \\ 1 \\ 0 \end{pmatrix}, \begin{pmatrix} 1 \\ 0 \\ -1 \\ 0 \end{pmatrix}, \begin{pmatrix} 1 \\ 0 \\ 0 \\ 1 \end{pmatrix}, \begin{pmatrix} 1 \\ 0 \\ 0 \\ -1 \end{pmatrix} \right\}, \tag{5.18}$$

where S_0 represents a linear polarization parallel to the angular reference axis, S_{90} represents a polarization orthogonal to this reference axis, $S45$ and $S{-45}$ of the linear polarizations at $45°$ respectively and $-45°$ of the reference axis and S_R and S_L the right and left circular polarization states.

From equation 5.15, we can deduce the relationship between Stokes components of a polarized wave as:

$$S_0^2 = S_1^2 + S_2^2 + S_3^2. \tag{5.19}$$

The normalized Stokes vector with respect to the S_0 component can be expressed as a function of angular parameters χ and ψ.

We obtain:

$$\begin{cases} S_1 = S_0\cos(2\chi)\cos(2\psi) \\ S_2 = S_0\cos(2\chi)\sin(2\psi) \\ S_3 = S_0\sin(2\chi) \end{cases} . \tag{5.20}$$

5.4.2/ POINCARÉ SPHERE

The normalized Stokes vector with respect to the S0 component can be represented by a point P on a sphere of unit radius, called the Poincaré sphere (Figure 5.4) [Poincaré, 1892]. On the sphere, longitudes represent the orientation angle and latitudes, ellipticity angle . In coordinates a state of polarization is identified by the components (S_1, S_2, S_3) from the vector of Stokes. In spherical coordinates, a polarization state is indicated by the ellipticity angles χ and orientation ψ.

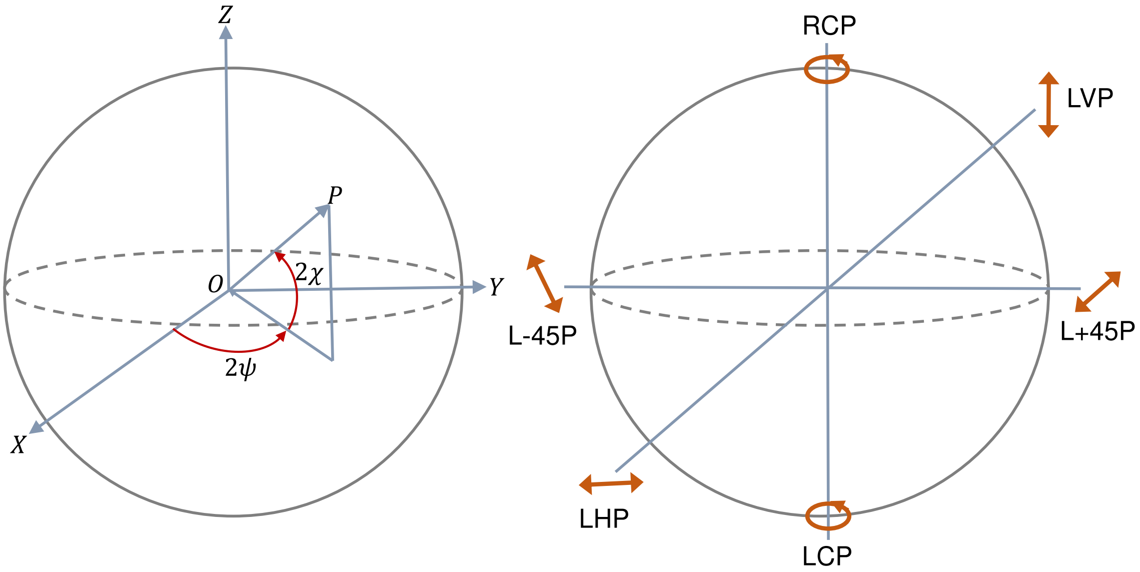

Figure 5.4: (left) Poincaré sphere and (right) Degenerated states of the elliptical polarization state on the sphere of Poincaré. Inspired from [Collett, 2003] .

The equator represents all linear polarizations ($\chi = 0$). The poles represent the circular polarizations ($\psi = pi/4$ and $\chi = pi/4$). Any point that is not located on the equator or at the poles of the sphere is the image of a state of elliptical polarization. When point P is located in the northern hemisphere, the ellipticity angle χ is positive and it is the image of a state of right polarization. Conversely, it is the image of a left polarization state when the ellipticity angle χ is negative [Huard, 1993].

On the sphere, the polarized light is represented by a point (Figure 5.5(a)). When the light is natural or depolarized, it contains all polarization states and therefore all points are equiprobable (Figure 5.5(b)). When the light is partially polarized, the points are more or less grouped around a single point which is the maximum probability point of the state of polarization (Figure 5.5(c)). The narrower the width of this distribution, the more light will feature as a polarized light characterized by the single point [Huard, 1993].

The Poincaré sphere is a very useful tool to evaluate the polarization states of a given optical beam: in what follows, we will use it to assess the performance of our robotic system.

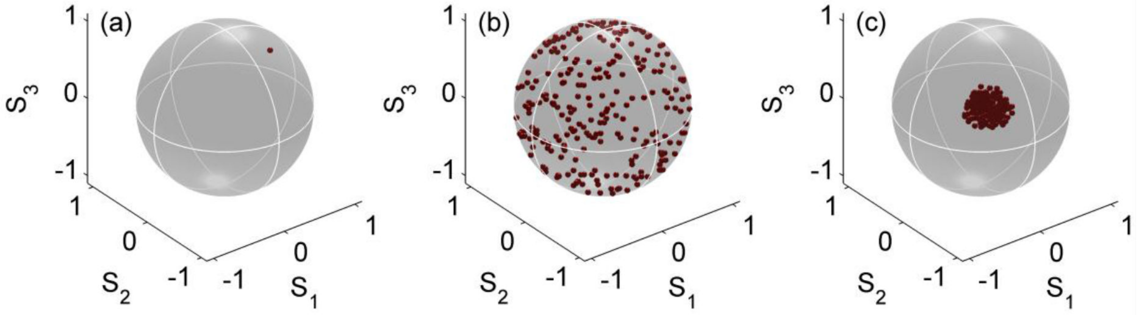

Figure 5.5: Representation of the different types of light on the Poincaré sphere (a) polarized light, (b) depolarized light and (c) partially polarized light [Morin, 2013] .

5.5/ OPTICAL POLARIZATION CONTROL

5.5.1/ BIREFRINGENT CRYSTALS

When light passes through a transparent material like a crystal, it interacts with the atoms in the material structure. Consequently, the speed of light inside the crystal becomes slower than that in air or vacuum. The speed v changes oppositely with the refractive index n of the crystal. That is $v = c/n$. The larger the refractive index, the more the light is retarded. The amount of phase retardation (or delay) δ that a monochromatic wave undergoes from traveling through the crystal is related to its speed (refractive index), wavelength, and the path length L inside the crystal [Hecht, 2014].

$$\delta = \frac{2p}{\lambda} nL \qquad (\delta \text{ in radians}). \tag{5.21}$$

The simplest category of crystals are those with cubic symmetry. In a cubic crystal, all 3 crystallographic directions or axes are equivalent. $n_x = n_y = n_z$, and the crystal is optically isotropic. Disregarding of how the light is polarized at the input of the crystal, it will experiment the same refractive index and phase delay. In other words, the polarization state remains unchanged after traversing through an isotropic crystal [Hecht, 2014].

However, there exists another interesting category of crystals that show asymmetric (or anisotropic) optical properties. They are called birefringent crystals. One birefringent type is uniaxial, meaning that one crystal axis is different from the other two: $n_x \neq n_y = n_z$. Common uniaxial crystals of optical quality are quartz, calcite and MgF_2. The single crystal axis that is unique is often called the “extraordinary” axis, and its associated refractive index is labeled n_e, while the other two axes are “ordinary” axes with index n_0 [Peatross et al., 2011].

5.5.2/ WAVE PLATES AND APPLICATIONS

Birefringent wave plates, or retardation plates, are very advantageous for applications where we want to synthesize and analyze light of different polarization states. For example, a quarter-wave plate can convert an input light beam from linear polarization to circular (or elliptical) polarization and vice versa. A half-wave plate can continuously adjust the polarization angle of a linearly-polarized beam. With just these two types of wave plates, an optical isolator, a variable attenuator, or a variable-ratio beam splitter can be built [Huard, 1997].

A wave plate is simply a cut and polished slice of uniaxial crystal. The plane of the slice contains the extraordinary axis. An input light beam that is normally incident on the wave plate will be resolved into ordinary and extraordinary axis components, each with a different refractive index. The beam that emerges has a phase-delay difference or retardation between the axes of [Hecht, 2014] :

$$\delta = \frac{2p}{\lambda}(n_e - n_0)L \qquad (\delta \textit{ in radians}). \tag{5.22}$$

If we choose the wave plate of thickness L so that the retardation corresponds to $\pi/2$ radians (or $90°$), then it is called a quarter-wave plate.

A phase shift of $\delta = \pi/2$ will convert linearly polarized light to circular and vice versa.

Half-wave plates have π radians (or $180°$) of retardation. A retardation of $\delta = \pi$ will flip linearly polarized light. If the incoming beam is at an angle θ with respect to the fast axis, the light will be flipped by 2θ around the fast axis [Hecht et al., 2001] [Huard, 1997] .

However, all these theoretical results are based on the hypothesis that the incident optical beam is orthogonal with the plane of the waveplates, which can be translated in optical vocabulary by saying that the incident wave is normal to the birefringent plate. A change in the incident angle will change the effective thickness seen by the wave and consequently the polarization state. And this is all the more true in reflection mode, where the beam reflects on the back face of the waveplate. In this case, the propagation length in indeed twice the plate thickness, so that the influence of the incident angle is also enhanced. The influence of the angle upon the polarization state is not that easy to obtain. One can refer to [Huard, 1993] for further details. It is however obvious that the thicker the plate, the larger the influence of the incide,t angle upon the polarization state.

5.5.3/ FABRICATED WAVE PLATE FOR EXPERIMENTAL INVESTIGATION

For the sake of illustration, we have produced a $5.83\ \mu$m thin plate through the lapping and polishing of birefringent X-cut $LiNbO_3$ wafers. These thin plates were then diced into $300\ \mu$m wide squares by means of a circular precision saw, as described in reference [Guyot et al., 2014] and as schematically depicted in figure. 5.6 (a). A corresponding SEM view of one optical component (thin plate) is depicted in Figure 5.6 (b).

When rotated around its X-axis, the wave plate is expected to show a constant phase shift (phase difference) between the two electric field components in plane axis. It is also expected to change the reflected polarization state, by changing the ratio E_{0x}/E_{0y} between the input electric field components. This is what we are going to verify with our bench.

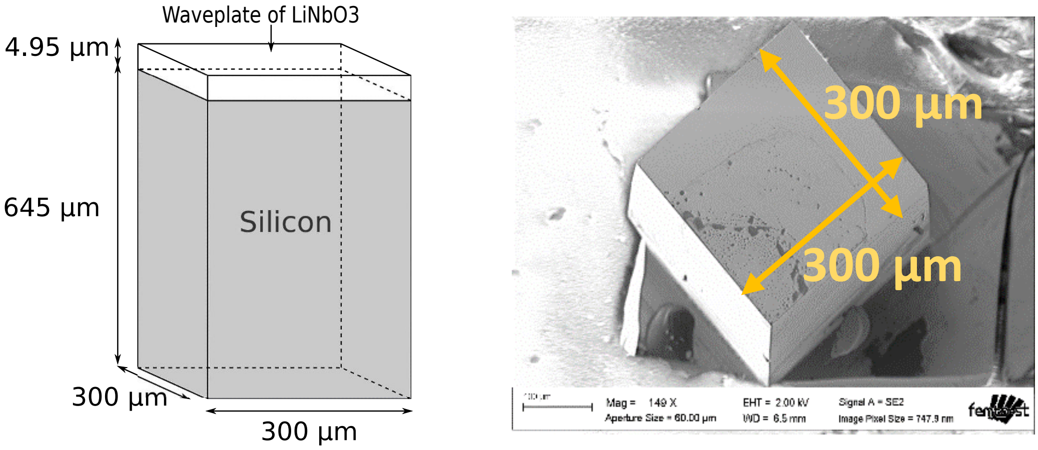

(a) (b)

Figure 5.6: (a) Optical wave plate model, (b) A SEM image of one Optical wave plate dedicated for the experimental investigation.

5.6/ EXPERIMENTAL RESULTS AND DISCUSSIONS

The experimental setup shown in Figure 5.1 is realized. The laser power is adjusted to 2 Watts. First, a mirror is mounted on the robot, then a step rotation of 2° from 0° to 46° is applied as shown in Figure 5.7, the reflected polarization state measure is realized for each step rotation. The obtained reflected polarization states for all rotation steps are shown on the Poincaré sphere in Figure 5.8. From the obtained results, we can notice that there is no polarization state modification for each rotation step, which is expected since the mirror is optically isotropic and light beam experiences the same refractive index and phase delay for whatever input polarization. Therefore, any polarized light, aside from accumulating a constant phase delay, remains unchanged, before and after rotation for calibrated robot or non-calibrated.

The same experiment is realized but, this time, the mirror is replaced with a phase wave plate, which is mounted first on a non-calibrated robot. Then, a step rotation of 2°, from 0° to 46° is applied, the polarization state measure is realized for each rotation step. The obtained polarization states for all rotation steps are shown on the Poincaré sphere in Figure 5.9. Each blue ball corresponds to a polarization state associated to a rotation state. The letter A corresponds to 0° and the letter B corresponds to 46°.

We can see in Figure 5.9 that in the case where the robot is not calibrated, the polarization state changes, but the changes are extremely difficult to interpret. This is due to the fact that the light beam is not aligned with the optical axis. In this case, when the wave plate is rotated, the incident angle changes with rotation, and this induces complex polarization variations.

Then, the robot is fully calibrated as explained and shown in chapter 3 and 4. After the same rotation is applied (a step rotation of 2° from 0° to 46°).The obtained polarization states for all rotation steps are shown on the Poincaré sphere in Figure 5.10. The obtained results demonstrate that, rotating the phase wave plate provides many different polarization states, the distribution of polarization states from state A to state B for a non-calibrated robot is random and non-expected, where after full robot calibration (accurate rotation around the optical axis and without misalignment angle), the distribution of polar-

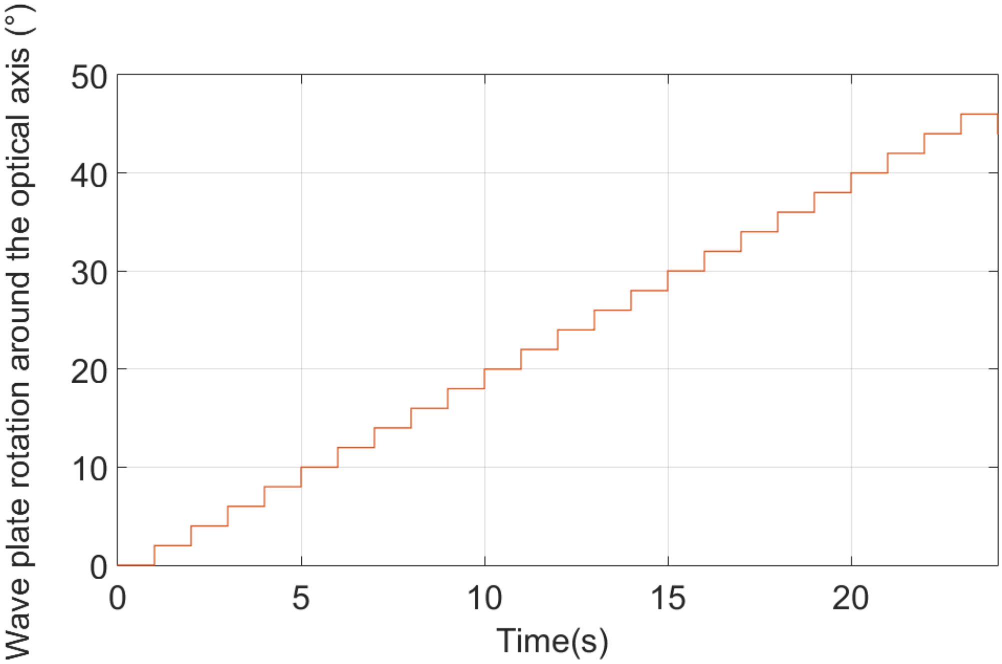

Figure 5.7: Wave plate rotation around the optical axis with a step rotation of 2°, from 0° to 46°. .

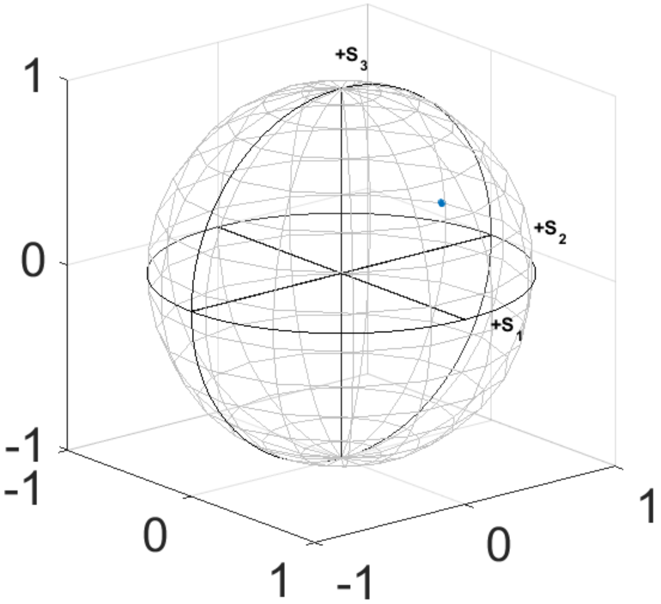

Figure 5.8: (left) Reflected polarization states distribution from a mirror for a step rotation of 2°, from 0° to 46°.

ization states from state A to state B is almost circular with almost the same normalized Poincaré sphere diameter. This is in full agreement with the theoretical models. Indeed, if the light beam is aligned with the optical axis, then only the ratio E_{0x}/E_{0y} changes when rotating the wave plate, which is expected to lead to a circle on the Poincaré sphere.

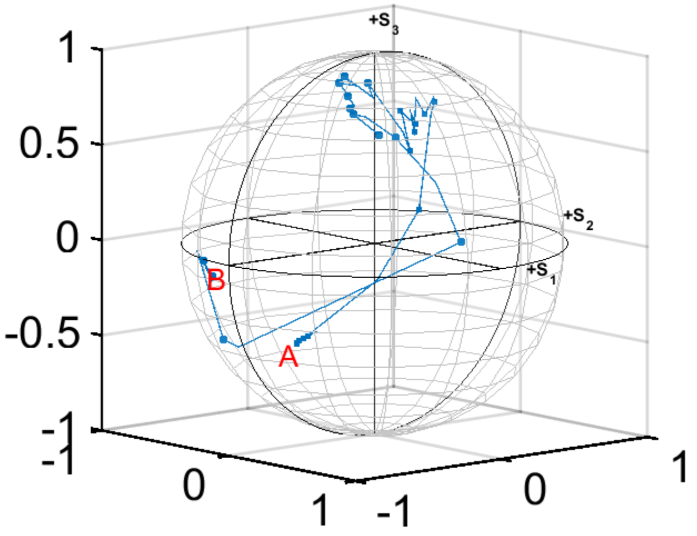

Figure 5.9: (left) Reflected polarization states distribution from a phase wave plate for a step rotation of 2°, from 0° to 46° before robot calibration.

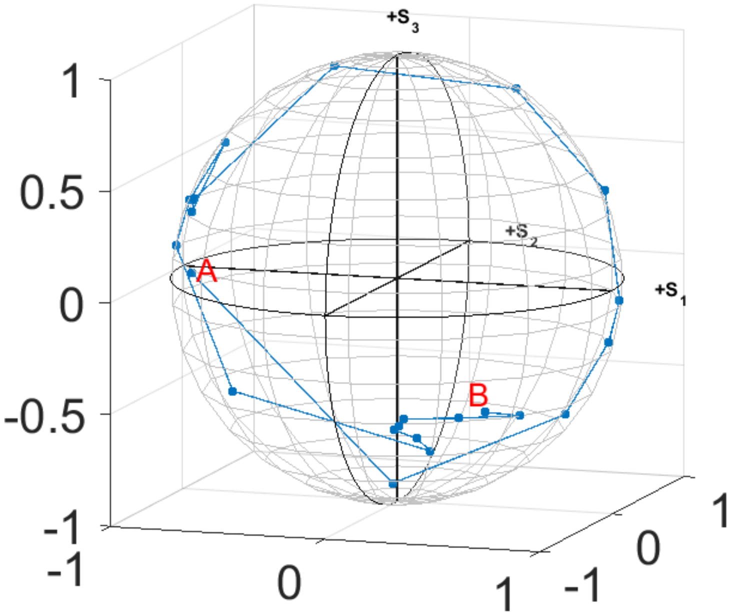

Figure 5.10: (left) Reflected polarization states distribution from a phase wave plate for a step rotation of 2°, from 0° to 46° after robot calibration.

The next experiment is the same as before, but in this case, a misalignment angle of 2° is applied, the obtained results are shown in Figure 5.11. Then a misalignment angle of 4° is applied, the obtained results are shown in Figure 5.12. From the obtained results, we can notice that as the misalignment angle increases, the diameter of circular envelope of polarization states decreases, which confirms that angular misalignments leads to polarization information loss.

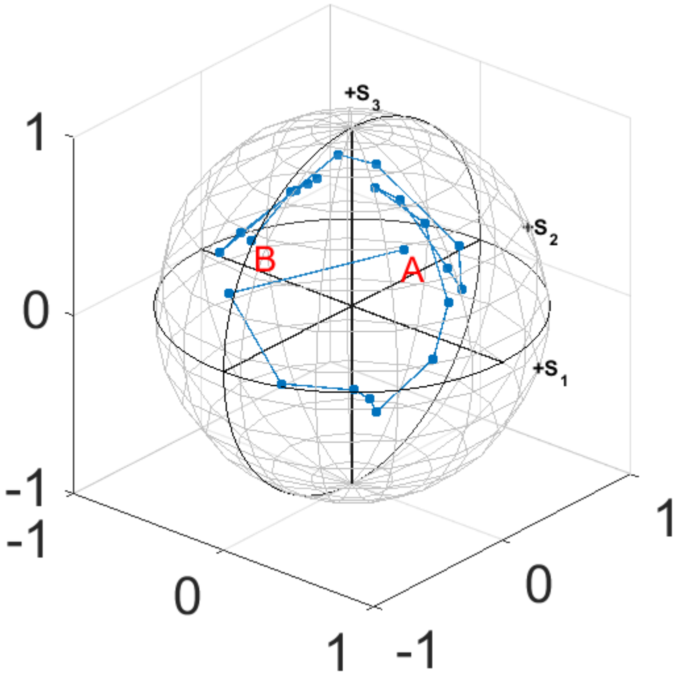

Figure 5.11: (left) Reflected polarization states distribution from a phase wave plate for a step rotation of 2°, from 0° to 46° after robot calibration with 2° of misalignment angles.

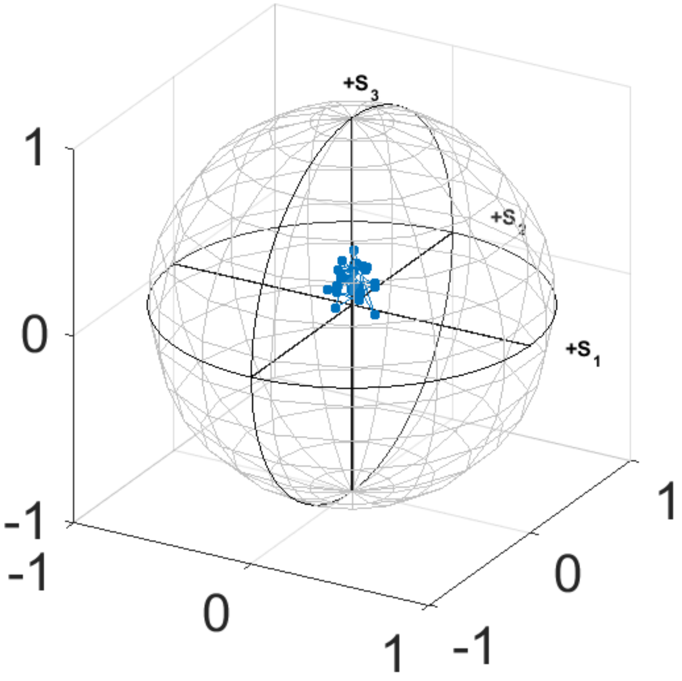

Figure 5.12: (left) Reflected polarization states distribution from a phase wave plate for a step rotation of 2°, from 0° to 46° after robot calibration with 4° of misalignment angles.

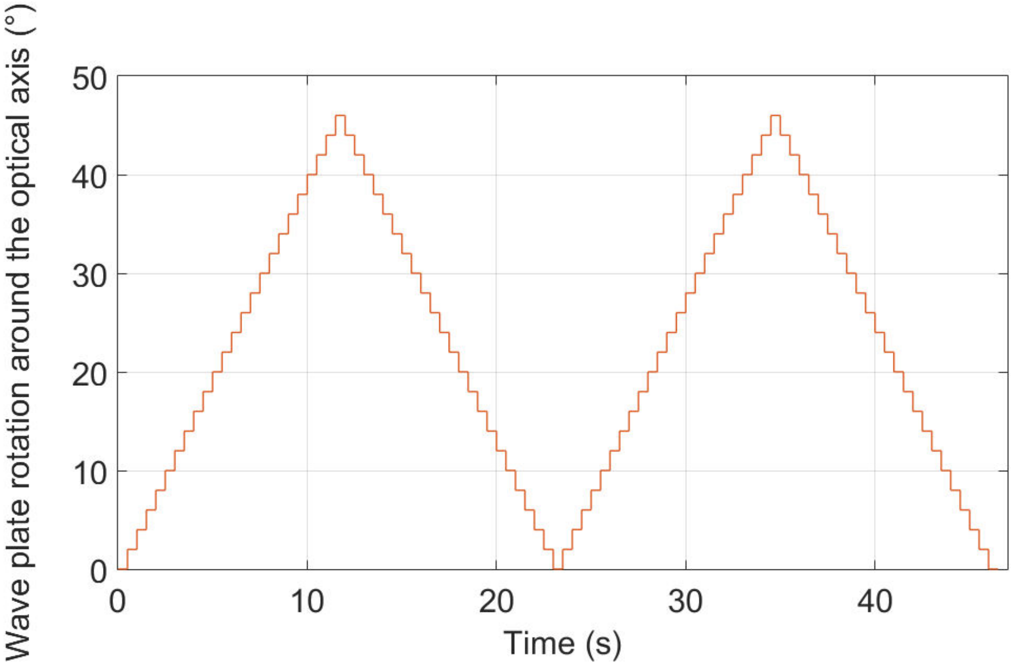

Figure 5.13: Two forward and two backward rotations of 46° of the wave plate around the optical axis . angle with step rotation of 2°.

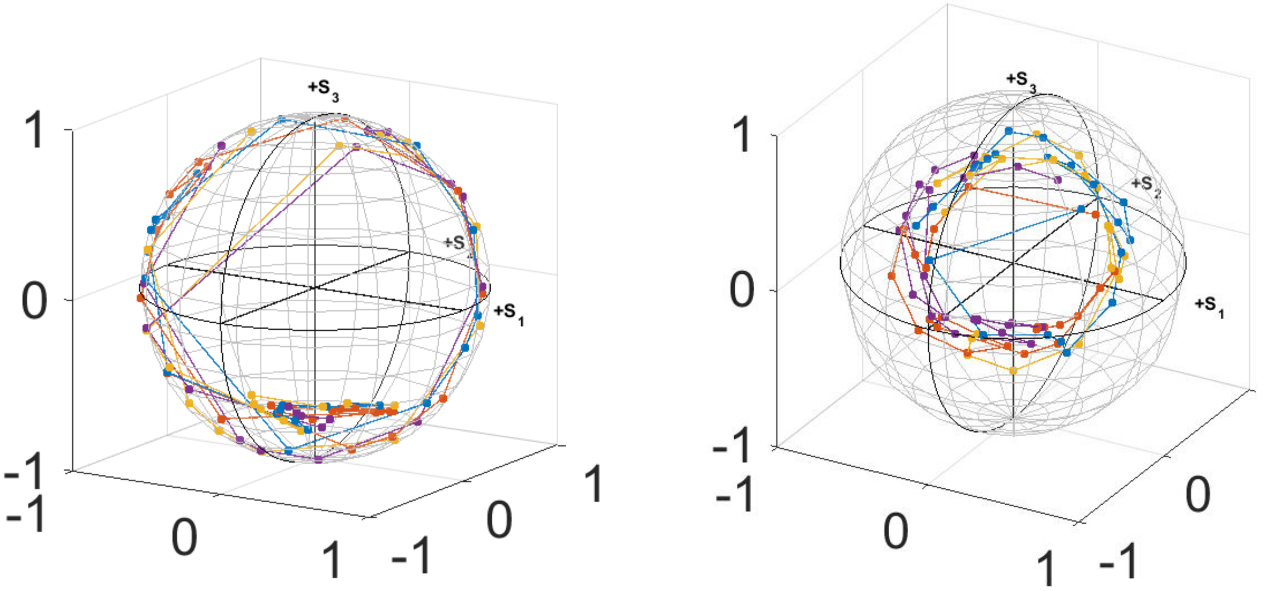

Figure 5.14: (left) Repeatability investigation of the reflected polarization states distribution from a phase wave plate for two forward and two backward rotations of 46° with a step rotation of 2° after robot calibration. (right) Repeatability investigation of the reflected polarization states distribution from a phase wave plate for two forward and two backward rotations of 46° with a step rotation of 2° after robot calibration with 2° of misalignment angles.

In order to investigate the repeatability of the polarization states, 4 rotations of 46° were applied with a step rotation of 2°, two forward rotations and two backward rotations as shown in Figure 5.13, for each step rotation a polarization state is measured. The obtained result is shown in Figure 5.14. The obtained results show a good repeatability of the circular distribution of the polarization states.

In summary, we have developped preliminary results showing first that, as expected, a rotating mirror has no effect on the reflected polarization states, and that rotating a wave plate mounted on a non-calibrated robot results in unexpected distribution of the reflected polarization states. After full robot calibration, a circular distribution of the reflected polarization states is observed. Introducing a misalignment angles leads to polarization information loss, which confirms the significant influence of incidence angle upon the reflected polarization state. The repeatability investigation showed a good repeatability of the circular distribution of the polarization states.

5.7/ CONCLUSION

Integrated thin birefringent plates controlling the polarization state of a light beam represent a promising alternative to conventional integrated birefringent waveguides, which are more than 1 mm long, and not convenient for compact photonic integrated circuits.

Our promising approach relies on high accurate rotation of the wave plate around the optical axis. The wave plate is attached to a calibrated robot. Rotating the wave plate produces a polarization change, due to the variable projection of the incident electric field on the crystal axis of the plate.

Different investigations were realized. Rotating a mirror around the optical axis showed with no surprise that it has no effect on the reflected polarization states. Then, rotating a wave plate around the optical axis mounted on a non-calibrated robot resulted in an unexpected distribution of the reflected polarization states. After full robot calibration, rotating a wave plate around the optical axis gave a circular distribution of the reflected polarization states on the Poincaré sphere. Introducing a misalignment angles leads to polarization information loss, with the same circular distribution of the polarization states. This is in full agreement with the theoretical models. Indeed, if the light beam is aligned with the optical axis, then only the ratio E_{0x}/E_{0y} changes when rotating the wave plate, which is expected to lead to a circle on the Poincaré sphere. Then, if the incident angle increases, the reflected light is not entirely collected by the fiber, leading to a progressive loss in the polarization control. The repeatability investigation showed a good repeatability of the circular distribution of the polarization states.

GENERAL CONCLUSION AND FUTURE WORKS

Realizing fast, automated 3D complex tasks of micro-manipulation and micro-assembly with very high accuracy is an ultimate goal in many application fields, such as advanced integrated optics manufacturing. Many emerging industrial on-demand applications made the field of integrated optics particularly challenging. The hybrid integration of individual photonic elements appears as promising, because it may provide high performances, propose new optical functionalities and products and exploit new propagation modes of light beams. This approach requires an accurate multi Degree-Of-Freedom (DOF) positioning of the individual photonic elements. Hence, the inaccurate multi-DOF measurement and robots control are the main locks to overcome, notably at the micro-scale. For this sake, the integrated optics is chosen as the targeted field of application for the PhD thesis, to achieve high accurate robotic multi-DOF positioning of optical components.

Contributions of the work

In the following, the contributions of our work are detailed by each chapter.

In chapter 2, conventional active alignment usually uses a non-referenced motion of the positioning system holding the optical component, in order to search the maximum irradiance. This produces Fabry-Perot cavity variation along the optical axis due to different coupled parameters modifications at the same time. As a result, it is difficult to analyze the source of this Fabry-Perot cavity variation, which leads to three main drawbacks: time consuming especially for multi-DOF positioning process to reach maximum irradiance, local maximum problem and the alignment task success relies on human expertise. In order to overcome the conventional active alignment drawbacks and to propose high accurate automated robotic 6-DOF positioning, a photo-robotic approach was proposed. The originality of the approach relies on multi-DOF robot motions associated with the use of 1-D Fabry-Perot interferometry measure, to realize multi-DOF pose measure. The approach is based on the correlation between the Fabry-Perot interferometry figure and a multi-DOF referenced nano-positioner motion. This correlation enables to identify the parameters inducing the FP cavity variation by applying a robotic referenced motion. Using the photo-robotic approach, rotational measurements are realized with an uncertainty based on standard deviation of 0.0021°, and translational measurements with an uncertainty based on standard deviation of 27.6 nm. In order to guarantee the maximum optical irradiance, the photo-robotic approach is also used. The first optical irradiance peak before contact has to be attained. Therefore, the contact detection is required in order to reach the optimal maximum optical irradiance. A new approach for contact detection based on Fabry-Perot interferometry is proposed. Contact detection realizes a high accurate contact detection with an error of $\epsilon = 80$ nm.

In chapter 3, it is demonstrated that the influence of geometric parameters are predominant. In order to achieve high positioning accuracy, these geometric parameters need to be identified and compensated through robotic calibration process. The discussed literature review about geometric calibration at macro-scale proved the effectiveness of relative distance calibration method to improve the robot end-effector positioning accuracy. However, measurement at the micro-scale is a very challenging issue in robot calibration. Micro-scale measurement requires sensing devices with high resolution (e.g., a few nanometers) and accuracy (e.g., tens of nanometers), because motion and errors in this scale are very small. In order to overcome the micro-scale measurement issue, some researchers investigated robot calibration for micro-scale applications based on different measurement strategies and calibration approaches. Based on their work, the highest positioning accuracy was achieved with less number of DOF and simple realized tasks, once the number of DOF or the task complexity increase the positioning accuracy decreases. In order to overcome the measurement step at micro scale, we have proposed to use Fabry-Perot interferometry measure, which is very accurate. This led to develop a photo-robotic approach for extrinsic parameters calibration for 6-DOF robot. The photo-robotic approach relates a 1-D relative distance with a multi-DOF robot motion in order to identify extrinsic geometric parameters. A photo-robotic platform dedicated for optical components 6-DOF nano-positioning and assembly was proposed. Applying the proposed photo-robotic approach for extrinsic parameters calibration improved considerably the positioning accuracy. We have achieved a Fabry-Perot cavity variation of about 0.39 μm during a square translations of (100 $\times$100) μm. And we have also achieved a Fabry-Perot cavity variation of about 1.56 μm for a rotation range of 6° around X_f and Y_f and of about 0.858 μm for a rotation range of 45.5° around Z_f. But, the existing Fabry-Perot cavity variation during positioning is supposed to be because of the non calibration of intrinsic parameters of the robot.

In chapter 4, due to the existence of Fabry-Perot cavity variation during positioning after calibrating extrinsic parameters of the robot, a photo-robotic approach for extrinsic and intrinsic parameters calibration was proposed. A photo-robotic model is proposed that relates a 1-D relative distance with a multi-DOF robot motion in order to identify extrinsic and intrinsic geometric parameters. A dedicated measurement strategy was proposed in order to cover the whole workspace of the robot and to achieve a rich measurement with high accuracy, where the 1-D relative distance measure is achieved based on the high accurate 1-D Fabry-Perot interferometry measure. The approach was validated experimentally and discussed. The quantification and durability analysis of optical and robotic performances are investigated. The estimated positioning accuracy of the robot is about $0.004°$. Extrinsic and intrinsic calibration can be maintained for about 8 hours, without parameters change. Optical irradiance deviation starts after 10 hours. The optical irradiance deviation is not due to the environmental conditions. All robot extrinsic parameters change from one day to another and only one intrinsic parameter that changes. Therefore optical irradiance deviation is because of extrinsic geometric parameters change. We realized extrinsic parameters calibration after 7 days from the full parameters calibration, and based on the obtained results, it demonstrates that some intrinsic parameters were changing slowly in time. For very high positioning accuracy demand, full robot extrinsic and intrinsic parameters calibration can be realized, to get optimal optical performances. For less positioning accuracy demand for some dedicated application, only extrinsic parameters calibration is satisfying.

In chapter 5, integrating devices after having controlled and manipulated the polarization state of a light beam represents a promising alternative to conventional lithographic technologies. Conventional lithographic technologies use very long (> 1 mm) integrated birefringent waveguides for polarization state modification, which is bulky and not convenient for the production of compact photonic integrated circuits. This promising approach relies on high accurate rotation of the wave plate about the optical axis which is attached to the calibrated robot. Rotating the wave plate produces a polarization shift, giving different polarization states with only one wave plate. The wave plate controls the polarization states in order to reach the desired polarization state and then integrating it to the optical system. Different investigations were realized. Rotating a mirror around the optical axis showed that it has no effect on the reflected polarization states, where rotating a wave plate around the optical axis mounted on a non-calibrated robot results a random and unexpected distribution of the reflected polarization states. After the full robot calibration, rotating a wave plate around the optical axis gave a circular distribution of the reflected polarization states. Introducing a misalignment angle leads to polarization information loss, with the same circular distribution of the polarization states. This is in full agreement with the theoretical models. Indeed, if the light beam is aligned with the optical axis, then only the ratio E_{0x}/E_{0y} changes when rotating the wave plate, which is expected to lead to a circle on the Poincaré sphere. The repeatability investigation showed a good repeatability of the circular distribution of the polarization states.

Future works

Photo-robotic micro-assembly with optimal optical performances for integrated optics.

The short term prospects is to combine all the 4 work contributions in order to achieve the whole procedure of photo-robotic micro-assembly with optimal optical performances for integrated optics. After having achieved the optimal optical performances based on our proposed photo-robotic approach, the second step is to control the optical polarization states to reach the desired polarization state. The third step is to realize contact detection based on the proposed approach in chapter 3, in order to identify the position that corresponds to the optimal optical irradiance along the optical axis toward the fiber. In the fourth step, we proposed to use UV-adhesive for bonding. Once the UV-adhesive drop is put, we position the optical component in the already identified position along the optical axis. The proposed procedure is shown in Figure 5.15.

Instrumented NanoTweezer based on Fabry-Perot interferometry measurement principle

In the literature, several works have studied robotic nano-assembly by using atomic force microscopes (AFM), scanning electron microscope (SEM) and nano-tweezers [Benson, 2011]. One of the main issues is the size of the components to manipulate, which can be as small as several tens of nanometers in the case of metamaterial plates. Additionally to the difficulty of handling such small objects, the challenge is also to ma-

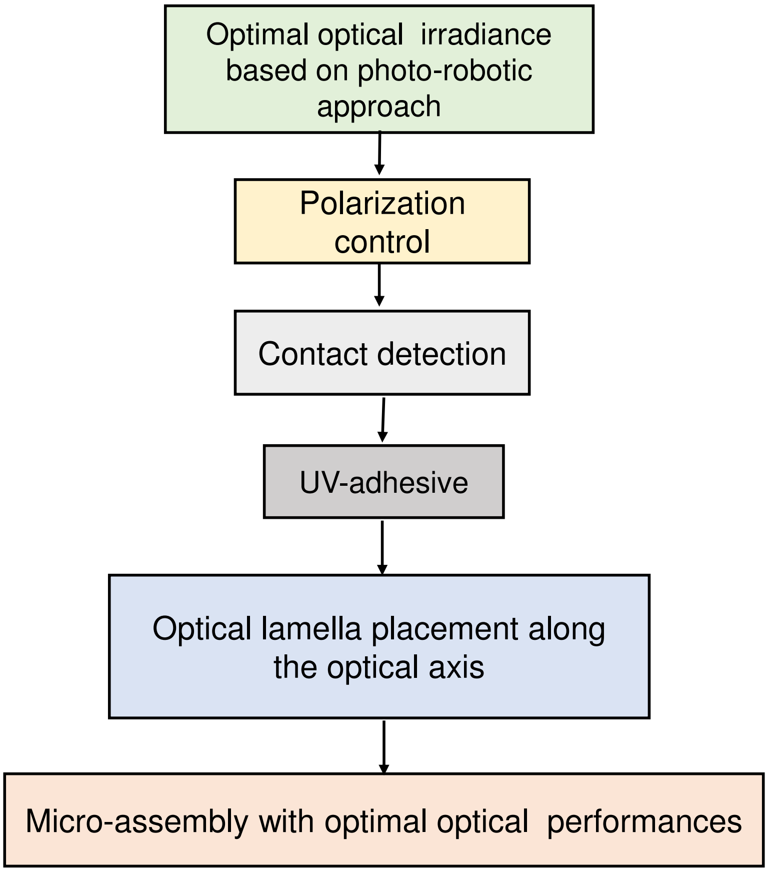

Figure 5.15: The whole proposed approach for micro-assembly with optimal optical performances for integrated optics.

nipulate the photonic elements without damaging them, and to position them inside the photonic circuits with a precision of the order of μrad in term of angles, and nanometer in term of distances. This task is all the more challenging as it has to take into account the dynamic adhesion forces that occur during positioning. By integrating force sensors in the micro-grippers, the scaling effect can be mastered, thereby increasing the dexterity for the assembly of small components while avoiding damages of the components and while controlling the contacts between the different photonic building blocks. We propose the development of a robotic tweezer for nano-manipulation that uses integrated optical principle consisting in using an optical fiber and the Fabry-Perot interferometric principle. This can meet high positioning accuracy and high manipulation abilities. Indeed, the gripper combines an innovative actuation principle based on smart materials (thick piezoelectric films) and integrated optical fibers (using Fabry-Perot interferometry) that enables on-line position measurement and gripping force estimation.

BIBLIOGRAPHY

[Agnus et al., 2008] Agnus, J., Boukallel, M., Clévy, C., Dembélé, S., et Régnier, S. (2008). **Architecture d'une station de micromanipulation.**

[Agnus et al., 2013] Agnus, J., Chaillet, N., Clévy, C., Dembélé, S., Gauthier, M., Haddab, Y., Laurent, G., Lutz, P., Piat, N., Rabenorosoa, K., et others (2013). **Robotic microassembly and micromanipulation at femto-st**. *Journal of Micro-Bio Robotics*, 8(2):91–106.

[Aoki et al., 2003] Aoki, K., Miyazaki, H. T., Hirayama, H., Inoshita, K., Baba, T., Sakoda, K., Shinya, N., et Aoyagi, Y. (2003). **Microassembly of semiconductor three-dimensional photonic crystals**. *Nature materials*, 2(2):117.

[Avci et al., 2015] Avci, E., Ohara, K., Nguyen, C.-N., Theeravithayangkura, C., Kojima, M., Tanikawa, T., Mae, Y., et Arai, T. (2015). **High-speed automated manipulation of microobjects using a two-fingered microhand**. *IEEE Transactions on Industrial Electronics*, 62(2):1070–1079.

[Benson, 2011] Benson, O. (2011). **Assembly of hybrid photonic architectures from nanophotonic constituents**. *Nature*, 480(7376):193.

[Bettahar et al., 2016] Bettahar, H., Caspar, A., Clévy, C., Courjal, N., et Lutz, P. (2016). **Photo-robotic positioning for integrated optics**. *IEEE Robotics and Automation Letters*, 2(1):217–222.

[Bingül et al., 2011] Bingül, Z., et Karahan, O. (2011). **Dynamic identification of staubli rx-60 robot using pso and ls methods**. *Expert Systems with Applications: An International Journal*, 38(4):4136–4149.

[Blöchliger et al., 2017] Blöchliger, F., Blösch, M., Fankhauser, P., Hutter, M., et Siegwart, R. (2017). **Foot-eye calibration of legged robot kinematics**. In *Advances in Cooperative Robotics*, pages 420–427. World Scientific.

[Born et al., 1999] Born, M., et Wolf, E. (1999). **Principles of optics, 7th (expanded) ed**. *Cambridge U. Press, Cambridge, UK*, 890.

[Böttger et al., 2016] Böttger, G., Weber, D., Scholz, F., Schröder, H., Schneider-Ramelow, M., et Lang, K.-D. (2016). **Fully automated hybrid diode laser assembly using high precision active alignment**. In *Components and Packaging for Laser Systems II*, volume 9730, page 97300E. International Society for Optics and Photonics.

[Boudaoud et al., 2012] Boudaoud, M., Haddab, Y., Le Gorrec, Y., et Lutz, P. (2012). **Study of thermal and acoustic noise interferences in low stiffness atomic force microscope cantilevers and characterization of their dynamic properties**. *Review of Scientific Instruments*, 83(1):013704.

[Carminati et al., 2015] Carminati, M., Grillanda, S., Ciccarella, P., Ferrari, G., Strain, M. J., Sampietro, M., Melloni, A., et Morichetti, F. (2015). **Fiber-to-waveguide alignment assisted by a transparent integrated light monitor**. *IEEE Photonics Technology Letters*, 27(5):510–513.

[Chaillet et al., 2013] Chaillet, N., et Régnier, S. (2013). **Microrobotics for micromanipulation**. John Wiley & Sons.

[Chiu et al., 2009] Chiu, C.-H., Wen, C.-M., Cheng, M.-Y., et Chuang, H.-S. (2009). **Positioning accuracy improvement of a vision-based optical fiber alignment motion stage based on fuzzy logic controller**. In *Control and Automation, 2009. ICCA 2009. IEEE International Conference on*, pages 2360–2365. IEEE.

[Clark et al., 2015] Clark, L., Shirinzadeh, B., Tian, Y., et Oetomo, D. (2015). **Laser-based sensing, measurement, and misalignment control of coupled linear and angular motion for ultrahigh precision movement**. *IEEE/ASME Transactions on Mechatronics*, 20(1):84–92.

[Clévy et al., 2014] Clévy, C., Lungu, I., Rabenorosoa, K., et Lutz, P. (2014). **Positioning accuracy characterization of assembled microscale components for micro-optical benches**. *Assembly Automation*, 34(1):69–77.

[Clévy et al., 2011] Clévy, C., Rakotondrabe, M., et Chaillet, N. (2011). **Signal measurement and estimation techniques for micro and nanotechnology**. Springer Science & Business Media.

[Cohen et al., 1992] Cohen, M. S., Cina, M. F., Bassous, E., Opyrsko, M., Speidell, J., Canora, F., et DeFranza, M. (1992). **Packaging of high density fiber/laser modules using passive alignment techniques**. *IEEE transactions on components, Hybrids, and Manufacturing Technology*, 15(6):944–955.

[Collett, 2003] Collett, E. (2003). **Polarized light in fiber optics**. SPIE Press.

[Corrielli et al., 2014] Corrielli, G., Crespi, A., Geremia, R., Ramponi, R., Sansoni, L., Santinelli, A., Mataloni, P., Sciarrino, F., et Osellame, R. (2014). **Rotated waveplates in integrated waveguide optics**. *Nature communications*, 5:4249.

[Dahdah et al., 2012] Dahdah, J., Hoblos, J., et Baida, F. I. (2012). **Nanocoaxial waveguide grating as quarter-wave plates in the visible range**. *IEEE Photonics J*, 4(1):87–94.

[Dai et al., 2012] Dai, D., Bauters, J., et Bowers, J. E. (2012). **Passive technologies for future large-scale photonic integrated circuits on silicon: polarization handling, light non-reciprocity and loss reduction**. *Light: Science & Applications*, 1(3):e1.

[Das et al., 2012] Das, A. N., Murthy, R., Popa, D. O., et Stephanou, H. E. (2012). **A multiscale assembly and packaging system for manufacturing of complex micro-nano devices**. *IEEE Transactions on Automation Science and Engineering*, 9(1):160–170.

[Datta et al., 2003] Datta, M., Hu, Z., et Dagenais, M. (2003). **A novel method for fabrication of a hybrid optoelectronic packaging platform utilizing passive-active alignment**. *Photonics Technology Letters, IEEE*, 15(2):299–301.

[Denavit, 1955] Denavit, J. (1955). **A kinematic notation for low pair mechanisms based on matrices**. *ASME J. Appl. Mech.*, 22:215–221.

[Devasia et al., 2007] Devasia, S., Eleftheriou, E., et Moheimani, S. R. (2007). **A survey of control issues in nanopositioning**. *IEEE Transactions on Control Systems Technology*, 15(5):802–823.

[Du et al., 2012] Du, B., Xi, N., et Nieves, E. (2012). **Industrial robot calibration using a virtual linear constraint.** *International Journal on Smart Sensing & Intelligent Systems*, 5(4).

[Elatta et al., 2004] Elatta, A., Gen, L. P., Zhi, F. L., Daoyuan, Y., et Fei, L. (2004). **An overview of robot calibration**. *Information Technology Journal*, 3(1):74–78.

[Escande et al., 2010] Escande, A., Mansard, N., et Wieber, P.-B. (2010). **Fast resolution of hierarchized inverse kinematics with inequality constraints**. In *ICRA 2010-IEEE International Conference on Robotics and Automation*, pages 3733–3738.

[Filion et al., 2018] Filion, A., Joubair, A., Tahan, A. S., et Bonev, I. A. (2018). **Robot calibration using a portable photogrammetry system**. *Robotics and Computer-Integrated Manufacturing*, 49:77–87.

[Fleming, 2013] Fleming, A. J. (2013). **A review of nanometer resolution position sensors: Operation and performance**. *Sensors and Actuators A: Physical*, 190:106–126.

[Friedrich et al., 1992] Friedrich, E. E., Oberg, M. G., Broberg, B., Nilsson, S., et Valette, S. (1992). **Hybrid integration of semiconductor lasers with si-based single-mode ridge waveguides**. *Journal of lightwave technology*, 10(3):336–340.

[Gauthier et al., 2015] Gauthier, M., Clévy, C., Hériban, D., et Kalio, P. (2015). **Industrial tools for micromanipulation**. In *Micro-and Nanomanipulation Tools*, volume 13. Wiley Online Library.

[Gu et al., 2016] Gu, H., Chen, X., Jiang, H., Zhang, C., Li, W., et Liu, S. (2016). **Accurate alignment of optical axes of a biplate using a spectroscopic mueller matrix ellipsometer**. *Applied optics*, 55(15):3935–3941.

[Guelpa et al., 2018] Guelpa, V., Kudryavtsev, A. V., Piat, N. L.-F., et Dembélé, S. (2018). **Accurate 3d-positioning in a sem through robot calibration**. In *2018 International Conference on Manipulation, Automation and Robotics at Small Scales (MARSS)*, pages 1–6. IEEE.

[Guelpa et al., 2015] Guelpa, V., Laurent, G. J., Sandoz, P., et Clévy, C. (2015). **Vision-based microforce measurement with a large range-to-resolution ratio using a twin-scale pattern**. *IEEE/ASME Transactions on Mechatronics*, 20(6):3148–3156.

[Guelpa et al., 2016] Guelpa, V., Sandoz, P., Vergara, M. A., Clévy, C., Le Fort-Piat, N., et Laurent, G. J. (2016). **2d visual micro-position measurement based on intertwined twin-scale patterns**. *Sensors and Actuators A: Physical*, 248:272–280.

[Guo et al., 2004] Guo, J., et Heyler, R. (2004). **Fast active alignment in photonics device packaging**. In *Electronic Components and Technology Conference, 2004. Proceedings. 54th*, volume 1, pages 813–817. IEEE.

[Guyot et al., 2014] Guyot, C., Ulliac, G., Dahdah, J., Qiu, W., Bernal, M.-P., Baida, F., et Courjal, N. (2014). **Optical characterization of ultra-short bragg grating on sslithium niobate ridge waveguide**. *Optics letters*, 39(2):371–374.

[Ha, 2008] Ha, I.-C. (2008). **Kinematic parameter calibration method for industrial robot manipulator using the relative position**. *Journal of mechanical science and technology*, 22(6):1084.

[Hage et al., 2011] Hage, H., Bidaud, P., et Jardin, N. (2011). **Practical consideration on the identification of the kinematic parameters of the stäubli tx90 robot**. In *Proceedings of the 13th World Congress in Mechanism and Machine Science, Guanajuato, Mexique*, page 43.

[Hasan et al., 2010] Hasan, A. T., Ismail, N., Hamouda, A. M. S., Aris, I., Marhaban, M. H., et Al-Assadi, H. (2010). **Artificial neural network-based kinematics jacobian solution for serial manipulator passing through singular configurations**. *Advances in Engineering Software*, 41(2):359–367.

[Hayashi, 1992] Hayashi, T. (1992). **An innovative bonding technique for optical chips using solder bumps that eliminate chip positioning adjustments**. *IEEE transactions on components, hybrids, and manufacturing technology*, 15(2):225–230.

[Hayati et al., 1985] Hayati, S., et Mirmirani, M. (1985). **Improving the absolute positioning accuracy of robot manipulators**. *Journal of Robotic Systems*, 2(4):397–413.

[Hecht, 2014] Hecht, E. (2014). **Optics. harlow**.

[Hecht et al., 2001] Hecht, E., et Zajac, A. (2001). **Optics, massachusetts**.

[Huard, 1993] Huard, S. (1993). **Polarisation de la lumière. 1993**.

[Huard, 1997] Huard, S. (1997). **Polarization of light**. *Polarization of Light, by Serge Huard, pp. 348. ISBN 0-471-96536-7. Wiley-VCH, January 1997.*, page 348.

[Ibarra et al., 1986] Ibarra, R., et Perreira, N. (1986). **Determination of linkage parameter and pair variable errors in open chain kinematic linkages using a minimal set of pose measurement data**. *Journal of Mechanisms, Transmissions, and Automation in Design*, 108(2):159–166.

[Jääskeläinen et al., 2009] Jääskeläinen, M., Sariola, V., et Zhou, Q. (2009). **Environmental effects on droplet self-alignment assisted hybrid microassembly**. In *Assembly and Manufacturing, 2009. ISAM 2009. IEEE International Symposium on*, pages 177–182. IEEE.

[Kapulainen et al., 2008] Kapulainen, M., Ylinen, S., Aalto, T., Harjanne, M., Solehmainen, K., Ollila, J., et Vilokkinen, V. (2008). **Hybrid integration of inp lasers with soi waveguides using thermocompression bonding**. In *5th IEEE International Conference on Group IV Photonics*.

[Karioja et al., 2000] Karioja, P., Ollila, J., Putila, V.-P., Keranen, K., Hakkila, J., et Kopola, H. (2000). **Comparison of active and passive fiber alignment techniques for multimode laser pigtailing**. In *Electronic Components & Technology Conference, 2000. 2000 Proceedings. 50th*, pages 244–249. IEEE.

[Kaufmann et al., 1986] Kaufmann, H., Buchmann, P., Hirter, R., Melchior, H., et Guekos, G. (1986). **Self-adjusted permanent attachment of fibres to gaas waveguide components**. *Electronics Letters*, 22(12):642–644.

[Khalil et al., 1999] Khalil, W., et Dombre, E. (1999). **Modélisation, identification et commande des robots**. Hermès science publ.

[Khalil et al., 2004] Khalil, W., et Dombre, E. (2004). **Modeling, identification and control of robots**. Butterworth-Heinemann.

[Khalil et al., 1995] Khalil, W., Garcia, G., et Delagarde, J.-F. (1995). **Calibration of the geometric parameters of robots without external sensors**. In *Robotics and Automation, 1995. Proceedings., 1995 IEEE International Conference on*, volume 3, pages 3039–3044. IEEE.

[Khalil et al., 1986] Khalil, W., et Kleinfinger, J. (1986). **A new geometric notation for open and closed-loop robots**. In *Robotics and Automation. Proceedings. 1986 IEEE International Conference on*, volume 3, pages 1174–1179. IEEE.

[Komati, 2014] Komati, B. (2014). **Automated microassembly using an active microgripper with sensorized end-effectors and hybrid force/position control**. PhD thesis, Université de Franche-Comté.

[Komati et al., 2016] Komati, B., Clévy, C., et Lutz, P. (2016). **High bandwidth microgripper with integrated force sensors and position estimation for the grasp of multistiffness microcomponents**. *IEEE/ASME Transactions on Mechatronics*, 21(4):2039–2049.

[Kratochvil et al., 2009] Kratochvil, B. E., Dong, L., et Nelson, B. J. (2009). **Real-time rigid-body visual tracking in a scanning electron microscope**. *The International Journal of Robotics Research*, 28(4):498–511.

[Krishnamoorthy et al., 2009] Krishnamoorthy, A. V., Cunningham, J. E., Zheng, X., Shubin, I., Simons, J., Feng, D., Liang, H., Kung, C.-C., et Asghari, M. (2009). **Optical proximity communication with passively aligned silicon photonic chips**. *IEEE Journal of Quantum Electronics*, 45(4):409–414.

[Kudryavtsev et al., 2015] Kudryavtsev, A. V., Laurent, G. J., Clévy, C., Tamadazte, B., et Lutz, P. (2015). **Stereovision-based control for automated moems assembly**. In *2015 IEEE/RSJ International Conference on Intelligent Robots and Systems (IROS)*, pages 1391–1396. IEEE.

[Landry et al., 2013] Landry, M., Kaddouri, A., Bouslimani, Y., et Ghribi, M. (2013). **Automated alignment of microstructured optical fibers and conventional single-mode fibers**. *Optical Engineering*, 52(6):065003.

[Li et al., 2005] Li, B., Wirz, H., et Sharon, A. (2005). **Optimizing fiber coupling with a quasi-passive microoptical bench**. *Journal of microelectromechanical systems*, 14(6):1339–1346.

[Li et al., 2012] Li, Y., et Xu, Q. (2012). **Design and robust repetitive control of a new parallel-kinematic xy piezostage for micro/nanomanipulation**. *IEEE/ASME Transactions on Mechatronics*, 17(6):1120–1132.

[Li et al., 2015] Li, Z., Liu, W., Cheng, H., Chen, S., et Tian, J. (2015). **Realizing broadband and invertible linear-to-circular polarization converter with ultrathin single-layer metasurface**. *Scientific reports*, 5:18106.

[Lin et al., 2013] Lin, F.-J., Lee, S.-Y., et Chou, P.-H. (2013). **Computed force control system using functional link radial basis function network with asymmetric membership function for piezo-flexural nanopositioning stage**. *IET Control Theory & Applications*, 7(18):2128–2142.

[Liu et al., 2012] Liu, L., Pal, S., et Xie, H. (2012). **Mems mirrors based on a curved concentric electrothermal actuator**. *Sensors and Actuators A: Physical*, 188:349–358.

[Maroufi et al., 2015] Maroufi, M., Bazaei, A., et Moheimani, S. R. (2015). **A high-bandwidth mems nanopositioner for on-chip afm: Design, characterization, and control**. *IEEE Transactions on Control Systems Technology*, 23(2):504–512.

[Mattos et al., 2009] Mattos, L. S., et Caldwell, D. G. (2009). **A fast and precise micropipette positioning system based on continuous camera-robot recalibration and visual servoing**. In *Automation Science and Engineering, 2009. CASE 2009. IEEE International Conference on*, pages 609–614. IEEE.

[Messay et al., 2016] Messay, T., Ordóñez, R., et Marcil, E. (2016). **Computationally efficient and robust kinematic calibration methodologies and their application to industrial robots**. *Robotics and Computer-Integrated Manufacturing*, 37:33–48.

[Miyazaki et al., 2000] Miyazaki, H. T., Miyazaki, H., Ohtaka, K., et Sato, T. (2000). **Photonic band in two-dimensional lattices of micrometer-sized spheres mechanically arranged under a scanning electron microscope**. *Journal of Applied Physics*, 87(10):7152–7158.

[Morin, 2013] Morin, P. (2013). **Nouveaux systèmes de contrôle de la polarisation de la lumière par effets non linéaires dans les fibres optiques**. PhD thesis, Université de Bourgogne.

[Mousavi et al., 2015] Mousavi, S. A., Plum, E., Shi, J., et Zheludev, N. I. (2015). **Coherent control of optical polarization effects in metamaterials**. *Scientific reports*, 5:8977.

[Nie et al., 2010] Nie, Z., Petukhova, A., et Kumacheva, E. (2010). **Properties and emerging applications of self-assembled structures made from inorganic nanoparticles**. *Nature nanotechnology*, 5(1):15.

[Nubiola et al., 2014] Nubiola, A., Slamani, M., Joubair, A., et Bonev, I. A. (2014). **Comparison of two calibration methods for a small industrial robot based on an optical cmm and a laser tracker**. *Robotica*, 32(3):447–466.

[Paul, 1981] Paul, R. P. (1981). **Robot manipulators: mathematics, programming, and control: the computer control of robot manipulators**. Richard Paul.

[Peatross et al., 2011] Peatross, J., et Ware, M. (2011). **Physics of light and optics**. Brigham Young University, Department of Physics.

[Peiper, 1968] Peiper, D. L. (1968). **The kinematics of manipulators under computer control**. Technical Report, Stanford Univ Ca Dept Of Computer Science.

[Poincaré, 1892] Poincaré, H. (1892). **Leçons sur la théorie de l'élasticité**. Georges Carré.

[Popa et al., 2009] Popa, D. O., Murthy, R., et Das, A. N. (2009). **M^3-deterministic, multiscale, multirobot platform for microsystems packaging: Design and quasi-static precision evaluation**. *IEEE Transactions on Automation Science and Engineering*, 6(2):345–361.

[Raghavan et al., 1993] Raghavan, M., et Roth, B. (1993). **Inverse kinematics of the general 6r manipulator and related linkages**. *Journal of Mechanical Design*, 115(3):502–508.

[Rakotondrabe et al., 2010] Rakotondrabe, M., Clévy, C., et Lutz, P. (2010). **Complete open loop control of hysteretic, creeped, and oscillating piezoelectric cantilevers**. *IEEE Transactions on Automation Science and Engineering*, 7(3):440–450.

[Reiss et al., 2009] Reiss, P., Protiere, M., et Li, L. (2009). **Core/shell semiconductor nanocrystals**. *small*, 5(2):154–168.

[REN et al., 2008] REN, Y.-j., ZHU, J.-g., YANG, X.-y., et Ye, S.-h. (2008). **Measurement robot calibration model and algorithm based on distance accuracy**. *Acta Metrologica Sinica*, 3:002.

[Santolaria et al., 2008] Santolaria, J., Aguilar, J.-J., Yagüe, J.-A., et Pastor, J. (2008). **Kinematic parameter estimation technique for calibration and repeatability improvement of articulated arm coordinate measuring machines**. *Precision Engineering*, 32(4):251–268.

[Santolaria et al., 2009] Santolaria, J., Yagüe, J.-A., Jiménez, R., et Aguilar, J.-J. (2009). **Calibration-based thermal error model for articulated arm coordinate measuring machines**. *Precision Engineering*, 33(4):476–485.

[Sariola et al., 2010] Sariola, V., Jääskeläinen, M., et Zhou, Q. (2010). **Hybrid microassembly combining robotics and water droplet self-alignment**. *intelligence*, 4:9.

[Sassen et al., 2008] Sassen, W., Henneken, V., Tichem, M., et Sarro, P. (2008). **An improved in-plane thermal folded v-beam actuator for optical fibre alignment**. *Journal of Micromechanics and Microengineering*, 18(7):075033.

[Shiakolas et al., 2002] Shiakolas, P., Conrad, K., et Yih, T. (2002). **On the accuracy, repeatability, and degree of influence of kinematics parameters for industrial robots**. *International journal of modelling and simulation*, 22(4):245–254.

[Stokes, 1851] Stokes, G. G. (1851). **On the composition and resolution of streams of polarized light from different sources**. *Transactions of the Cambridge Philosophical Society*, 9:399.

[Sugihara, 2011] Sugihara, T. (2011). **Solvability-unconcerned inverse kinematics by the levenberg–marquardt method**. *IEEE Transactions on Robotics*, 27(5):984–991.

[Švaco et al., 2014] Švaco, M., Šekoranja, B., Šuligoj, F., et Jerbić, B. (2014). **Calibration of an industrial robot using a stereo vision system**. *Procedia Engineering*, 69:459–463.

[Takigawa et al., 2011] Takigawa, R., Higurashi, E., Suga, T., et Kawanishi, T. (2011). **Passive alignment and mounting of linbo $_3$ waveguide chips on si substrates by low-temperature solid-state bonding of au**. *IEEE Journal of Selected Topics in Quantum Electronics*, 17(3):652–658.

[Tamadazte et al., 2011] Tamadazte, B., Piat, N. L.-F., et Dembélé, S. (2011). **Robotic micromanipulation and microassembly using monoview and multiscale visual servoing**. *IEEE/ASME Transactions on Mechatronics*, 16(2):277–287.

[Tan, 2013] Tan, N. (2013). **Calibration of micro and nanorobotic systems: Contribution of influential parameters to the geometric accuracy.** PhD thesis, Université de Franche-Comté.

[Tan et al., 2015a] Tan, N., Clévy, C., et Chaillet, N. (2015a). **Calibration of nanopositioning stages**. *Micromachines*, 6(12):1856–1875.

[Tan et al., 2015b] Tan, N., Clevy, C., Laurent, G., Sandoz, P., et Chaillet, N. (2015b). **Accuracy quantification and improvement of serial micropositioning robots for in-plane motions**. *IEEE Transactions on Robotics*, 31(6):1497 – 1507.

[Tan et al., 2015c] Tan, N., Clévy, C., Laurent, G. J., Sandoz, P., et Chaillet, N. (2015c). **Accuracy quantification and improvement of serial micropositioning robots for in-plane motions**. *IEEE Transactions on robotics*, 31(6):1497–1507.

[Tang et al., 2001] Tang, Z., Zhang, R., et Shi, F. (2001). **Effects of angular misalignments on fiber-optic alignment automation**. *Optics Communications*, 196(1-6):173–180.

[Torbrügge et al., 2010] Torbrügge, S., Schaff, O., et Rychen, J. (2010). **Application of the kolibrisensor® to combined atomic-resolution scanning tunneling microscopy and noncontact atomic-force microscopy imaging**. *Journal of Vacuum Science & Technology B, Nanotechnology and Microelectronics: Materials, Processing, Measurement, and Phenomena*, 28(3):C4E12–C4E20.

[Tseng et al., 2005] Tseng, C.-Y., et Wang, J.-P. (2005). **Automation of multi-degree-of-freedom fiber-optic alignment using a modified simplex method**. *International Journal of Machine Tools and Manufacture*, 45(10):1109–1119.

[van Gurp et al., 2013] van Gurp, J. F. C., Tichem, M., Staufer, U., et Zhao, J. (2013). **Passive photonic alignment with submicrometer repeatability and accuracy**. *Components, Packaging and Manufacturing Technology, IEEE Transactions on*, 3(11):1971–1979.

[Veitschegger et al., 1986] Veitschegger, W., et Wu, C.-H. (1986). **Robot accuracy analysis based on kinematics**. *IEEE Journal on Robotics and Automation*, 2(3):171–179.

[Wang et al., 2014] Wang, H.-Y., Fan, K.-C., Ye, J.-K., et Lin, C.-H. (2014). **A long-stroke nanopositioning control system of the coplanar stage**. *IEEE/ASME Transactions on Mechatronics*, 19(1):348–356.

[Weber et al., 2012] Weber, N., Zappe, H., et Seifert, A. (2012). **A tunable optofluidic silicon optical bench**. *Journal of Microelectromechanical Systems*, 21(6):1357–1364.

[Wold et al., 1984] Wold, S., Ruhe, A., Wold, H., et Dunn, III, W. (1984). **The collinearity problem in linear regression. the partial least squares (pls) approach to generalized inverses**. *SIAM Journal on Scientific and Statistical Computing*, 5(3):735–743.

[Wu et al., 2010] Wu, J., Wang, J., et You, Z. (2010). **An overview of dynamic parameter identification of robots**. *Robotics and computer-integrated manufacturing*, 26(5):414–419.

[Zhang et al., 2018] Zhang, J., Wang, X., Wen, K., Zhou, Y., Yue, Y., et Yang, J. (2018). **A simple and rapid calibration methodology for industrial robot based on geometric constraint and two-step error**. *Industrial Robot: An International Journal*.

[Zhang, 2004] Zhang, R. (2004). **Study of novel algorithms for fiber-optic alignment and packaging automation.**

[Zhang et al., 2003] Zhang, R., et Shi, F. G. (2003). **Novel fiber optic alignment strategy using hamiltonian algorithm and matlab/simulink**. *Optical Engineering*, 42(8):2240–2246.

[Zhao et al., 2018] Zhao, D., Dong, C., Guo, H., et Tian, W. (2018). **Kinematic calibration based on the multicollinearity diagnosis of a 6-dof polishing hybrid robot using a laser tracker**. *Mathematical Problems in Engineering*, 2018.

[Zhao et al., 2015] Zhao, Y. M., Lin, Y., Xi, F., et Guo, S. (2015). **Calibration-based iterative learning control for path tracking of industrial robots**. *IEEE Transactions on industrial electronics*, 62(5):2921–2929.

[Zheng et al., 2009] Zheng, Y., et Duan, J.-a. (2009). **Coupling analysis between planar optical waveguide and fiber array [j]**. *Journal of Central South University (Science and Technology)*, 3:026.

[Zheng et al., 2012] Zheng, Y., et Duan, J.-a. (2012). **Alignment algorithms for planar optical waveguides**. *Optical Engineering*, 51(10):103401–1.

[Zhenhua et al., 2014] Zhenhua, W., Hui, X., Guodong, C., Rongchuan, S., et Sun, L. (2014). **A distance error based industrial robot kinematic calibration method**. *Industrial Robot: An International Journal*, 41(5):439–446.

[Zhou et al., 2002] Zhou, Q., del Corral, C., Esteban, P. J., Aurelian, A., et Koivo, H. N. (2002). **Environmental influences on microassembly**. In *Intelligent Robots and Systems, 2002. IEEE/RSJ International Conference on*, volume 2, pages 1760–1765. IEEE.

[Zhuang et al., 1995] Zhuang, H., Masory, O., et Yan, J. (1995). **Kinematic calibration of a stewart platform using pose measurements obtained by a single theodolite**. In *Intelligent Robots and Systems 95.'Human Robot Interaction and Cooperative Robots', Proceedings. 1995 IEEE/RSJ International Conference on*, volume 2, pages 329–334. IEEE.

[Zhuang et al., 1996] Zhuang, H., et Roth, Z. S. (1996). **Camera-aided robot calibration**. CRC press.

[Zimmermann et al., 2011] Zimmermann, L., Preve, G. B., Tekin, T., Rosin, T., et Landles, K. (2011). **Packaging and assembly for integrated photonics-a review of the epix-pack photonics packaging platform**. *IEEE Journal of Selected Topics in Quantum Electronics*, 17(3):645–651.

[Zimmermann et al., 2015] Zimmermann, S., Tiemerding, T., et Fatikow, S. (2015). **Automated robotic manipulation of individual colloidal particles using vision-based control**. *IEEE/ASME Transactions on Mechatronics*, 20(5):2031–2038.

LIST OF FIGURES

LIST OF TABLES

Title: High accurate 3-D photo-robotic nano-positioning for hybrid integrated optics.

Keywords: Nano-positioning, Micro-assembly, Micro-robotics, Photo-robotic, Robot calibration, integrated optics.

Abstract :

The hybrid integration of individual photonic elements appears as promising, because it may provide high performances, propose new optical functionalities and products and exploit new propagation modes of light beams. This approach requires an accurate multi Degree-Of-Freedom (DOF) positioning of the individual photonic elements. Hence, the inaccurate multi-DOF measurement and robots control are the main locks to overcome, notably at the micro-scale. For this sake, an original photo-robotic approach has been proposed, relying on multi-DOF robot motion associated with the use of 1-D Fabry-Perot interferometry measure to realize multi-DOF pose measure. This approach notably integrates the issue of 6-DOF robot calibration that has been studied through extrinsic and/or intrinsic geometric parameters calibration. In order to find the appropriate calibration strategy for high positioning accuracy and adapted to the context of micro-positioning of optical components, a quantification and durability analysis of optical and robotic performances have been investigated. Experimental investigations demonstrate that a rotational and translational positioning accuracy of 0.004° and 27.6 nm have been obtained respectively.

This photo-robotic approach has especially been applied to achieve the 6-DOF positioning of an optical lamella relative to an optical fiber with high accuracy that also conduct to maximum optical performances. The approach has also been applied to control the optical polarization states at the output of an hybrid optical system through achieving high accurate rotations of a specific optical wave plate around the optical axis. The experimental results notably demonstrate that the high positioning accuracy enables to accurately control of the optical polarization state.

Titre : Nano-positionnement photo-robotique 3-D de haute précision pour l'optique hybride intégrée.

Mots clés : Nano-positionnement, Micro-assemblage, Micro-robotique, Photo-robotique, Etalonnage des robots, Optique intégrée.

Résumé :

L'intégration hybride d'éléments photoniques individuels offre la promesse de fournir des performances très élevées, de proposer de nouvelles fonctionnalités et produits optiques mais aussi pour exploiter de nouveaux modes de propagation des faisceaux lumineux. Cette approche repose sur la capacité d'un positionnement multi Degré-De-Liberté (DDL) précis des éléments photoniques individuels. Ainsi, la mesure multi-DDL imprécise et le contrôle inexact des robots sont les principaux verrous à surmonter, notamment à l'échelle micrométrique. Pour cela, une approche photo-robotique originale a été proposée, s'appuyant sur les mouvements d'un robot à plusieurs DDL associé à l'utilisation de l'interférométrie Fabry-Perot 1-D pour réaliser une mesure de pose multi-DOF. Cette approche intègre notamment la question de l'étalonnage des robots 6-DDL qui a été étudiée à travers l'étalonnage des paramètres géométriques extrinsèques et/ou intrinsèques. Afin de trouver la stratégie d'étalonnage appropriée pour une grande précision de positionnement et adaptée au contexte du micro-positionnement de composants optiques, une quantification et une analyse de durabilité des performances optiques et robotiques ont été étudiées. Des études expérimentales ont démontré qu'une précision de positionnement en rotation et en translation de 0.004° et 27.6 nm ont été obtenues respectivement.

Cette approche photo-robotique a été notamment appliquée pour réaliser le positionnement 6-DDL d'une lamelle optique par rapport à une fibre optique avec une grande précision ce qui conduit également à des performances optiques maximales. L'approche a également été appliquée pour contrôler les états de polarisation à la sortie d'un système optique hybride en réalisant des rotations très précises d'une lamelle d'onde optique spécifique autour de son axe optique. Les résultats expérimentaux démontrent notamment que la grande précision du positionnement permet un contrôle précis de l'état de polarisation optique.

Université Bourgogne Franche-Comté
32, avenue de l'Observatoire
25000 Besançon